SDU NEWTEC

Ph.D. Thesis

Advances in Hyperspectral Long Wave Infrared Imaging

System Modeling and Applications

Author
Mads Nibe Larsen

Supervisors
Jakob Kjelstrup-Hansen
Bjarke Jørgensen

A thesis submitted in fulfillment of the requirements for the degree of Doctor of Philosophy

January 2025

Mads Clausen Institute
The Faculty of Engineering
University of Southern Denmark

Use of LaTeX template

The layout of this thesis is based on a LaTeX template by Goro Akechi. It is licensed under the Creative Commons Attribution-NonCommercial 4.0 License, which can be found at https://creativecommons.org/licenses/by-nc-sa/4.0.

Acknowledgment of AI Assistance

Portions of this thesis have been developed with the assistance of AI-generated text such as ChatGPT and Grammarly. The AI was used to improve clarity, streamline the writing process, and provide suggestions for phrasing. All content has been carefully reviewed and edited to ensure accuracy, originality, and alignment with the thesis objectives. Additionally, AI-generated images created using tools like Midjourney and Adobe Firefly have been incorporated to enhance the visual presentation of the thesis. These images serve purely aesthetic purposes and do not influence the interpretation or understanding of the content.

Abstract

This industrial PhD project represents a collaboration between Newtec Engineering A/S and NanoSYD at the University of Southern Denmark, with financial support from the Innovation Fund Denmark. The project focuses on the development and application of a hyperspectral imaging system that combines a microbolometer-based thermal camera and a low-order scanning Fabry-Pérot interferometer (SFPI). The system operates in the long-wave infrared (LWIR) spectral range, ranging from 8 µm to 15 µm wavelengths. The SFPI consists of two partially transmitting, mutually parallel mirrors placed only micrometers apart to form an optical cavity. The precise cavity length determines the distribution of transmitted wavelengths, and by capturing images at different cavity lengths, hyperspectral data cubes can be generated.

A substantial portion of this thesis is dedicated to describing and modeling the SFPI, which gives the imaging system its hyperspectral capabilities. Unlike conventional systems that provide spectral information in terms of wavelengths or wavenumbers, the SFPI acquires an interferogram with the spectral axis expressed in terms of the cavity length. This presents unique challenges in data processing and interpretation of results.

A key challenge is understanding how incident radiation transforms into recorded interferograms. An even more complex issue arises in the inverse process: converting the interferograms to the wavelength domain. This inverse problem is inherently underdetermined, which makes the reconstruction process non-trivial. Several potential solutions to this problem are explored in detail.

Finally, this thesis highlights several potential applications of the proposed technology, including classifying commercial plastics containing carbon black, mineral analysis, and detecting hydrocarbon fuel signatures through flame imaging. These applications demonstrate the versatility and promise of the hyperspectral imaging system within various scientific and industrial contexts.

Resumé

Dette industrielle ph.d.-projekt er et samarbejde mellem Newtec Engineering A/S og NanoSYD ved Syddansk Universitet med finansiel støtte fra Innovationsfonden. Projektet fokuserer på udvikling og anvendelse af et hyperspektralt billedsystem, der kombinerer et termisk kamera udstyret med en mikrobolometerdetektor og et lavordens skannende Fabry-Pérot-interferometer (SFPI). Systemet opererer i det langbølgede infrarøde (LWIR - Long Wave Infrared) spektralområde, der dækker bølgelængder fra 8 µm til 15 µm. SFPI'et består af to delvist transmitterende spejle, som er placeret tæt på hinanden (i størrelsesordenen mikrometer) for at danne et optisk kavitet. Den præcise kavitetlængde er afgørende for fordelingen af transmitterede bølgelængder. Det er muligt at konstruere en hyperspektral datakube ud fra billeder taget ved forskellige kavitetslængder.

En væsentlig del af denne afhandling er dedikeret til at beskrive og modellere SFPI'et, som giver billedsystemet dets hyperspektrale egenskaber. I modsætning til konventionelle systemer, hvor den spektrale akse agives i bølgelængder eller i bølgetal, måler SFPI'et i kavitetlængder, hvilket effektivt resulterer i et interferogram. Dette medfører unikke udfordringer både inden for databehandling og ved fortolkningen af resultater.

En central udfordring er at forstå sammenhængen mellem den indkommende stråling og de målte interferogrammer. En endnu mere kompleks problemstilling opstår ved det inverse problem, hvor interferogrammerne skal konverteres tilbage til bølgelængde-domænet. Denne inverse problemstilling er underbestemt, hvilket vansekliggør beregningerne. Flere potentielle løsninger på dette problem udforskes i detaljer.

Afslutningsvis fremhæver denne afhandling flere potentielle anvendelser af den præsenterede teknologi, herunder klassifikation af kommercielle, sorte plasttyper, mineralanalyse og klassificering af forskellige kulbrinteholdige flammer. Disse anvendelser demonstrerer alsidigheden af det hyperspektrale billedsyst og dets potentiale inden for forskellige videnskabelige og industrielle sammenhænge.

Acknowledgements

This thesis marks the culmination of three years of work with the hyperspectral long-wave infrared imager, as detailed in the many following pages. It would not have been possible without the support and guidance of many individuals, to whom I am deeply grateful.

First and foremost, I express my sincere gratitude to my supervisors, Jakob Kjelstrup-Hansen from SDU and Bjarke Jørgensen from Newtec Engineering A/S. Their guidance has been invaluable in helping me navigate this project, distinguishing between my good ideas and those more questionable. Their support, encouragement, and ability to help me stay focused and motivated have been instrumental, especially during challenging moments when the project felt particularly demanding.

I have been fortunate to work alongside a wonderful group of colleagues and collaborators at Newtec, who have made daily life both enjoyable and rewarding. In particular, I would like to thank Anders Løcthe Jørgensen for being an exceptional sidekick in driving this project forward. It has been a pleasure brainstorming solutions and improvements for the imager and embarking on road trips across Denmark to test its capabilities, even freezing our fingers off in the cold Danish weather. Special thanks are also due to Victor Petrunin, whose profound insights and expertise in physics and spectrometry have been invaluable in diagnosing challenges with the camera - especially when my intuition led me astray. Additionally, I wish to express my gratitude to my other colleagues at Newtec, especially to Henrik Andersen, Marianna Buschle, Elmedina (Dina) Dervisevic, Sune Fink, Mathias Hansen, Wei-Chih Huang, Bjarke Jensen, Jens-Christian Pedersen, and Mads Peters. It has been an honor and privilege to share my daily work with all of you.

I want to express my gratitude to Dr. Andersen Ang from the University of Southampton for generously sharing his expertise in linear algebra. A significant portion of chapter 5 owes its existence to his guidance and insights. Remarkably, he was always reachable, regardless of the hour, and never settled for a brief answer, ensuring every discussion was both enlightening and comprehensive.

During this project, I had the privilege of being part of Mogens Hinge's research group, Plastic and Polymer Engineering, at the Department of

Biological and Chemical Engineering, Aarhus University. Here, I had the pleasure of meeting and working with many wonderful people. My office mates, Ditte Gravgaard, Rune Groven, and Iben Hansen-Bruhn, deserve special mention for making the long train rides absolutely worth it. Whether it was sharing ice cream, drinking beers while dressed as unicorns, or, on rare occasions, actually working, you made every moment a delight. Collaborating with Mogens Hinge and Martin Henriksen was equally rewarding, particularly in advancing the project's work on plastic classification. This was true even as Mogens and I occasionally debated the optimal amount of colors to include in scientific publications - the answer might depend on who you ask.

I cannot forget to thank my amazing friends, who consistently reminded me that life is about more than thermal cameras, interferometers, and expensive hot plates. Whether it's unwinding with spike ball on Tuesdays, hammering nails and Beaujolais on the weekend, having huge laughs and discussing the state of the world over some remarkably average games of Rocket League, laughing and cursing (mostly the latter) on the golf course, or indulging in late-night ice cream sessions, you've all been there to recharge my batteries and keep me going. Your support has been as vital as anything else in this project.

I want to thank my family, especially my parents, who patiently listened to my thoughts and challenges over the years. Their support, particularly towards the end of this project, was invaluable. I am especially grateful for their help as an impromptu food delivery service. It made the writing process much easier by stocking the fridge with classics such as "meatballs in curry" and "Swedish-style sausage dish".

Also, I must not forget to thank Chad for being a patient and ever-available collaborator. Whether helping me rewrite sentences or keeping me company during late-night writing sessions, your assistance was invaluable.

Finally, I extend my gratitude to everyone I have had the pleasure of interacting with over the past three years who is not mentioned above. This thesis reflects not only my work but also stands as a testament to your support and encouragement.

Thank you

Contents

I Project Background

1 Introduction 3

2 Background 7

2.1 Fundamentals of Light 8

2.1.1 Wavelenghts and Wavenumbers 10

2.2 Radiometry 11

2.2.1 Absorptance, Reflectance, and Transmittance 19

2.3 Blackbody radiation 21

2.3.1 Emissivity 27

2.4 Hyperspectral Imaging 31

2.4.1 Hyperspectral Imaging Techniques 32

2.5 Processing Methods for Hyperspectral Data 34

2.6 Principal Component Analysis 39

2.7 Summary 42

3 Long-Wave Infrared Hyperspectral Imager 43

3.1 Overview of Hyperspectral Imager 44

3.2 Camera Body 46

3.3 Microbolometer 48

3.3.1 Temperature Change of Microbolometer 49

3.3.2 Measuring Temperature Change of Microbolometer 51

3.3.3 Non-Uniformity Correction 52
3.3.4 Photon Detectors 52
3.4 Thermal Lens 55
3.5 Overview of Scanning Fabry-Pérot Interferometer . . 56
3.5.1 Dielectric mirrors 56
3.5.2 Mirror Mounting and Displacement 57
3.5.3 Mirror Control 59
3.6 Summary 64

II Scanning Fabry-Pérot Interferometer

4 Scanning Fabry-Pérot Interferometer 67
4.1 Interference 68
4.1.1 Interference Condition of a Fabry-Pérot Interferometer . . 70
4.2 The Airy Function 71
4.2.1 Interference Conditions Based on Physical Units 75
4.2.2 Free Spectral Range 75
4.2.3 Fabry-Pérot Full Width at Half Maximum 76
4.2.4 Spectral Resolution 77
4.2.5 Dispersion 78
4.3 Concave Mirror Substrates 80
4.4 Angular Spectral Shift 83
4.5 The Transfer Matrix Method 87
4.5.1 Calculating Refractive Indices 92
4.6 Generalized Matrix Method 94
4.6.1 Modelling Concave Mirror Substrates in GMM 97
4.7 Spectral Resolution Based on GMM Calculations . 100
4.8 Measuring SFPI Transmittance Matrix Using FTIR . . . 102
4.9 Phase Change Upon Reflection 104
4.10 Summary 109

5 Spectral Reconstruction 111
5.1 Modelling the Imaging System 112

5.2 Estimation of Detector's Spectral Response 114
5.2.1 Least Squares Solution 119
5.2.2 Solution Using Gradient Descent 122
5.2.3 System Response Matrix 128
5.3 Converting Interferogram to Spectrum 129
5.3.1 Fourier Transform 129
5.3.2 Remapping of Interferograms 130
5.3.3 Solving for the Incident Spectrum Explicitly 133
5.3.4 Nonnegative Matrix Factorization 134
5.3.5 Sensitivity to Spectral Misalignment 143
5.4 Summary 145

III Practical Applications

6 Plastic Classification 149
6.1 Introduction to Hyperspectral Imaging of Plastics . 150
6.2 Materials and Methods 151
6.2.1 Samples and Experimental Setup 151
6.2.2 Data Processing 155
6.2.3 Classification Method 158
6.3 Results and Discussion 159
6.3.1 Non-black Plastics 159
6.3.2 Black Plastics 164
6.3.3 Industrial Implications 167
6.4 Conclusions 168

7 Analysis of Diffusion Flames 169
7.1 Introduction to Flame Imaging and Spectroscopy 170
7.2 Materials and Methods 171
7.2.1 Experimental Setup 171
7.2.2 Data Processing 172
7.3 Results and Discussion 176
7.3.1 Spectral Analysis of Hydrogen Flame 176
7.3.2 Analysis of Regions of Interest 177
7.3.3 Pearson Correlation Coefficient Analysis 178

7.3.4 Principal Component Analysis 180
7.4 Conclusions 183

8 Various Preliminary Studies 185
8.1 Combination of Incidence Spectra 186
8.2 Relationship Between Absorbance and Interferogram Intensity 187
8.3 Imaging Reflections 189
8.3.1 Experimental Setup 189
8.3.2 Results and Discussion 190
8.4 Imaging Minerals 197
8.4.1 Imaging Mineral Samples 197
8.4.2 Imaging Gemstones 201
8.4.3 Imaging Cliff Face 205
8.5 Applications' summary 208

IV Summary and Outlook

9 Summary and Outlook 211

V Appendices

A Conference Proceedings: A hyperspectral thermal imager based on a low order scanning Fabry-Pérot interferometer 217

B Paper: Classification of commercial plastics using hyperspectral long wave infrared emission imaging 229

C Paper: Classification of black plastic types by hyperspectral imaging based on long-wave infrared emission spectroscopy 239

D Manuscript: Long-wave infrared hyperspectral imager based on a scanning Fabry-Pérot interferometer 249

E Manuscript: Signatures of Flames by Long-Wave Infrared Hyperspectral Imaging 273

F Digital PID Controller for SFPI 325

G Generalized Matrix Method Python Function . 329

H Python GUI: Hyperspectral Viewer 341

I Posters 347

I.1 International Association for Spectral Imaging 2022 348

I.2 SPIE Defence and Commercial Sensing 2024 349

I.3 International Association for Spectral Imaging 2024 350

Bibliography 351

Index 363

List of Abbreviations

AGD	**A**ccelerated **G**radient **D**escent
AR	**A**nti-**R**eflective
BB	**B**lack**b**ody
CVD	**C**hemical **V**apor **D**eposition
FFT	**F**ast **F**ourier **T**ransvorm
FN	**F**alse **N**egative
FOV	**F**ield **o**f **V**iew
FP	**F**alse **P**ositive
FSR	**F**ree **S**pectral **R**ange
FTIR	**F**ourier **T**ransform **I**nfrared
FWHM	**F**ull **W**idth at **H**alf **M**aximum
GGG	**G**adolinium **G**allium **G**arnet
GMM	**G**eneralized **M**atrix **M**ethod
GT	**G**round **T**ruth
GUI	**G**raphical **U**ser **I**nterface
HPHT	**H**igh-**P**ressure **H**igh-**T**emperature
HSC	**H**yper**s**pectral **C**amera
HSI	**H**yper**s**pectral **I**mage
LED	**L**ight **E**mitting **D**iode
LN	**L**iquid **N**itrogen
LWIR	**L**ong-**W**ave **I**nfra**r**ed
MCT	**M**ercury-**C**admium-**T**elluride
MSI	**M**ulti**s**pectral **I**maging
MSE	**M**ean **S**quared **E**rror
MWIR	**M**id-**W**ave **I**nfra**r**ed
NaN	**N**ot-**a**-**N**umber
NEP	**N**oise **E**quivalent **P**ower
NETD	**N**oise **E**quivalent **T**emperature **D**ifference

NMF	**N**onnegative **M**atrix **F**actorization
NUC	**N**on-**U**niformity **C**orrection
PCA	**P**rincipal **C**omponent **A**nalysis
PCB	**P**rinted **C**ircuit **B**oard
PC	**P**rincipal **C**omponent
PID	**P**roportional–**I**ntegral–**D**erivative
RGB	**R**ed **G**reen **B**lue
RMSE	**R**oot **M**ean **S**quared **E**rror
ROIC	**R**ead-**O**ut **I**ntegrated **C**ircuit
ROI	**R**egion **o**f **I**nterest
SEM	**S**canning **E**lectron **M**icroscope
SFPI	**S**canning **F**abry-**P**érot **I**nterferometer
SNV	**S**tandard **N**ormal **V**ariate
SNR	**S**ignal-to-**N**oise-**R**atio
SVD	**S**ingular **V**alue **D**ecomposition
TCR	**T**emperature **C**oefficient of **R**esistance
TESSA	**T**hermal **E**mission **S**pectrum **S**ensing **A**pparatus
TMM	**T**ransfer **M**atrix **M**ethod
TN	**T**rue **N**egative
TP	**T**rue **P**ositive
UB	**U**ltra**B**lack
UV	**U**ltra**v**iolet
YAG	**Y**ttrium **A**luminium **G**arnet

Project Background

1 Introduction 3

2 Background 7
2.1 Fundamentals of Light 8
2.2 Radiometry 11
2.3 Blackbody radiation 21
2.4 Hyperspectral Imaging 31
2.5 Processing Methods for Hyperspectral Data 34
2.6 Principal Component Analysis 39
2.7 Summary 42

3 Long-Wave Infrared Hyperspectral Imager 43
3.1 Overview of Hyperspectral Imager 44
3.2 Camera Body 46
3.3 Microbolometer 48
3.4 Thermal Lens 55
3.5 Overview of Scanning Fabry-Pérot Interferometer 56
3.6 Summary 64

1. Introduction

This thesis documents the advancements in developing a hyperspectral long-wave infrared (LWIR) imager, building on the foundation established in the PhD thesis by A. L. Jørgensen [1]. This hyperspectral camera (HSC) with the nickname TESSA (**T**hermal **E**mission **S**pectrum **S**ensing **A**pparatus) integrates a thermal camera with a scanning Fabry-Pérot interferometer (SFPI). The interferometer comprises two parallel, partially transmitting mirrors separated by approximately 10 µm, forming an optical cavity. The precise cavity length governs the transmittance of the interferometer. Interferograms are generated and organized into a hyperspectral data cube by capturing images at varying cavity lengths.

Thermal cameras typically operate in the LWIR regime (8 µm to 15 µm wavelengths) to remotely measure surface temperatures based on emitted thermal radiation. However, the amount of thermal radiation emitted varies between materials, even at identical temperatures. This variation is governed by *emissivity*, a spectral property that describes how much radiation an object emits relative to a blackbody. A blackbody is an idealized emitter that radiates the maximum theoretical amount of energy at a given temperature. Since emissivity is wavelength-dependent, materials can be distinguished by their emission spectra.

The LWIR range is often used to analyze and distinguish materials using Fourier Transform Infrared (FTIR) spectrometers, which generally measure in transmittance or reflectance modes. FTIR spectrometers are typically single-point measurement techniques, limiting the types of samples that can be analyzed and sacrificing spatial information. In contrast, a plane-scanning hyperspectral imager (like the one described

in this project) captures spectral data across an entire image simultaneously, allowing any object that fits within the frame to be imaged and analyzed.

Few spectral imagers operate in the LWIR range, and those that do are typically bulky and expensive [2], limiting their widespread adoption. One of the key focuses of this thesis is, therefore, to explore potential fields where this relatively novel technology can be effectively applied.

Another objective is to deepen the understanding of how the hyperspectral imager can be modeled mathematically. The SFPI used in the imager is a low-order scanner, which introduces unique challenges compared to other spectroscopic technologies. This includes the simultaneous transmission of multiple wavelengths and angular-dependent spectral shifts. As a result, a single image in a hyperspectral data cube may correspond to contributions from entirely different wavelengths, complicating the interpretation of results. A key priority is the ability to predict the camera's output based on various incident spectra. An even more ambitious goal is to estimate the input spectrum from the measured output.

This thesis is designed for readers new to hyperspectral LWIR imaging and Fabry-Pérot spectrometry who may not have an extensive background in optics or spectrometry. It aims to serve as both a guide and a reference, covering a broad spectrum of topics. These range from foundational concepts such as radiometry, blackbody radiation, and hyperspectral imaging to more specialized subjects, including the operation of the SFPI, the interpretation of data generated by the imager, and practical applications of the hyperspectral imaging system.

Overview of Thesis

- **Chapter 2** provides an overview of the foundational physics relevant to the project. This includes the properties of light, radiometric concepts, an introduction to hyperspectral imaging, and common preprocessing steps for hyperspectral data.
- **Chapter 3** introduces the hyperspectral imager, which is the central focus of this thesis. It outlines the major components of the imager and explains their fundamental operating principles.
- **Chapter 4** provides a detailed examination of the SFPI, the central component that enables the imager to capture hyperspectral data. This includes an analysis of the relationship between the cavity length and its transmittance profile and an estimation of its spectral resolution.
- **Chapter 5** explores the methods used to estimate the interferogram output of the imager based on the incident light spectrum. It also describes the estimation of the detector's spectral response and addresses the inverse problem of reconstructing the incident spectrum from the measured interferogram.
- **Chapter 6** explores the application of the HSC in distinguishing various types of commercial plastics, both with and without carbon black. This differentiation is achieved by analyzing the emission signals from plastic samples heated to 60 °C, as reported in [3, 4].
- **Chapter 7** presents the results of using the HSC to analyze diffusion flames of pure hydrocarbon and hydrogen fuels. The study identifies distinct reaction regions within the flames, highlighting areas where key intermediate combustion reactions occur.
- **Chapter 8** introduces additional applications of the HSC, focusing primarily on mineral analysis and the effects of varying lighting conditions. While the findings in this chapter are promising, they are not yet fully developed to the extent required for publication.
- **Chapter 9** concludes the thesis by summarizing the key findings and providing an outlook for future research directions.

Contributory Publications

The following publications and manuscripts were produced during the course of this project and are included in their entirety in the Appendix of this thesis.

- M. N. Larsen, A. L. Jørgensen, V. Petrunin, J. Kjelstrup-Hansen, and B. Jørgensen, "A hyperspectral thermal imager based on a low order scanning Fabry-Pérot interferometer," in *Image Sensing Technologies: Materials, Devices, Systems, and Applications XI*, N. K. Dhar, A. K. Dutta, and S. R. Babu, Eds., vol. 13030, International Society for Optics and Photonics, SPIE, 2024, p. 130300E. doi: 10.1117/12.3013384

- M. N. Larsen, A. L. Jørgensen, M. L. Henriksen, V. Petrunin, J. Kjelstrup-Hansen, B. Jørgensen, and M. Hinge, "Classification of commercial plastics using hyperspectral long wave infrared emission imaging," *Spectrochimica Acta Part A: Molecular and Biomolecular Spectroscopy*, vol. 329, p. 125501, Mar. 2025. doi: 10.1016/j.saa.2024.125501

- M. N. Larsen, A. L. Jørgensen, V. Petrunin, J. Kjelstrup-Hansen, B. Jørgensen, and M. Hinge, "Classification of black plastic types by hyperspectral imaging based on long-wave infrared emission spectroscopy," *Polymer Testing*, vol. 141, p. 108629, Dec. 2024. doi: 10.1016/j.polymertesting.2024.108629

- M. N. Larsen, A. L. Jørgensen, V. Petrunin, J. Kjelstrup-Hansen, B. Jørgensen, "Long-wave infrared hyperspectral imager based on a scanning Fabry-Pérot interferometer," Submitted to *Review of Scientific Instruments*, Submitted Sep. 2024

- M. N. Larsen, I. Hansen-Bruhn, A. L. Jørgensen, B. Jørgensen, J. Kjelstrup-Hansen, "Signatures of Flames by Long-Wave Infrared Hyperspectral Imaging," Submitted to *Applied Spectroscopy*, Submitted Jan. 2025

2. Background

This chapter lays the foundational knowledge required to understand the main content presented in subsequent chapters of this thesis. It begins by introducing fundamental concepts related to light, including wavenumbers and wavelengths, which are essential for understanding spectral phenomena. The discussion then transitions to the basics of radiometry, providing insights into how cameras perceive the world and how electromagnetic radiation interacts with objects. This is followed by an exploration of blackbody radiation, which is a key concept related to thermal imaging. The chapter also offers an overview of hyperspectral imaging techniques, highlighting their principles and applications. Finally, common preprocessing methods for analyzing hyperspectral data cubes are presented, along with a detailed explanation of principal component analysis (PCA), which is a widely used tool for dimensionality reduction and data interpretation.

2.1 Fundamentals of Light

Light is a fundamental component of the physical world, integral to numerous natural phenomena and technological applications. It exhibits both wave-like and particle-like behavior, a concept known as wave-particle duality, which is a cornerstone of modern physics. This duality allows light to propagate through space as electromagnetic waves while also interacting with matter in discrete packets of energy called photons.

Albert Einstein's early 20th-century work on the photoelectric effect demonstrated the particle-like behavior of light, as he observed photons ejecting electrons from a metal surface when exposed to light of a specific frequency [5]. At the same time, light's wave-like properties, such as interference and diffraction, are best explained by treating it as an electromagnetic wave.

A photon is a quantum particle associated with light, carrying a discrete amount of energy, $\mathscr{U}$, which is directly related to its frequency, ν. This relationship was formulated by Max Planck in 1900 and expressed in Eq. (2.1).

$$\mathscr{U} = h\nu \tag{2.1}$$

Here, $h = 6.63 \times 10^{-34}$ J·s is Planck's constant. This equation shows that a photon's energy is determined solely by its frequency and is independent of its speed. Photons travel at the speed of light, $c = 2.998 \times 10^8$ m/s, in vacuum. When propagating through a medium, the phase velocity, v_p, is affected by the real part of the refractive index, n', of the medium following Eq. (2.2).

$$v_p = \frac{c}{n'} \tag{2.2}$$

The refractive index describes how much the speed of light is slowed down when propagating through a material compared to in a vacuum. How much light is absorbed is incorporated into the refractive index, making it a complex quantity as described by Eq. (2.3)

$$\tilde{n} = n' + j\kappa \tag{2.3}$$

Here, κ is the extinction coefficient and $j = \sqrt{-1}$ is the imaginary unit.

Because light propagates as a wave, v_p is related to both its wavelength, λ, and its frequency following the relation:

$$v_p = \lambda\nu \tag{2.4}$$

Another commonly used descriptor for light is its *wavenumber*, $\tilde{\nu}$ [cm^{-1}], which is defined as the inverse of the wavelength, as shown in Eq. (2.5):

$$\tilde{\nu} = \frac{1}{\lambda} \tag{2.5}$$

Light's wavelength (or wavenumber) directly influences its energy and properties, dictating its interaction with matter. The electromagnetic spectrum encompasses all wavelengths, from gamma rays with extremely short wavelengths to radio waves with long wavelengths. Figure 2.1 demonstrates a slice of the electromagnetic spectrum and spans from gamma rays (wavelengths below 10 pm) to radio waves (wavelengths on the meter scale). The boundaries between different regions of the spectrum are based on the work by Pedrotti [6] but are not universally defined, as they are often based on convention and context.

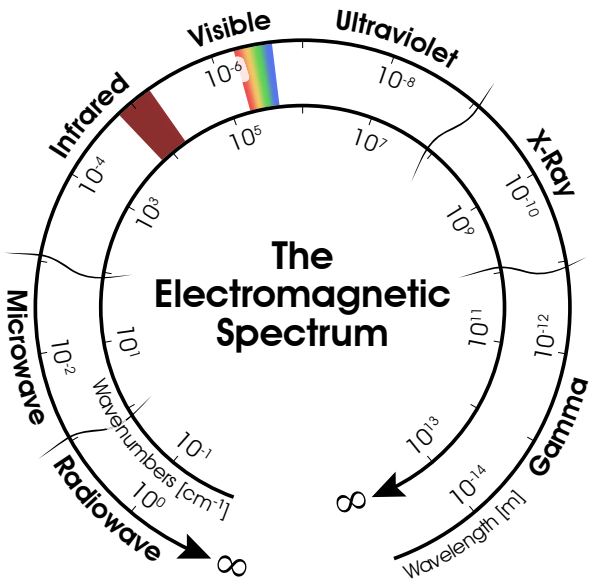

Figure 2.1: The electromagnetic spectrum represented in wavelengths and wavenumbers. The visible part of the light spectrum is indicated in rainbow colors, while the LWIR regime is shown in dark red.

Visible light, occupying a narrow band of the electromagnetic spectrum between 380 nm and 770 nm, is marked by its association with the colors the human eye perceives. This thesis, however, focuses on the Long-Wave Infrared (LWIR) region, which spans from 8 µm to 15 µm. This range is particularly significant due to its alignment with the sensitivity of microbolometer detectors, making it suitable for numerous infrared imaging applications (highlighted in dark red in Figure 2.1).

2.1.1 Wavelenghts and Wavenumbers

In this work, both wavelengths, λ, and wavenumbers, $\tilde{\nu}$, are used to describe light. This choice arises from the fact that interferometric phenomena are often more intuitively described in terms of wavelengths [µm], whereas chemical analyses are typically conducted in wavenumbers [cm^{-1}]. Additionally, wavenumbers provide a mathematical advantage due to their linear relationship with light's energy (or frequency), in contrast to the reciprocal relationship between energy and wavelength.

2.2 Radiometry

Understanding the principles of radiometry is essential for explaining how a camera sees the world. Radiometry provides a framework for quantifying the interaction between light and matter on a macroscopic scale. It defines radiometric quantities that describe the energy emitted and received as radiation.

Solid Angle

The concept of solid angle is essential for quantifying how light energy is distributed over space and how it propagates from a source. In most cases, a distant observer can only detect a fraction of the radiation emitted by a source, as the emission typically occurs in multiple directions. Consider a point source emitting radiation uniformly in all directions, forming a complete sphere, as shown in Figure 2.2a. In this scenario, only the radiation intersecting a differential area dS on the surface of the sphere with radius r is captured, which could, for example, represent the aperture of a camera lens. To quantify the fraction of the sphere covered by this area, finding an expression analogous to how the ratio of the arc length to the radius of a circle defines an angle in two dimensions is useful. In three dimensions, the corresponding quantity is the *solid angle* Ω [sr], defined as the ratio of the area element dS to the square of

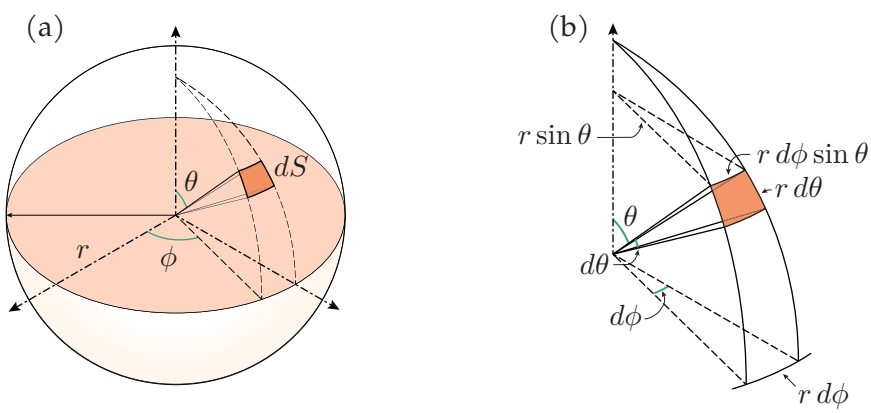

Figure 2.2: Illustration of the solid angle, showing the portion of the surface area of a sphere with radius r subtended by the area element dS. (a) illustrates the entire sphere, while (b) shows a magnified section.

the sphere's radius, as given by Eq. (2.6).

$$\Omega = \frac{dS}{r^2} \tag{2.6}$$

The area element dS can be approximated as a differential rectangle with side lengths $r\,d\theta$ and $r\sin\theta\;\,d\phi$, as illustrated in Figure 2.2b. Hence, the differential surface area is expressed as:

$$dS = r^2 \sin\theta\, d\theta\, d\phi \tag{2.7}$$

Here, θ and ϕ denote the polar and azimuthal angles, respectively. The total surface area of a sphere can then be obtained by integrating over the full range of θ and ϕ, as follows:

$$S = r^2 \int_0^{2\pi} \int_0^{\pi} \sin\theta\, d\theta\, d\phi = 4\pi r^2 \tag{2.8}$$

By combining the result from Eq. (2.8) with the definition of the solid angle in Eq. (2.6), it follows that the solid angle subtended by a complete sphere is 4π steradians (sr), and by a hemisphere is 2π sr.

Radiometric Quantaties

Radiometry provides a systematic framework for quantifying the energy transported by electromagnetic radiation, enabling the characterization of its interaction with matter—for example, with photodetectors in cameras. The primary radiometric quantities are summarized in Table 2.1 and Figure 2.3 and will be examined in detail in the following.

Radiant energy, denoted by $\mathcal{Q}$ [J], represents the total energy emitted by an object. The energy incident on an area dA is described by the *radiant exposure* H $[\mathrm{J} \cdot \mathrm{m}^{-2}]$:

$$H = \frac{d\mathcal{Q}}{dA} \tag{2.9}$$

A more widely used quantity is *radiant flux*, Φ [W], which describes the amount of radiant energy emitted per unit of time - often referred to as *radiant power*.

In many cases, it is necessary to relate the power to the area of the emitting surface. This leads to the quantity *exitance*, M $[\mathrm{W} \cdot \mathrm{m}^{-2}]$, which

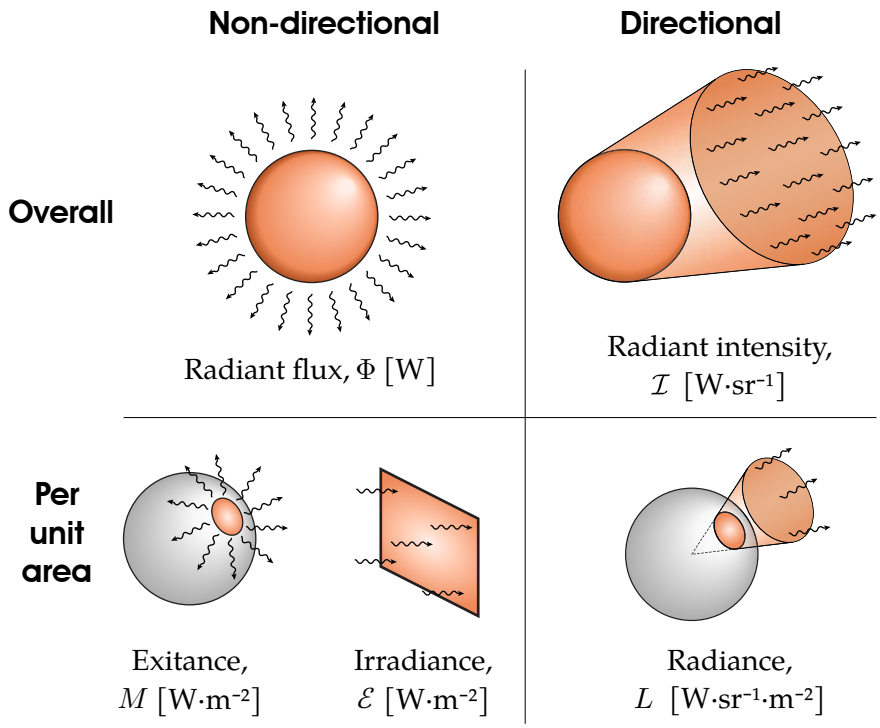

Figure 2.3: Illustration of the five radiometric quantities related to the radiated power.

represents the radiant flux emitted per unit area from the surface of the object. The relationship is formalized in Eq. (2.10), where exitance is expressed as the radiant flux emitted by an infinitesimal area element dA on the object's surface.

$$M = \frac{d\Phi}{dA} \tag{2.10}$$

When radiation is instead *incident* on the object, the term *irradiance*, $\mathcal{E}$ $[\mathrm{W} \cdot \mathrm{m}^{-2}]$, is used. Irradiance describes the radiant flux received per unit area.

It is also often important to describe the directionality of radiation. *Radiant intensity*, $\mathcal{I}$ $[\mathrm{W} \cdot \mathrm{sr}^{-1}]$, quantifies the radiant flux emitted per unit solid angle as described by Eq. (2.11).

$$\mathcal{I} = \frac{d\Phi}{d\Omega} \tag{2.11}$$

Table 2.1: Overview of radiometric quantities, including their symbols and units.

Term	Symbol	units
Radiant energy	$\mathcal{Q}$	$[\mathrm{J}]$
Radiant flux/Radiant power	Φ	$[\mathrm{W}]$
Radiant exposure	H	$[\mathrm{J} \cdot \mathrm{m}^{-2}]$
Exitance	M	$[\mathrm{W} \cdot \mathrm{m}^{-2}]$
Irradiance	$\mathcal{E}$	$[\mathrm{W} \cdot \mathrm{m}^{-2}]$
Radiant intensity	$\mathcal{I}$	$[\mathrm{W} \cdot \mathrm{sr}^{-1}]$
Radiance	L	$[\mathrm{W} \cdot \mathrm{sr}^{-1} \cdot \mathrm{m}^{-2}]$

Radiant intensity can be used to describe the inverse square law, which states that irradiance is inversely proportional to the square of the distance from the emitter. This relationship is given in Eq. (2.12), where a point source is assumed to emit radiation uniformly in all directions.

$$\mathcal{E} = \frac{d\Phi}{dA} = \frac{\Phi}{A} = \frac{4\pi\mathcal{I}}{4\pi r^2} = \frac{\mathcal{I}}{r^2} \tag{2.12}$$

This relationship is further illustrated in Figure 2.4, which shows that the surface area of the sphere increases proportionally to r^2.

Lastly, *radiance*, L $[\mathrm{W} \cdot \mathrm{sr}^{-1} \cdot \mathrm{m}^{-2}]$, provides a measure of the radiant flux emitted per solid angle per unit of projected area of the emitting surface. The projected area accounts for the emitter appearing smaller from the observer's perspective when viewed at an angle. This concept is illustrated in Figure 2.5, where an observer views a differential area element dA at an angle θ. From the observer's viewpoint, the area is

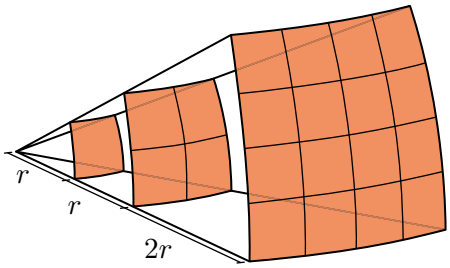

Figure 2.4: Illustration of the inverse square law. The flux propagating an area at a distance r from the source is spread over an area 16 times larger at a distance of $4r$.

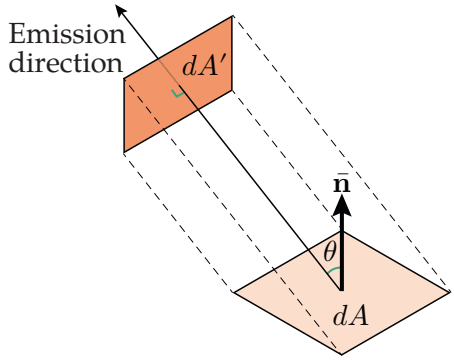

Figure 2.5: Illustration of the projected area dA'. When observing the area dA at an angle, it appears smaller by a factor of $\cos\theta$. $\bar{\mathbf{n}}$ represents the unit normal vector to the differential surface with area dA.

projected to become perpendicular to the viewing direction. Therefore, the projected area is given by $dA' = dA\cos\theta$. Consequently, radiance can be expressed as shown in Eq. (2.13):

$$L = \frac{d\mathcal{I}}{dA'} = \frac{d\mathcal{I}}{dA\cos\theta} = \frac{d^2\Phi}{d\Omega(dA\cos\theta)} \tag{2.13}$$

$$\Rightarrow d^2\Phi = L\cos\theta d\Omega\, dA \tag{2.14}$$

From Eq. (2.14), it is clear that the total radiant power emitted by an object can be obtained by integrating the radiance over the entire surface area and the solid angle of the hemisphere, as shown in Eq. (2.15):

$$\Phi = \iint L\cos\theta d\Omega\, dA \tag{2.15}$$

Furthermore, the exitance can be determined by integrating radiance over the solid angle. When the integration is performed solely over the solid angle, the expression for exitance is:

$$M = \frac{d\Phi}{dA} = \int L\cos\theta d\Omega \tag{2.16}$$

Similarly, the radiant intensity can be derived by integrating radiance over the surface area, as shown in Eq. (2.17) :

$$\mathcal{I} = \frac{d\Phi}{d\Omega} = \int L \cos\theta dA \tag{2.17}$$

Spectral Quantities

It is important to note that all the radiometric quantities discussed have spectral variants, indicated by a subscript λ for wavelength or $\tilde{\nu}$ for wavenumber. This notation reflects that these quantities are, in practice, dependent on the spectral distribution of radiation. For instance, the spectral exitance represents the spectral density of the exitance and is expressed as:

$$M_\lambda = \frac{dM}{d\lambda} \left[\mathrm{W} \cdot \mathrm{m}^{-2} \cdot \mu\mathrm{m}^{-1}\right] \tag{2.18}$$

$$M_{\tilde{\nu}} = \frac{dM}{d\tilde{\nu}} \left[\mathrm{W} \cdot \mathrm{m}^{-2} \cdot \left(\mathrm{cm}^{-1}\right)^{-1}\right] \tag{2.19}$$

Analogous expressions apply to the other quantities listed in Table 2.1.

Lambertian Radiators

A Lambertian radiator is an idealized emitter or reflector that radiates with constant radiance in all directions, independent of the observation angle. This behavior is illustrated in Figure 2.6, where the radiance remains constant for all angles, while the radiant intensity varies with the cosine of the emission angle, as described by Eq. (2.20):

$$\mathcal{I}_\mathcal{L} = L_\mathcal{L} \cos\theta \int dA = L_\mathcal{L} \cos\theta A \tag{2.20}$$

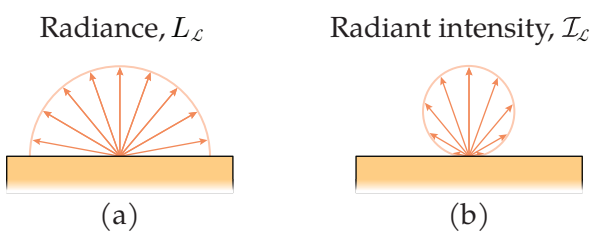

Figure 2.6: Illustration of a Lambertian radiator in terms of (a) radiance and (b) intensity as a function of emission angle.

Here, A represents the surface area of the emitter, and the subscript $\mathcal{L}$ indicates that the radiating surface is Lambertian. The relationship between the exitance and radiance for a Lambertian emitter is given by:

$$M_{\mathcal{L}} = L_{\mathcal{L}} \int \cos\theta d\Omega = L_{\mathcal{L}} \int \cos\theta \sin\theta d\theta \, d\phi = \pi L_{\mathcal{L}} \tag{2.21}$$

This integral demonstrates that the exitance of a Lambertian radiator is proportional to the radiance by a factor of π. Real-world materials that diffuse light strongly upon reflection can be approximated as Lambertian radiators. Another example is blackbodies, which are theoretical constructs further discussed in section 2.3.

Radiative Transfer Between Surfaces

It is often useful to quantify the amount of radiation exchanged between surfaces. Figure 2.7 illustrates the radiative interaction between two differential surface elements, dA_1 and dA_2. In this figure, θ_1 and θ_2 denote the angles between the central ray of length r that connects the two surface elements and their respective surface normals, $\bar{\mathbf{n}}_\mathbf{1}$ and $\bar{\mathbf{n}}_\mathbf{2}$. The radiant power emitted from dA_1 and intercepted by dA_2 is given by Eq. (2.22), which is derived from Eq. (2.14). For simplicity, both surface elements are assumed to be Lambertian radiators.

$$d^2\Phi_{1\to 2} = L_{\mathcal{L},1} \cos\theta_1 d\Omega_2 \, dA_1 \tag{2.22}$$

Here, $L_{\mathcal{L},1}$ represents the radiance emitted from surface element dA_1, and Ω_2 denotes the solid angle subtended by dA_2 as seen from dA_1. The

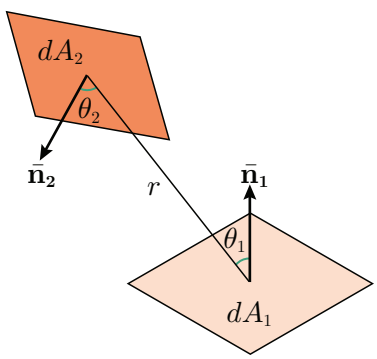

Figure 2.7: Radiative transfer between two differential surface elements dA_1 and dA_2. $\bar{\mathbf{n}}_\mathbf{1}$ and $\bar{\mathbf{n}}_\mathbf{2}$ are the unit normal vectors of the two differential surface elements.

solid angle Ω_2 is the projected solid angle, and Eq. (2.22) can be rewritten using the definition of the solid angle given in Eq. (2.6), leading to:

$$d\Omega_2 = \frac{\cos\theta_2 dA_2}{r^2} \tag{2.23}$$

The fundamental law of radiometry can be derived by substituting this expression into Eq. (2.22), as shown in Eq. (2.24) [7]:

The Fundamental Law of Radiometry

$$d^2\Phi_{1\to 2} = \frac{L_{\mathcal{L},1}\cos\theta_1\cos\theta_2}{r^2} dA_1\, dA_2 \tag{2.24}$$

The total radiant power transferred from a surface of area A_1 to another surface of area A_2 can then be determined by evaluating the following double integral:

$$\Phi_{1\to 2} = L_{\mathcal{L},1} \iint \frac{\cos\theta_1\cos\theta_2}{r^2} dA_1\, dA_2 \tag{2.25}$$

The total radiant power emitted into the hemisphere by a Lambertian emitter with a surface area A_1 can be expressed as:

$$\Phi_1 = M_{\mathcal{L},1} A_1 = \pi L_{\mathcal{L},1} A_1 \tag{2.26}$$

In practical scenarios, only a fraction of this radiation is directed towards a specific direction of interest, such as when captured by a camera lens with an aperture area A_2. This fraction is quantified by the view factor $\mathfrak{F}$, defined as:

$$\mathfrak{F}_{1\to 2} = \frac{\Phi_{1\to 2}}{\Phi_1} = \frac{1}{\pi A_1} \iint \frac{\cos\theta_1\cos\theta_2}{r^2} dA_1\, dA_2 \tag{2.27}$$

By the principle of reciprocity, the view factor remains unchanged if the roles of emitting and receiving surfaces are swapped. Therefore, the following relationship holds:

$$A_1\mathfrak{F}_{1\to 2} = A_2\mathfrak{F}_{2\to 1} \tag{2.28}$$

Different geometrical configurations require specific view factor calculations, and there are comprehensive compilations where these integrals

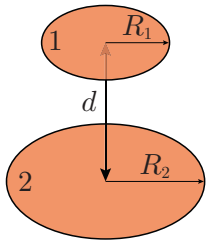

Figure 2.8: Two coaxial discs with radii R_1 and R_2, separated by a distance d.

have been evaluated for various configurations. One example is provided by Eq. (2.29) and illustrated in Figure 2.8, which presents the view factor for two coaxial discs [8]. For instance, this scenario can be relevant when determining the flux from a blackbody source (often having a circular aperture) that is incident on the lens of a thermal imaging camera.

$$\mathfrak{F}_{1\to 2} = \frac{1}{2}\left[1 + \frac{R_2^2 + d^2}{R_1^2} - \sqrt{\left(1 + \frac{R_2^2 + d^2}{R_1^2}\right)^2 - 4\frac{R_2^2}{R_1^2}}\right] \tag{2.29}$$

Here, R_1 and R_2 denote the radii of the two discs, and d is the distance between them.

2.2.1 Absorptance, Reflectance, and Transmittance

Light can be reflected, transmitted, or absorbed when interacting with a material, as illustrated in Figure 2.9. The fraction of the incident irradiance that is reflected is termed the reflectance, $\mathcal{R}$, the fraction absorbed is the absorptance, α, and the fraction transmitted is the transmitance, $\mathcal{T}$. These relationships are mathematically defined in Eq. (2.30)–Eq. (2.32), and visually represented in Figure 2.9.

$$\mathcal{R} = \frac{\mathcal{E}_{\text{ref}}}{\mathcal{E}}, \qquad 0 \leq \mathcal{R} \leq 1 \tag{2.30}$$

$$\alpha = \frac{\mathcal{E}_{\text{abs}}}{\mathcal{E}}, \qquad 0 \leq \alpha \leq 1 \tag{2.31}$$

$$\mathcal{T} = \frac{\mathcal{E}_{\text{trans}}}{\mathcal{E}}, \qquad 0 \leq \mathcal{T} \leq 1 \tag{2.32}$$

According to the principle of energy conservation, the sum of the reflected, absorbed, and transmitted fractions must equal the total incident

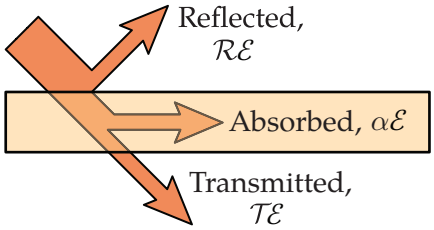

Figure 2.9: Illustration of light interacting with a semitransparent medium, where portions are reflected, absorbed, and transmitted.

energy, as expressed in Eq. (2.33) and Eq. (2.34).

$$\mathcal{E}_{\text{ref}} + \mathcal{E}_{\text{abs}} + \mathcal{E}_{\text{trans}} = \mathcal{E} \tag{2.33}$$

$$\mathcal{R} + \alpha + \mathcal{T} = 1 \tag{2.34}$$

For an opaque material, where $\mathcal{T} = 0$, it is possible to determine the absorptance by measuring only the reflectance. However, the reflected light can be distributed across the entire hemisphere, as depicted in Figure 2.10. Here, incident light interacts with a surface in three scenarios. In Figure 2.10a, the surface acts as a perfect diffuse reflector, scattering light uniformly across the hemisphere. In contrast, Figure 2.10c represents a perfectly specular reflector, where the reflected light follows the angle of incidence, as observed in mirror-like surfaces. The more common case is shown in Figure 2.10b, where the surface exhibits a combination of specular and diffuse reflection, with most of the radiation reflected in the direction of specular reflection, while a portion is scattered diffusely.

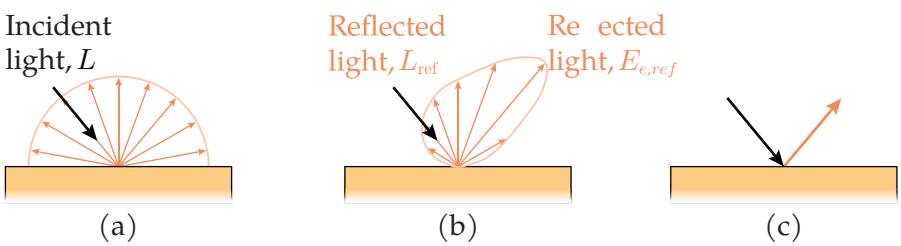

Figure 2.10: Illustration of light reflection behavior: (a) perfect diffuse reflection, (b) semi-diffuse reflection, and (c) perfect specular reflection. The black arrow indicates incident light, while the orange arrows denote reflected rays.

2.3 Blackbody radiation

All objects with temperatures above absolute zero emit thermal radiation, resulting from the energy transitions of the atoms and electrons they are comprised of [9]. These transitions increase in energy and frequency as the temperature increases, leading to the emission of more thermal radiation. Besides temperature, the amount of thermal radiation emitted also depends on the material properties. A blackbody, however, is an idealized object that emits the maximum possible thermal radiation for any given temperature. It is a perfect emitter (and absorber) that radiates uniformly in all directions, as illustrated in Figure 2.11. The total exitance of a blackbody can be expressed by the Stefan-Boltzmann law [9] as shown in Eq. (2.35):

The Stefan-Boltzmann Law

$$M_{\mathrm{BB}}(T) = \int_0^\infty M_{\mathrm{BB},\lambda}(T)\, d\lambda = \int_0^\infty M_{\mathrm{BB},\tilde{\nu}}(T)\, d\tilde{\nu} = \sigma T^4 \quad (2.35)$$

where $\sigma = 5.67 \times 10^{-8}$ $[\mathrm{W} \cdot \mathrm{m}^{-2} \cdot K^{-4}]$ is the Stefan-Boltzmann constant, and T denotes the absolute temperature of the blackbody. The subscript "BB" indicates that the quantity refers to a blackbody. Eq. (2.35) represents the emissive power integrated over all wavelengths. However, the *spectral* exitance describes the density of the exitance as a function of wavelength. The spectral exitance of a blackbody was derived by Max Planck in 1900 [10] and is given by Eq. (2.36):

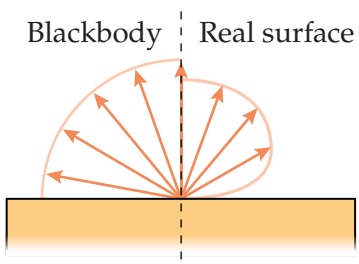

Figure 2.11: Radiance of a blackbody surface and a 'real' material. The figure shows that the radiance of a blackbody has no angular dependence, while a 'real' material exhibits angular dependence. Additionally, no 'real' surface can emit more radiation than a blackbody at the same temperature.

Planck's Law in Terms of Wavelength

$$M_{\mathrm{BB},\lambda}(T) = \frac{2\pi hc^2}{\lambda^5} \frac{1}{\exp\left\{\frac{hc}{k_B \lambda T}\right\} - 1} \tag{2.36}$$

$k_B = 1.38 \times 10^{-23} \ \left[\mathrm{J} \cdot \mathrm{K}^{-1}\right]$ is the Boltzmann constant. It is necessary to account for their non-linear relationship to convert from wavelengths to wavenumbers. The exitance within a small spectral band from λ to $d\lambda$ can be expressed as described in Eq. (2.37).

$$M_{\mathrm{BB},\lambda \to d\lambda}(T) = M_{\mathrm{BB},\lambda}(T)\, d\lambda = \frac{2\pi hc^2}{\lambda^5} \frac{1}{\exp\left\{\frac{hc}{k_B \lambda T}\right\} - 1}\, d\lambda \tag{2.37}$$

The wavelength can be substituted by wavenumbers using the relation $\lambda = 1/\tilde{\nu}$, as stated in Eq. (2.5). The corresponding derivative is:

$$\left|\frac{d\lambda}{d\tilde{\nu}}\right| = \frac{1}{\tilde{\nu}^2} \Rightarrow d\lambda = \frac{d\tilde{\nu}}{\tilde{\nu}^2} \tag{2.38}$$

The negative sign, normally resulting from $d\lambda/d\tilde{\nu}$, is omitted because it merely indicates that the curve is reflected from left to right. This is because:

$$\lambda_2 - \lambda_1 \geq 0, \qquad \lambda_2 \geq \lambda_1, \tag{2.39}$$

$$\Rightarrow \tilde{\nu}_2 - \tilde{\nu}_1 \leq 0, \qquad \tilde{\nu}_2 \leq \tilde{\nu}_1, \qquad \tilde{\nu}_2 = \frac{1}{\lambda_2}, \quad \tilde{\nu}_1 = \frac{1}{\lambda_1} \tag{2.40}$$

Thus, the spectral exitance in terms of wavenumbers can be expressed by Eq. (2.41):

Planck's Law in Terms of Wavenumber

$$M_{\mathrm{BB},\tilde{\nu}}(T) = 2\pi hc^2 \tilde{\nu}^3 \frac{1}{\exp\left\{\frac{hc\tilde{\nu}}{k_B T}\right\} - 1} \tag{2.41}$$

The two spectral densities, $M_{\mathrm{BB},\lambda}(T)$ and $M_{\mathrm{BB},\tilde{\nu}}(T)$, are presented in Figure 2.12, illustrating distinctly different distributions due to the non-linear relationship between step sizes $d\lambda$ and $d\tilde{\nu}$.

As the blackbody temperature varies, so does the location of the maximum in the spectral densities as described by Wien's displacement

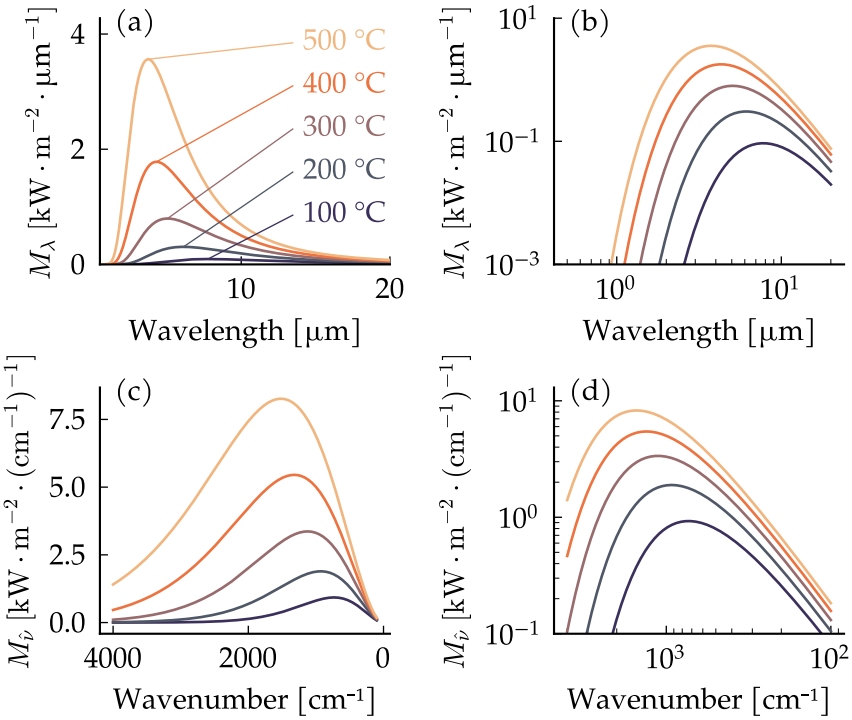

Figure 2.12: Spectral exitance of blackbodies at temperatures ranging from 100 °C to 500 °C, shown as a function of wavelength in plots (a) and (b), and as a function of wavenumber in plots (c) and (d). The color legend in (a) applies consistently across all plots.

law [7], which can be derived by differentiating the spectral densities and setting them to zero. In terms of wavelength and wavenumber, the resulting expressions are provided in Eq. (2.42) and Eq. (2.43), respectively.

Wien's Displacement Law

$$\lambda_{\max} T = 2897.8\ \mu\text{m} \cdot \text{K} \tag{2.42}$$

$$\frac{\tilde{\nu}_{\max}}{T} = 1.961\ \text{cm}^{-1} \cdot \text{K}^{-1} \tag{2.43}$$

It should be noted that since the spectral densities are described in terms

of two different spectral units, the locations of the maxima calculated using either Eq. (2.42) or Eq. (2.43) are not equal. For instance, at a temperature of 100 °C, the maximum occurs at 7.77 µm as determined by Eq. (2.42), while Eq. (2.43) results in a peak location at 731.7 cm^{-1}, corresponding to an equivalent wavelength of $1/\tilde{\nu} = 13.67\,\mu\mathrm{m}$. However, when the curves are integrated over an identical spectral interval, the exitance remains consistent between the two representations. However, integrating these spectral exitance curves analytically is challenging, as no exact solution exists, though an approximate solution can be derived, as explained in the following sections.

Energy Within a Spectral Range

Quantifying the exitance, or energy, within a specific spectral region is often useful. For instance, assessing the portion of blackbody radiation emitted within the sensitivity range of a detector, as illustrated in Figure 2.13. Here, the spectral exitance of a blackbody emitter at 100 °C is plotted within the range $\lambda_1 = 8\,\mu\mathrm{m}$ to $\lambda_2 = 15\,\mu\mathrm{m}$, which corresponds to the spectral sensitivity of the detector utilized in this work. Ideally, determining the exitance within this interval requires integrating Eq. (2.36) or Eq. (2.41) over the specified range. Although no analytical solution exists for this integral, an approximation is achievable through the method outlined in the following derivation, based on the approach by Duncan Lawson [11].

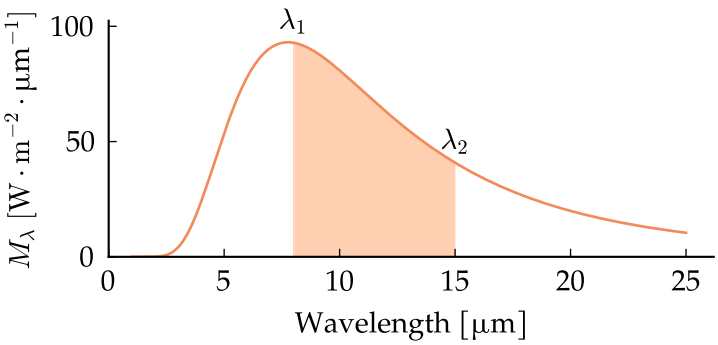

Figure 2.13: Spectral exitance of a 100 °C blackbody emitter. λ_1 and λ_2 denote the range within which exitance integration is required.

To determine the exitance within a specific spectral band, a *blackbody radiation function*, f, is introduced:

$$f_{\lambda_1}(T) = \frac{\int_0^{\lambda_1} M_{\mathrm{BB},\lambda}(T)d\lambda}{\int_0^{\infty} M_{\mathrm{BB},\lambda}(T)d\lambda} = \frac{\int_0^{\lambda_1} M_{\mathrm{BB},\lambda}(T)d\lambda}{\sigma T^4} \tag{2.44}$$

This function represents the fraction of exitance contained between $\lambda = 0$ and $\lambda = \lambda_1$. For the exitance between wavelengths λ_1 and λ_2, the following expression applies:

$$f_{\lambda_1 \to \lambda_2}(T) = f_{\lambda_2}(T) - f_{\lambda_1}(T) \tag{2.45}$$

To solve the otherwise "unsolvable" blackbody integral from Eq. (2.44), it is observed from Wien's displacement law that $\lambda_{\max} T$ remains constant across wavelengths and temperatures, permitting integration with respect to $x = \lambda T$ rather than λ. This allows Eq. (2.44) to be reformulated as follows:

$$f_{\lambda_1}(T) = \frac{1}{\sigma T^4} \int_0^{\lambda_1} \frac{2\pi h c^2}{\lambda^5} \frac{1}{\exp\left\{\frac{hc}{k_B \lambda T}\right\} - 1} \, d\lambda \tag{2.46}$$

$$= \frac{1}{\sigma} \int_0^{\lambda_1 T} \frac{2\pi h c^2}{x^5} \frac{1}{\exp\left\{\frac{hc}{k_B x}\right\} - 1} \, dx \tag{2.47}$$

Substituting constants $C_1 = 2\pi h c^2$ and $C_2 = \frac{hc}{k_B}$, along with the variable change $\varkappa = C_2/x$, $dx = -C_2 \varkappa^{-2} \, d\varkappa$, yields:

$$f_{\lambda_1}(T) = \frac{C_1}{\sigma C_2^4} \int_{C_2/(\lambda_1 T)}^{\infty} \frac{\varkappa^3 \exp\{-\varkappa\}}{1 - \exp\{-\varkappa\}} \, d\varkappa \tag{2.48}$$

By expanding $(1 - \exp\{-\varkappa\})^{-1}$ as an infinite sum:

$$(1-a)^{-1} = \sum_{n=0}^{\infty} a^n, \qquad |a| < 1 \tag{2.49}$$

with a being a dummy variable, the following expression emerges:

$$f_{\lambda_1}(T) = \frac{C_1}{\sigma C_2^4} \sum_{n=1}^{\infty} \int_{C_2/(\lambda_1 T)}^{\infty} \varkappa^3 \exp\{-n\varkappa\} \, d\varkappa \tag{2.50}$$

Following repeated integration by parts, the final expression for $\mathscr{f}$ is:

$$\mathscr{f}_{\lambda_1}(T) = \frac{C_1}{\sigma C_2^4} \sum_{n=1}^{\infty} \frac{\exp\{-n\varkappa\}}{n} \left(\varkappa^3 + \frac{3\varkappa^2}{n} + \frac{6\varkappa}{n^2} + \frac{6}{n^3} \right) \tag{2.51}$$

$$= \frac{C_1}{\sigma C_2^4} \sum_{n=1}^{\infty} c_n(\varkappa) \exp\{-n\varkappa\} \tag{2.52}$$

The more terms, N, of the infinite series which are included in Eq. (2.52), the smaller the error, $e(N)$, becomes (error of the truncated infinite series). The error is bounded by the following inequality [11]

$$e(N) < \frac{C_1}{\sigma C_2^4} c_{N+1}(\varkappa) \frac{\exp\{-(N+1)\varkappa\}}{1 - \exp\{-\varkappa\}} \tag{2.53}$$

The larger the value of λT, the more terms must be included to maintain the same error bounds since $\varkappa \propto 1/\lambda T$. For example, at a temperature of 100 °C, a wavelength of $\lambda_1 = 1\,\mu\text{m}$ and $N = 5$ included terms, the truncation error is $e(N) = 1.5 \times 10^{-10}$.

Wavenumber Representation

Finding a similar blackbody radiation function valid for the wavenumber representation can be achieved by substituting λT with $\tilde{\nu}/T$, yielding

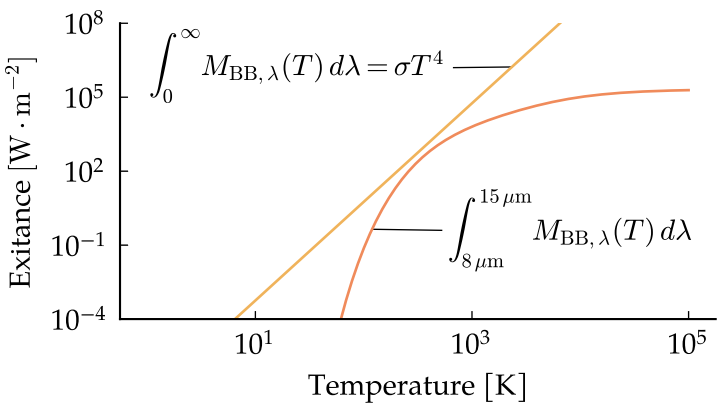

Figure 2.14: Temperature dependence of the integrated spectral exitance. Across wavelengths, the exitance follows the Stefan-Boltzmann law, $M_{\text{BB}} \propto T^4$. This relationship, however, does not apply when integration is limited to the 8–15 µm range.

the following expression for $f_{\tilde{\nu}1}(T)$:

$$f_{\tilde{\nu}1}(T) = \frac{C_1}{\sigma C_2^4} \sum_{n=1}^{\infty} -\frac{\exp(-ny)}{n} \left(y^3 + \frac{3y^2}{n} + \frac{6y}{n^2} + \frac{6}{n^3} \right) + \frac{6}{n^4} \quad (2.54)$$

where $y = \tilde{\nu}_1 C_2 / T$, and the constants remain $C_1 = 2\pi hc^2$ and $C_2 = \frac{hc}{k_B}$.

Figure 2.14 illustrates the relationship between the integrated spectral exitance across all wavelengths and within a restricted band from $\lambda_1 = 8\,\mu\text{m}$ to $\lambda_2 = 15\,\mu\text{m}$. As the Stefan-Boltzmann law describes, the integrated exitance over the entire spectrum is proportional to T^4. However, this proportionality no longer applies when integration is confined to the specified spectral range, resulting in a lower total exitance. At elevated temperatures (above approximately 850 °C), the slope of the curve further diminishes as a greater fraction of energy shifts to wavelengths below the defined range.

Example 2.1 Calculating the exitance within the spectral range from $\lambda_1 = 8\,\mu\text{m}$ to $\lambda_2 = 15\,\mu\text{m}$ (with the corresponding wavenumbers: $\tilde{\nu}_1 = 1250\,\text{cm}^{-1}$ and $\tilde{\nu}_2 = 666.7\,\text{cm}^{-1}$) should yield the same results using either Eq. (2.52) or Eq. (2.54). With the blackbody being 100 °C and truncating the infinite series after $N = 5$ terms, the ratio of the spectral exitance below $\lambda_1 = 8\,\mu\text{m}$ is $f_{8\,\mu\text{m}}(100\,°\text{C}) = 26.99\%$. However, $f_{1250\,\text{cm}^{-1}}(100\,°\text{C}) = 72.83\%$, indicating that 72.83% of the exitance is contained between $\tilde{\nu} = 0\,\text{cm}^{-1}$ and $\tilde{\nu} = 1250\,\text{cm}^{-1}$. Similarly, the upper integration bound yields $f_{15\,\mu\text{m}}(100\,°\text{C}) = 70.07\%$ and $f_{666.7\,\text{cm}^{-1}}(100\,°\text{C}) = 29.74\%$. Finally, the total fraction of exitance contained within the interval is: $f_{15\,\mu\text{m}}(100\,°\text{C}) - f_{8\,\mu\text{m}}(100\,°\text{C}) = 43.09\%$ and $f_{1250\,\text{cm}^{-1}}(100\,°\text{C}) - f_{666.7\,\text{cm}^{-1}}(100\,°\text{C}) = 43.09\%$. Thus, even though the spectral densities exhibit different distributions, their integrals of the same spectral range are equal. ■

2.3.1 Emissivity

As previously stated, blackbodies emit the maximum thermal radiation theoretically possible for any given temperature. Real materials, however, emit less than blackbodies, but some materials, like human skin [12] and water [13], approximate blackbody behavior and are often described as graybodies since they are "almost-blackbodies." How much the emissions

of a material resemble that of a blackbody is quantified by the *emissivity*, ε, which represents the ratio of the material's exitance to that of a blackbody at the same temperature as shown in Eq. (2.55).

Emissivity

$$\varepsilon(T) = \frac{M(T)}{M_{\text{BB}}(T)} \tag{2.55}$$

This quantity is sometimes referred to as the *hemispherical emissivity* as it represents the total emissions into the hemisphere. ε can take on values in the range $0 \leq \varepsilon \leq 1$, where $\varepsilon = 1$ represents a perfect emitter (blackbody). Similar to exitance, emissivity often varies with wavelength, giving rise to the concept of *spectral hemispherical emissivity* as expressed in Eq. (2.56) and Eq. (2.57).

$$\varepsilon_\lambda(T) = \frac{M_\lambda(T)}{M_{\text{BB},\lambda}(T)} \tag{2.56}$$

$$\varepsilon_{\tilde{\nu}}(T) = \frac{M_{\tilde{\nu}}(T)}{M_{\text{BB},\tilde{\nu}}(T)} \tag{2.57}$$

Real materials do not emit with the uniform radiance characteristic of blackbodies (or Lambertian radiators), resulting in a directional dependence of emissivity. This is described by the *directional emissivity*, ε_Ω, defined as follows:

$$\varepsilon_\Omega(T) = \frac{L(T)}{L_{\text{BB}}(T)} \tag{2.58}$$

Surfaces with near-constant emissivity over a spectral range are sometimes called 'gray,' while surfaces with relatively constant emissivity across all solid angles are referred to as diffuse. When both spectral and directional dependencies are considered, the *spectral directional emissivity* is defined as:

$$\varepsilon_{\lambda,\Omega}(T) = \frac{L_\lambda(T)}{L_{\text{BB},\lambda}(T)} \tag{2.59}$$

$$\varepsilon_{\tilde{\nu},\Omega}(T) = \frac{L_{\tilde{\nu}}(T)}{L_{\text{BB},\tilde{\nu}}(T)} \tag{2.60}$$

Kirchhoff's Law of Thermal Radiation

Figure 2.15 illustrates a small particle with surface area A suspended within a larger cavity maintained at temperature T. The cavity serves as an isothermal blackbody emitter with an exitance of σT^4, as described by Eq. (2.35). The particle is in thermal equilibrium with the surrounding cavity. Under these conditions, the irradiance absorbed by the particle is given by

$$\mathcal{E}_{\text{abs}} = \alpha\mathcal{E} = \alpha\sigma T^4 \tag{2.61}$$

while the radiation emitted by the particle is

$$\mathcal{E}_{\text{emit}} = \varepsilon\sigma T^4 \tag{2.62}$$

Since the particle is in thermal equilibrium with the cavity, there is no net heat flux; the particle emits radiation at the same rate it absorbs. This relationship can be written as:

$$\Phi_{\text{emit}} = \Phi_{\text{abs}} \Rightarrow A\varepsilon\sigma T^4 = A\alpha\sigma T^4 \tag{2.63}$$

which implies that the emissivity and absorptance of the particle are equal. This equality, known as *Kirchhoff's law*, is expressed as:

Kirchhoff's Law

$$\alpha(T) = \varepsilon(T) \tag{2.64}$$

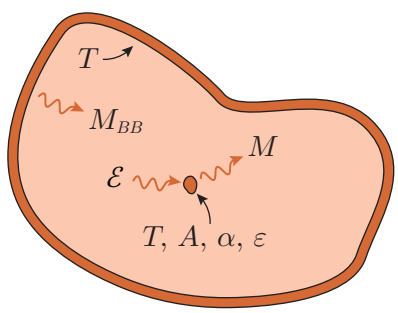

Figure 2.15: A particle suspended in a larger cavity with which it is in thermal equilibrium. The particle emits as much radiation as it absorbs from the cavity.

Kirchhoff's law extends to spectral and directional emissivity, expressed as

$$\alpha_\lambda(T) = \varepsilon_\lambda(T) \tag{2.65}$$

$$\alpha_{\lambda,\Omega}(T) = \varepsilon_{\lambda,\Omega}(T) \tag{2.66}$$

and similarly holds for frequency representations. Thus, for opaque materials, both ε, α, and $\mathcal{R}$ can be determined from a single measurement since:

$$\mathcal{R} = 1 - \alpha, \qquad \text{iff.} \qquad \mathcal{T} = 0 \tag{2.67}$$

Care must be taken when applying Kirchhoff's law, as it is derived under the assumption that the illuminated surface and the radiation source are at thermal equilibrium. If the temperature difference between the surface and the source exceeds several hundred degrees, thermal equilibrium is no longer maintained, and Kirchhoff's law becomes invalid [9]. In such cases, much energy is directed toward heating the object rather than maintaining radiative balance.

2.4 Hyperspectral Imaging

A standard color image, such as those captured by digital cameras or smartphones, consists of three spectral channels: *RGB* corresponding to red, green, and blue wavelengths (Figure 2.16a). These channels are combined to produce color images that approximate how humans perceive colors in the visible spectrum. Multispectral and hyperspectral imaging extend this concept by increasing the number of spectral channels, allowing for more detailed spectral information.

In multispectral imaging (MSI), the images consist of a relatively limited number of discrete spectral channels, typically ranging from 3 to 10 (but can contain more), and these channels do not necessarily cover a continuous portion of the spectrum. Conversely, hyperspectral imaging (HSI) involves capturing images with a much larger number of spectral channels, often exceeding 100, which form a near-continuous spectrum. [14].

Hyperspectral images can be considered a three-dimensional data structure, often referred to as a *data cube*. This data cube comprises two spatial dimensions corresponding to the width and height of the image and a third spectral dimension representing the spectrum at each pixel location. In contrast to conventional photos, where each pixel contains information from three color channels, each pixel in a hyperspectral image contains a detailed spectrum that provides information across a wide range of wavelengths.

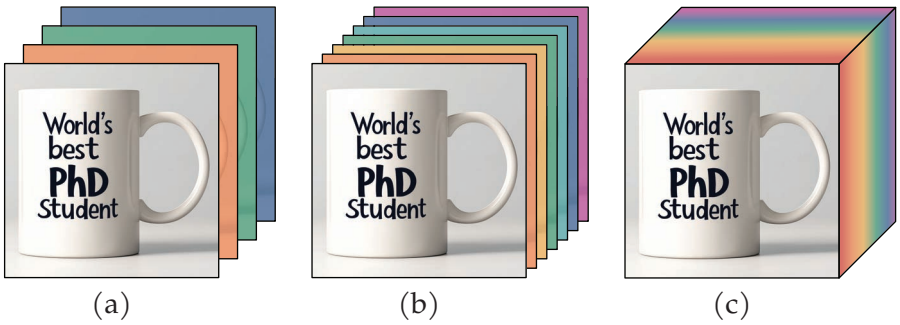

Figure 2.16: Different kinds of color imaging: (a) RGB, (b) multispectral, and (c) hyperspectral.

2.4.1 Hyperspectral Imaging Techniques

Hyperspectral data can be acquired through various methods, utilizing different types of equipment. This section overviews four common techniques, highlighting their fundamental principles without delving into specific technical details. These approaches are illustrated in Figure 2.17.

Whisk Broom

The whisk broom technique is one of the simplest yet most time-intensive hyperspectral imaging methods. It involves acquiring the spectrum of each pixel individually, which requires either the subject or the detector to be moved incrementally between each spectral measurement. Despite its slower acquisition process, the whisk broom approach can achieve very high spectral resolution and is relatively straightforward to implement using existing equipment, such as Raman microscopes.

Push Broom

Push broom imaging improves upon the whisk broom technique by simultaneously capturing the spectra of an entire row of pixels, signifi-

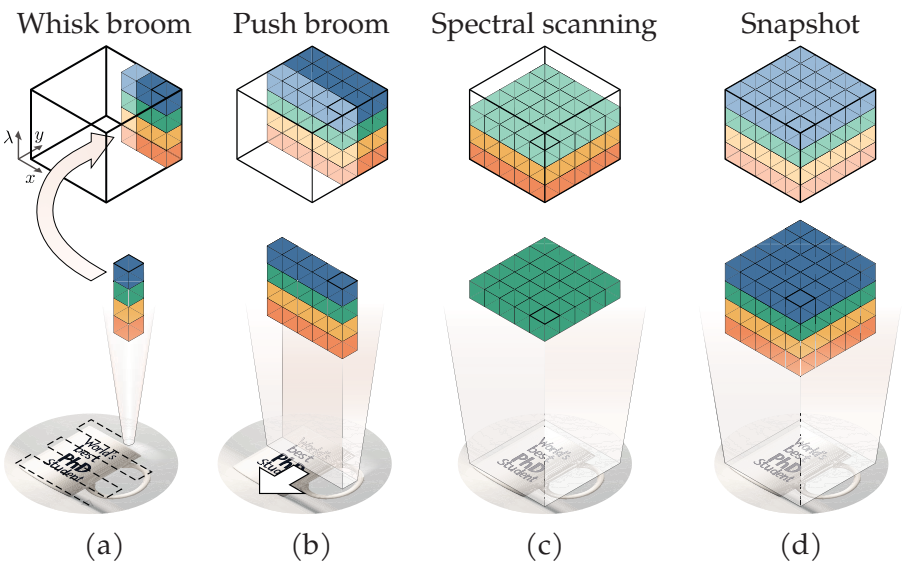

Figure 2.17: Schematic illustration of how the hyperspectral data cube is acquired using different imaging techniques. (a) whisk broom (b) push broom (c) spectral scanning (d) snapshot.

cantly reducing the acquisition time. However, relative motion between the detector and the subject is still required to acquire the complete spatial information. This requirement typically limits the size of the samples that can be imaged, as they must fit within the given measurement setup.

Spectral Scanning

Unlike the push broom method, spectral scanning captures all spatial information simultaneously but only within a narrow spectral band. This means that rather than sequentially acquiring slices along a spatial axis, it captures slices along the spectral axis, gradually building up the data cube. A key advantage of this approach is that it eliminates the need for relative movement between the detector and the subject, offering greater flexibility for various imaging scenarios.

Snapshot

Snapshot hyperspectral imaging captures *both* spatial and spectral information simultaneously, making it the most versatile acquisition technique. This method is also the fastest, as it does not rely on scanning. However, this increased speed and versatility come at the cost of higher complexity, often necessitating sophisticated algorithms to accurately reconstruct the hyperspectral data cube [15].

2.5 Processing Methods for Hyperspectral Data

Hyperspectral imaging integrates data processing methods from image and spectral analysis, although this thesis emphasizes spectral techniques more. This section defines the processing methods used throughout the thesis. Let $\mathbf{D} \in \mathbb{R}^{M \times N \times L}$ (M rows, N columns, and L spectral channels) denote the hyperspectral data cube, with entries $\mathbf{D}_{m,n,l}$ representing the data point at pixel index (m, n) in spectral channel l.

In many of the processing techniques used in this work, the spatial dimensions of the data cube are disregarded. The data is instead reshaped into a two-dimensional matrix, $\mathbf{X} \in \mathbb{R}^{P \times L}$, where $P = M \cdot N$ is the total number of pixels. Each row of $\mathbf{X}$ represents the spectral vector for a single pixel in this format. This reshaped representation is sometimes referred to as the *flattened* or simply *reshaped* data cube. p and l subscripts are used for denoting rows and columns, respectively. Throughout this thesis, bold capital letters refer to matrices (or data cubes when applicable), bold lowercase letters denote row vectors and regular/plain symbols are used for scalar values.

The *spectral* processing methods disregard the spatial coordinates of the images. Therefore, only two-dimensional matrix operations are considered in this section, focusing on standard processing techniques used throughout the analysis.

Row-wise Versus Colum-wise Operations

Many of the processing steps demonstrated in this section are performed row-by-row, meaning they process one pixel or sample at a time. This approach is chosen because the variables (columns of $\mathbf{X}$) represent spectral channels, all of which share the same units. In much of the literature [16, 17, 18], such processing steps are typically applied on a column-by-column basis. This method is particularly suitable for datasets measuring variables in different units. This could be a dataset containing people's shoe size and weight. In such cases, individually scaling and centering each variable ensures comparability across different units.

However, when working with spectral data, column-wise preprocessing introduces specific implications. Consider imaging a green jelly bean against a plain white background and extracting its spectrum. If the entire flattened data cube is scaled and mean-centered column-wise,

the spectrum of the jelly bean would change if the background were replaced with something else. This occurs because column-wise operations depend on the global distribution of each variable within the dataset. While this approach is practical when the relative variability between pixels is of interest, it may alter the spectral shape of individual samples.

Row-wise processing is preferred to preserve the spectral shape and ensure the processing steps are independent of the rest of the data cube. This method treats each pixel spectrum independently, making it unaffected by the surrounding data. Therefore, unless stated otherwise, the processing steps employed in this thesis are performed on a row-wise basis.

Mean Centering

Mean centering is a preprocessing step that involves shifting the spectral axes such that each row of the flattened data cube has a mean value of zero. This adjustment is often important to remove bias in subsequent analyses, including Principal Component Analysis (PCA, page 39), where non-centered data can cause the mean to dominate the first principal component. The mean centering operation is mathematically defined as:

$$\mathbf{X}' = \mathbf{X} - \bar{\mathbf{x}}\mathbf{1}^\top, \quad \bar{x}_p = \frac{1}{L}\sum_{l=1}^{L} X_{p,l}, \quad p = 1, \ldots, P, \tag{2.68}$$

where $\mathbf{1}^\top \in \mathbb{R}^{1\times L}$ broadcasts the mean vector $\bar{\mathbf{x}}$ to match the dimensions of $\mathbf{X}$.

Column-wise mean centering: This is to show an example of what changes when converting the processing step from row- to column-wise operation:

$$\mathbf{X}' = \mathbf{X} - \mathbf{1}\bar{\mathbf{x}}^\top, \quad \bar{x}_l = \frac{1}{P}\sum_{p=1}^{P} X_{p,l}, \quad l = 1, \ldots, L, \tag{2.69}$$

Here, $\mathbf{1} \in \mathbb{R}^{P\times 1}$.

Baseline Correction

The hyperspectral imager used in this work is based on a microbolometer detector (both are described in detail in Chapter 3). Due to manufac-

turing imperfections, each bolometer pixel exhibits unique response and offset characteristics, leading to variations in their output for the same incident radiation. One common approach to address this issue is Non-Uniformity Correction (NUC, detailed in Chapter 3.3.3).

The scanning Fabry-Pérot interferometer (SFPI) provides an alternative correction method, giving the camera hyperspectral capabilities. The SFPI consists of two mutually parallel, partially transmitting mirrors forming a cavity, where the cavity length governs the transmission profile. When the mirrors are positioned close together, minimal light passes through, effectively acting as a "dark frame." In the hyperspectral data cubes, the first spectral channel corresponds to the starting position of the SFPI, where the mirrors are closest. The pixel offsets are corrected by subtracting this spectral channel from the remaining channels, effectively aligning all rows to start at zero. This correction is expressed mathematically as:

$$\mathbf{X}' = \mathbf{X} - \mathbf{x}_1 \mathbf{1}^\top, \quad \mathbf{x}_1 = \mathbf{X}_{:,1} \in \mathbb{R}^{P \times 1} \tag{2.70}$$

where $\mathbf{x}_1$ is the first collumn of $\mathbf{X}$ and $\mathbf{1}^\top \in \mathbb{R}^{1 \times L}$ is a row vector containing only 1's.

Normalization

Normalization is often useful for standardizing data and improving comparability across observations. Various normalization techniques can be applied, depending on the specific requirements of the analysis. A common approach involves rescaling the entire flattened hyperspectral data cube such that its maximum value is 1. This global normalization is achieved by dividing the matrix by its maximum element:

$$\mathbf{X}' = \frac{\mathbf{X}}{\max\{\mathbf{X}\}} \tag{2.71}$$

In some cases, it is more appropriate to normalize each row of the data cube individually, ensuring that the maximum value of each row is 1. This row-wise normalization is defined as:

$$\mathbf{X}' = \mathbf{X} \oslash \left(\mathbf{v}\mathbf{1}^\top\right), \quad v_p = \max\{\mathbf{X}_{p,:}\}, \quad p = 1, \ldots, P, \tag{2.72}$$

where $\oslash$ denotes elementwise division (Hadamard division). Here, $\mathbf{v}\mathbf{1}^\top$ represents a matrix constructed by replicating the row-wise maximum values of $\mathbf{X}$ across all columns for each row.

Another commonly used normalization method is to scale the entire flattened data cube such that its Frobenius norm equals 1. This global Frobenius normalization is performed as follows:

$$\mathbf{X}' = \frac{\mathbf{X}}{\|\mathbf{X}\|_F}, \qquad \|\mathbf{X}\|_F = \sqrt{\sum_{p,l} |X_{p,l}|^2} \tag{2.73}$$

Analogously, normalization can also be performed row by row, ensuring that the Frobenius norm of each row vector is equal to 1. This row-wise Frobenius normalization is given by:

$$\mathbf{X}' = \mathbf{X} \oslash \left(\mathbf{u}\mathbf{1}^\top\right), \quad u_p = \|\mathbf{X}_{p,:}\|_F, \quad p = 1, \ldots, P \tag{2.74}$$

Standard Normal Variate

Standard Normal Variate (SNV) is a standardization technique that simultaneously mean-centers and scales each row of a flattened data cube to have a standard deviation of 1. This method is particularly beneficial for data analysis techniques such as Principal Component Analysis, which often benefit from mean-centered data and are highly sensitive to differences in scaling among variables. By removing the influence of mean offsets and scaling variations, SNV enhances spectral data's comparability and improves subsequent analyses' robustness.

$$\mathbf{X}' = \left(\mathbf{X} - \bar{\mathbf{x}}\mathbf{1}^\top\right) \oslash \left(\boldsymbol{\varsigma}\mathbf{1}^\top\right), \tag{2.75}$$

$$\varsigma_p = \sqrt{\frac{1}{L}\sum_{l=1}^{L}(X_{p,l} - \bar{x}_p)^2}, \quad p = 1, \ldots, P,$$

where ς_p and $\bar{x}_p$ denote the standard deviation and the mean of the pth row of $\mathbf{X}$, respectively.

Savitzky-Golay Filtering

The final spectral processing technique discussed in this section is the Savitzky-Golay filter, which is a digital smoothing filter [19]. While the detailed mechanics of the filter are beyond the scope of this thesis, it can be briefly described as follows: the filter applies a sliding window of size

$2n + 1$ (where n is an integer denoting the number of samples) across the signal. Within the window, a polynomial of order p is fit to the data points using a least-squares method. Furthermore, the filter allows for calculating derivatives of order m based on the fitted polynomial, which can be useful in specific applications.

The `savgol_filter` function from the SciPy library is utilized for implementing the Savitzky-Golay filter in this thesis [20].

2.6 Principal Component Analysis

Principal Component Analysis (PCA) is a well-established technique commonly employed for exploratory spectral data analysis, warranting a dedicated section within this thesis. Hyperspectral imaging typically involves large datasets that can be computationally intensive to process. In many cases, especially in spectral processing, the variables within these datasets are highly correlated, leading to significant redundancy. Consequently, portions of the data can often be excluded without substantially altering the overall informational content.

PCA addresses this challenge by identifying the directions within the dataset that exhibit the greatest variance. Specifically, PCA transforms the dataset into a new coordinate system where the variance is maximized along each axis. The objective is to compute an orthogonal basis, $\{\mathbf{p}_1, \mathbf{p}_2, \ldots, \mathbf{p}_L\}$, where $\mathbf{p}_l \in \mathbb{R}^L$, such that the variance of the projections $\mathbf{X}\mathbf{p}_l$ is maximized. The first basis vector aligns with the direction of maximum variance, while each subsequent vector is orthogonal to the preceding ones and corresponds to the next highest variance. Thus, PCA is useful for isolating significant spectral features that may otherwise be obscured by noise or redundant components within the signal.

This transformation further enables the projection of the original data $\mathbf{x} \in \mathbb{R}^L$ onto a reduced-dimensional subspace, $\mathbf{t} \in \mathbb{R}^Q$, where $Q \leq L$. By reducing dimensionality in this manner, PCA facilitates the extraction of essential features, thereby simplifying analysis while preserving the underlying structure of the data.

The covariance matrix quantitatively measures how the different variables (spectral channels) are correlated. The eigenvectors of this covariance matrix represent the directions of greatest variance within the data [21]. To compute the covariance matrix, the *columns* of $\mathbf{X}$ must first be mean-centered, as described by Eq. (2.76) (and also presented in Eq. (2.69)):

$$\mathbf{X_c} = \mathbf{X} - \mathbf{1}\bar{\mathbf{x}}^\top, \tag{2.76}$$

where $\bar{\mathbf{x}}$ is the column mean vector. The covariance matrix of the mean-centered data is then calculated as:

$$\mathbf{C} = \frac{1}{P-1}\mathbf{X_c}^\top\mathbf{X_c} \tag{2.77}$$

Here, the diagonal elements $\mathbf{C}_{i,i}$ represent the variance of the ith variable (column) of $\mathbf{X_c}$, while the off-diagonal elements $\mathbf{C}_{i,j}$ describe the covariance between the ith and j^{th} variables.

To identify the directions of maximum variance within $\mathbf{X_c}$, the eigenvalue problem for the covariance matrix is solved:

$$\mathbf{C}\mathbf{p}_i = \lambda_i \mathbf{p}_i, \tag{2.78}$$

where $\mathbf{p}_i$ and λ_i are the ith eigenvector and eigenvalue, respectively. It should be noted that λ in this context does not refer to wavelengths; this notation is employed to remain consistent with the convention commonly used in the literature, where eigenvalues are typically denoted by λ. In the context of PCA, the eigenvectors $\mathbf{v}_i$ are referred to as the *loadings* or *principal components* (PCs) and serve as orthogonal basis vectors. The eigenvector associated with the largest eigenvalue corresponds to PC 1, the one with the second largest eigenvalue is PC 2, and so on. This ordering satisfies $\lambda_1 \geq \lambda_2 \geq \cdots \geq \lambda_L \geq 0$. By truncating the calculation at the Qth eigenvalue, a low-rank approximation of $\mathbf{X_c}$ can be obtained in the new orthogonal basis:

$$\mathbf{T} = \mathbf{X_c}\mathbf{P}_Q, \tag{2.79}$$

where $\mathbf{T}$ represents the *scores*, i.e., the projection of $\mathbf{X_c}$ onto the basis vectors. The eigenvalues indicate the proportion of the total variance captured by the ith component, a metric commonly referred to as the *explained variance*. This is computed as:

$$\xi_i = \frac{\lambda_i}{\sum_{j=1}^{L} \lambda_j} \tag{2.80}$$

Similarly, the cumulative explained variance, representing the total variance explained by the first Q components, is calculated as:

$$\xi_{\text{cumulative}}(Q) = \frac{\sum_{i=1}^{Q} \lambda_i}{\sum_{j=1}^{L} \lambda_j} \tag{2.81}$$

Utilizing the property $\mathbf{P}_Q\mathbf{P}_Q^\top = \mathbf{I}$, where $\mathbf{I}$ is the identity matrix, the original data $\mathbf{X_c}$ can be approximated as:

$$\tilde{\mathbf{X}}_\mathbf{c} = \mathbf{T}\mathbf{P}_Q^\top + \mathbf{E}, \tag{2.82}$$

where $\mathbf{E}$ represents the residual error not captured by the first Q components.

Although solving the eigenvalue problem for the covariance matrix provides an intuitive understanding of PCA, it becomes computationally expensive for large datasets, mainly when the number of variables is large. Singular Value Decomposition (SVD) is preferred in such cases, as it is computationally more efficient and numerically stable [22]. However, in the datasets used in this thesis, which typically involve approximately 150 spectral bands, directly calculating the covariance matrix remains the more efficient approach for implementing PCA.

The processing techniques discussed in this chapter, along with additional methods for handling data from the HSC, have been implemented in a Python package designed to facilitate data processing. This package includes functionalities for data handling, preprocessing, PCA, and simulation and is available at `https://pypi.org/project/HSTI/`. Furthermore, a dedicated hyperspectral image viewer has been developed to streamline data analysis and PCA visualization. A more detailed discussion of this tool is provided in Appendix H.

2.7 Summary

This chapter has provided a broad overview of key concepts relevant to both thermal and hyperspectral imaging. Fundamental radiometric quantities, such as exitance and radiance, have been introduced alongside a discussion of blackbody radiators, which play a central role in thermal imaging. The spectral distribution of blackbody radiation is governed by Planck's law of thermal radiation and, when combined with emissivity, serves as an approximation for the thermal radiation emitted by various materials. Emissivity, a spectral property, quantifies the extent to which a material emits thermal radiation. Detecting spectral features in emissivity can thus be employed for material classification. Kirchhoff's law has also been introduced, establishing that emissivity and absorptance are equal for a material in thermal equilibrium. This principle allows the emission spectrum of a material to be directly inferred from its absorptance.

In addition, hyperspectral imaging techniques have been discussed, with a focus on spectral scanning hyperspectral imagers. Common hyperspectral data processing methods have been presented, including PCA, which is a valuable tool for identifying variance within a dataset and can be leveraged in various classification techniques.

The following chapters provide a more detailed examination of the specific hyperspectral imager used in this project and its key components.

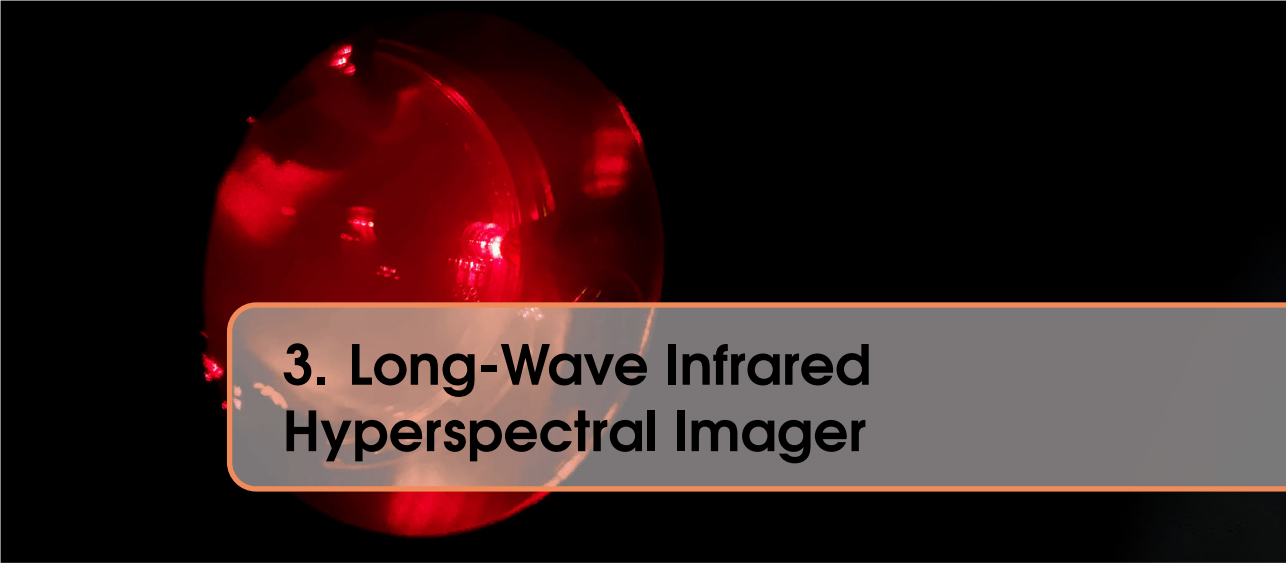

3. Long-Wave Infrared Hyperspectral Imager

This chapter provides an overview of the LWIR hyperspectral camera (HSC) used in this project, detailing its primary components and their functions. Iterative upgrades were made to the HSC over the course of the project, with the three most significant modifications outlined here. Particular emphasis is placed on the physics of the microbolometer detector, as understanding its working principles is essential for accurate interpretation of its output. The chapter concludes with an introductory description of the scanning Fabry-Pérot interferometer, setting the foundation for a more detailed discussion in the subsequent chapter.

3.1 Overview of Hyperspectral Imager

This work explores the underlying principles and potential applications of the LWIR HSC (also sometimes referred to as hyperspecral imager) shown in Figure 3.2. Here, the front part of the imager is cut away to reveal the components inside the lens housing. This imager integrates a microbolometer-based thermal camera (components 3 and 4 in Figure 3.2) with an SFPI (components 1 and 2 in Figure 3.2). The SFPI is described in further detail in subsequent sections and consists of two partially transmitting mirrors placed microns apart, forming a cavity. The distribution of wavelengths that can be transmitted through the SFPI depends on the cavity length, ℓ. The SFPI thus functions as a variable bandpass filter when the cavity length can be precisely controlled. A hyperspectral image can, therefore, be captured by acquiring images at different cavity lengths.

The HSC has gone through iterative improvements throughout the PhD project. The model presented in Figure 3.2 is a newer iteration of the prototype presented in Figure 3.1a, which has been used to capture most of the results presented in this thesis. The most notable difference between the two prototypes is the way the metal flange in which the SFPI mirrors are mounted. The differences are described in further detail in the designated section in section 3.5. The newest prototype at the time of writing (q1 2025) is presented in Figure 3.1b. This prototype is made by Sandholt ID and encapsulates all components inside a single box with a carrying handle. At present, this HSC has been 3D printed into a

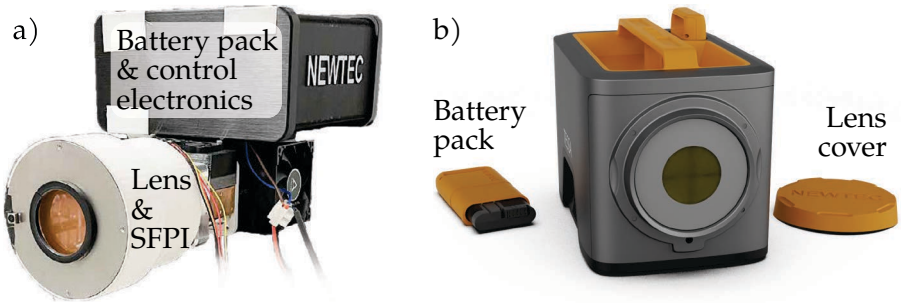

Figure 3.1: (a) Image of the prototype LWIR HSC, which has been used to capture the majority of the data presented in this thesis. (b) Render of imager made by Sandholt ID. At the time of writing (Q1 2025), this is the most current version of the imager and has been 3D-printed as a functioning prototype.

function prototype. However, some modifications to the software still need to be done before the camera can function as a standalone device (without using an external computer to operate it).

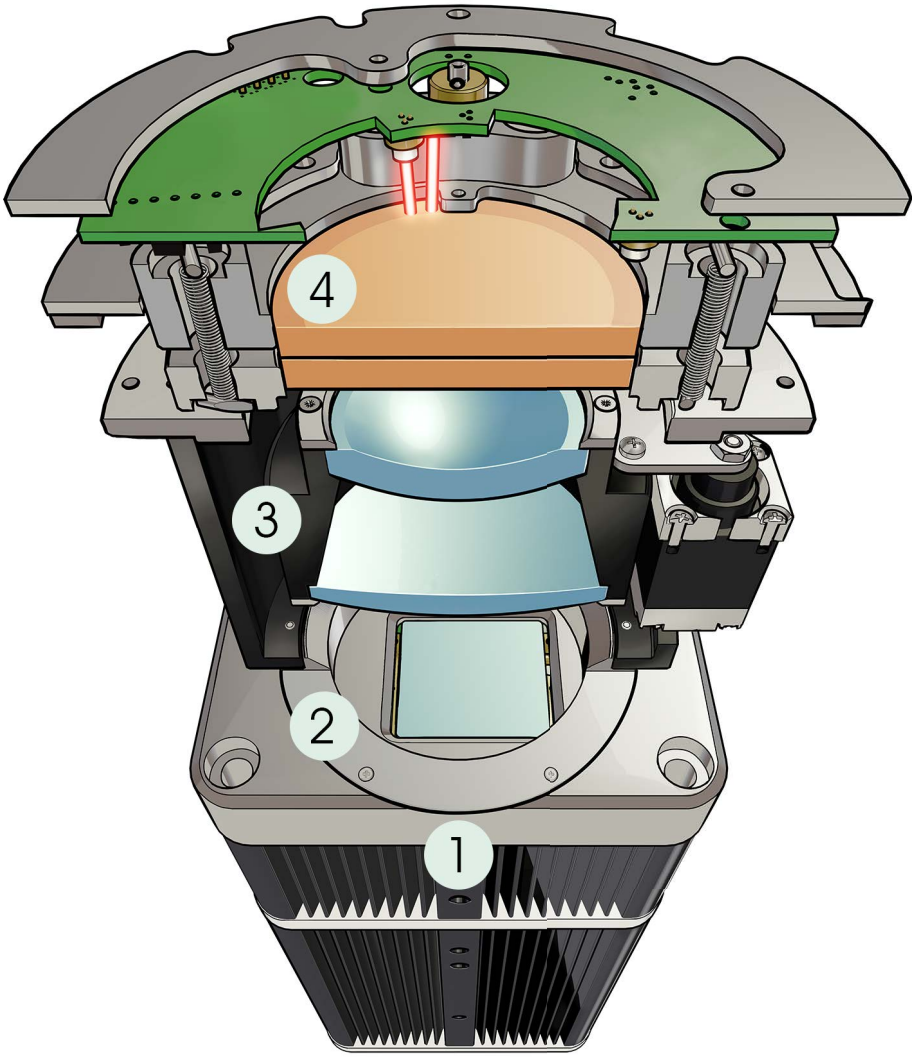

Figure 3.2: 3D illustration of the LWIR HSC with a cutaway to reveal the components inside the lens housing: 1) QT5222 camera body; 2) Lynred Pico1024Gen2™ microbolometer detector; 3) Germanium objective (35 mm, $f/1$); 4) Scanning Fabry-Pérot interferometer.

3.2 Camera Body

The camera body houses all electronics required to process data from the detector into usable images. The older QT5022 and the newer QT5222 models share a similar external appearance but exhibit significant differences in processing power. The QT5022 features an AMD G-T56N (1.65 GHz, dual-core, 2-thread) processor from 2011, while the QT5222 is equipped with an AMD Ryzen Embedded V1605B (2.0 GHz, quad-core, 8-thread) processor from 2018. The increased processing capability of the QT5222 enables faster image processing, allowing the camera to capture more images in the duration of a hyperspectral image acquisition sweep. Beyond this performance difference, the two models yield comparable data quality.

The camera's graphical user interface (GUI) enables user control and is primarily developed by colleague A. L. Jørgensen and consultant O. Deyneka. Through this interface, users can monitor key information, such as the detector temperature and the position of the mirrors in the SFPI, as well as adjust the camera's focal length. Figure 3.3 displays two screenshots of the GUI, illustrating its layout and functionality. Colleague H. Andersen and consultant B. Popyk have primarily written other software related to the HSC operation.

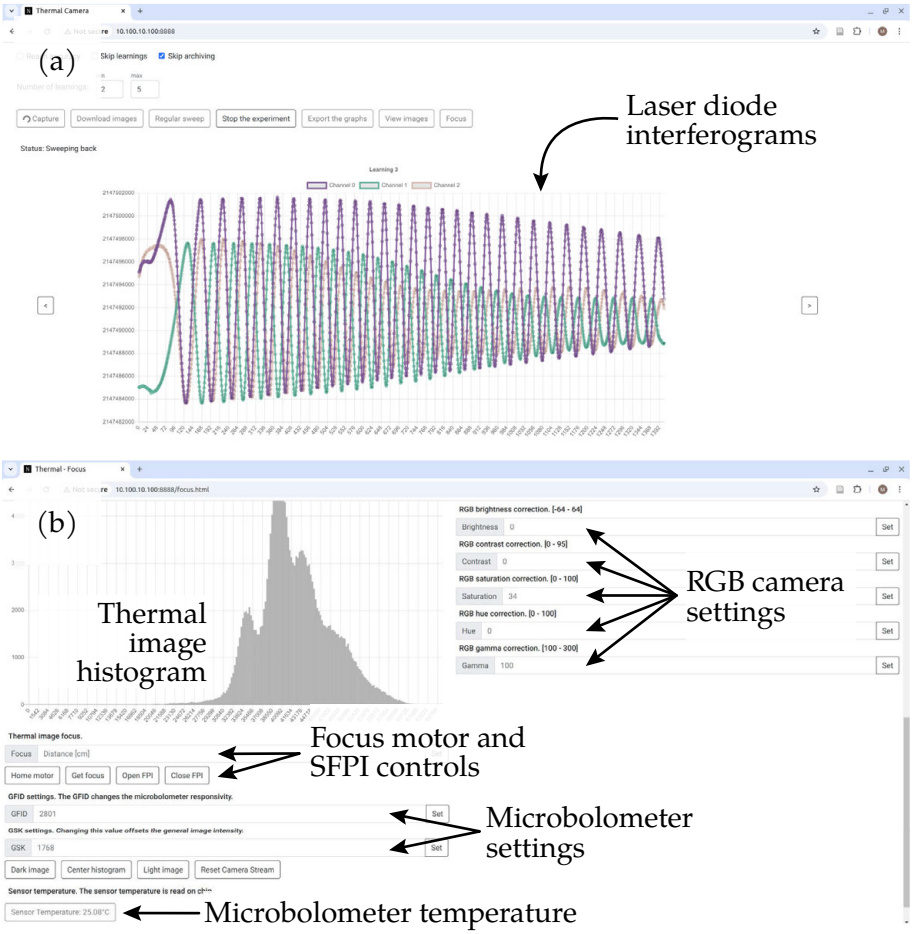

Figure 3.3: Screenshots of the GUI used for controlling the HSC. (a) Plot of the three laser diode interferograms that updates for each forward and backward sweep, during both calibration and acquisition. This is used to monitor the operation of the SFPI and make sure the mirrors are moving correctly. (b) Control interface for managing various camera functions, including focus adjustments, temperature monitoring, and configuration of microbolometer settings.

3.3 Microbolometer

A microbolometer is a thermal radiation detector that converts incident radiation into thermal energy, resulting in a temperature rise within the detector. The HSC is equipped with a 1024×768-pixel uncooled microbolometer detector (Pico1024Gen2™, Lynred, FR) featuring a 17 µm pixel pitch, a thermal time constant < 12 ms, and a specified spectral sensitivity range of 8 – 14 µm (1250 – 714 cm^{-1}) [23]. However, experimental observations indicate that the detector can also respond to wavelengths beyond this range. Although the LWIR regime is commonly defined as spanning 8 – 14 µm, this thesis extends the range to 8 – 15 µm (1250 – 667 cm^{-1}) to reflect the observed spectral response of the detector.

This section aims to give an overview of the microbolometer technology, focusing on the physical process of converting LWIR radiation into an electrical signal. The physics of these detectors is rather complex. Since it is not the main focus of this thesis, most of the analysis involving noise and sensitivity, such as noise equivalent power (NEP) and noise equivalent temperature difference (NETD), will not be covered. Usually, these detectors consist of entire arrays of microbolometers, but this discussion will focus on a single bolometer for simplicity.

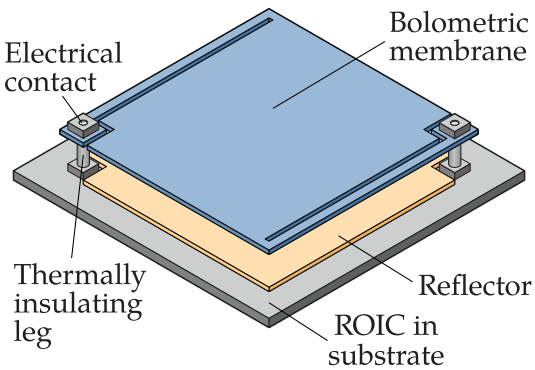

Figure 3.4: Schematic representation of microbolometer. The bolometric membrane is made from a material with temperature-dependent resistivity. Most incident light is absorbed. The transmitted fraction reflects off the reflector behind the membrane to increase the chance of absorption. The membrane is lifted above the rest of the substrate and is only connected through thermally insulating legs, which connect it to the rest of the ROIC.

The microbolometer consists of a bolometric membrane (Figure 3.4) suspended on two thermally insulating legs. The membrane is typically composed of a material such as amorphous silicon (a-Si), which exhibits a high absolute temperature coefficient of resistance (TCR) of $\beta \approx -3\%\,\mathrm{K}^{-1}$ [24]. The negative sign indicates that the material's resistance decreases with increasing temperature, in contrast to metals, which generally have a positive TCR on the order of $\approx +0.4\%\,\mathrm{K}^{-1}$ [25]. The membrane is designed to be as thin as possible to reduce its heat capacity, enhancing the sensitivity of the bolometer. The thermally insulating legs not only isolate the membrane from the substrate but also facilitate electrical measurements by allowing the voltage drop across the membrane to be measured when a small current is applied. A reflector is deposited on the substrate beneath the membrane to enhance the detector's absorptivity, reflecting incident light that is not absorbed on its initial pass through the membrane, thereby providing multiple opportunities for absorption. The substrate beneath the membrane also contains the readout integrated circuit (ROIC), which is responsible for measuring the resistance of the membrane.

3.3.1 Temperature Change of Microbolometer

The resistivity of the microbolometer membrane varies with temperature and, therefore, with the amount of absorbed radiation. The relationship between absorbed radiant flux, $\alpha_\mathrm{d}\Phi_0$, over time t, and the resulting temperature change ΔT_d of the detector is given by Eq. (3.1) [7].

Microbolometer Energy Conversion

$$\alpha_\mathrm{d}\Phi_0 = C_\mathrm{th}\frac{d\Delta T_\mathrm{d}}{dt} + G_\mathrm{th}\Delta T_\mathrm{d} \tag{3.1}$$

Here, $\Phi_0 = \Phi(T_\mathrm{inc}) - \Phi(T_\mathrm{d})$ represents the net radiation power transferred to the detector, reflecting the difference between incident flux from the observed scene, $\Phi(T_\mathrm{inc})$, and the detector's outward flux, $\Phi(T_\mathrm{d})$. α_d, C_th $[\mathrm{J}\cdot\mathrm{K}^{-1}]$, and G_th $[\mathrm{W}\cdot\mathrm{K}^{-1}]$ denote the detector's absorptivity, heat capacity, and thermal conductance, respectively. Solving the differential equation yields the expression for temperature change:

$$\Delta T_\mathrm{d} = \frac{\alpha_\mathrm{d}\Phi_0}{G_\mathrm{th}}\left(1 - \exp\left\{-\frac{t}{\gamma_\mathrm{th}}\right\}\right), \qquad \gamma_\mathrm{th} = \frac{C_\mathrm{th}}{G_\mathrm{th}} \tag{3.2}$$

where γ_{th} is the time constant. A smaller time constant is preferred for the detector to detect rapid changes in radiant flux. This can be achieved by reducing membrane heat capacity (reducing its mass) or increasing thermal conductance by, e.g., decreasing the cross-sectional area of the insulating legs. However, lower G_{th} is generally favored as it enhances temperature change — and consequently signal strength — in response to absorbed radiation.

The behavior described by Eq. (3.2) is depicted in Figure 3.5. Here, a microbolometer experiences a square pulse of radiation where the heating and subsequent cooling can be observed. The time constant γ_{th} describes how quickly the microbolometer reacts to changes in net radiation flux. If the net radiation flux changes at $t = 0$, the signal will achieve approximately 63.2% of its total change after a single time constant. Specifically, for an increasing signal (initially zero), it reaches 63.2% of its final asymptotic value after one time constant. Conversely, for a decreasing signal (approaching zero), the value will be approximately 36.8% of its initial value after one time constant. In thermal imaging, accurate temperature measurements typically require five time constants, at which point the detector signal has achieved about 99.3% of its total change.

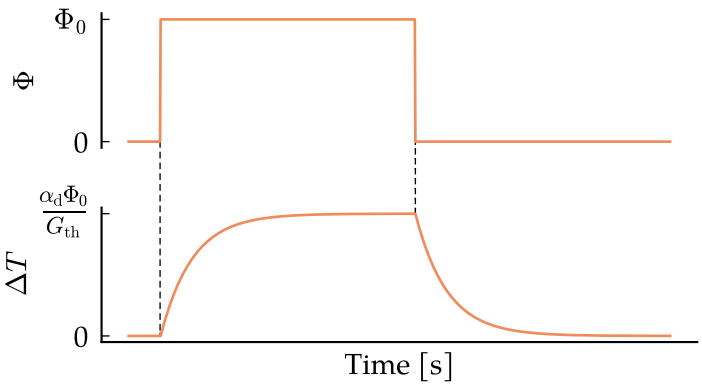

Figure 3.5: Heating and cooling of a thermal detector under a pulse of incident radiation.

The steady-state temperature change of the microbolometer can be determined from Eq. (3.2) as:

$$\Delta T_{\mathrm{d},t\to\infty} = \frac{\alpha_{\mathrm{d}}\Phi_0}{G_{\mathrm{th}}} \tag{3.3}$$

It is important to note that while $\Delta T_{\mathrm{d},t\to\infty} \propto \Phi_0$, Φ_0 itself is not directly proportional to the scene temperature T. This is because blackbody flux is $\Phi_{\mathrm{BB}} \propto T^4$, following the Stefan-Boltzmann law (Eq. (2.35)), though here, it is scaled by the area of the emitter. Additionally, Φ_0 is also offset by the outgoing flux of the detector, $\Phi(T_{\mathrm{d}})$.

3.3.2 Measuring Temperature Change of Microbolometer

The resulting resistance change from temperature increase is given by:

$$\Delta R = \beta \bar{R} \Delta T_{\mathrm{d}} \tag{3.4}$$

where $\bar{R}$ is the average membrane resistance within the interval ΔT_{d}. Combining Eq. (3.3) and Eq. (3.4) shows that *the steady-state resistance change is proportional to the net radiation transfer*:

$$\Delta R_{t\to\infty} = \frac{\beta \bar{R} \alpha_{\mathrm{d}} \Phi_0}{G_{\mathrm{th}}} \tag{3.5}$$

A bias current I is applied to measure membrane resistance, and the resulting voltage drop U is measured. According to Ohm's law, the steady-state voltage drop is:

$$U_{t\to\infty} = I \frac{\beta \bar{R} \alpha_{\mathrm{d}} \Phi_0}{G_{\mathrm{th}}} \tag{3.6}$$

The slope of the voltage drop relative to net radiation flux is:

$$\mathscr{R}_U = I \frac{\beta \bar{R} \alpha_{\mathrm{d}}}{G_{\mathrm{th}}} \tag{3.7}$$

This slope is known as the responsivity of the microbolometer $[\mathrm{V} \cdot \mathrm{W}^{-1}]$, and it increases with the bias current, but this, in turn, introduces self-heating, which elevates noise. However, there is a limit to how short the integration time can be since the signal-to-noise-ratio (SNR) is affected by the sampling time due to thermal noise known as Johnson noise

[26]. This noise is $U_{\text{noise}} \propto 1/\sqrt{t_{\text{int}}}$, where t_{int} is the integration time. Thus, longer integration times are needed to reduce the impact of this noise. To balance signal strength and self-heating, short integration times (typically tens of microseconds) are used to minimize self-heating. Often, only one line of pixels is read at a time, allowing the microbolometers to cool before being read again in the next frame [27].

3.3.3 Non-Uniformity Correction

Non-uniformity correction (NUC) is employed to account for pixel response variations caused by manufacturing tolerances. Pixels exposed to the same irradiance do not necessarily produce identical outputs, and their sensitivity to changes in irradiance may also differ, resulting in inconsistent signal variations under changing irradiance levels. The NUC compensates for these discrepancies.

Implementing the NUC must account for various factors, including detector temperature and the GSK voltage. The GSK voltage is a detector parameter that offsets the output signals to ensure they remain within the detector's dynamic range. Consequently, the NUC requires multiple calibration measurements to relate the influence of these parameters to the detector output.

However, the use of the NUC has been limited in this project, as initial offset corrections can be effectively performed using the SFPI.

While a microbolometer detector has been chosen for this project, it is not the only method for detecting infrared radiation. The following section provides a brief overview of photon detectors, which operate on principles distinctly different from those of microbolometer sensors.

3.3.4 Photon Detectors

A brief overview of photon detectors is warranted, as they employ a distinctly different detection method for LWIR radiation compared to microbolometers and are often used in high-end thermal cameras. Photon detectors provide an alternative method for sensing thermal radiation, functioning similarly to the detectors found in consumer electronics, such as smartphone cameras. These detectors operate by capturing electrons excited by incident radiation, as depicted in Figure 3.6. For electron excitation to occur, the incident radiation must have an energy $\mathcal{U} = h\nu$

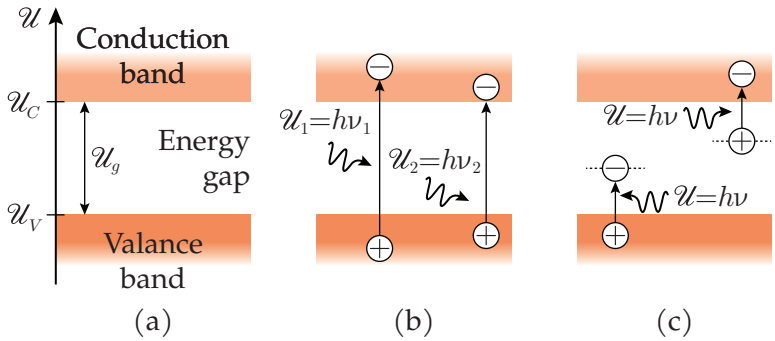

Figure 3.6: (a) Simplified illustration of the energy-band structure. $\mathcal{U}_V$ denotes the upper boundary of the valence band, while $\mathcal{U}_C$ marks the lowest energy level of the conduction band. $\mathcal{U}_g$ represents the energy gap between these bands. (b) Incident photons must possess sufficient energy to excite electrons across the energy gap, enabling transitions from the valence band to the conduction band. (c) Local impurities within the material create localized electronic states, which require significantly lower energy for electrons to reach.

that matches or exceeds the material's bandgap energy, $\mathcal{U}_g$. Localized impurities, however, can introduce intermediate energy states within the band gap, enabling electron excitation by lower-energy photons with longer wavelengths.

A widely used photon detector in thermal imaging is the mercury cadmium telluride (MCT) detector. The spectral sensitivity of an MCT detector is tunable based on the relative concentrations of mercury and cadmium. Pure cadmium telluride, for example, is sensitive to wavelengths around 0.83 µm [28]. By adjusting the mercury content, intermediate energy states are introduced, allowing photodiode detectors to operate at wavelengths as long as 13 µm.

Since photovoltaic detectors convert photons directly into electrical signals, their response time is very fast, typically on the order of nanoseconds. The integration time, which in the case of photon detectors defines the period over which incoming light is accumulated, directly influences signal strength. Longer integration times mean more time to fill the electron well, thus yielding stronger signals. For photon detectors, this integration time is usually on the order of microseconds [29]. This makes the photon detectors capable of capturing fast-moving subjects much better than the microbolometers, which are inherently limited by their

characteristic time constants.

However, the small electronic band gap of photon detectors does mean that even thermal energy within the detector itself is enough to generate free charge carriers, leading to increased noise. Consequently, most MCT detectors (and other LWIR photon counters) are cryogenically cooled to approximately 77 K using liquid nitrogen (LN). This cooling requirement significantly increases the cost and complexity of MCT detectors compared to microbolometers, which can operate effectively at room temperature. The higher price of MCT detectors also stems from the complexity of their fabrication and the specialized materials involved. Additionally, MCT detectors require advanced readout electronics to support their fast response times, allowing them to handle high-speed data acquisition. Consequently, MCT-equipped cameras tend to be significantly more expensive (≈ 30 times the price of a microbolometer of similar resolution) and bulkier than microbolometer-based systems of comparable resolution.

3.4 Thermal Lens

To capture an image, light must be focused onto the detector plane. Conventional camera lenses are unsuitable for this application, as the imager operates in the LWIR regime. Consequently, a pair of germanium lenses (Ophir Optronics Solutions Ltd., IL) are used to focus light onto the detector (Figure 3.7). The front element is a Ø35.2 mm aspheric lens with an effective focal length of approximately 135 mm, and the rear element is a Ø52.3 mm spherical lens with a focal length of approximately 45 mm. Together, they form an objective lens with an effective focal length of 35 mm, producing a $\approx 34.6\,^{\circ}$ diagonal field of view (FOV) and an aperture of f/1. The lenses are housed in a lens tube, with the rear element adjustable via an electric motor (either inchworm or stepper) controlled by user inputs through the camera's GUI server.

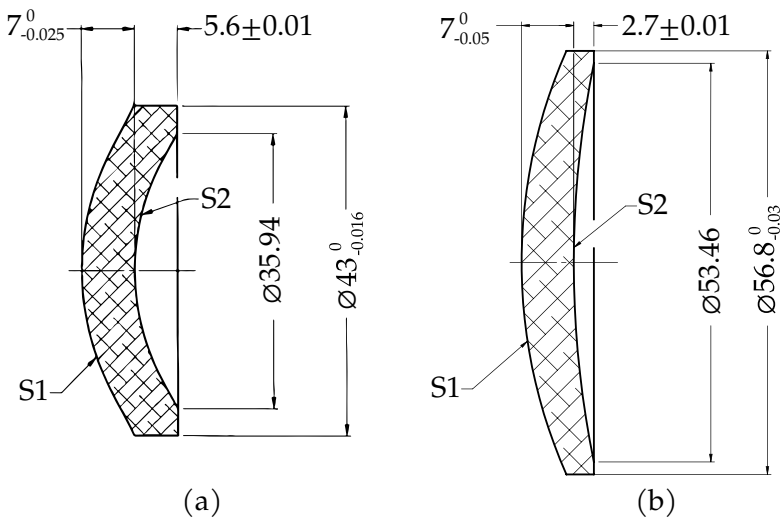

Figure 3.7: Lenses used in the hyperspectral LWIR imager. (a) Front element. (b) Rear element. Illustrations adapted from the Ophir data sheet. All units are in millimeters.

3.5 Overview of Scanning Fabry-Pérot Interferometer

The SFPI provides the hyperspectral capability of the HSC. Chapter 4 delves deeper into the physics underlying this interferometer, so the primary goal of *this* section is to outline the practical realization and control of the SFPI.

3.5.1 Dielectric mirrors

The core of the SFPI consists of two semitransparent, dielectric multilayer mirrors (Coherent Corp, USA). Each mirror substrate is a Ø50.8 mm, 5 mm thick zinc selenide (ZnSe) disk, with a Ø43 mm dielectric coating on one side and an antireflective (AR) coating on the opposite side. The composition of the dielectric films can be found in Table 3.1 and scanning electron microscope (SEM) images of a crosssection of a mirror in Figure 3.8. Note the bright region inside ThF_4 (Figure 3.8a) is caused by charging effects while scanning with the electron beam. Fourier transform infrared (FTIR) reflectance and transmittance measurements of the mirrors have been performed, and the results are presented in Figure 3.10.

The SFPI acts as a variable bandpass filter, where the transmitted wavelength distribution is determined by the mirror separation, also known as the cavity length, ℓ. In an ideal SFPI, the condition for a wavelength to transmit through the cavity is given by Eq. (3.8) and a derivation based

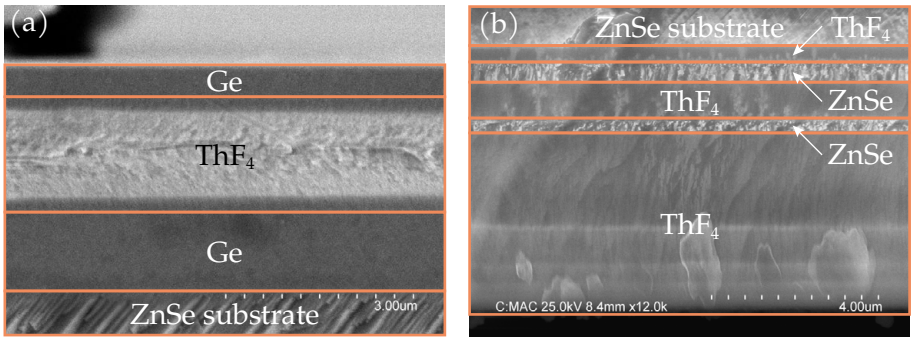

Figure 3.8: SEM images of mirror cross-section: (a) mirror coating. There are $\approx$ 20 nm ZnS binding layers between the Ge and ThF_4 layers which are too small to see at this scale. (b) anti-reflective coating. Note that the scales differ in the two images (3 µm vs 4 µm scalebars).

on geometrical considerations is provided in section 4.1.1.

$$\lambda = \frac{2n'\ell\cos\theta}{m}, \qquad m = 1, 2, 3, \ldots \tag{3.8}$$

$$\ell = \frac{m\lambda}{2}\frac{1}{n'\cos\theta} \tag{3.9}$$

where n' is the real part of the refractive index of the medium between the mirrors (assumed to be 1, as the SFPI operates in atmospheric air), θ is the angle of incidence, and m represents the transmission order. Analogous to standing waves on a string with fixed ends, constructive interference occurs when the cavity length is an integer multiple of half the wavelength (at normal incidence), allowing light of that wavelength to pass through, as shown in Figure 3.9.

3.5.2 Mirror Mounting and Displacement

Although the general principle of an SFPI is straightforward, implementing it requires careful consideration regarding the physical mounting and control of the mirrors. This is due to SFPI's high sensitivity to changes in its cavity length, which is typically on the order of 10 µm – approximately one-tenth the diameter of a human hair. Ideally, the mirrors should always remain parallel, and even slight misalignments noticeably decrease the performance of the SFPI. Figure 3.11 illustrates the components comprising the SFPI in the prototype, which has been used throughout most of this project. While a newer prototype exists (depicted in Figure 3.2), the fundamental operating principle remains essentially unchanged.

The two mirrors are mounted within separate halves of a steel flange. Set screws at the bottom of each half apply pressure to a steel plate,

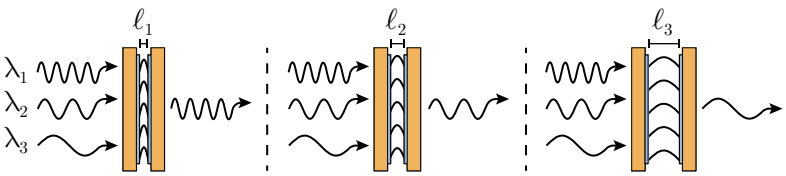

Figure 3.9: Illustration of transmission condition of a perfect SFPI, where light is only transmitted when the cavity length ℓ is an integer multiple of half the wavelength.

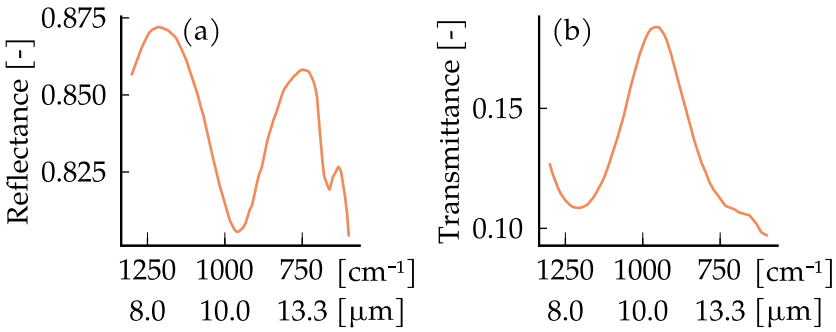

Figure 3.10: FTIR reflectance (a) and transmittance (b) measurements of a dielectric mirror.

which in turn secures the mirrors in place. The mounting pressure must be minimal, as excessive force causes the mirrors to buckle. Once the mirror positioning is optimized, they are fixed to the flange with a low-stress, UV-curing glue. Although gluing is not strictly necessary, it helps prevent unintentional shifts during handling.

Three piezo actuators (PK2FMP2, 400 N force, 11.2 µm max expansion, 75 V max voltage, Thorlabs, USA) are positioned between the metal

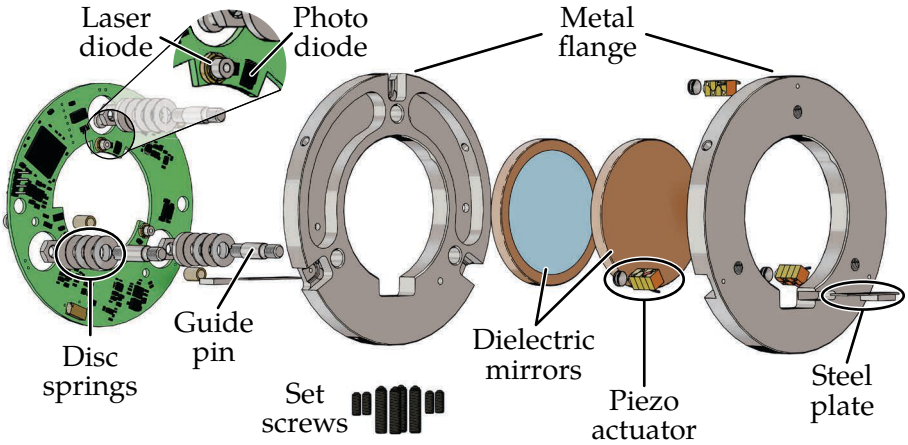

Figure 3.11: This illustrates an exploded view of the SFPI predominantly used in this work. It represents an earlier version of the SFPI depicted in Figure 3.2, which accounts for the differences in appearance. Nevertheless, their fundamental principles are consistent.

Table 3.1: Thicknesses of the different layers of a LWIR mirror. From the top: the dielectric mirror coating, then a mirror substrate, and finally the antireflective coating. The materials are germanium (Ge), Zinc sulfide (ZnS), Thorium Fluoride ThF_4, and Zinc Selenide (ZnSe).

Mirror Material	**Thickness [μm]**
Ge	0.51
ZnS	0.02
ThF_4	1.79
ZnS	0.02
Ge	1.26
Total Mirror Thickness	3.60
ZnSe substrate	5000
AR Material	
ThF_4	0.34
ZnSe	0.50
ThF_4	0.94
ZnSe	0.25
ThF_4	4.35
Total AR Thickness	6.38

flange halves. When a voltage is applied, the actuators expand, pushing the flange halves – and thus also the mirrors – apart. To maintain parallel alignment between the flange halves, three guide pins are secured to the back flange, allowing the front flange to glide along them smoothly. To ensure the flanges return to their initial positions when the potential across the actuators is removed, each guide pin is fitted with a stack of four disc springs, held in place by nuts tightened to exert a consistent force of approximately 400 N.

3.5.3 Mirror Control

The performance of the SFPI critically depends on maintaining the mirrors in a mutually parallel configuration as the cavity length is adjusted. Initially, the mirrors are positioned close together and are separated by the piezo actuators, thereby increasing the cavity length. Subsequently, the voltage applied to the actuators is gradually reduced, allowing the

mirrors to return to their initial position. This cyclical process, consisting of a single forward (increasing) and backward (decreasing) adjustment of the cavity length, is referred to as a *sweep*. When specifically describing the phase of increasing the cavity length, it is referred to as the *forward sweep*. In contrast, the phase of decreasing the cavity length is termed the *backward sweep*.

Three laser diodes with a nominal wavelength of 650 nm (ADL-65075TL, Arima Lasers Corporation, TW) illuminate an uncoated region of the cavity, and the reflected light is monitored by three photodiodes positioned adjacent to the laser diodes. The reflected light undergoes alternating constructive and destructive interference as the cavity length changes. These laser-diode interferograms are used to track changes in the cavity length, and an example is shown in Figure 3.12.

Applying the same voltage to all three piezo actuators does not guarantee identical expansion due to manufacturing tolerances of the piezo elements and non-uniform clamping pressure exerted by the metal flange. This discrepancy is evident in Figure 3.12b, where the interferograms are plotted as a function of applied voltage, showing a phase drift between the three interferograms over the course of the forward sweep. To mitigate this issue, the sweep is divided into 1500 discrete steps, with each step assigned a unique set of voltages tailored to ensure uniform expansion across all three actuators. As a result, the phase difference remains constant when the interferograms are plotted against the step number, as shown in Figure 3.13a.

The step-specific voltages are determined during initial calibration sweeps performed prior to the final acquisition sweep. During calibration, the mirrors execute a series of forward and backward sweeps (typically 5 to 10 cycles, as defined by the user), during which the phase differences between the interferograms are minimized. The interferograms shown in Figure 3.12b were recorded after these initial calibration sweeps, illustrating that the 'Diode 0'-interferogram does not reach the same voltage level as the other two interferograms. This discrepancy arises because the actuator associated with 'Diode 0' has a longer stroke length, requiring a lower voltage to achieve the same expansion as the other actuators. The total number of steps is correspondingly decreased to account for this reduced range.

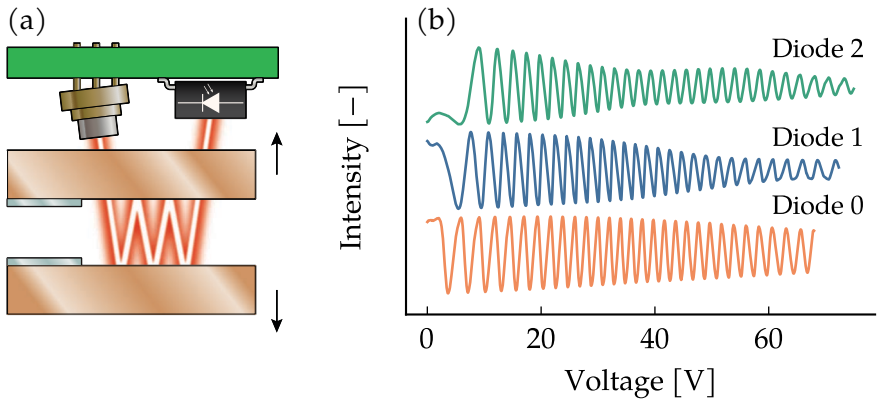

Figure 3.12: (a) Schematic representation of light from the laser diode being reflected off an uncoated region of the SFPI cavity and captured by a photodiode (not to scale). The light undergoes alternating constructive and destructive interference as the voltage applied to the piezo actuators increases the cavity length, resulting in the laser diode interferogram shown in (b).

During operation, the camera captures images while the mirrors expand the cavity length. In an earlier prototype, an image was captured at every 10th step, producing data cubes with approximately 145 spectral channels. In the software version used at the time of writing, the camera captures images continuously at its maximum frame rate while associating each image with its corresponding step number. This improvement results in data cubes containing approximately 160 spectral channels. In the earlier version, a forward sweep required approximately 35 seconds to complete, whereas in the latest iteration, this duration has been reduced to approximately 8 seconds. Data cubes recorded with both versions are presented in this work.

The spectral axis of the data cubes corresponds to the cavity length; however, at this stage, it is represented in the arbitrary unit of 'steps.' The following sections detail the methodology for relating the step-dependent interferograms to the physical cavity length of the SFPI.

Calibrated Cavity Length

Following Eq. (3.8), the expansion of the SFPI can be inferred from the laser interferograms. The cavity expansion corresponding to the transition from a peak to a neighboring trough (Figure 3.13a) is given

by $\lambda/(4\cos\theta)$, assuming a refractive index of $n' = 1$. However, both the angle of incidence θ and the precise wavelength of the laser diodes are unknown. To address this, an effective wavelength $\lambda_{\text{eff}} = \lambda/(\cos\theta)$ is introduced. This value is experimentally determined to be $\lambda_{\text{eff}} = 680$ nm based on hyperspectral data cubes of various bandpass filters. Assuming a nominal laser wavelength of 650 nm, this corresponds to an angle of incidence $\theta = 17°$.

The peaks and troughs in the laser interferograms are identified in terms of step number and plotted against the corresponding mirror displacement (Figure 3.13b). The position of the first peak or trough is defined as a displacement of 0 µm, and subsequent peaks or troughs indicate a cavity expansion of $\lambda_{\text{eff}}/4 = 170$ nm. A third-order polynomial is fitted to these data points, allowing each step number to be related to a corresponding mirror displacement. A third-order polynomial is chosen to account for the hysteresis inherent in piezoelectric actuators [30].

Due to the monochromatic nature of the laser diodes, an external spectral reference is required to relate the relative mirror displacement to the absolute cavity length. Typically, a bandpass filter is employed for this purpose. In this case, a 996 cm^{-1} (10.04 µm) bandpass filter with a full width at half maximum (FWHM) of 35 cm^{-1} (Andover Corporation, US) is used. The position of the first transmission order is located at step 414 based on a fit of a Gaussian profile (Figure 3.13c). This peak is known to occur at a cavity length of 5.37 µm based on numerical calculations described in Eq. (5.32).

Using this spectral reference, the polynomial fit is offset such that step 414 aligns with a cavity length of 5.37 µm (Figure 3.13d). This calibration establishes a direct relationship between step numbers and absolute cavity length.

Ongoing research aims to infer the cavity length without relying on monochromatic laser diodes. One approach under investigation involves combining multiple wavelengths to produce multiple interference patterns, potentially simplifying the determination of the cavity length. Additionally, the use of white light-emitting diodes (LEDs) in conjunction with spectrometers has been proposed. This method estimates the cavity length by applying a Fast Fourier Transform (FFT) to the recorded reflectance spectrum.

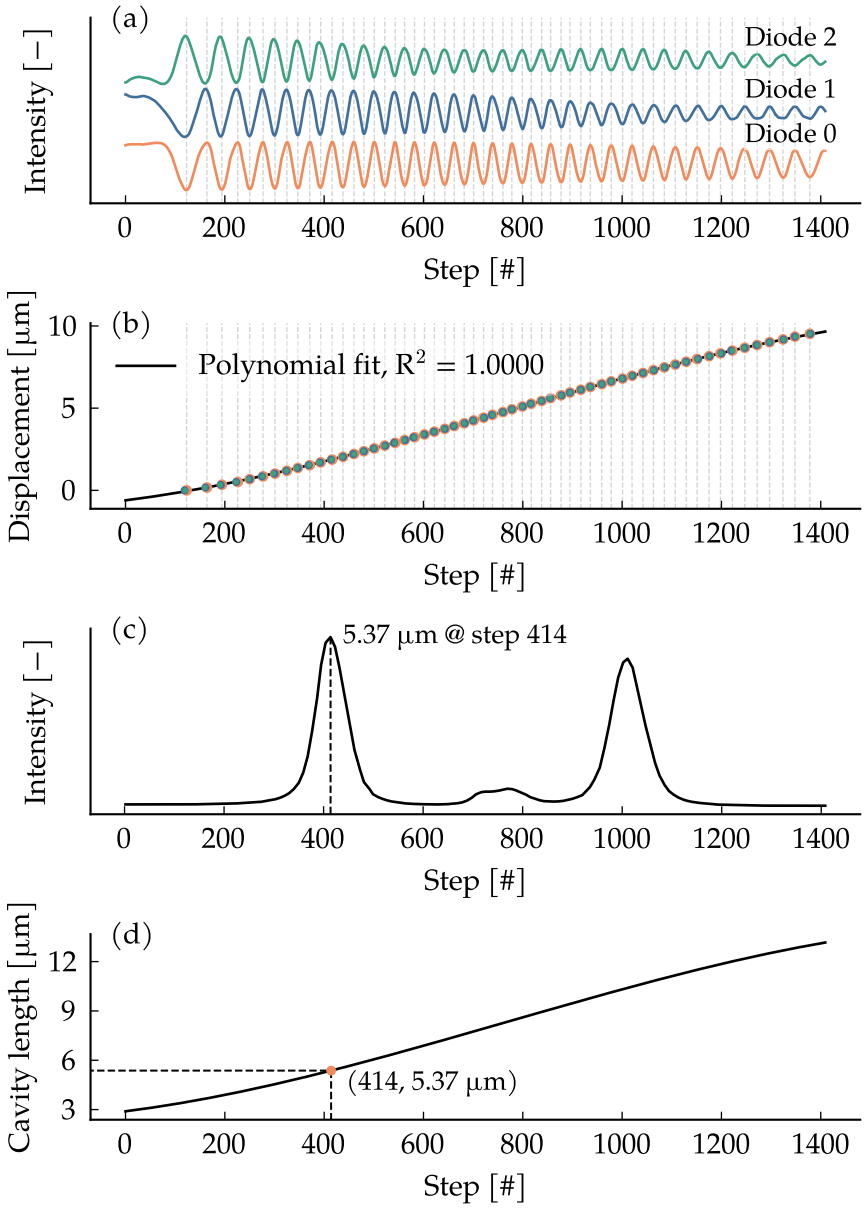

Figure 3.13: (a) Laser diode interferograms after alignment sweeps. (b) The polynomial fit of mirror displacement vs. step number. (c) The first transmission order of the bandpass filter. (d) Calibrated cavity length axis after offset adjustment.

3.6 Summary

The components of the HSC have been presented in this chapter, along with a detailed description of their underlying operating principles. Particular emphasis has been placed on the microbolometer detector, which differs fundamentally from conventional photon detectors commonly used in imaging systems. Unlike photon-counting detectors, microbolometers measure the temperature of their pixels, making their detection mechanism inherently distinct.

The SFPI has also been introduced, covering both its construction and operational principles. It consists of two partially transmitting mirrors forming an optical cavity, where the cavity length dictates the transmitted and reflected wavelengths. To monitor cavity expansion, laser diode reflections are utilized, allowing precise tracking of mirror displacement as piezo actuators control the separation. The SFPI is the key component that enables the HSC's hyperspectral capabilities, and its function is examined in greater detail in the following chapter.

II Scanning Fabry-Pérot Interferometer

4 Scanning Fabry-Pérot Interferometer 67

4.1 Interference 68
4.2 The Airy Function 71
4.3 Concave Mirror Substrates 80
4.4 Angular Spectral Shift 83
4.5 The Transfer Matrix Method 87
4.6 Generalized Matrix Method 94
4.7 Spectral Resolution Based on GMM Calculations 100
4.8 Measuring SFPI Transmittance Matrix Using FTIR . . 102
4.9 Phase Change Upon Reflection 104
4.10 Summary 109

5 Spectral Reconstruction 111

5.1 Modelling the Imaging System 112
5.2 Estimation of Detector's Spectral Response 114
5.3 Converting Interferogram to Spectrum 129
5.4 Summary 145

4. Scanning Fabry-Pérot Interferometer

The SFPI is the key component that enables the imager's hyperspectral capabilities. This chapter thoroughly examines its operation and the numerical methods used to compute its transmission profile. The discussion begins with an idealized model of the SFPI, introducing key properties under the assumption of a 'perfect' SFPI that neglects wavelength-dependent mirror reflectance and assumes perfectly flat and parallel mirrors.

The transfer matrix method (TMM) and generalized matrix method (GMM) are introduced to compute the SFPI transmission profile as a function of wavelength and cavity length. These numerical methods determine the electric field distribution within the dielectric mirror coatings, enabling precise predictions of the transmission profile. This analysis reveals a characteristic feature of low-order SFPIs, where the distinction between physical and effective cavity lengths becomes significant. Finally, the computed transmission profiles are validated against FTIR measurements, showing excellent agreement.

Subsequent sections use wavelengths as the spectral unit to facilitate a more intuitive interpretation of the interference conditions. However, it is important to note that wavelength and cavity length are the two key variables in an SFPI, both expressed in units of length [μm].

4.1 Interference

Plane Wave Interference

The interference of two monochromatic plane waves with identical wavelengths but different wave vectors, $\mathbf{k_1}$ and $\mathbf{k_2}$, is considered here, as illustrated in Figure 4.1. The electric fields of the waves are expressed as:

$$\mathbf{E_1} = \mathbf{E_{01}} \cos\left(\mathbf{k_1} \cdot \mathbf{r} - \omega t + \varphi_1\right), \quad |\mathbf{k_1}| = \frac{2\pi n'}{\lambda} \tag{4.1}$$

$$\mathbf{E_2} = \mathbf{E_{02}} \cos\left(\mathbf{k_2} \cdot \mathbf{r} - \omega t + \varphi_2\right), \quad |\mathbf{k_2}| = \frac{2\pi n'}{\lambda} \tag{4.2}$$

where $\mathbf{E_{01}}$ and $\mathbf{E_{02}}$ are the amplitude vectors of the electric fields, oscillating perpendicular to the plane of the page, as shown in Figure 4.1. The position vector is $\mathbf{r}$, while ω and t denote the angular frequency and time, respectively. The real part of the refractive index of the medium is given by n'. The resultant electric field at point q arises from the superposition of the two waves:

$$\mathbf{E_q} = \mathbf{E_1} + \mathbf{E_2} \tag{4.3}$$

Light oscillates at very high frequencies, on the order of 10^{13} Hz for wavelengths in the LWIR regime, far exceeding the temporal resolution of conventional detectors. As a result, detectors measure the energy

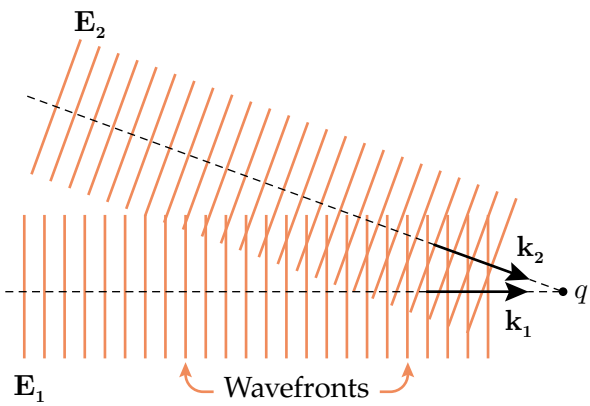

Figure 4.1: Interference of two plane waves. The electric fields are assumed here to oscillate perpendicular to the plane of the page.

transferred by the electric field, which corresponds to the time-averaged square of the wave amplitude, also referred to as the irradiance, $\mathcal{E}$ [10]. At the point q this is expressed as:

$$\mathcal{E}_q = \epsilon_0 c \langle \mathbf{E_q} \cdot \mathbf{E_q} \rangle, \tag{4.4}$$

where ϵ_0 is the vacuum permittivity, and c is the speed of light in vacuum. Expanding Eq. (4.4) results in:

$$\mathcal{E}_q = \epsilon_0 c \langle \mathbf{E_1} \cdot \mathbf{E_1} + \mathbf{E_2} \cdot \mathbf{E_2} + 2\mathbf{E_1} \cdot \mathbf{E_2} \rangle = \mathcal{E}_1 + \mathcal{E}_2 + \mathcal{E}_{12}, \tag{4.5}$$

where $\mathcal{E}_{12}$ represents the interference term. Using trigonometric identities, the interference term is expanded and rewritten to:

$$\mathcal{E}_{12} = \epsilon_0 c \mathbf{E_{01}} \cdot \mathbf{E_{02}} \cos\delta, \quad \delta = (\mathbf{k_1} - \mathbf{k_2}) \cdot \mathbf{r} + (\varphi_1 - \varphi_2) \tag{4.6}$$

Thus, the interference of two monochromatic plane waves with the same wavelength is time-independent. For waves originating from the same source (i.e., self-interference), the initial phase difference is $(\varphi_1 - \varphi_2) = 0$. Constructive interference occurs when the spatial phase difference δ satisfies:

$$\delta = (\mathbf{k_1} - \mathbf{k_2}) \cdot \mathbf{r} = m \cdot 2\pi, \quad m \in \mathbb{Z} \tag{4.7}$$

Conversely, destructive interference arises when:

$$\delta = (\mathbf{k_1} - \mathbf{k_2}) \cdot \mathbf{r} = \frac{(2m+1)}{2}\pi, \quad m \in \mathbb{Z} \tag{4.8}$$

The spatial phase difference can also be expressed in terms of the optical path difference Δl:

$$\delta = (\mathbf{k_1} - \mathbf{k_2}) \cdot \mathbf{r} = \frac{2\pi n'}{\lambda} \Delta l \tag{4.9}$$

Thus, following Eq. (4.7) and Eq. (4.9), constructive interference occurs whenever the condition in Eq. (4.10) is met.

Interference Condition

$$n' \Delta l = m\lambda, \qquad m = 1, 2, 3, \ldots \tag{4.10}$$

4.1.1 Interference Condition of a Fabry-Pérot Interferometer

Consider the configuration depicted in Figure 4.2, wherein monochromatic light is incident on the SFPI with a cavity length ℓ at an angle θ. At each interface, the incident light undergoes partial transmission and reflection, resulting in multiple parallel rays propagating at the same angle. The optical path difference Δl between two neighboring rays (Figure 4.2) is used to evaluate the interference condition:

$$\Delta l = (bc + cd - gf)n', \quad bc = cd = ab, \quad gf = eg \sin\theta,$$

$$ab = \frac{\ell}{\cos\theta}, \quad bh = \ell \tan\theta, \quad eg = bd = 2bh,$$

$$\Rightarrow \Delta l = \left(\frac{2\ell}{\cos\theta} - 2\ell \sin\theta \tan\theta\right) n' = 2n'\ell\cos\theta, \tag{4.11}$$

Constructive interference within the cavity occurs under the condition $n'\ell\cos\theta = m\lambda/2$. This leads to the interference conditions of the SFPI as presented in Eq. (4.12) and Eq. (4.13).

Interference Condition of a Fabry-Pérot Interferometer

$$\lambda = \frac{2n'\ell\cos\theta}{m}, \qquad m = 1, 2, 3, \ldots \tag{4.12}$$

$$\ell = \frac{m\lambda}{2}\frac{1}{n'\cos\theta} \tag{4.13}$$

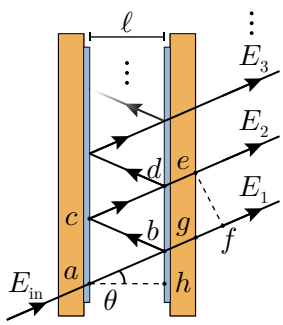

Figure 4.2: Schematic of a light ray passing through an SFPI, illustrating the optical path. Only the light transmitted through the right interface is considered, while some is also transmitted through the left.

4.2 The Airy Function

The interference conditions of the SFPI, as described by Eq. (4.12) and Eq. (4.13), define the resonance behavior of the system. However, these conditions do not provide insight into the transmission characteristics when the SFPI operates off-resonance. A fraction of the light is transmitted each time it reflects off one of the mirrors. While this is true for both the left and right mirrors, the analysis here considers only the right-going light. The electric field of each transmitted ray is denoted as $E_1, E_2, E_3, \ldots$ as illustrated in Figure 4.2. Each successive ray contains a diminishing fraction of the incident electric field, E_{in}. The electric fields can be expressed as:

$$
\begin{aligned}
E_1 &= \tau_{\mathrm{m}}^2 \exp\left\{\frac{j2\pi\tilde{n}\ell}{\lambda\cos\theta}\right\} E_{\mathrm{in}}, \\
E_2 &= \tau_{\mathrm{m}}^2 \exp\left\{\frac{j2\pi\tilde{n}\ell}{\lambda\cos\theta}\right\} \rho_{\mathrm{m}}^2 \exp\left\{\frac{j2\pi\Delta l}{\lambda}\right\} E_{\mathrm{in}}, \\
E_3 &= \tau_{\mathrm{m}}^2 \exp\left\{\frac{j2\pi\tilde{n}\ell}{\lambda\cos\theta}\right\} \left(\rho_{\mathrm{m}}^2 \exp\left\{\frac{j2\pi\Delta l}{\lambda}\right\}\right)^2 E_{\mathrm{in}}, \\
&\vdots \\
E_{\mathrm{out}} &= \sum_{w=1}^{\infty} E_w
\end{aligned}
$$

Here, τ_{m} and ρ_{m} are the complex transmission and reflection coefficients, respectively, and subscript m indicate the relationship to the SFPI mirror. Utilizing that the transmittance $\mathcal{T} = |\tau|^2 = (1 - \mathcal{R})$ and reflectance $\mathcal{R} = |\rho|^2$ yields:

$$
E_{\mathrm{out}} = (1 - \mathcal{R}_{\mathrm{m}}) \exp\left\{\frac{j2\pi\tilde{n}\ell}{\lambda\cos\theta}\right\} \sum_{w=0}^{\infty} \left(\mathcal{R}_{\mathrm{m}} \exp\left\{\frac{j2\pi\Delta l}{\lambda}\right\}\right)^w E_{\mathrm{in}} \quad (4.14)
$$

The resulting series is of the form

$$
\sum_{w=0}^{\infty} a^w = \frac{1}{1-a} \qquad |a| \leq 1, \quad (4.15)
$$

where a is a dummy variable. This allows Eq. (4.14) to be rewritten as

$$\frac{E_{\text{out}}}{E_{\text{in}}} = \frac{(1-\mathcal{R}_{\text{m}})\exp\left\{\frac{j2\pi\tilde{n}\ell}{\lambda\cos\theta}\right\}}{1-\mathcal{R}_{\text{m}}\exp\left\{\frac{j2\pi\Delta l}{\lambda}\right\}} \tag{4.16}$$

The electric field is related to the irradiance following $\mathcal{E} \propto |E|^2$. Additionally, $\mathcal{E}_{\text{out}}/\mathcal{E}_{\text{in}} = \mathcal{T}$, meaning that the transmittance of the SFPI is given by

$$\begin{aligned}
\mathcal{T}_{\text{SFPI}} &= \frac{\left|(1-\mathcal{R}_{\text{m}})\exp\left\{\frac{j2\pi\tilde{n}\ell}{\lambda\cos\theta}\right\}\right|^2}{\left|1-\mathcal{R}_{\text{m}}\exp\left\{\frac{j2\pi\Delta l}{\lambda}\right\}\right|^2} \\
&= \frac{(1-\mathcal{R}_{\text{m}})^2}{\left(1-\mathcal{R}_{\text{m}}\exp\left\{\frac{j2\pi\Delta l}{\lambda}\right\}\right)\left(1-\mathcal{R}_{\text{m}}\exp\left\{-\frac{j2\pi\Delta l}{\lambda}\right\}\right)} \\
&= \frac{(1-\mathcal{R}_{\text{m}})^2}{1+\mathcal{R}_{\text{m}}^2-2\mathcal{R}_{\text{m}}\left(\frac{\exp\left\{\frac{j2\pi\Delta l}{\lambda}\right\}+\exp\left\{-\frac{j2\pi\Delta l}{\lambda}\right\}}{2}\right)} \\
&= \frac{(1-\mathcal{R}_{\text{m}})^2}{1+\mathcal{R}_{\text{m}}^2-2\mathcal{R}_{\text{m}}\cos\frac{2\pi\Delta l}{\lambda}}
\end{aligned}$$

Utilizing that $\cos 2a = 1-\sin^2 a$, it is possible to rewrite

$$\mathcal{T}_{\text{SFPI}} = \frac{(1-\mathcal{R}\text{m})^2}{1+\mathcal{R}\text{m}^2-2\mathcal{R}\text{m}-4\mathcal{R}\text{m}\sin^2\frac{\pi\Delta l}{\lambda}}$$

Factorizing $\mathcal{R}_{\text{m}}^2-2\mathcal{R}_{\text{m}}+1=(1-\mathcal{R}_{\text{m}})^2$ and inserting $\Delta l = 2n'\ell\cos\theta$ yields the Airy function presented in Eq. (4.17).

Airy Function

$$\mathcal{T}_{\mathrm{SFPI}} = \frac{1}{1 + \frac{4\mathcal{R}_{\mathrm{m}}}{(1-\mathcal{R}_{\mathrm{m}})^2}\sin^2\left(\frac{\delta}{2} + \varphi\right)}, \quad \delta = \frac{4\pi n' \ell}{\lambda}\cos\theta, \tag{4.17}$$

$$= \frac{1}{1 + F\sin^2\left(\frac{\delta}{2} + \varphi\right)} = \frac{1}{1 + \left(\frac{4\mathcal{F}^2}{\pi^2}\right)\sin^2\left(\frac{\delta}{2} + \varphi\right)} \tag{4.18}$$

$$F = \frac{4\mathcal{R}_{\mathrm{m}}}{(1 - \mathcal{R}_{\mathrm{m}})^2}, \quad \text{Coefficient of Finesse,} \tag{4.19}$$

$$\mathcal{F} = \frac{\pi\sqrt{F}}{2} = \frac{\pi\sqrt{\mathcal{R}_{\mathrm{m}}}}{1 - \mathcal{R}_{\mathrm{m}}}, \quad \text{Finesse} \tag{4.20}$$

An additional phase term, φ, is introduced into Eq. (4.17) and represents the phase shift upon reflection [31]. For high-order SFPIs, the phase is dominated by δ, but for lower-order SFPIs like the one presented in this work, φ has a noticeable impact. The implication of this phase shift is discussed in further detail in section 4.9, but for now, it is assumed to be $\varphi = 0$. Unless otherwise stated, the mirrors are assumed to be perfectly flat, mutually parallel, and lossless. The impact of mirror curvature is discussed in deeper detail in section 4.3 and 4.6.1. The Airy function would be scaled by $\frac{\mathcal{T}_{\mathrm{m}}^2}{(1-\mathcal{R}_{\mathrm{m}})^2}$ if the mirrors are no longer assumed to be lossless.

The Airy function is depicted as a function of the spatial phase difference in Figure 4.3. The plot illustrates the transmittance profiles of three lossless Fabry-Pérot cavities, each characterized by distinct reflectances.

The coefficient of finesse, F, and the finesse, $\mathcal{F}$, are commonly employed metrics for characterizing the performance of a Fabry-Pérot cavity with perfectly flat and mutually parallel mirrors. Both parameters are determined exclusively by the reflectance of the mirrors. The coefficient of finesse, F, quantifies the fringe contrast, defined as the ratio of the difference between the maximum and minimum values of the transmittance profile to the minimum value. Conversely, the finesse, $\mathcal{F}$, represents the ratio of the free spectral range (the spacing between adjacent peaks) to the FWHM of the peaks.

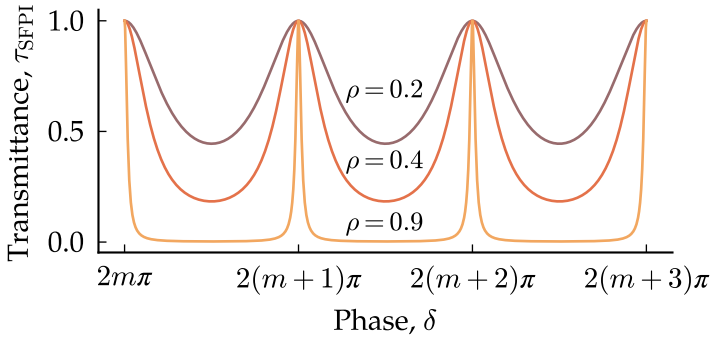

Figure 4.3: Transmittance of Fabry-Pérot interferometer with different reflectances as a function of phase difference as described by the Airy function presented in Eq. (4.17).

High spectral resolution requires high mirror reflectance, ensuring a narrow distribution of transmitted wavelengths. However, increased reflectance reduces the overall amount of transmitted light, thereby decreasing the signal-to-noise ratio. In this project, mirrors with an average reflectance of 84% in the spectral range from 8 – 15 µm were designed to provide a balanced trade-off between spectral resolution and signal strength. The corresponding average finesse is 18.6 and the average coefficient of finesse is 144. A more detailed discussion on the spectral resolution of the SFPI is supplied in section 4.2.3 and section 4.7.

Relating the Airy function to physical units such as wavelength or cavity length often provides greater physical intuition. Figure 4.4 illustrates the Airy function for a Fabry-Pérot cavity with mirrors having a reflectance of $\mathcal{R}_{\mathrm{m}} = 0.9$. This figure highlights that both the spacing of the transmission orders and their shape depend on the chosen independent variable. Specifically, the spacing is uniform when the cavity length or wavenumber is varied, whereas the spacing becomes reciprocal in the wavelength representation. The following sections discuss key concepts such as the free spectral range (FSR) and the FWHM for these different representations (Figure 4.5). The real part of the refractive index n' is omitted in the coming sections to reduce notational clutter since $n' \approx 1$ as the SFPI cavity is filled with air.

4.2.1 Interference Conditions Based on Physical Units

Eq. (4.17) reaches its maximum whenever $\sin^2(\delta/2) = 0$, which corresponds to the condition

$$\delta/2 = m\pi, \qquad m = 1, 2, 3, \ldots \tag{4.21}$$

$$\Rightarrow \delta = 2m\pi \tag{4.22}$$

The constructive interference conditions in terms of physical unists are presented in Eqs. (4.23) to (4.26).

Interference Conditions

$$\delta = 4\pi\tilde{\nu}\ell = \frac{4\pi\ell}{\lambda} = 2m\pi \tag{4.23}$$

$$\tilde{\nu} = \frac{m}{2\ell} \tag{4.25}$$

$$\ell = \frac{m}{2\tilde{\nu}} = \frac{m\lambda}{2} \tag{4.24}$$

$$\lambda = \frac{2\ell}{m} \tag{4.26}$$

4.2.2 Free Spectral Range

The separation between consecutive maxima is denoted as the FSR and can be derived as follows:

$$\delta_{fsr} = 2(m+1)\pi - 2m\pi = 2\pi \tag{4.27}$$

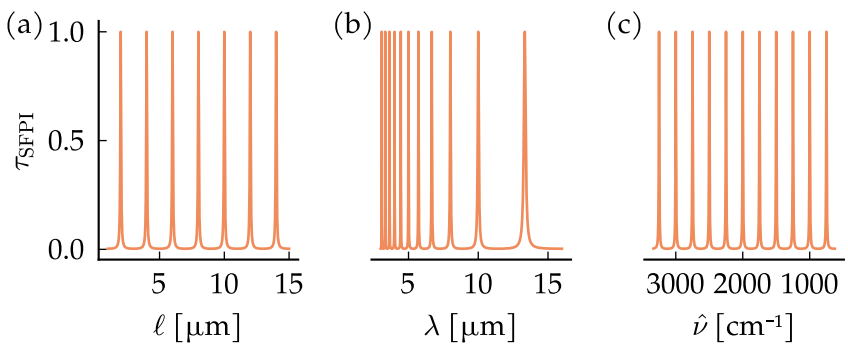

Figure 4.4: Transmittance profile of $\mathcal{R}_{\mathrm{m}} = 0.9$ Fabry-Pérot cavity with different independent variables. (a): Varying cavity length and constant wavelength of 4 µm. (b) and (c): Varying wavelength or wavenumber with a constant cavity length of 20 µm.

Similarly, the FSR of the cavity length and wavenumber is straightforward to derive as presented in Eq. (4.29) and Eq. (4.30), respectively. However, since the wavelength representation is proportional to $1/m$, the derivation is slightly more complex:

$$\lambda_{fsr} = \frac{2\ell}{m} - \frac{2\ell}{m+1}$$

$$\xRightarrow{m=2\ell/\lambda} \lambda_{fsr} = \frac{2\ell}{2\ell/\lambda} - \frac{2\ell}{2\ell/\lambda+1} = \lambda - \frac{2\ell}{2\ell/\lambda+1}$$

$$\Rightarrow \lambda_{fsr} = \frac{\lambda^2}{2\ell+\lambda}$$

In the context of Fabry-Pérot cavities, the cavity lengths are typically much larger than the wavelength of the light. Consequently, the term $+\lambda$ in the denominator is often neglected in much of the literature. However, this approximation is not appropriate when working with low-order SFPIs, such as the one utilized in this project.

The FSRs in all representations are given in Eqs. (4.28) to (4.31).

Free Spectral Range

$$\delta_{\text{fsr}} = 2\pi \tag{4.28}$$

$$\tilde{\nu}_{\text{fsr}} = \frac{1}{2\ell} \tag{4.30}$$

$$\ell_{\text{fsr}} = \frac{\lambda}{2} = \frac{1}{2\tilde{\nu}} \tag{4.29}$$

$$\lambda_{\text{fsr}} = \frac{\lambda^2}{2\ell+\lambda} \tag{4.31}$$

4.2.3 Fabry-Pérot Full Width at Half Maximum

The FWHM of the transmission profile corresponds to the phase shift required for the transmission to drop to half its maximum value. This occurs when

$$\mathcal{T}_{\text{SFPI}} = \frac{1}{1+F\sin^2(\delta/2)} = \frac{1}{2}$$

$$\Rightarrow 2 = 1 + F\sin^2(\delta/2)$$

$$\Rightarrow \sin^2(\delta/2) = \frac{1}{F} = \frac{\pi^2}{4\mathcal{F}^2}$$

At half-maximum, the phase shift δ is expressed as

$$\begin{aligned}
\delta &= 2m\pi + \frac{\delta_{\text{FWHM}}}{2} \\
\sin^2\left(\frac{\delta}{2}\right) &= \sin^2\left(m\pi + \frac{\delta_{\text{FWHM}}}{4}\right) \\
&= \sin^2\left(\frac{\delta_{\text{FWHM}}}{4}\right) \approx \frac{\delta_{\text{FWHM}}^2}{16} \\
\Rightarrow \delta_{\text{FWHM}} &= 2\pi/\mathcal{F},
\end{aligned}$$

when utilizing that $\sin^2\left(\frac{\delta}{2}\right) = \frac{\pi^2}{4\mathcal{F}^2}$. This approximation is valid only for systems with high finesse, where δ_{FWHM} is small. Furthermore, employing the definition of the FWHM as the point where $\mathcal{T} = 0.5$ implies that the FWHM becomes undefined if the Airy function does not drop below 0.5. This situation occurs only when $\mathcal{R}_{\text{m}} < 0.17$. Finally, the finesse is defined by Eq. (4.32).

$$\mathcal{F} = \frac{\delta_{fsr}}{\delta_{\text{FWHM}}} \tag{4.32}$$

4.2.4 Spectral Resolution

The FWHM also serves as a measure of the minimum separation required for two adjacent peaks to be resolvable. The spectral resolution corresponding to cavity length, wavelength, and wavenumbers can be derived

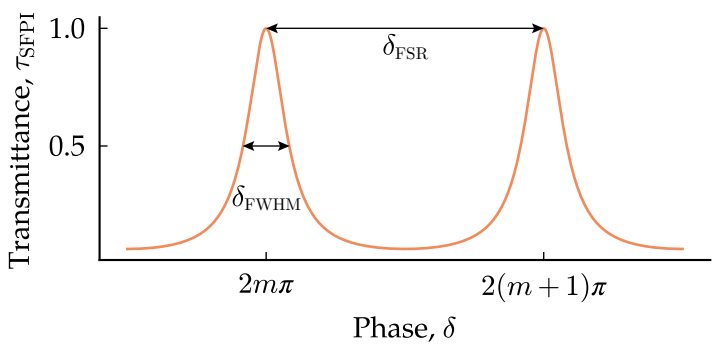

Figure 4.5: Example of how FSR and FWHM are defined with regards to the Airy function. In this example, the reflectance of the mirrors is $\mathcal{R}_m = 0.6$.

from the expression for finesse given in Eq. (4.32). These resolutions are summarized in Eqs. (4.33) to (4.36).

Spectral Resolution

$$\Delta\delta_{\text{min}} = \frac{2\pi}{\mathcal{F}} \tag{4.33}$$

$$\Delta\tilde{\nu}_{\text{min}} = \frac{1}{2\ell\mathcal{F}} \tag{4.35}$$

$$\Delta\ell_{\text{min}} = \frac{1}{2\tilde{\nu}\mathcal{F}} = \frac{\lambda}{2\mathcal{F}} \tag{4.34}$$

$$\Delta\lambda_{\text{min}} = \frac{\lambda^2}{(2\ell+\lambda)\mathcal{F}} \tag{4.36}$$

The spectral resolution of all quantities except δ depend on each other. Namely, the spectral resolution in terms of cavity length depends on the wavelength/wavenumber and vice versa. Additionally, the spectral resolution in terms of wavelengths also depends on the wavelength itself.

4.2.5 Dispersion

While the FWHM indicates the minimum resolvable spectral differences, the sensitivity quantifies the required change in cavity length, $\Delta\ell$, to distinguish between two closely spaced wavelengths, λ_1 and λ_2, or wavenumbers, $\tilde{\nu}_1$ and $\tilde{\nu}_2$.

Wavelength Representation:

Consider two wavelengths λ_1 and λ_2:

$$\lambda_1 = \frac{2\ell_1}{m}, \qquad \lambda_2 = \frac{2\ell_2}{m}$$

$$\Rightarrow \lambda_2 - \lambda_1 = \Delta\lambda = \frac{2(\ell_2 - \ell_1)}{m} = \frac{2\Delta\ell}{m}$$

Substituting $m = \frac{2\ell_1}{\lambda_1}$, the expression becomes:

$$\Delta\lambda = \frac{2}{2\ell_1/\lambda_1}\Delta\ell$$

$$\Rightarrow \frac{\Delta\lambda}{\lambda_1} = \frac{\Delta\ell}{\ell_1}$$

This demonstrates that longer cavity lengths (i.e., higher orders) require greater mirror displacement to displace transmission from λ_1 to λ_2. Con-

sequently, if two wavelengths are indistinguishable in the first order, they may still be resolved in higher orders.

Wavenumber Representation:

Similarly, consider the corresponding wavenumbers $\tilde{\nu}_1$ and $\tilde{\nu}_2$:

$$\tilde{\nu}_1 = \frac{m}{2\ell_1}, \qquad \tilde{\nu}_2 = \frac{m}{2\ell_2}$$

$$\Rightarrow \tilde{\nu}_1 - \tilde{\nu}_2 = \Delta\tilde{\nu} = \frac{m}{2\ell_1} - \frac{m}{2\ell_2} = \frac{m(\ell_2 - \ell_1)}{2\ell_1\ell_2}$$

Using $m = 2\tilde{\nu}_1\ell_1$, the relationship simplifies to:

$$\Delta\tilde{\nu} = \frac{2\tilde{\nu}_1\ell_1\Delta\ell}{2\ell_1\ell_2} = \frac{\tilde{\nu}_1\Delta\ell}{\ell_2} = \frac{\tilde{\nu}_1\Delta\ell}{\ell_1 + \Delta\ell_1}$$

$$\Rightarrow \frac{\Delta\tilde{\nu}}{\tilde{\nu}_1} = \frac{\Delta\ell}{\ell_1 + \Delta\ell}$$

The conclusion is the same in terms of wavenumbers; higher transmission orders have a better chance of separating closely spaced features. The two representations are repeated in Eqs. (4.37) and (4.38).

Dispersion Relations

$$\frac{\Delta\lambda}{\lambda_1} = \frac{\Delta\ell}{\ell_1} \tag{4.37}$$

$$\frac{\Delta\tilde{\nu}}{\tilde{\nu}_1} = \frac{\Delta\ell}{\ell_1 + \Delta\ell} \tag{4.38}$$

4.3 Concave Mirror Substrates

The dielectric mirror coatings induce mechanical stress on the ZnSe substrates, resulting in a spherical deformation, making the mirrors concave [32]. Figure 4.6a illustrates a dielectric mirror positioned beneath a $\lambda/10$ reference optical flat and illuminated by a sodium light source ($\lambda = 589$ nm). The resulting interference fringe pattern reveals variations in the gap between the mirror and the optical flat. The transition from a bright to a dark fringe corresponds to a change in the gap size of $\lambda/4$.

In this instance, the fringe pattern is centered on the mirror's midpoint, transitioning from a bright spot at the center to a dark fringe near the edge. Beyond the dark fringe, a partial transition toward a bright fringe is observed at the periphery. This pattern indicates a height difference between the center and the edge of the mirror, estimated to lie between $\lambda/4 = 147$ nm and $\lambda/2 = 295$ nm. The near-complete transition past the dark fringe suggests that the height difference is closer to $\lambda/4$. Additionally, short-range forces between the mirror and the optical flat may affect the estimation of the height difference. Accurately determining the

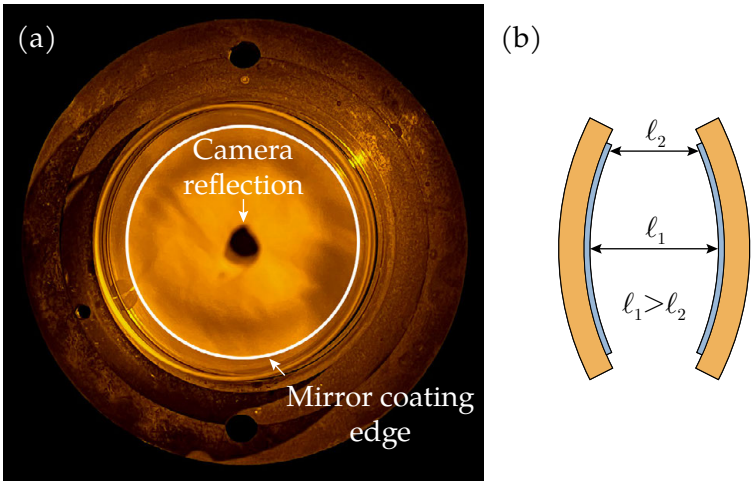

Figure 4.6: (a): Dielectric mirror positioned beneath a $\lambda/10$ optical flat and illuminated by a sodium light source ($\lambda = 589$ nm). The observed fringe pattern indicates a height difference of $> \lambda/4 = 147$ nm between the center and edge of the mirror. (b): Two (exaggeratedly) concave mirrors form a cavity, leading to the mirrors' edges being closer to their center.

height difference is challenging due to the limited number of observable fringes. Furthermore, reflections of the camera in the setup introduce visual artifacts, complicating the distinction between interference fringes and shadowing effects in the reflections. For the remainder of this thesis, the height difference between the center and the edge of the mirror is assumed to be 150 nm, which has proved to align well with simulations and experimental results.

The curvature of the mirrors induces a broadening effect of the transmission spectrum, as the cavity length can no longer be characterized by a single, uniform distance (Figure 4.6b). To account for this, the mirror can be conceptually divided into concentric rings, each associated with a distinct cavity length. The corresponding transmission spectra are then averaged and weighted by the respective areas of the rings. A detailed explanation of this approach and the SFPI transmission calculation using GMM is provided in section 4.6.1.

This section estimates the spectral broadening resulting from mirror curvature derived from the Airy function. Rearranging Eqs. (4.37) and (4.38) and applying the interference condition $\ell_1 = m\lambda_1/2 = m/(2\tilde{\nu}_1)$, obtains the following expressions for spectral broadening with constant $\Delta\ell$:

Spectral Broadening

$$\Delta\lambda = \frac{2\Delta\ell}{m} \tag{4.39}$$

$$\Delta\tilde{\nu} = \frac{2\Delta\ell\tilde{\nu}^2}{2\Delta\ell\tilde{\nu} + m} \tag{4.40}$$

These equations indicate that spectral broadening remains constant in terms of wavelength within a single transmission order, while it depends on the wavenumber. Notably, higher transmission orders lead to reduced spectral broadening in both representations. It should also be emphasized that these calculations assume "perfect" mirrors, where reflection occurs exclusively at the mirror surface. However, in the case of the dielectric mirrors employed in this study, the reflection plane can be located either within or beyond the mirror coating itself. This phenomenon is discussed further in section 4.9.

Assuming an offset in mirror height of 150 nm ($\Delta\ell = 300$ nm), the spectral broadening for the first and third transmission orders is calculated to

be $\Delta\lambda_{m=1} = 600\,\text{nm}$ and $\Delta\lambda_{m=3} = 200\,\text{nm}$, respectively. The broadening in terms of wavenumber depends not only on the transmission order but also on the specific wavenumber. Considering the spectral range of the detector ($1250\,\text{cm}^{-1}$ to $666\,\text{cm}^{-1}$), the maximum and minimum broadening within the first three transmission orders are determined to be $\Delta\tilde{\nu}_{m=1} = 87.2\ \text{cm}^{-1}$ and $\Delta\tilde{\nu}_{m=3} = 8.8\ \text{cm}^{-1}$, respectively. It should be noted that the range of cavity lengths of the SFPI does not cover the entirety of the third transmission order, meaning that the actual minimum broadening is larger than the stated value. Section 4.7 provides a detailed discussion of this limitation.

4.4 Angular Spectral Shift

Light hitting different parts of the detector passes through the SFPI at different incidence angles, which affects the phase of Equation 4.17. This effect has previously been called *spectral bending* [33], but is in this work referred to as *angular spectral shift*. Assuming the thermal lens objective can be modeled as a thin lens with a focal length of $f = 35$ mm, the incidence angle of the light hitting the detector can be calculated following Equation 4.41.

$$\theta = \tan^{-1} \frac{r}{f}, \tag{4.41}$$

where r denotes the distance from the center of the detector to the relevant pixel. With the 1024×768-pixel detector and a pixel pitch of 17 µm, the maximum incidence angle becomes 17.3°. The angle is depicted as a function of pixel index in Figure 4.7a, and $\cos\theta$ is depicted in Figure 4.7b. The difference in incidence angle shifts the transmission spectrum of the SFPI. Close to the edges, the transmission spectra appear to correspond to shorter cavity lengths due to the scaling of $\cos\theta$. This effectively means that the interferograms measured at the edges of the detector appear delayed (in terms of cavity expansion) compared to the center.

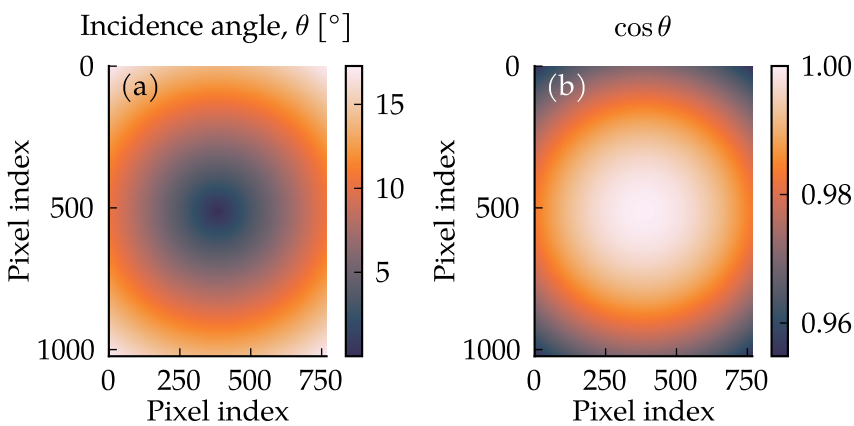

Figure 4.7: (a) Incidence angle, θ, of the light hitting different parts of the detector assuming a thin lens with a 35 mm focal length. (b) The cosine of the incidence angle is how much the phase is scaled. This illustrates the scaling factor as a function of detector coordinates.

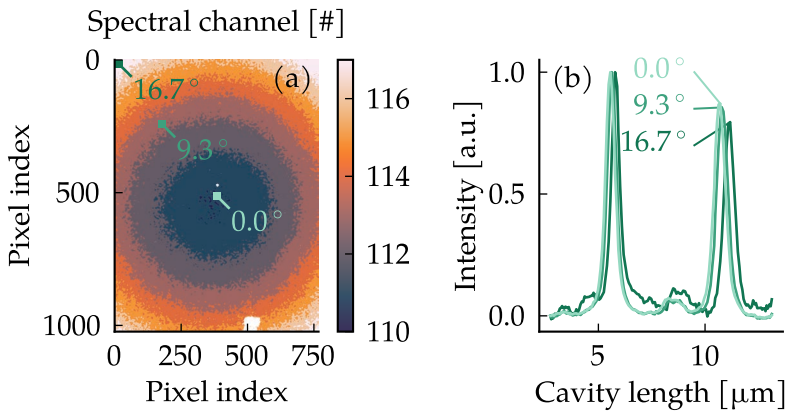

Figure 4.8: (a): Position (in spectral channels) of the 2nd transmission order of a hot plate imaged through a 10.23 μm bandpass filter. (b): Averaged interferograms across the 30×30-pixel regions highlighted in (a). The angles denote the incidence angles of light on each detector region.

This effect is observable, as illustrated in Figure 4.8, where a hot plate set to 75 °C was imaged through a 10.23 μm (978 cm^{-1}) bandpass filter (Andover Corporation, US). Figure 4.8a depicts the position (measured in spectral channels) of the second transmission order. The concentric rings indicate the interferograms' delay toward the detector's edges. White pixels in the image correspond to regions where the location of the second peak could not be determined (a metal nozzle was present in the frame since this measurement was performed as part of an analysis of flames as presented in chapter 7). Figure 4.8b presents normalized interferograms averaged across the 30×30-pixel regions highlighted in (a). The indicated angles represent the incidence angle of light sampled at the center of the highlighted regions, calculated using Eq. (4.41).

The observed spectral shift complicates comparisons between interferograms at the center of the frame and those at its edges. This effect can be corrected by scaling Δl (and thereby also ℓ) by $\cos\theta$, as described by Eq. (4.17), based on the spatial position on the detector (Figure 4.7b). Consequently, each pixel is associated with an Δl different from that in the center. A common optical path difference describing all pixels is subsequently found by interpolation.

It is important to note that, since $\cos\theta \leq 1$, portions of the spectral data will be absent following the scaling of off-center spectral axes. The function provided in Code Block 4.1 addresses this by assigning NaN (Not a Number) values to missing data. Alternatively, all spectra could be truncated to align with the shortest spectral axis, typically corresponding to pixels near the corners of the detector.

Additionally, the 'center' of the frame is not precisely at the geometric center of the detector due to a slight misalignment in the optical system. As can be observed in Figure 4.8a, the center of the concentric rings is located at pixel $[550, 380]$ [row, column], rather than at $[512, 384]$, which corresponds to the detector's geometric center.

```
import numpy as np
def shift_corrrection(cube, cavity_length):
    center = [380,550] #(x,y) center of correction
    pixel_pitch = 17e-6
    f = 33e-3 #focal length of the lens
    X, Y = np.meshgrid(np.arange(cube.shape[1]),
        np.arange(cube.shape[0]))
    X = (X - center[0])*pixel_pitch
    Y = (Y - center[1])*pixel_pitch
    Z = np.cos(np.arctan(np.sqrt(X**2+Y**2)/f))
    Z = Z.reshape(-1) #Reshape correction factor
    cavity_length_corrected = (Z *
        cavity_length.reshape(-1, 1)).T
    flat_cube = cube.reshape(cube.shape[0] *
        cube.shape[1], cube.shape[2])
    cube_interp = np.zeros_like(flat_cube)
    for i in range(flat_cube.shape[0]):
        cube_interp[i] = np.interp(cavity_length,
            cavity_length_corrected[i], flat_cube[i],
            left=np.nan, right=np.nan)
    return cube_interp.reshape(cube.shape)
```

Code Block 4.1: Python function for performing spectral shift correction on a data cube (`cube`) based on the calibrated cavity length axis (`cavity_length`). The parameter `center` specifies the center of the concentric rings, where the incidence angle is $0°$. A focal length of 33 mm is used instead of 35 mm, as this provides improved results.

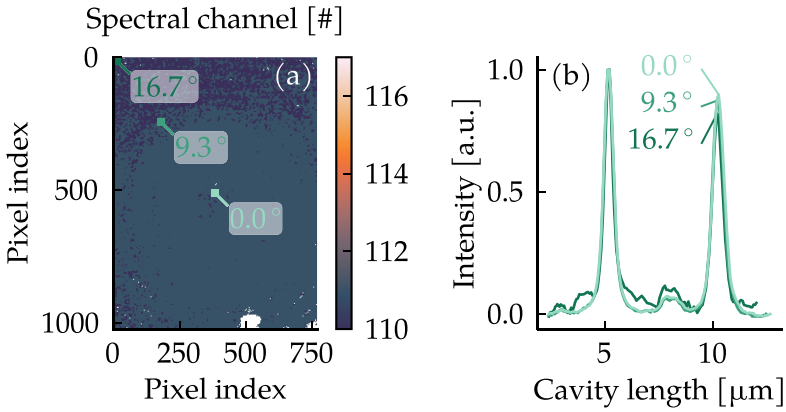

Figure 4.9: The same measurements as presented in Figure 4.8, but after compensation of angular spectral shift. (a): Location (measured in spectral channels) of the 2nd transmission order of a 10.23 µm bandpass filter. (b): Averaged interferograms from highlighted regions in (a) after the compensation has been applied. Note the interferograms with larger incidence angles appear shorter than the center due to a smaller optical path difference.

Figure 4.9 illustrates how the spectral shift can be compensated using the Python function `shift_correction(cube, cavity_length)` provided in Code Block 4.1. Following this correction, the shift in the second transmission peak is reduced to a single channel when comparing the center and edges of the detector. However, minor variations in peak location remain, which may result from the thermal lens deviating from the idealized thin lens model, as well as other aberrations introduced by the optical system. Note that to perform this correction, it is necessary to know the cavity length, which is not always possible without an external spectral reference to shift the relative cavity expansion axes provided by the monochromatic laser diodes.

4.5 The Transfer Matrix Method

While the Airy function provides valuable analytical insights into the influence of various performance parameters of the SFPI, it exhibits a significant limitation: it requires consideration of the phase change upon reflection (φ in Eq. (4.17)), which has been neglected thus far. This parameter becomes particularly critical for low-order SFPIs. A numerical simulation technique known as the transfer matrix method (TMM) is employed to address this limitation. TMM calculates the electric field as it propagates through a dielectric stack [34]. This approach enables the determination of the electric field strength at all points within the stack and accounts for the interactions occurring at material interfaces, thereby incorporating the phase shifts experienced by the light. As a result, the TMM facilitates the computation of transmittance, reflectance, and absorbance for any combination of wavelength and cavity length.

At each interface within a dielectric stack, a portion of the incident light is transmitted while the remainder is reflected. The ratio between transmitted and reflected light is determined by the angle of incidence and the refractive indices of the two media. These ratios are predicted by the Fresnel transmission and reflection coefficients, τ and ρ, respectively. Consider the configuration illustrated in Figure 4.10, where light propagates from a medium with refractive index $\tilde{n}_1$ to another medium with refractive index $\tilde{n}_2$ at an incidence angle θ. Here, θ_t and θ_r denote the angles of transmission and reflection, respectively.

It is important to distinguish between s- and p-polarized light, as these polarizations alter the boundary conditions and, consequently, the Fresnel

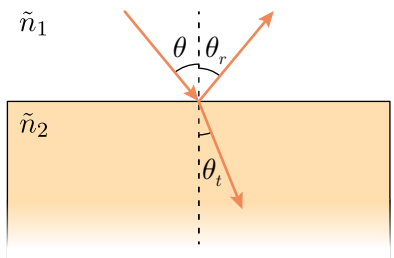

Figure 4.10: Reflection and transmission of light at an interface between two media with different refractive indices. The vectors indicate the wavevectors and the direction of energy transport.

coefficients. s-polarized light (commonly referred to as TE polarization) has its electric field oriented perpendicular to the plane of incidence, while p-polarized light (TM polarization) has its electric field oscillating parallel to the plane of incidence. The Fresnel reflection coefficients for these polarizations are given by [10]:

$$\rho_s = \frac{E_r}{E} = \frac{\cos\theta - \sqrt{\eta^2 - \sin^2\theta}}{\cos\theta + \sqrt{\eta^2 - \sin^2\theta}} \tag{4.42}$$

$$\rho_p = \frac{E_r}{E} = \frac{-\eta^2\cos\theta + \sqrt{\eta^2 - \sin^2\theta}}{\eta^2\cos\theta + \sqrt{\eta^2 - \sin^2\theta}} \tag{4.43}$$

$$\eta = \frac{\tilde{n}_2}{\tilde{n}_1} \tag{4.44}$$

Here, E and E_r represent the electric fields of the incident and reflected waves, respectively, while η is the relative refractive index. Similarly, the Fresnel transmission coefficients are expressed as:

$$\tau_s = \frac{E_t}{E} = \frac{2\cos\theta}{\cos\theta + \sqrt{\eta^2 - \sin^2\theta}} \tag{4.45}$$

$$\tau_p = \frac{E_t}{E} = \frac{2\eta\cos\theta}{\eta^2\cos\theta + \sqrt{\eta^2 - \sin^2\theta}} \tag{4.46}$$

With E_t representing the electric field amplitude of the transmitted wave. For simplicity, only light at normal incidence ($\theta = 0$) is considered in the subsequent analysis. At normal incidence, the Fresnel coefficients become identical for s- and p-polarization, simplifying to:

$$\rho_{1\to 2} = \frac{\tilde{n}_1 - \tilde{n}_2}{\tilde{n}_1 + \tilde{n}_2} \tag{4.47}$$

$$\tau_{1\to 2} = \frac{2\tilde{n}_1}{\tilde{n}_1 + \tilde{n}_2} \tag{4.48}$$

The subscript $1 \to 2$ indicates light transitioning *from* a medium with refractive index $\tilde{n}_1$ *to* a medium with refractive index $\tilde{n}_2$.

Light accumulates phase as it propagates through a medium. The phase acquired over a propagation distance d is given by:

$$p = \exp\left(j2\pi\frac{\tilde{n}d}{\lambda}\right), \tag{4.49}$$

where $\tilde{n}$ is the refractive index, d the propagation distance, and λ the wavelength of the light.

Consider the dielectric stack illustrated in Figure 4.11a, consisting of $N-1$ layers. The electric field within each layer is decomposed into a rightward-moving wave, $E^{(r)}$, and a leftward-moving wave, $E^{(l)}$. The electric field in the ith layer is further described as follows:

- Subscript A denotes the electric field immediately to the right of the interface with the $(i-1)^{\text{th}}$ layer.
- Subscript B denotes the electric field immediately to the left of the interface with the $(i+1)^{\text{th}}$ layer.

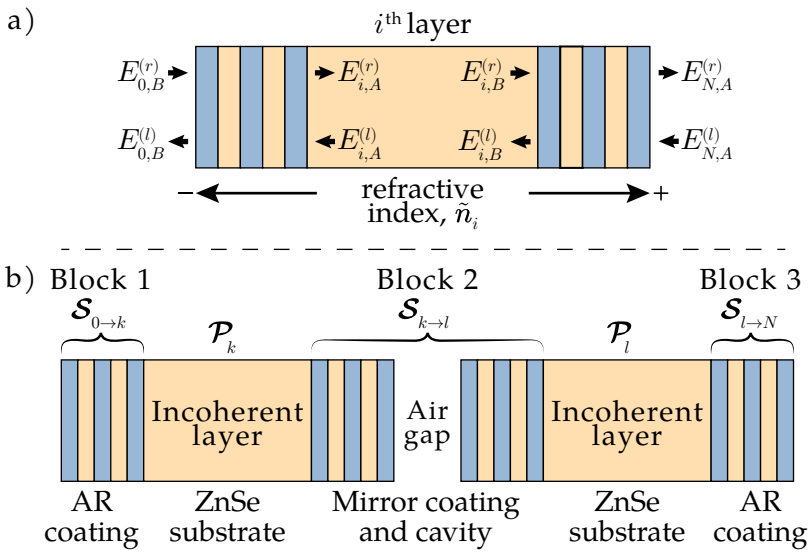

Figure 4.11: (a) Thin-film stack illustrating the electric fields of rightward- and leftward-moving waves on either side of each interface. (b) Multiple film stacks with thick, incoherent layers in between represent the two mirrors constituting the SFPI. Blocks 1 and 3 represent anti-reflective coatings, and Block 2 represents the dielectric mirror coatings and the air gap.

The electric field on either side of an interface can be calculated using Eqs. (4.47) and (4.48):

$$E_{i+1,A}^{(r)} = \rho_{i+1\to i} E_{i+1,A}^{(l)} + \tau_{i\to i+1} E_{i,B}^{(r)} \tag{4.50}$$

$$E_{i,B}^{(l)} = \rho_{i\to i+1} E_{i,B}^{(r)} + \tau_{i+1\to i} E_{i+1,A}^{(l)} \tag{4.51}$$

Utilizing that $\tau_{i\to i+1}\tau_{i+1\to i} - \rho_{i\to i+1}\rho_{i+1\to i} = 1$, Eqs. (4.50) and (4.51) can be rearranged and expressed in matrix form presented in Eq. (4.52):

$$\begin{aligned}\begin{bmatrix} E_{i,B}^{(r)} \\ E_{i,B}^{(l)} \end{bmatrix} &= \frac{1}{\tau_{i\to i+1}} \begin{bmatrix} 1 & -\rho_{i+1\to i} \\ \rho_{i\to i+1} & 1 \end{bmatrix} \begin{bmatrix} E_{i+1,A}^{(r)} \\ E_{i+1,A}^{(l)} \end{bmatrix} \\ &= \boldsymbol{\mathcal{D}}_{i\to i+1} \begin{bmatrix} E_{i+1,A}^{(r)} \\ E_{i+1,A}^{(l)} \end{bmatrix}\end{aligned} \tag{4.52}$$

Here, $\boldsymbol{\mathcal{D}}_{i\to i+1}$ represents the *refraction matrix*, which describes the transition characteristics between two layers i and $i+1$.

Similarly, the phase accumulation within the ith layer is described by the *phase matrix*, $\boldsymbol{\mathcal{P}}_i$ given in Eq. (4.53):

$$\begin{aligned}\begin{bmatrix} E_{i,A}^{(r)} \\ E_{i,A}^{(l)} \end{bmatrix} &= \begin{bmatrix} \exp\{-j2\pi\tilde{n}_i d_i/\lambda\} & 0 \\ 0 & \exp\{j2\pi\tilde{n}_i d_i/\lambda\} \end{bmatrix} \begin{bmatrix} E_{i,B}^{(r)} \\ E_{i,B}^{(l)} \end{bmatrix} \\ &= \boldsymbol{\mathcal{P}}_i \begin{bmatrix} E_{i,B}^{(r)} \\ E_{i,B}^{(l)} \end{bmatrix}\end{aligned} \tag{4.53}$$

The phase matrix, $\boldsymbol{\mathcal{P}}_i$, incorporates the phase change as light propagates through a given layer. The total system transfer matrix for the stack is computed by successive matrix multiplications, as shown below:

$$\begin{bmatrix} E_{0,B}^{(r)} \\ E_{0,B}^{(l)} \end{bmatrix} = \boldsymbol{\mathcal{D}}_{0\to 1} \left(\prod_{i=1}^{N-1} \boldsymbol{\mathcal{P}}_i \boldsymbol{\mathcal{D}}_{i\to i+1} \right) \begin{bmatrix} E_{N,A}^{(r)} \\ E_{N,A}^{(l)} \end{bmatrix} \tag{4.54}$$

$$= \boldsymbol{\mathcal{S}}_{0\to N} \begin{bmatrix} E_{N,A}^{(r)} \\ E_{N,A}^{(l)} \end{bmatrix} \tag{4.55}$$

From the system transfer matrix, $\boldsymbol{\mathcal{S}}_{0\to N}$, the transmission coefficient of the entire stack can be derived as:

$$\begin{bmatrix} E_{0,B}^{(r)} \\ E_{0,B}^{(l)} \end{bmatrix} = \boldsymbol{\mathcal{S}}_{0\to N} \begin{bmatrix} E_{N,A}^{(r)} \\ 0 \end{bmatrix}$$

$$\Rightarrow \tau_{0\to N} = \frac{1}{\boldsymbol{\mathcal{S}}_{0\to N}^{(1,1)}} \tag{4.56}$$

Similarly, the reflection coefficient is determined as:

$$\rho_{0\to N} = \frac{\boldsymbol{\mathcal{S}}_{0\to N}^{(2,1)}}{\boldsymbol{\mathcal{S}}_{0\to N}^{(1,1)}} \tag{4.57}$$

The transmittance and reflectance of the entire dielectric stack can thus be calculated as

$$\mathcal{T}_{0\to N} = \frac{\sqrt{\eta_{0,N}^2 - \sin^2\theta}}{\cos\theta} |\tau_{0\to N}|^2, \quad \eta_{0,N} = \frac{\tilde{n}_N}{\tilde{n}_0} \tag{4.58}$$

$$\mathcal{R}_{0\to N} = |\rho_{0\to N}|^2 \tag{4.59}$$

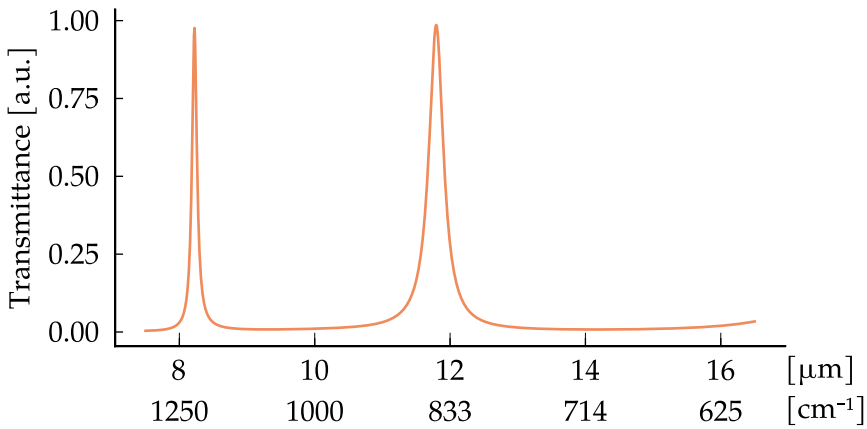

Figure 4.12: Transmittance spectrum of an SFPI consisting solely of the mirror coatings (with semi-infinite ZnSe substrates on either side) at a mirror separation of 12.3 μm. The x-axis shows both the wavelength and wavenumber of the incident light.

The absorption is nonzero if materials of complex refractive indices are included in the calculation and is calculated as

$$\alpha_{0\to N} = 1 - \mathcal{T}_{0\to N} - \mathcal{R}_{0\to N} \tag{4.60}$$

The system transfer matrix describes the behavior of the dielectric stack at a single wavelength. Since the refractive indices of the materials vary with wavelength, a new transfer matrix must be computed for each relevant wavelength. The following section outlines the functions used to calculate the wavelength-dependent refractive indices of the materials comprising the dielectric stack.

4.5.1 Calculating Refractive Indices

As the refractive index varies with wavelength, a separate transfer matrix must be computed for each relevant wavelength. The refractive indices

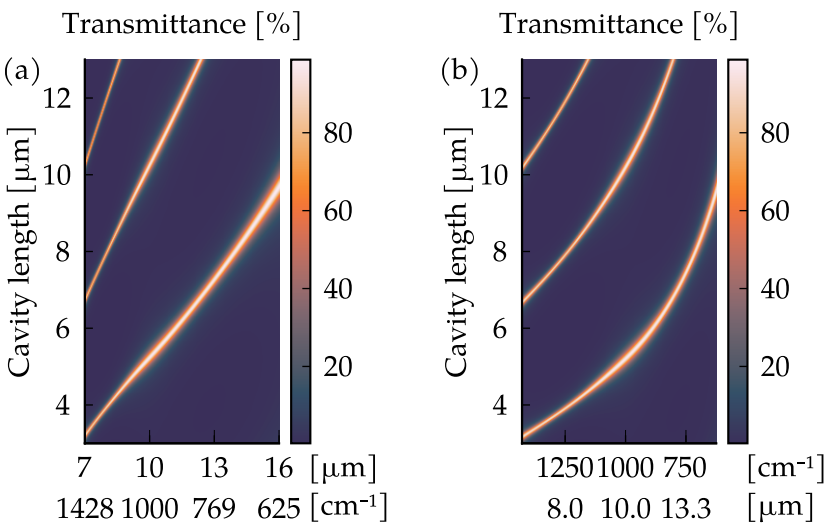

Figure 4.13: Transmittance matrix calculated using the TMM considering only the mirror coatings and assuming semi-infinite substrates. The cavity length denotes the size of the air gap separating the two mirrors. The anti-reflective coating is disregarded. (a) show a linear x-axis in terms of wavelengths, while (b) has a linear x-axis in terms of wavenumbers, though both plots show the same data.

of various materials are often determined using polynomial expressions from the literature. In the expressions below, the complex refractive index $\tilde{n}$ consists of the real part n' and the extinction coefficient κ.

Refractive Indices of Materials

Thorium Fluoride, ThF_4, [35, page 1051]:

$$n' = 1.118 + \frac{2.46}{\lambda} - \frac{2.98}{\lambda^2}, \quad \lambda \text{ in } \mu\text{m}$$

$$\kappa = 0.00189 - 0.00015\lambda + 0.00001\lambda^2$$

Zinc Selinide, ZnSe [35, page 737]

$$n' = \sqrt{4 + \frac{1.6\lambda^2}{\lambda^2 - 0.113}}, \quad \lambda \text{ in } \mu\text{m}$$

Germanium, Ge [36]

$$n' = 4.1463 + \frac{0.57268}{\lambda^2} + \frac{0.087329}{\lambda^4}, \quad \lambda \text{ in } \mu\text{m}$$

$$\kappa = 0.064314 \exp\left\{\frac{\frac{1.24}{\lambda} - 0.77285}{0.142}\right\}$$

Zinc Sulfide, ZnS [37, page 600]

$$\tilde{n} = \sqrt{5.7\left(1 + \frac{352^2 - 282^2}{282^2 - \tilde{\nu}^2 + 6.77j \cdot \tilde{\nu}}\right)}, \quad \tilde{\nu} \text{ in cm}^{-1}$$

A transmittance spectrum is obtained by computing transfer matrices over a range of wavelengths, as shown in Figure 4.12. The calculations use the layer configuration from Table 3.1 but consider only the mirror materials, modeling the SFPI as two dielectric mirrors separated by an air gap with semi-infinite ZnSe substrates. The spectrum in Figure 4.12 corresponds to a cavity length of 12.3 µm. Extending these calculations to varying cavity lengths yields the transmittance matrix in Figure 4.13.

4.6 Generalized Matrix Method

A fundamental limitation of TMM is its assumption of perfectly coherent light. This assumption becomes problematic when layer thicknesses exceed the coherence length of the light. The coherence length can be approximated as:

$$L_c \approx \frac{\lambda^2}{\Delta\lambda}, \tag{4.61}$$

where λ is the central wavelength and $\Delta\lambda$ is the spectral bandwidth of the radiation [10]. For $\lambda = 11.5\ \mu\text{m}$ and $\Delta\lambda = 15\ \mu\text{m} - 8\ \mu\text{m} = 7\ \mu\text{m}$, the coherence length is approximately $L_c \approx 19\ \mu\text{m}$. Given that the ZnSe substrates in the system are 5 mm thick, their optical path lengths exceed the coherence length by several orders of magnitude.

Figure 4.14 shows the transmittance spectrum of an SFPI with an 8 µm cavity length, including the contributions of anti-reflective coatings and ZnSe substrates. When calculated using TMM, high-frequency oscillations appear superimposed on the expected SFPI spectrum. These oscillations arise because the FSR is inversely proportional to the layer

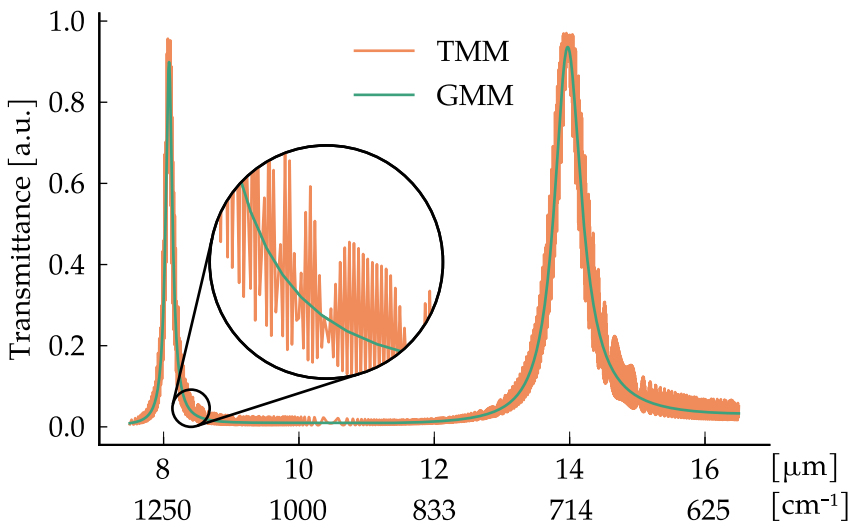

Figure 4.14: Transmittance spectrum calculated using TMM and GMM for an SFPI with an 8 µm cavity length, including finite ZnSe substrates and anti-reflective coatings.

thickness, as given by $\mathrm{FSR} \propto \ell^{-1}$ (Eqs. (4.30) and (4.31)). For a 5 mm thick substrate, the FSR becomes approximately 0.3 pm, leading to rapid fluctuations in the spectrum.

To address this issue, the Generalized Matrix Method (GMM) provides an extension to TMM that accommodates layers with thicknesses exceeding the coherence length [38]. GMM also accounts for losses due to scattering at rough interfaces, producing a smoother and more physically realistic transmittance spectrum compared to TMM (Figure 4.14). While GMM retains the general methodology of TMM — reducing a thin-film stack to a single 2×2 transfer matrix — it introduces modifications to handle partially or completely incoherent layers. For systems containing purely coherent layers, GMM reduces exactly to TMM. Partial coherence arises due to microscopic surface/interface roughness, which modifies the Fresnel coefficients in the refraction matrix as follows:

$$\rho'_{i\to i+1} = \rho_{i\to i+1} \exp\left\{-2\left(\frac{s\tilde{n}_i}{\lambda}\right)^2\right\} \tag{4.62}$$

$$\rho'_{i+1\to i} = \rho_{i+1\to i} \exp\left\{-2\left(\frac{s\tilde{n}_{i+1}}{\lambda}\right)^2\right\} \tag{4.63}$$

$$\tau'_{i\to i+1} = \tau_{i\to i+1} \exp\left\{-\frac{1}{2}\left(\frac{s}{\lambda}\right)^2 (\tilde{n}_{i+1} - \tilde{n}_i)^2\right\} \tag{4.64}$$

$$\tau'_{i+1\to i} = \tau_{i+1\to i} \exp\left\{-\frac{1}{2}\left(\frac{s}{\lambda}\right)^2 (\tilde{n}_i - \tilde{n}_{i+1})^2\right\} \tag{4.65}$$

$$s = 2\pi h_{\mathrm{RMS}} \tag{4.66}$$

where h_{RMS} is the root-mean-square (RMS) height of surface roughness at the interface. The partially coherent layers have *not* been included in the model in this project.

Additional steps are required for systems containing completely incoherent layers. The stack must be partitioned into smaller blocks, each with its own system transfer matrix. Figure 4.11b illustrates this process for two incoherent layers located at positions k and l. The transfer matrices for the coherent (or partially coherent) blocks are computed as before. The phase information is ' discarded ' as light propagates through the

incoherent layer. Mathematically, this is described by replacing the transmission and reflection coefficients with their squared amplitudes. This transforms the transfer matrix into the *intensity matrix* which for the block $0 \to k$ is given as:

$$\bar{\boldsymbol{\mathcal{S}}}_{0\to k} = \frac{1}{\left|\tau'_{0\to k}\right|^2} \begin{bmatrix} 1 & -\left|\rho'_{k\to 0}\right|^2 \\ \left|\rho'_{0\to k}\right|^2 & \left|\tau'_{0\to k}\tau'_{k\to 0}\right|^2 - \left|\rho'_{0\to k}\rho'_{k\to 0}\right|^2 \end{bmatrix} \tag{4.67}$$

Here, the Fresnel coefficients can be extracted from the transfer matrix (not the intensity matrix) following:

$$\rho'_{0\to k} = \frac{\boldsymbol{\mathcal{S}}^{(2,1)}_{0\to k}}{\boldsymbol{\mathcal{S}}^{(1,1)}_{0\to k}}, \qquad \rho'_{k\to 0} = -\frac{\boldsymbol{\mathcal{S}}^{(1,2)}_{0\to k}}{\boldsymbol{\mathcal{S}}^{(1,1)}_{0\to k}},$$

$$\tau'_{0\to k} = \frac{1}{\boldsymbol{\mathcal{S}}^{(1,1)}_{0\to k}}, \qquad \tau'_{k\to 0} = \frac{\det\left(\boldsymbol{\mathcal{S}}_{0\to k}\right)}{\boldsymbol{\mathcal{S}}^{(1,1)}_{0\to k}}$$

For incoherent layers, the phase matrix is similarly modified by squaring its elements:

$$\bar{\boldsymbol{\mathcal{P}}}_i = \begin{bmatrix} \left|\exp\{-j2\pi\tilde{n}_i d_i/\lambda\}\right|^2 & 0 \\ 0 & \left|\exp\{j2\pi\tilde{n}_i d_i/\lambda\}\right|^2 \end{bmatrix} \tag{4.68}$$

The total transfer matrix for the system, including incoherent layers, is then obtained by combining all relevant intensity matrices and phase matrices:

$$\hat{\boldsymbol{\mathcal{S}}}_{0\to N} = \bar{\boldsymbol{\mathcal{S}}}_{0\to k}\bar{\boldsymbol{\mathcal{P}}}_k\bar{\boldsymbol{\mathcal{S}}}_{k\to l}\bar{\boldsymbol{\mathcal{P}}}_l\bar{\boldsymbol{\mathcal{S}}}_{l\to N} \tag{4.69}$$

The final intensity matrix $\hat{\boldsymbol{\mathcal{S}}}_{0\to N}$ no longer contains phase information but can still be used to calculate reflectance $\mathcal{R}$ and transmittance $\mathcal{T}$:

$$\mathcal{T}_{0\to N} = \frac{\tilde{n}_N}{\tilde{n}_0}\frac{1}{\hat{\boldsymbol{\mathcal{S}}}^{(1,1)}_{0\to N}} \tag{4.70}$$

$$\mathcal{R}_{0\to N} = \frac{\hat{\boldsymbol{\mathcal{S}}}^{(2,1)}_{0\to N}}{\hat{\boldsymbol{\mathcal{S}}}^{(1,1)}_{0\to N}} \tag{4.71}$$

4.6.1 Modelling Concave Mirror Substrates in GMM

As outlined in Section 4.3, the mirrors are concave due to stresses in the mirror coating, resulting in the edges protruding relative to the center. This implies that the SFPI cavity length is greater at the center than at the edges. Since the SFPI is positioned directly in front of the lens and thus significantly out of focus, this introduces a broadening effect across the entire detector. This effect is incorporated into the GMM calculations by evaluating the transmission of the SFPI at multiple cavity lengths and computing a weighted average. The cavity length at the center of the SFPI is treated as the *actual* cavity length, while a negative offset is applied to the cavity length based on the distance from the center.

The mirrors are spherically deformed, and the radius of curvature can be determined using Eq. (4.72):

$$R_{\text{curv}} = \frac{h_{\text{mirror}}}{2} + \frac{d_{\text{mirror}}^2}{8h_{\text{mirror}}} \tag{4.72}$$

Here, $h_{\text{mirror}} = 150$ nm represents the total height difference between the center and the circumference of the mirror, and $d_{\text{mirror}} = 43$ mm is the diameter of the mirror. Substituting these values yields a curvature of $R_{\text{curv}} = 1541$ m. The cavity length offset as a function of the radial

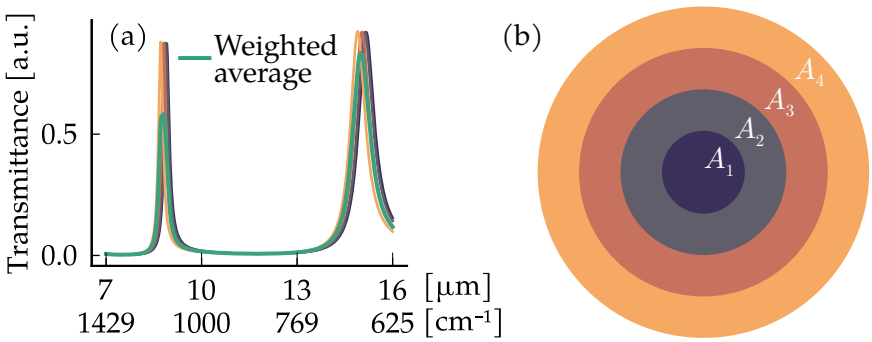

Figure 4.15: (a) transmittance spectra calculated using GMM with optical path differences varying from 17.54 μm to 18.0 μm ($\ell = 8.77$ μm to 9.00 μm). The colors correspond to the colored segments in (b), which show a mirror coating divided into concentric rings. Each ring is associated with its own cavity lengths based on the curvature of the mirror due to film stresses. The weighted average in (a) is based on the area fractions of each ring in (b).

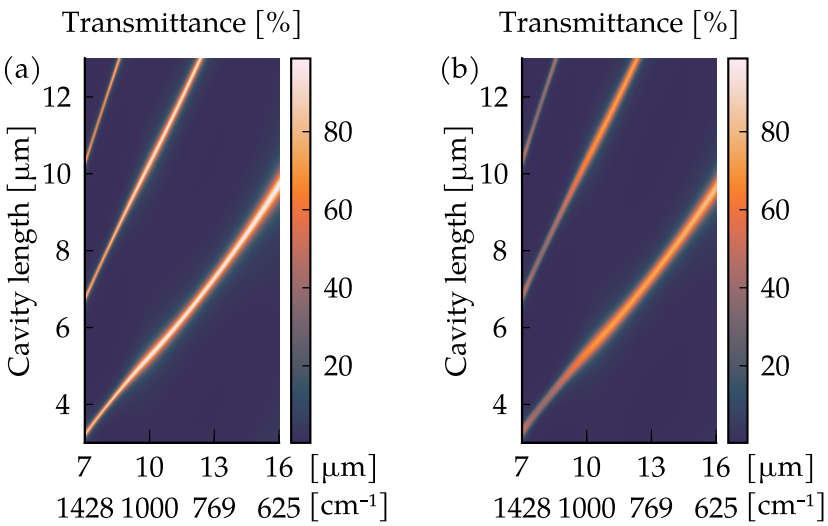

Figure 4.16: (a) The same transmittance matrix as presented in Figure 4.13a. In this case, (b) has been broadened due to the concave mirrors, resulting in a total cavity length variation of $\Delta\ell = 300$ nm across the SFPI. This variation is achieved by calculating a weighted average of nine concentric rings, as depicted in Figure 4.15.

distance r from the center can be expressed as:

$$\Delta\ell = -\left(2R_{\text{curv}} - 2\sqrt{R_{\text{curv}}^2 - r^2}\right) \tag{4.73}$$

The variation in cavity length is incorporated into the GMM calculations by segmenting the mirror into concentric rings, as depicted in Figure 4.15b. The cavity offset is determined based on the radial distance from the center of each ring segment to the center of the mirror. Subsequently, the transmission profile is computed for each segment using GMM, accounting for the respective offset distances. An area-weighted average transmission profile is then calculated based on all ring segments (Figure 4.15a).

Unless otherwise specified, nine ring divisions are used for averaging, ensuring sufficient overlap to maintain a smooth averaged transmission curve across all wavelengths and cavity lengths. For illustrative purposes, Figure 4.15 demonstrates the method with only four divisions.

Figure 4.16b illustrates the impact of broadening on the transmittance matrix of the SFPI. In comparison to the non-broadened case (Figure 4.16a), it is evident that the energy is distributed over a broader range of wavelengths/cavity lengths, leading to a reduction in peak transmittance. Furthermore, it is observed that the broadening effect diminishes progressively with higher transmission orders when measured in terms of wavelength.

4.7 Spectral Resolution Based on GMM Calculations

The closest two spectral features can be to each other and still be distinguishable is within one FWHM of each other. This determines the spectral resolution limit of the interferometer. Due to the multiple transmission orders, a single number cannot characterize the resolution. This arises because the FWHM depends on both the cavity length (and thereby the transmission order) and the finesse, $\mathcal{F}$, of the interferometer (see section 4.2.4). In the wavelength representation of the Airy function, the FWHM is also influenced by the wavelength itself, while in the wavenumber representation, it remains constant across the spectral range.

To account for the broadening introduced by mirror bending, the spectral resolution of the SFPI is calculated based on the broadened transmittance matrix. For each row in Figure 4.16b (corresponding to a single cavity length), the FWHM of each peak is determined alongside its location. The FWHMs for the observable portions of the transmission orders are plotted in Figure 4.17. The figure illustrates that the resolution improves with higher transmission orders. The shape of the curves can be attributed to the reflectance of the mirror, which directly governs the finesse and exhibits a similar shape (Figure 3.10).

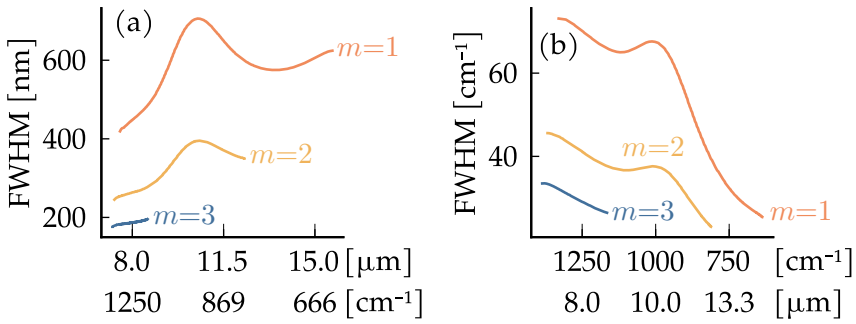

Figure 4.17: The SFPI resolution presented in terms of wavelengths (a) and wavenumbers (b) for the first three transmission orders ($m = 1, 2, 3$). The FWHM values are derived from the calculated transmittance profile of the SFPI using the GMM method. These correspond to the FWHM of the peaks in each row of Figure 4.13, with the broadening effect due to mirror bending incorporated.

Furthermore, the second and third transmission orders do not span the full spectral range due to the limited range of the piezo actuators. Consequently, it is not possible to fully exploit their superior spectral resolution across all wavelengths. Additionally, the higher transmission orders lead to greater overlap between orders, meaning the signals of multiple transmission orders can be observed at the same cavity length. This overlap complicates spectral reconstruction, as discussed further in Chapter 5.

In terms of wavelengths, the resolution spans from 176–706 nm, while in terms of wavenumbers, it spans from 26–73 cm^{-1}. To obtain a more precise measure of the spectral resolution, it is necessary to specify the part of the spectrum being examined, the available transmission orders, and whether they overlap.

4.8 Measuring SFPI Transmittance Matrix Using FTIR

To validate the transmittance matrix obtained via GMM (Figure 4.13), experimental transmittance measurements were performed using an FTIR spectrometer. Acquiring transmittance data at varying cavity lengths provides an empirical basis for comparison with the calculated transmittance matrix. However, this approach is complicated by the fact that the monochromatic laser diodes only provide information about the relative cavity expansion. An absolute determination of the mirror separation is essential for a meaningful comparison between experimental and theoretical results.

Maintaining a constant cavity length while performing FTIR measurements also presents a challenge. Piezoelectric actuators, which control the cavity length, are prone to drift under a constant voltage, necessitating the implementation of a feedback loop to stabilize the cavity length. Appendix F details the methodology for achieving this stabilization. The cavity expansion is derived from laser diode interferograms, with an additional offset applied to determine the absolute cavity length axis.

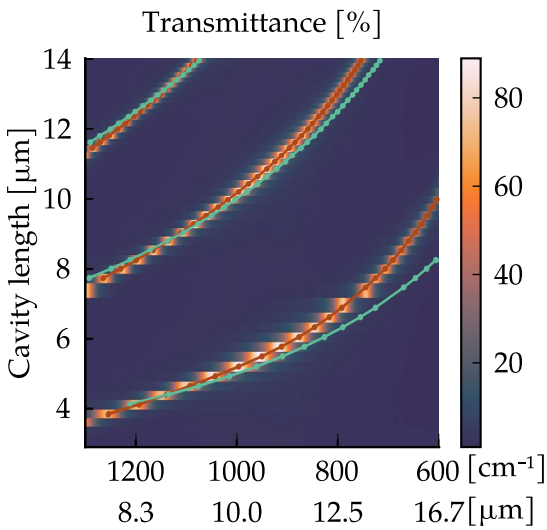

Figure 4.18: FTIR transmittance measurement of SFPI at various cavity lengths. The overlayed connected dots indicate the peak location calculated using GMM (red) and the Airy function (green). No broadening has been included in the calculation due to the relatively small spot size of the FTIR instrument.

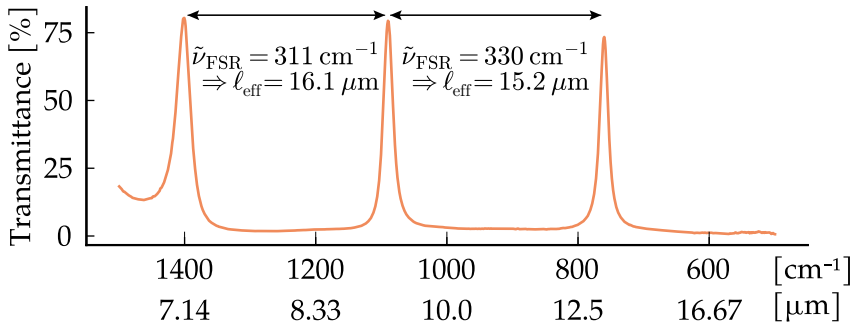

Figure 4.19: FTIR transmittance measurement of SFPI at a physical cavity length of 15.2 µm (derived from laser diode interferograms). Differences in the derived effective cavity lengths illustrate how the position of the plane of reflection affects the transmittance profile spectrally.

This offset is calibrated to align with the GMM calculations, shown as an overlay on the FTIR measurement in Figure 4.18. In this figure, only the positions of the GMM transmission peaks are displayed to enhance interpretability. Excellent agreement is observed between the positions of maximum transmission found by GMM and the FTIR transmittance measurements.

For comparison, the Airy function (Eq. (4.17)) is also overlayed; however, the agreement is noticeably worse. This discrepancy is attributable to the phase shift upon reflection, which is set to $\varphi = 0$ in the Airy function calculations. Notably, for low-order dielectric SFPI devices, this phase change varies with wavelength and is important to include in the model. This becomes evident when using the FSR of the FTIR transmittance spectra to derive the physical cavity length since these are directly related (Eq. (4.29)). As depicted in Figure 4.19, the FSR observed in different parts of the spectrum will lead to drastically different effective cavity lengths (ℓ_{eff} is calculated based on measured FSR and Eq. (4.24)). This is because the "plane of reflection" where the electric field approaches zero, does not necessarily coincide with the physical surface of the mirror. Instead, it may lie either within or outside the mirror. This effect is accounted for in GMM calculations and will be discussed in greater detail in the following section.

4.9 Phase Change Upon Reflection

When light reflects at an interface transitioning from a lower to a higher refractive index — such as in the case of a perfectly reflecting mirror — it undergoes a phase change of 180°. However, for dielectric mirrors, each interface between layers produces partial reflection and transmission, resulting in multiple reflected waves. Unlike a single interface, where reflection occurs precisely at the boundary between two media, the effective reflection in a dielectric mirror is distributed across the entire multilayer stack. The "plane of reflection" is thus not confined to a specific physical boundary but is determined by the multilayer structure's collective behavior. Additionally, due to the wavelength-dependent refractive indices of the layer materials, the phase change upon reflection also varies with wavelength.

The variation of the phase change with wavelength can be simulated using GMM for a single dielectric mirror. In this simulation, the antireflective coating is excluded, and the material stack consists of a semi-infinite ZnSe layer, alternating layers of Ge and ThF_4, and a semi-infinite air layer. The electric field is calculated at the air-side of the Ge/air interface

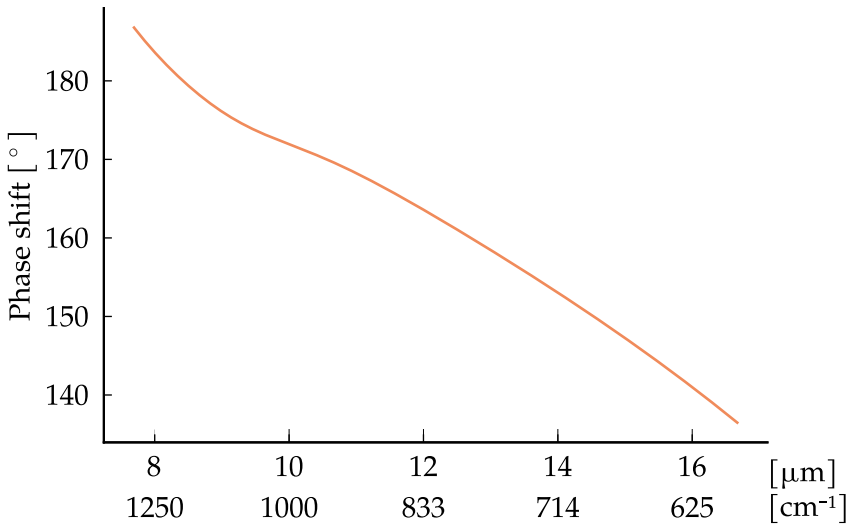

Figure 4.20: Phase shift upon reflection for a single dielectric mirror calculated using GMM and semi-infinite ZnSe and air layers on either side of dielectric stack.

for both the rightward- and leftward-propagating waves. Their phase difference is then plotted as a function of wavelength in Figure 4.20.

To calculate the electric field within the stack, the field on either side of the SFPI is first determined using the total system transfer matrix, given by:

$$E_{N,A}^{(r)} = \frac{E_{0,B}^{(r)}}{\boldsymbol{\mathcal{S}}_{0\to N}^{(1,1)}}$$

$$E_{0,B}^{(l)} = \boldsymbol{\mathcal{S}}_{0\to N}^{(2,1)} E_{N,A}^{(r)}$$

where $E_{0,B}^{(r)}$ is the incident field strength and $E_{N,A}^{(l)} = 0$. To determine the electric field at an arbitrary position x within the stack, a new system matrix $\boldsymbol{\mathcal{S}}_{x\to N}$, representing all layers to the right of x, is computed. The electric fields of the rightward- and leftward-traveling waves at position

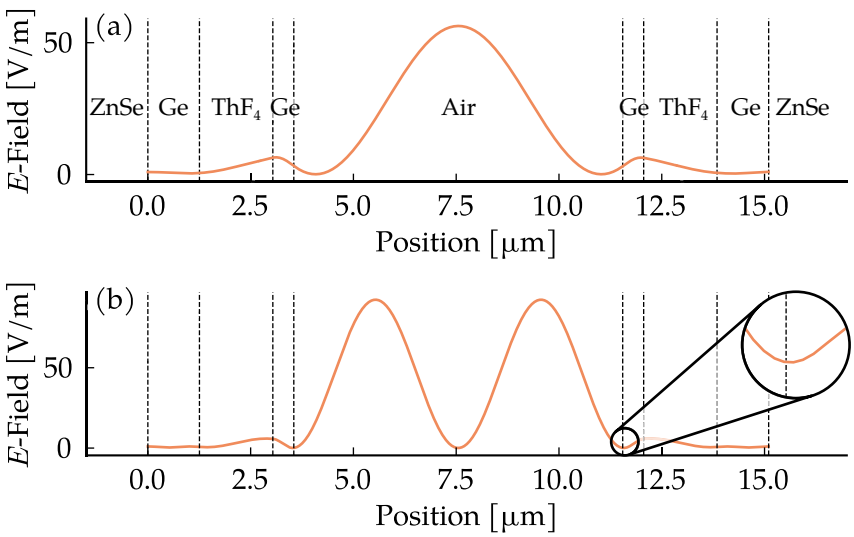

Figure 4.21: Electric field distribution within the SFPI at a cavity length of $\ell = 8$ μm, for wavelengths of (a) 13.9 μm and (b) 8.05 μm, calculated using the GMM method. Dashed vertical lines indicate the transitions between layers in the SFPI dielectric stack. The inset in (b) illustrates the plane of reflection inside the Ge layer for the shorter wavelength, compared to its location outside the Ge layer for the longer wavelength in (a).

x are then given by:

$$E_x^{(r)} = \boldsymbol{S}_{x\to N}^{(1,1)} E_{N,A}^{(r)}$$

$$E_x^{(l)} = \boldsymbol{S}_{x\to N}^{(2,1)} E_{N,A}^{(r)}$$

As shown in Figure 4.20, the phase change upon reflection decreases with increasing wavelength, falling below 180° at a wavelength of 8.45 µm (1183 cm^{-1}). A phase change of less than 180° suggests that the plane of reflection lies outside the mirror coating. This implies that the effective cavity length (ℓ_{eff}) of the SFPI is shorter than the physical cavity length (ℓ) at longer wavelengths. This behavior is further illustrated in Figure 4.21, where the electric field within the SFPI is calculated for different positions in the layer stack. At a wavelength of 13.9 µm (Figure 4.21a), the plane of reflection lies inside the SFPI cavity (making ℓ_{eff} shorter). Conversely, for a shorter wavelength of 8.05 µm (Figure 4.21b), the plane of reflection shifts into the Ge layer (though only just), consistent with the phase difference shown in Figure 4.20.

The relationship between the physical cavity length and the effective cavity length is illustrated in Figure 4.22 for the first four transmission orders. The physical cavity length is derived from GMM predictions, while

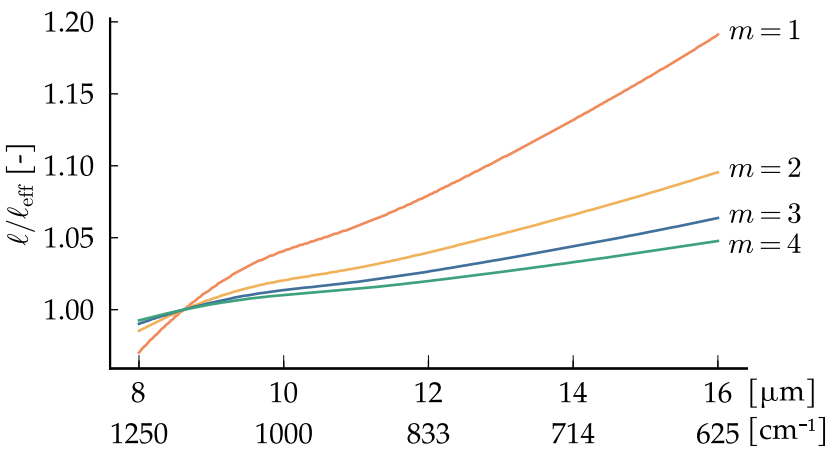

Figure 4.22: Relationship between ℓ/ℓ_{eff} and the wavelength. The fraction gets closer to unity for higher transmission orders.

the effective cavity length is defined as $\ell_{\text{eff}} = m\lambda/2$, where m denotes the transmission order. The figure highlights that lower transmission orders exhibit significantly greater sensitivity to variations in the phase change upon reflection compared to higher orders. This behavior arises because, as the cavity length increases, the phase term in the Airy function (Eq. (4.17)) becomes increasingly dominated by the contribution from ℓ. Furthermore, at wavelengths longer than 8.45 µm, the ratio ℓ/ℓ_{eff} exceeds unity ($\ell/\ell_{\text{eff}} > 1$) due to the phase change upon reflection falling below 180°.

As an additional investigation, the phase change upon reflection predicted by GMM, as shown in Figure 4.20, was incorporated into the Airy function to evaluate whether this adjustment improves the agreement with FTIR transmittance measurements. Here, φ in Eq. (4.17) is set equal to the values presented in Figure 4.20. The results for both the original and phase-adjusted Airy functions are overlaid with the FTIR measurements in Figure 4.23. A significantly improved agreement between the phase-adjusted Airy function and the FTIR measurements is observed. However, minor discrepancies remain between the FTIR measurements and the phase-adjusted Airy function.

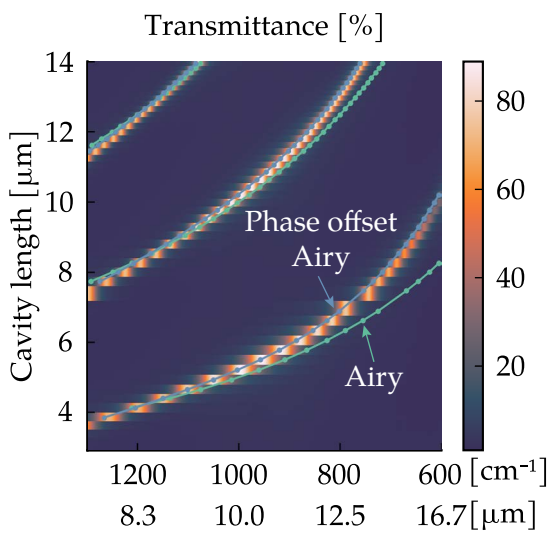

Figure 4.23: Same FTIR transmittance measurements as in Figure 4.18, but now with overlaid Airy functions with and without the phase offset presented in Figure 4.20.

These deviations may arise from differences in the modeling approaches. Specifically, the results in Figure 4.18 are derived from GMM calculations that include the antireflective coating and the incoherent ZnSe substrate. In contrast, the predictions in Figure 4.20 are based on TMM calculations, which only account for the mirror stack and treat the ZnSe substrate as a semi-infinite layer.

Due to these modeling differences — and because the broadening effects of concave mirrors can be more readily incorporated into GMM — GMM is employed as the primary tool for simulating the SFPI transmittance profile despite its higher computational cost.

4.10 Summary

The SFPI has been examined in detail throughout this chapter. The Airy function provides a fundamental analytical framework for understanding its operation and offers insight into key relationships, such as the dependence of spectral resolution on wavenumber and cavity length.

To obtain more precise estimates of the SFPI's transmission profile, GMM has been employed. This method accounts for all material layers within the SFPI, enabling the estimation of its transmittance, reflectance, and absorbance for any combination of wavenumber and cavity length. Additionally, GMM is used to assess spectral broadening effects induced by the spherical curvature of the mirrors and to analyze reflection planes within the cavity. Notably, it is confirmed that the reflection does not necessarily occur at the physical surface of the mirrors. Since the mirrors are comprised of dielectric layer stacks, multiple waves reflect and interact, and the effective reflection plane can thus reside either within or beyond the material stack, depending on the wavenumber.

The transmittance matrix, derived from GMM calculations, plays a crucial role in the subsequent chapter, where the relationship between the spectral distribution of incident light and the SFPI's transmittance is central to predicting interferograms from a given incident spectrum. This relationship becomes even more critical when addressing the inverse problem — estimating the incident spectrum from measured interferograms.

5. Spectral Reconstruction

The spectral axis of the hyperspectral data cubes recorded with the LWIR HSC is expressed in terms of the SFPI cavity length rather than wavelengths or wavenumbers, as is common with other spectrometers. Consequently, these measurements are referred to as interferograms. This representation complicates the interpretation of results, particularly when comparing them with measurements obtained using other types of equipment. Therefore, a significant focus of this thesis has been exploring methods for remapping interferograms into spectra, enabling more straightforward comparison with existing databases. While remapping is unnecessary if the sole aim is to differentiate between materials based on their interferograms, it becomes an essential tool for the interpretation of data.

This chapter presents the mathematical modeling of the imaging system and demonstrates how this modeling can be formulated as a linear minimization problem. The system can be modeled in various ways, depending on the context and what parts of the equation need to be solved for. In the simplest scenario, the system is formulated to describe how incident spectra are recorded as interferograms. However, the primary focus is solving the inverse problem: converting interferograms into spectra. This problem is inherently underdetermined, having infinitely many solutions. As such, imposing suitable constraints is crucial to restrict the solution space and ensure physically meaningful results.

5.1 Modelling the Imaging System

The goal is to identify a model that describes how the camera observes incident radiation. Experimental results are used to complement and validate this model. A schematic of the experimental setup is presented in Figure 5.1, where radiant flux emitted by a blackbody source, denoted as Φ_{BB}, is transmitted through a sample (in this case a gas cell), Φ_t. Additionally, radiation originating from the environment, Φ_{env}, is reflected off the sample, Φ_r. The SFPI subsequently filters these components of radiation. The camera itself also emits radiation, a portion of which is reflected off the SFPI and back onto the detector, while the remainder is transmitted and lost to the environment. The radiation incident on the detector is the combined transmitted and reflected light in the direction from the SFPI to the detector and is denoted as Φ_{in}. The distance between the camera and the black body emitter is approximately 60 cm.

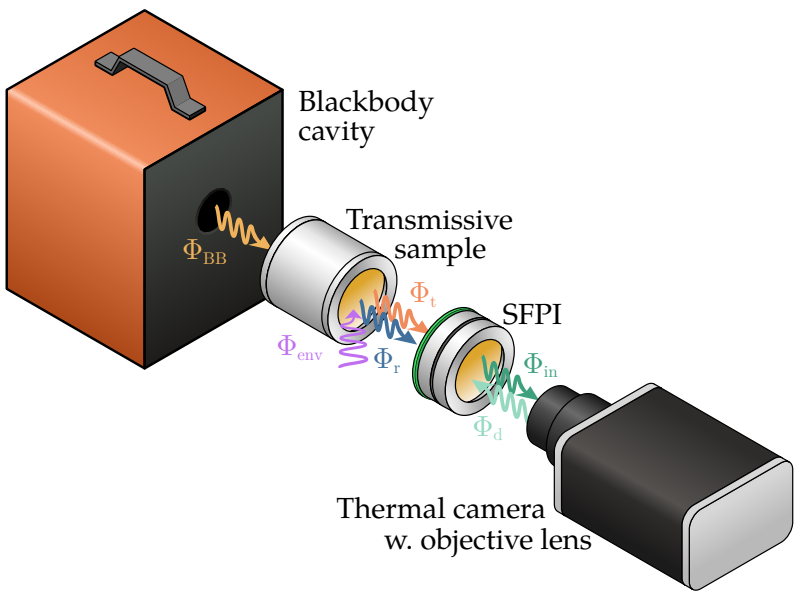

Figure 5.1: Blackbody radiation, Φ_{BB}, is transmitted through the sample Φ_t. Environmental radiation, Φ_{env}, is reflected off the sample, Φ_r. Part of the radiation emitted by the camera itself, Φ_d, reflects off the SFPI, while the rest is absorbed or transmitted to the environment. The combined radiation in the direction of the detector is denoted Φ_{in}. (Not drawn to scale)

The radiation entering the camera is mathematically expressed as:

$$\begin{aligned}\Phi_{\mathrm{in},\lambda} =&[\Phi_{\mathrm{BB}}(\lambda, T_{\mathrm{BB}})\mathcal{T}_{\mathrm{s}}(\lambda) + \Phi_{\mathrm{env}}(\lambda, T_{\mathrm{env}})\mathcal{R}_{\mathrm{s}}(\lambda)]\mathcal{T}_{\mathrm{SFPI}}(\lambda, \ell) \\ &+ \Phi_{\mathrm{d}}(\lambda, T_{\mathrm{d}})\mathcal{R}_{\mathrm{SFPI}}(\lambda, \ell),\end{aligned} \tag{5.1}$$

where $\mathcal{T}_{\mathrm{s}}$ and $\mathcal{R}_{\mathrm{s}}$ denote the transmittance and reflectance of the sample, while $\mathcal{T}_{\mathrm{SFPI}}$ and $\mathcal{R}_{\mathrm{SFPI}}$ represent the transmittance and reflectance of the SFPI, respectively. The term Φ_{d} corresponds to the radiant flux emitted by the detector itself and $\Phi_{\mathrm{env}}(\lambda, T_{\mathrm{env}})\mathcal{R}_{\mathrm{s}}(\lambda) = \Phi_{\mathrm{r}}$ is the radiation reflected off the sample. The temperatures of the emitters are indicated by T with corresponding subscripts. For simplicity, the fluxes of all emitters are approximated as blackbody sources.

The detector signal is not directly proportional to the incident flux but rather to the flux difference between the incident and outgoing fluxes, as described in Eq. (3.6):

$$\psi \propto (\Phi_{\mathrm{in}} - \Phi_{\mathrm{d}}), \qquad \Phi \propto \int_{\lambda_1}^{\lambda_2} M_\lambda s(\lambda)\, d\lambda \tag{5.2}$$

Here, ψ represents the measured signal strength, which is encoded as a 16-bit value for raw data but can take on any value after data preprocessing (However, it is still limited by the 14-bit depth of the recorded data). The flux Φ is evaluated only within the spectral range where the detector is sensitive ($\lambda_1 = 8$ µm to $\lambda_2 = 15$ µm). The spectral response of the detector is denoted by $s(\lambda)$. This response is largely unknown and is inferred from measurements performed using the setup illustrated in Figure 5.1 and described in section 5.2.

5.2 Estimation of Detector's Spectral Response

The transmittance matrix computed using GMM does not incorporate the microbolometer detector's spectral sensitivity or the imaging system's objective lens. However, this spectral sensitivity is crucial in predicting how incident radiation is converted into a digital signal. By combining Eqs. (5.1) and (5.2) and rewriting in terms of spectral exitance, the signal strength of the setup illustrated in Figure 5.1 can be expressed as:

$$\psi \propto \int_{\lambda_1}^{\lambda_2} \Big\{ \mathcal{T}_{\mathrm{SFPI}}(\lambda, \ell) \left[M_{\mathrm{BB},\lambda}(T_{\mathrm{BB}}) \mathcal{T}_{\mathrm{s}}(\lambda) + M_{\mathrm{env},\lambda}(T_{\mathrm{env}}) \mathcal{R}_{\mathrm{s}}(\lambda) \right] + M_{\mathrm{d},\lambda}(T_{\mathrm{d}}) \mathcal{R}_{\mathrm{SFPI}}(\lambda, \ell) - M_{\mathrm{d},\lambda}(T_{\mathrm{d}}) \Big\} s(\lambda)\, d\lambda \tag{5.3}$$

This expression can be reformulated as an $\mathbf{A}\mathbf{x} = \mathbf{b}$ problem to determine the detector sensitivity. The components are defined as follows:

$$\mathbf{A} = \boldsymbol{\mathcal{T}}_{\mathbf{SFPI}} \circ_{\mathrm{r}} \left(\mathbf{m}_{\mathbf{BB},\boldsymbol{\lambda}} \circ \boldsymbol{t}_{\mathbf{s}} + \mathbf{m}_{\mathbf{env},\boldsymbol{\lambda}} \circ \boldsymbol{r}_{\mathbf{s}} \right)^{\top} + \boldsymbol{\mathcal{R}}_{\mathbf{SFPI}} \circ_{\mathrm{r}} \mathbf{m}_{\mathbf{d},\boldsymbol{\lambda}}{}^{\top} - \mathbf{m}_{\mathbf{d},\boldsymbol{\lambda}}{}^{\top}$$

$$\mathbf{x} = \mathbf{s}$$

$$\mathbf{b} = \boldsymbol{\psi}$$

Here, bold capital letters denote matrices, and bold lowercase letters denote vectors. $\circ$ represents the Hadamard product (element-wise product), while $\circ_{\mathrm{r}}$ denotes the row-wise Hadamard product, meaning that $\mathbf{A} \circ_{\mathrm{r}} \mathbf{x}^{\top}$ produces a matrix where each row of $\mathbf{A}$ is multiplied elementwise with $\mathbf{x}^{\top}$. $\boldsymbol{\mathcal{T}}_{\mathbf{SFPI}}$ and $\boldsymbol{\mathcal{R}}_{\mathbf{SFPI}}$ are matrices describing the transmittance and reflectance of the SFPI, respectively, as calculated using GMM. Each row corresponds to the transmittance or reflectance spectrum at a single cavity length, as shown in Figure 4.16. From this point onward, these matrices are reordered such that the first (top) row corresponds to the shortest cavity length. $\mathbf{m}_{\mathbf{env},\boldsymbol{\lambda}}$ is the spectral exitance of the environment, and for all these experiments, this has been set to 22 °C. Since $\mathbf{m}_{\mathbf{d},\boldsymbol{\lambda}}$ is a vector, $\left(\boldsymbol{\mathcal{R}}_{\mathbf{SFPI}} \circ_{\mathrm{r}} \mathbf{m}_{\mathbf{d},\boldsymbol{\lambda}}{}^{\top}\right) - \mathbf{m}_{\mathbf{d},\boldsymbol{\lambda}}{}^{\top}$ indicates element-wise subtraction in the rows.

The vectors $\mathbf{m}$ represent the spectral exitances of the different emitters in the scene, with subscripts BB, env, and d referring to the blackbody

emitter, the environment, and the detector, respectively. $\boldsymbol{t}_s$ and $\boldsymbol{r}_s$ are the FTIR transmittance and reflectance spectra of the sample, respectively. The length of the vectors is dictated by the length/resolution of the FTIR measurements used for the transmittance and reflectance spectra of the samples. For the remainder of this chapter, if nothing else is stated, the spectral unit is wavenumbers to match the FTIR measurements. Even though the spectral resolution of the FTIR measurements is $\leq$1 cm^{-1}, the interferograms have been interpolated to a resolution of 2.9 cm^{-1}, yielding 256 sample points from 1300 cm^{-1} to 600 cm^{-1}. This span is greater than expected of the detector, but this is done to ensure that no signal that could be sensed by the detector is accidentally excluded. The vector $\mathbf{s}$ represents the unknown detector sensitivity, while ψ corresponds to the interferogram measured by the camera. The interferograms are obtained as 40×40-pixel averages of hyperspectral data cubes. Figure 5.2 presents averaged interferograms extracted from a hyperspectral data cube of a gas cell containing ammonia vapor (of unknown concentration) placed in front of a 150°C blackbody emitter

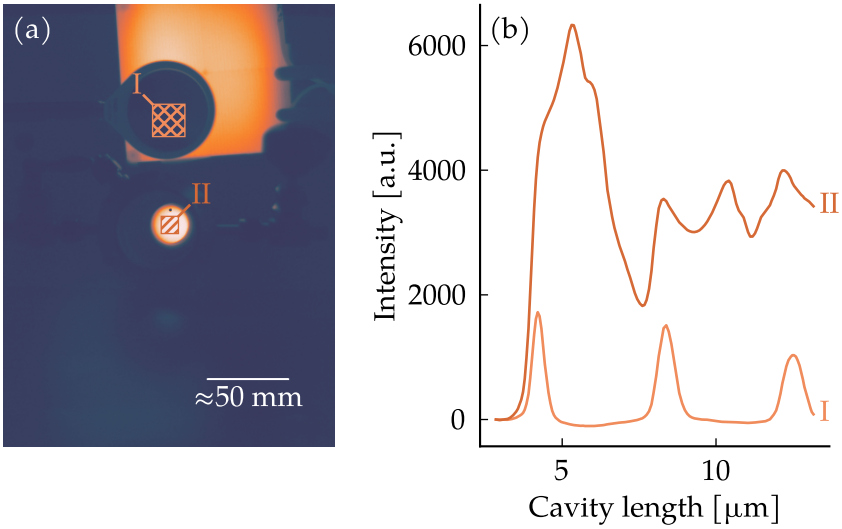

Figure 5.2: (a) Image from a hyperspectral data cube of a gas cell containing ammonia vapor placed in front of a 150 °C blackbody emitter. Two hatched regions are indicated. I: a 75×75-pixel area corresponding to the 8.226 μm bandpass filter placed in front of an 80 °C hot plate, used for spectral alignment; and II: a 40×40-pixel area representing the ammonia vapor. (b) Averaged interferograms corresponding to the hatched regions in (a).

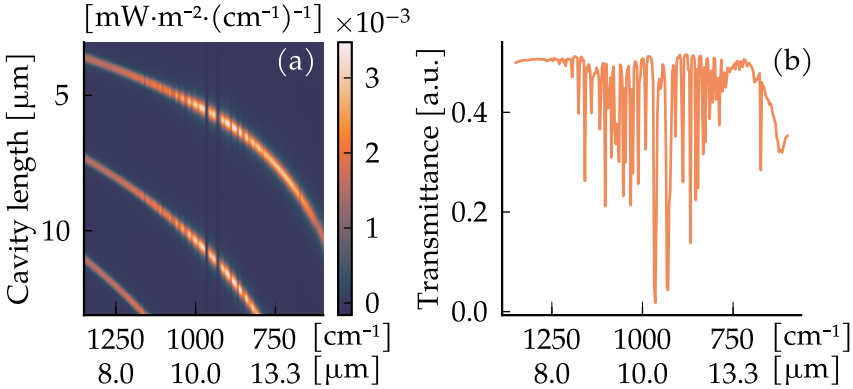

Figure 5.3: (a) $\mathbf{A}_{NH3}$-matrix describing the spectral exitance of the ammonia vapor-containing gas cell presented in Figure 5.2. (b) FTIR measurement of the gas cell containing ammonia.

(LS series 1050-100, Electro Optical Industries Inc., FR). Two hatched regions are indicated: I: a 75×75-pixel area corresponding to an 8.226 µm bandpass filter (Andover Corporation, US) placed in front of an 80 °C hot plate; and II: a 40×40-pixel area covering a section of the gas cell and corresponds to ψ.

The approximate scale bar arises from the varying distances of the subjects in the scene from the camera. The averaged interferograms corresponding to the hatched regions are shown in Figure 5.2b.

$\mathbf{A}$ is presented in Figure 5.3a for the gas cell containing ammonia vapors along with the FTIR transmittance spectrum shown in Figure 5.3b. Transmittance FTIR is performed using a Perkin Elmer Spectrum 65 FTIR spectrometer with a resolution of 0.25 cm^{-1}, but the spectra have been interpolated to a resolution of 2.9 cm^{-1} to reduce computation times. Reflectance FTIR measurements have been performed on a Shimadzu IRAFFINITY-1S FTIR spectrometer with a specular reflectance attachment. After interpolation, all FTIR measurements present the same spectral resolution. Some entries in $\mathbf{A}$ are negative. This occurs when the exitance of the detector is greater than that of the incident radiation. The net radiant flux of the detector thus becomes negative.

To achieve a more robust solution to the $\mathbf{Ax} = \mathbf{b}$ problem, additional data is required. A comprehensive list of all transmission samples is

presented in Table 5.1, along with each measurement's corresponding blackbody temperature settings. The samples include a mix of gas (G), vapor (V), and solid (S) materials.

A gas cell (diameter: 50.8 mm, length: 50 mm) fitted with ZnSe substrates was used to contain the samples for the gas and vapor samples. The concentrations of the gaseous samples are unknown. FTIR measurements were performed immediately after imaging with the LWIR imager. The sample labeled *Air after NO exposure* refers to the same gas cell containing air but after exposure to NO gas, which altered the ZnSe window and consequently affected its transmission spectrum. The sample labeled *II-VI Mirror* corresponds to the mirror used in the SFPI, while the *Sønderborg Mirror* represents a custom-made dielectric mirror.

All measurements were formulated as $\mathbf{Ax} = \mathbf{b}$ by concatenating the matrices and vectors, as shown in Eq. (5.4). Each submatrix has dimensions of 150×256 ($M\text{rows} \times N\text{columns}$), and a total of $J = 83$ matrices are concatenated, leading to a total matrix size of 12450×256. All interferograms in the data set have been spectrally aligned across data cubes using the 8.226 µm bandpass filter and subsequent interpolation. Additionally, all interferograms have been baseline corrected to have their first channel starting at zero, as described in Eq. (2.70).

$$\begin{bmatrix} \mathbf{A_{acetone}} \\ \mathbf{A_{NH3}} \\ \vdots \\ \mathbf{A_{toluene}} \end{bmatrix} \mathbf{x} = \begin{bmatrix} \mathbf{b_{acetone}} \\ \mathbf{b_{NH3}} \\ \vdots \\ \mathbf{b_{toluene}} \end{bmatrix} \quad \Rightarrow \quad \mathbf{A_{cmb}x} = \mathbf{b_{cmb}} \tag{5.4}$$

Table 5.1: List of transmission samples and temperatures used in the setup presented in Figure 5.1. (G), (V), and (S) refer to gas, vapor and solid respectively.

Material	T_{BB} [°C]
Acetone (V)	150
Air (G)	150
Air after NO exposure (G)	150, 300
Ammonia, NH3 (V)	150
Benzene (V)	150
Blackbody (no sample)	50, 60, 70, 80, 90, 100, 110, 120, 130, 140, 150, 160, 170, 180, 190, 200
BP 7769 nm (S)	100, 110, 120, 130, 150, 225, 300
BP 10040 nm (S)	100, 150, 225, 300
BP 10225 nm (S)	100, 110, 120, 130, 150, 225, 300
BP 11322 nm (S)	100, 110, 120, 130, 150, 225, 300
Butan & Propan (G)	150
Butane (G)	150
Chloroform (V)	150
CO_2 (G)	150
Dichloromethane (V)	150
Ethanol (V)	150
Ethylene (G)	150
II-VI Mirror (S)	150, 300
Isopropanol (V)	150
Kapton tape (S)	150, 300
LDPE (S)	150
Methanol (V)	150
NO (G)	150
Packing Tape (S)	150
Parafilm (S)	100, 110, 150, 225, 300
Plastic Foil (unknown) (S)	150
PMMA (S)	150, 225, 300
Polystyrene (S)	150
PP 30um (S)	150
PP 50um (S)	100, 110, 150, 225
Sønderborg Mirror (S)	150, 225, 300
Toluene (V)	150
Tetrafluorethane (G)	150

5.2.1 Least Squares Solution

As $\mathbf{A_{cmb}}$ is overdetermined, an exact solution is unlikely to exist. Instead, the problem is reformulated as a least squares minimization problem, aiming to minimize the squared residual error, as shown in Eq. (5.5).

$$\arg\min_{\mathbf{x}} \frac{1}{2}\|\mathbf{b_{cmb}} - \mathbf{A_{cmb}}\mathbf{x}\|_2^2 \tag{5.5}$$

The term $\frac{1}{2}\|\mathbf{b_{cmb}} - \mathbf{A_{cmb}}\mathbf{x}\|_2^2$, is often referred to as the cost function and denoted $\mathcal{J}$. The prefactor $\frac{1}{2}$ cancels in differentiation. Expressing this function via the trace operator facilitates solving for $\mathbf{x}$. The following trace properties from [39] are particularly relevant:

Properties of the Trace

$$\|\mathbf{A}\|_F^2 = \mathrm{Tr}\left[\mathbf{A}^\top\mathbf{A}\right] \tag{5.6}$$

$$\mathrm{Tr}\left[\mathbf{A}+\mathbf{B}\right] = \mathrm{Tr}\left[\mathbf{A}\right] + \mathrm{Tr}\left[\mathbf{B}\right] \tag{5.7}$$

$$\mathrm{Tr}\left[\mathbf{ABC}\right] = \mathrm{Tr}\left[\mathbf{CAB}\right] = \mathrm{Tr}\left[\mathbf{BCA}\right] \tag{5.8}$$

$$\mathrm{Tr}\left[\mathbf{A}^\top\right] = \mathrm{Tr}\left[\mathbf{A}\right] \tag{5.9}$$

To solve the minimization problem, the cost function is differentiated with respect to $\mathbf{x}$ and set equal to zero. The resulting expression is then solved for $\mathbf{x}$. Therefore, the following trace derivatives will be handy going forward [39].

Trace Derivatives

$$\nabla_{\mathbf{X}}\mathrm{Tr}\left[\mathbf{AX}\right] = \mathbf{A}^\top \tag{5.10}$$

$$\nabla_{\mathbf{X}}\mathrm{Tr}\left[\mathbf{X}^\top\mathbf{A}\right] = \mathbf{A} \tag{5.11}$$

$$\nabla_{\mathbf{X}}\mathrm{Tr}\left[\mathbf{X}^\top\mathbf{AX}\right] = \left(\mathbf{A}+\mathbf{A}^\top\right)\mathbf{X} \tag{5.12}$$

$$\nabla_{\mathbf{X}}\mathrm{Tr}\left[\mathbf{XAX}^\top\right] = \mathbf{X}\left(\mathbf{A}^\top+\mathbf{A}\right) \tag{5.13}$$

The derivation of the least squares solution thus becomes

$$\frac{1}{2}\|\mathbf{b}_{\mathbf{cmb}} - \mathbf{A}_{\mathbf{cmb}}\mathbf{x}\|_2^2 = \frac{1}{2}\mathrm{Tr}\left[(\mathbf{b}_{\mathbf{cmb}} - \mathbf{A}_{\mathbf{cmb}}\mathbf{x})^\top (\mathbf{b}_{\mathbf{cmb}} - \mathbf{A}_{\mathbf{cmb}}\mathbf{x})\right]$$

$$= \frac{1}{2}\mathrm{Tr}\left[\mathbf{b}_{\mathbf{cmb}}^\top \mathbf{b}_{\mathbf{cmb}} - \mathbf{b}_{\mathbf{cmb}}^\top \mathbf{A}_{\mathbf{cmb}}\mathbf{x} - \mathbf{x}^\top \mathbf{A}_{\mathbf{cmb}}^\top \mathbf{b}_{\mathbf{cmb}} + \mathbf{x}^\top \mathbf{A}_{\mathbf{cmb}}^\top \mathbf{A}_{\mathbf{cmb}}\mathbf{x}\right]$$

$$\overset{\nabla_{\mathbf{x}}}{\Longrightarrow} \mathbf{A}_{\mathbf{cmb}}^\top \mathbf{A}_{\mathbf{cmb}}\mathbf{x} - \mathbf{A}_{\mathbf{cmb}}^\top \mathbf{b}_{\mathbf{cmb}} = \mathbf{0}$$

$$\Rightarrow \mathbf{x} = \left(\mathbf{A}_{\mathbf{cmb}}^\top \mathbf{A}_{\mathbf{cmb}}\right)^{-1} \mathbf{A}_{\mathbf{cmb}}^\top \mathbf{b}_{\mathbf{cmb}}$$

As described, solving the least squares problem directly yields the response shown in Figure 5.4a. However, the resulting solution exhibits rapid non-physical oscillations. The mean squared error (MSE) is a common error metric in optimization and is defined as

$$\mathrm{MSE}(\mathbf{y}, \hat{\mathbf{y}}) = \frac{1}{n}\sum_{i=1}^{n}(y_i - \hat{y}_i)^2 \tag{5.14}$$

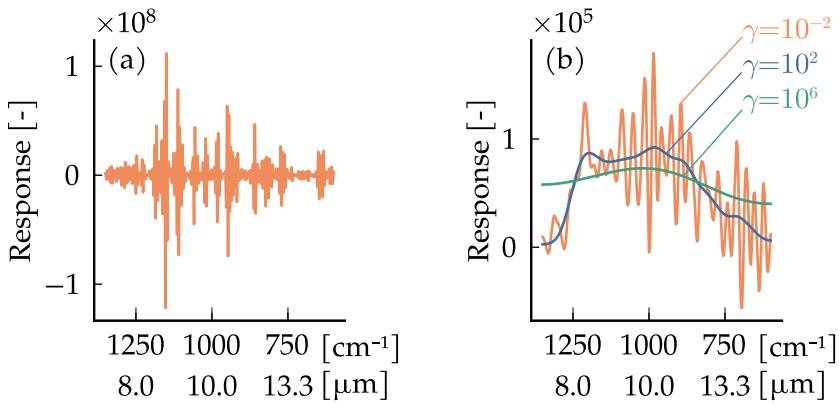

Figure 5.4: (a) Detector response obtained using the least squares solution to Eq. (5.5). The absence of regularization results in an unstable solution with an $\mathrm{MSE} = 5.6 \times 10^5$. (b) Solutions to the regularized optimization problem in Eq. (5.15) for varying levels of the regularization parameter γ. Higher values of γ yield more stable solutions but increase the residual error. From the lowest to the highest γ, the MSE are 1.1×10^6, 1.2×10^6, and 2.5×10^6, respectively.

In Eq. (5.14), $\mathbf{y}$ and $\hat{\mathbf{y}}$ are two vectors of length n. While the least squares approach minimizes the MSE (In this case $\mathrm{MSE} = 5.6 \times 10^5$), such a solution is not useful due to rapid oscillations (Figure 5.4a). For context, the average maximum value of the interferograms is 8400 with an average span of 8442. To address the unstable solution, a regularization term is introduced, as defined in Eq. (5.15):

$$\arg\min_{\mathbf{x}} \left(\frac{1}{2} \|\mathbf{b_{cmb}} - \mathbf{A_{cmb}}\mathbf{x}\|_2^2 + \frac{1}{2}\gamma \|\boldsymbol{\mathcal{M}}\mathbf{x}\|_2^2 \right) \tag{5.15}$$

Here, $\boldsymbol{\mathcal{M}}$ is an $N \times N$ matrix defined in Eq. (5.16), designed to suppress oscillations in the solution. For instance, the second row of $\boldsymbol{\mathcal{M}}$ (Eq. (5.16)) imposes the condition that $(2x_2 - x_1 - x_3)$ should be driven closer to zero. $\boldsymbol{\mathcal{M}}$ is also known as the matrix representation of the first-order derivative operator [40], and this form of regularization scheme is known as Tikhonov regularization [41]. The strength of this regularization is controlled by the regularization parameter γ.

$$\boldsymbol{\mathcal{M}} = \begin{bmatrix} 1 & -1 & 0 & 0 & 0 & \dots \\ -1 & 2 & -1 & 0 & 0 & \dots \\ 0 & -1 & 2 & -1 & 0 & \dots \\ \vdots & \ddots & \ddots & \ddots & \ddots & \ddots \\ \dots & 0 & 0 & -1 & 2 & -1 \\ \dots & 0 & 0 & 0 & -1 & 1 \end{bmatrix} \tag{5.16}$$

As with the unregularized problem, it is possible to compute the solution to Eq. (5.15) explicitly:

$$\mathbf{x} = \left(\mathbf{A}_{\mathbf{cmb}}^\top \mathbf{A_{cmb}} + \gamma \boldsymbol{\mathcal{M}}^\top \boldsymbol{\mathcal{M}} \right)^{-1} \mathbf{A}_{\mathbf{cmb}}^\top \mathbf{b_{cmb}} \tag{5.17}$$

This derivation utilizes that $\gamma \frac{1}{2} \|\boldsymbol{\mathcal{M}}\mathbf{x}\|_2^2 = \gamma \frac{1}{2} \mathrm{Tr}\left[\mathbf{x}^\top \boldsymbol{\mathcal{M}}^\top \boldsymbol{\mathcal{M}}\mathbf{x}\right]$, which, when differentiated with respect to $\mathbf{x}$, yields $\nabla_{\mathbf{x}} = \gamma \boldsymbol{\mathcal{M}}^\top \boldsymbol{\mathcal{M}}\mathbf{x}$. The matrix inverse in Eq. (5.17) is, in fact, the Moore-Penrose pseudo inverse which can handle both rectangular matrices and is more numerically stable for ill-conditioned matrices [42].

The solutions for $\gamma = [10^{-2}, 10^2, 10^6]$ are shown in Figure 5.4b. As γ increases, the solutions become smoother, but this comes at the expense

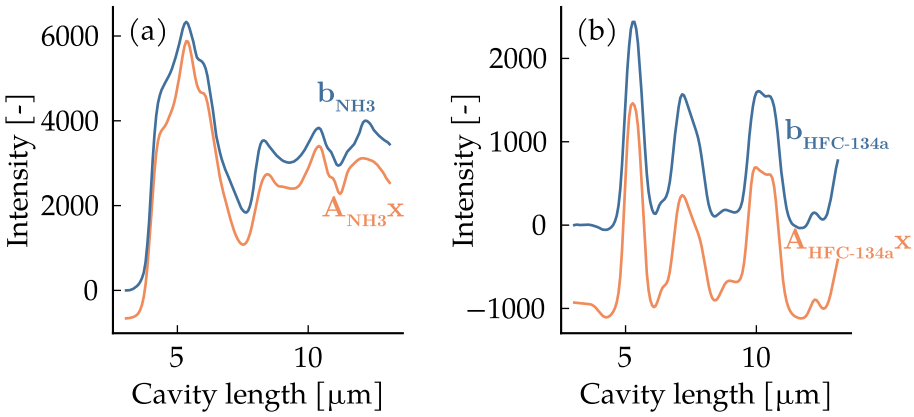

Figure 5.5: Reconstructed interferograms of (a) ammonia (NH3) with an MSE of 5.0×10^5 and (b) tetrafluoroethane (HFC-134a) with an MSE of 1.1×10^6.

of higher residual squared errors. Specifically, the MSEs for increasing γ are 1.1×10^6, 1.2×10^6, and 2.5×10^6, respectively.

The interferograms can be reconstructed using $\mathbf{A}$ and the response calculated with $\gamma = 10^2$. Two examples are provided in Figure 5.5, illustrating the reconstruction of the ammonia interferogram ($\mathrm{MSE} = 5.0 \times 10^5$) and the tetrafluoroethane interferogram ($\mathrm{MSE} = 1.1 \times 10^6$). While the overall shapes of the reconstructed interferograms align well with the original data, the reconstructions exhibit an offset. This offset should be accounted for in the estimate of the detector response. However, this offset is slightly different for each interferogram due to changes in detector temperature. The offset, therefore, becomes unique to each measurement and thus cannot be solved explicitly like done so far. The following section will present a gradient descent method for solving the problem and describe how the measurement-specific offset is implemented.

5.2.2 Solution Using Gradient Descent

Instead of solving the optimization problem explicitly, it is solved through a sequence of iterative steps that follow the gradient of the cost function. All variables being optimized are represented by a single parameter vector, $\boldsymbol{\theta}$. While in this specific context, $\boldsymbol{\theta}$ represents $\mathbf{x}$, it can encompass multiple variables simultaneously. The iterative update process follows

the scheme:

$$\boldsymbol{\theta}^{(k+1)} = \boldsymbol{\theta}^{(k)} - \mu \nabla \mathcal{J}(\boldsymbol{\theta}^{(k)}), \tag{5.18}$$

where μ denotes the step size (also commonly referred to as the learning rate), and $\nabla \mathcal{J}(\boldsymbol{\theta}^{(k)})$ represents the gradient of the cost function. The superscript (k) indexes the iteration number. Convergence of this scheme is guaranteed if the step size satisfies the condition $0 < \mu \leq 2/\mathscr{L}$, where $\mathscr{L}$ is the Lipschitz constant satisfying the Lipschitz condition [43]:

$$\|\nabla \mathcal{J}(\mathbf{u}) - \nabla \mathcal{J}(\mathbf{v})\| \leq \mathscr{L} \|\mathbf{u} - \mathbf{v}\|, \tag{5.19}$$

where $\mathbf{u}$ and $\mathbf{v}$ are vectors. The Lipschitz condition ensures that the gradient of the cost function $\mathcal{J}$ does not change too abruptly, resulting in instability. Rewriting Eq. (5.19), the Lipschitz constant can be bounded as:

$$\mathscr{L} \geq \frac{\|\nabla \mathcal{J}(\mathbf{u}) - \nabla \mathcal{J}(\mathbf{v})\|}{\|\mathbf{u} - \mathbf{v}\|} \tag{5.20}$$

This formulation resembles the mean value theorem. Consequently, the largest step size in the update scheme Eq. (5.18) is related by:

$$2/\mu = \|\nabla^2 \mathcal{J}(\boldsymbol{\theta})\| \leq \mathscr{L} \tag{5.21}$$

For the specific optimization problem presented in Eq. (5.15), the update step becomes:

$$\mathbf{x}^{(k+1)} \leftarrow \mathbf{x}^{(k)} + \mu \left(\mathbf{A}_{\mathbf{cmb}}^{\top} \mathbf{A}_{\mathbf{cmb}} \mathbf{x}^{(k)} + \gamma \boldsymbol{\mathcal{M}}^{\top} \boldsymbol{\mathcal{M}} \mathbf{x}^{(k)} \right) \tag{5.22}$$

$$\mu = \frac{2}{\|\mathbf{A}_{\mathbf{cmb}}^{\top} \mathbf{A}_{\mathbf{cmb}}\|_F + \gamma \|\boldsymbol{\mathcal{M}}^{\top} \boldsymbol{\mathcal{M}}\|_F}$$

The pseudo-code for the accelerated gradient descent (AGD) scheme is provided in Algorithm 1. This approach incorporates extrapolation to enhance convergence speed and is specifically referred to as the heavy ball method [44], as depicted in Figure 5.6. Here, the update step involves extrapolation, as shown in Figure 5.6:

$$\beta^{(k)} \left(\mathbf{x}^{(k+2)} - \mathbf{x}^{(k+1)} \right) \tag{5.23}$$

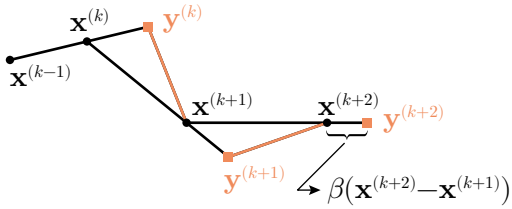

Figure 5.6: Illustration of gradient descent accelerated using the heavy ball method.

This accelerates convergence since the direction $\left(\mathbf{x}^{(k+2)} - \mathbf{x}^{(k+1)}\right)$ lies between the directions $\left(\mathbf{x}^{(k+1)} - \mathbf{y}^{(k)}\right)$ and $\left(\mathbf{x}^{(k+2)} - \mathbf{y}^{(k+1)}\right)$ [45]. The update for $\mathbf{x}$ involves an intermediate update for $\mathbf{y}$, as stated in Eq. (5.24):

$$\mathbf{x}^{(k+1)} = \text{update}\left(\mathbf{y}^{(k)}\right) \tag{5.24}$$

$$\text{update}\left(\mathbf{y}^{(k)}\right) = \mathbf{x}^{(k)} + \beta^{(k)}\left(\mathbf{x}^{(k)} - \mathbf{x}^{(k-1)}\right) \tag{5.25}$$

The extrapolation length, also referred to as momentum, is defined in Eq. (5.26) [46].

$$\beta^{(k)} = \frac{k-1}{k+2} \tag{5.26}$$

Additionally, the AGD scheme incorporates a non-negativity constraint (line 6 in Algorithm 1). This is achieved by projecting the solution onto the positive plane, expressed as:

$$\text{proj}_{+}\left[\mathbf{x}\right] = \max\left(\mathbf{0}, \mathbf{x}\right), \tag{5.27}$$

where negative entries in $\mathbf{x}$ are replaced with zeros.

Compensating Interferogram Offset

Interferograms recorded with the HSC are affected by an offset that depends on various detector parameters, such as temperature, gain, and skimming voltage (GSK voltage). The skimming voltage adjusts the detector output to remain within the dynamic range, ensuring that objects in the scene are not overexposed. This unknown offset is calculated

Algorithm 1 Accelerated Gradient Descent Algorithm

1: Initialize $\mathbf{x}^{(\mathbf{0})}$ with random numbers
2: $\mathbf{y}^{(\mathbf{0})} \leftarrow \mathbf{x}^{(\mathbf{0})}$
3: $\mu \leftarrow \frac{2}{\|\mathbf{A}_{\mathbf{cmb}}^\top \mathbf{A}_{\mathbf{cmb}}\|_F + \gamma \|\boldsymbol{\mathcal{M}}^\top \boldsymbol{\mathcal{M}}\|_F}$
4: **for** $k = 1, 2, \ldots, k_{\max}$ **do**
5: $\quad \nabla_{\mathbf{y}} f\left(\mathbf{y}^{(k-1)}\right) \leftarrow \left(\mathbf{A}_{\text{cmb}}^\top \mathbf{A}_{\text{cmb}} \mathbf{y}^{(k-1)} + \gamma \boldsymbol{\mathcal{M}}^\top \boldsymbol{\mathcal{M}} \mathbf{y}^{(k-1)}\right)$
6: $\quad \mathbf{x}^{(k)} \leftarrow \text{proj}_+ \left[\mathbf{y}^{(k-1)} - \mu \nabla_{\mathbf{y}} f\left(\mathbf{y}^{(k-1)}\right)\right]$
7: $\quad \mathbf{y}^{(k)} \leftarrow \mathbf{x}^{(k)} + \beta^{(k)} \left(\mathbf{x}^{(k)} - \mathbf{x}^{(k-1)}\right)$
8: **end for**
9: **return** $\mathbf{x}^{(k_{\max})}$

based on the following cost function:

$$\arg\min_{\zeta} \|\mathbf{b} - \mathbf{A}\mathbf{x} - \zeta \mathbf{1}\|_2^2 = \arg\min_{\zeta} \|\mathbf{c} - \zeta \mathbf{1}\|_2^2 \tag{5.28}$$

$$\mathbf{c} = \mathbf{b} - \mathbf{A}\mathbf{x}$$

where ζ is a constant scalar offset, and $\mathbf{1}$ is a vector of ones with the same dimension as $\mathbf{b}$ (and thus also as $\mathbf{c}$). Since the offset is unique for each interferogram, it is no longer possible to work on the combined matrix $\mathbf{A}_{\mathbf{cmb}}$. Consequently, the calculation of ζ cannot be incorporated into the AGD scheme outlined in Algorithm 1. Instead, the two cost functions (Eqs. (5.15) and (5.28)) are solved sequentially. Specifically, Eq. (5.15) is addressed using the AGD scheme presented in Algorithm 1, while the solution for ζ requires expanding Eq. (5.28):

$$\begin{aligned} \|\mathbf{c} - \zeta \mathbf{1}\|_2^2 &= \text{Tr}\left(\mathbf{c}^\top \mathbf{c} - \zeta \mathbf{c}^\top \mathbf{1} - \zeta \mathbf{1}^\top \mathbf{c} + \zeta^2 \mathbf{1}^\top \mathbf{1}\right) \\ &= \|\mathbf{c}\|_2^2 - 2\zeta \langle \mathbf{c} | \mathbf{1} \rangle + \zeta^2 \|\mathbf{1}\|_2^2, \end{aligned} \tag{5.29}$$

Here, it is utilized that the inner product is defined as $\langle \mathbf{A} | \mathbf{B} \rangle = \text{Tr}(\mathbf{A}^\top \mathbf{B})$, and the trace operator is invariant under transposition (Eq. (5.9)).

This formulation reveals that the objective function is a quadratic function of ζ, which can be rewritten as:

$$\|\mathbf{c}\|_2^2 - 2\zeta \langle \mathbf{c} | \mathbf{1} \rangle + \zeta^2 \|\mathbf{1}\|_2^2 = a_1 + a_2 \zeta + a_3 \zeta^2, \tag{5.30}$$

$$a_1 = \|\mathbf{c}\|_2^2, \quad a_2 = -2\langle \mathbf{c} | \mathbf{1} \rangle, \quad a_3 = \|\mathbf{1}\|_2^2$$

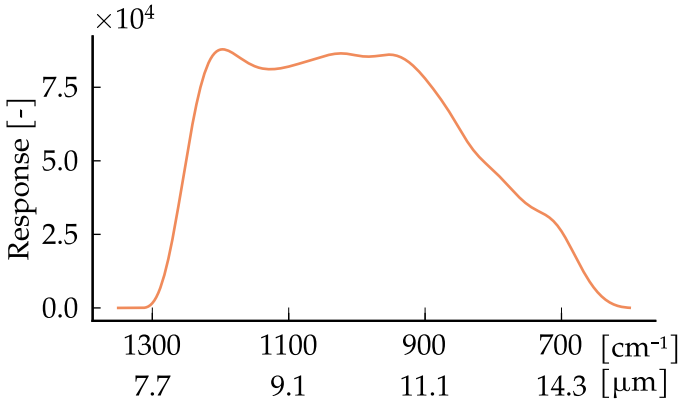

Figure 5.7: Detector response calculated using gradient decent with $k_{\max} = 10000$ AGD iterations, $\gamma = 50$ and $i_{\max} = 20$ offset iterations. This response will be used for all future calculations involving the system matrix.

The term $\langle \mathbf{c}|\mathbf{1}\rangle$ represents the sum of the elements of $\mathbf{c}$, while $\|\mathbf{1}\|_2^2$ corresponds to the number of elements in $\mathbf{c}$. The optimal value of ζ, which minimizes the objective function, is determined by setting the derivative with respect to ζ to zero. This leads to a closed-form expression for ζ:

$$\zeta = \frac{-a_2}{2a_3} = \frac{\langle \mathbf{c}|\mathbf{1}\rangle}{\|\mathbf{1}\|_2^2}, \tag{5.31}$$

which is simply to the mean of $\mathbf{c}$.

In Algorithm 2, each offset is stored in a vector $\boldsymbol{\zeta}$, with J elements (the number of individual interferograms in $\mathbf{b_{cmb}}$). $\mathbf{b}_j$ refers to the jth interferogram in $\mathbf{b_{cmb}}$ and ζ_j to the corresponding offset. The initial guess for $\boldsymbol{\zeta}$ is the minimum value of each of the interferograms. The algorithm does not converge to a correct solution if the initial guess deviates significantly from its true value. Subsequently, a new combined interferogram vector $\mathbf{b_{offset}}$, is constructed by subtracting the offsets from each of the interferograms in $\mathbf{b_{cmb}}$. The detector response is then calculated using the offset-corrected interferogram vector, using Algorithm 1. New offsets are then calculated based on the newly computed detector response. A new detector response is then calculated based on new offsets, and this cycle continues.

The unnormalized detector response in Figure 5.7 is computed using Algorithm 2 with $i_{\max} = 20$ iterations of Algorithm 2 and $k_{\max} = 10000$

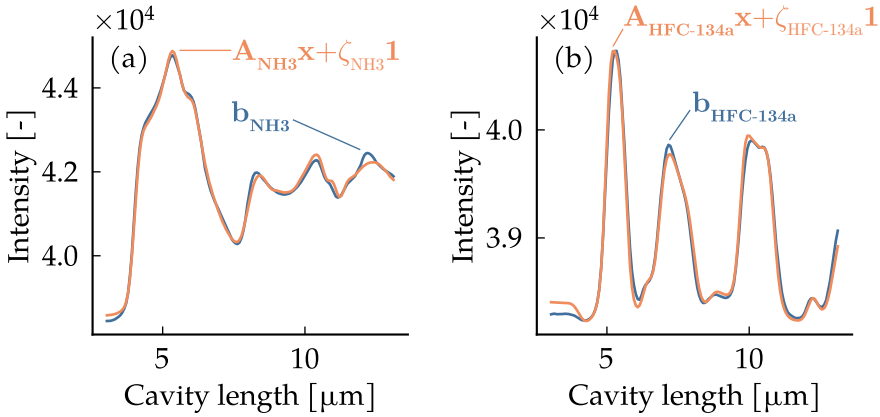

Figure 5.8: Reconstructed interferograms of (a) ammonia (NH_3) with an MSE of 9.3×10^3 and (b) tetrafluoroethane (HFC-134a) with an MSE of 5.1×10^3. This time, an offset is implemented in the reconstruction, as well as the detector response presented in Figure 5.7.

Algorithm 2 Computing detector while compensating for offset, ζ

1: **for** $j = 1, 2, \ldots, J$ **do**
2: $\quad \zeta_j^{(0)} \leftarrow \min(\mathbf{b}_{\mathbf{cmb},j})$
3: **end for**
4: **for** $i = 1, 2, \ldots, i_{\max}$ **do**
5: $\quad$ **for** $j = 1, 2, \ldots, J$ **do**
6: $\quad\quad \mathbf{b}_{\mathbf{offset},j} \leftarrow \mathbf{b}_{\mathbf{cmb},j} - \zeta_j^{(i)}\mathbf{1}$
7: $\quad$ **end for**
8: $\quad$ Solve $\mathbf{x}^{(i)}$ using Algorithm 1 and $\mathbf{b}_{\mathbf{offset}}$ with $k_{\max}$ iterations
9: $\quad$ **for** $j = 1, 2, \ldots, J$ **do**
10: $\quad\quad \zeta_j^{(i)} \leftarrow \frac{\langle \mathbf{b}_{\mathbf{cmb},j} - \mathbf{A}_{\mathbf{cmb},j}\mathbf{x}^{(i)} | \mathbf{1} \rangle}{\|\mathbf{1}\|_2^2}$
11: $\quad$ **end for**
12: **end for**
13: **return** $\mathbf{x}^{(i_{\max})}$

iterations of Algorithm 1, applying a regularization parameter of $\gamma = 50$. This response accounts for both the detector and the optics, exhibiting the expected characteristics of germanium with an antireflective coating [47]. The response exceeds 10% of its maximum between 1285 cm^{-1} (7.8 μm) and 660 cm^{-1} (15.2 μm) and is used in all subsequent calcu-

lations unless otherwise stated. Figure 5.8 presents the same interferograms as Figure 5.5, but reconstructed using the detector response from Figure 5.7 while incorporating the computed offsets. This adjustment reduces the MSE by nearly two orders of magnitude. Reconstructions of all interferograms are available at https://madsnibe.com/HSTI/images/interferogram_reconstructions.pdf.

5.2.3 System Response Matrix

The reconstructions in Figure 5.8 incorporate the incident spectrum into the rows of $\mathbf{A}$, and the interferogram is computed as the dot product between $\mathbf{A}$ and the detector response, $\mathbf{s}$. While this formulation embeds the incident spectrum in $\mathbf{A}$, a more practical approach is to integrate the detector response directly into the matrix formulation. This is illustrated in Figure 5.9, where the SFPI transmission matrix (Figure 4.16b) and detector response (Figure 5.7) are combined to form the *system matrix* $\boldsymbol{\mathcal{A}}$. The interferogram is then estimated as the dot product between $\boldsymbol{\mathcal{A}}$ and the incident spectrum $\boldsymbol{\phi}$, as described in Eq. (5.32), yielding results equivalent to Figure 5.8 but without offset correction.

$$\boldsymbol{\mathcal{A}}\boldsymbol{\phi} = \boldsymbol{\psi} \tag{5.32}$$

$$\boldsymbol{\mathcal{A}} = \boldsymbol{\mathcal{T}}_{\mathbf{SFPI}} \circ_{\mathrm{r}} \mathbf{s} \tag{5.33}$$

The system matrix is essential for most system modeling, which involves relating the incident spectra and the output interferograms.

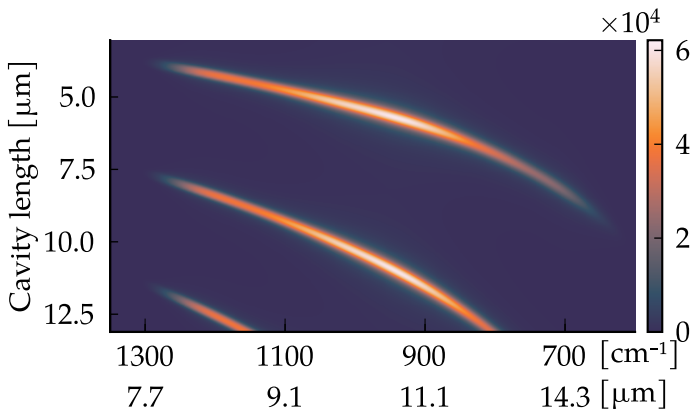

Figure 5.9: System matrix $\boldsymbol{\mathcal{A}}$ combining the detector response (Figure 5.7) and the SFPI transmission matrix (Figure 4.16b).

5.3 Converting Interferogram to Spectrum

Spectral measurements with the hyperspectral LWIR imager are recorded as a function of the cavity length rather than in terms of wavenumbers or wavelengths, as in most traditional spectroscopy methods. Therefore, the interferograms must be converted into frequency spectra to compare the imager's measurements with those of more conventional techniques.

One of the primary challenges in performing this conversion is that multiple transmission orders are simultaneously visible at specific cavity lengths. This means that the signal at particular measurements may originate from entirely different parts of the spectrum, as illustrated by the case of $\ell = 8$ µm in Figure 5.9. Consequently, it is not possible to uniquely associate each cavity length with light from a single frequency.

The following sections will explore various methods for achieving this conversion.

5.3.1 Fourier Transform

The FFT is the fundamental principle behind FTIR spectroscopy, enabling the conversion of recorded interferograms into frequency-dependent spectra. These instruments are typically based on Michelson interferometers, where light is split into two paths using a beam splitter. Each path reflects off a mirror (one fixed and one moveable) before recombining at the splitter. The resulting interference pattern depends on the path length difference between the two arms. The FFT is then applied to convert the interferograms into spectra. The spectral resolution $\Delta\tilde{\nu}$ of an interferometer is related to the maximum optical path difference Δl_{max} achievable, as expressed by Eq. (5.34) [48]:

$$\Delta\tilde{\nu} = \frac{1}{\Delta l_{\text{max}}} \tag{5.34}$$

A similar relation can be derived by analyzing the problem in the context of the FFT, as shown in Eq. (5.35):

$$\Delta\tilde{\nu} = \frac{\tilde{\nu}_{\text{sampling}}}{N} = \frac{N/\Delta l'}{N} = \frac{1}{\Delta l'} \tag{5.35}$$

Here, $\tilde{\nu}_{\text{sampling}}$ is the sampling frequency, $\Delta l'$ is the *change* in optical path difference, and N is the number of samples. Thus, to achieve a

spectral resolution of $1\ \mathrm{cm}^{-1}$, the optical path difference must be 1 cm. In a Michelson interferometer, this corresponds to a mirror movement of 0.5 cm (the change of path length is double that of the mirror movement).

Using the FFT directly on the interferograms from the HSC would yield a spectral resolution of approximately $500\ \mathrm{cm}^{-1}$ ($\Delta l_{\mathrm{max}} \approx 10\ \mu\mathrm{m}$). The mirrors in this setup do not move far enough for the FFT to be a viable method for converting the SFPI interferograms into spectra. Furthermore, the resolution of the SFPI is superior to that predicted by Eq. (5.34) since the optical path difference is enhanced by the finesse $\mathcal{F}$ of the cavity. Consequently, the resolution of the SFPI can be expressed as $\Delta\tilde{\nu}_{\mathrm{SFPI}} \approx 1/(\mathcal{F}\Delta l)$. For a mirror reflectance of $\mathcal{R}_{\mathrm{m}} = 0.85$, the finesse is approximately $\mathcal{F} \approx 19$, resulting in a resolution of $\Delta\tilde{\nu}_{\mathrm{SFPI}} \approx 26\ \mathrm{cm}^{-1}$, which aligns with the prediction in Figure 4.17.

Given these limitations, an alternative method for translating the interferograms into frequency spectra is required. Subsequent sections discuss these methods.

5.3.2 Remapping of Interferograms

One of the simplest methods for translating the data involves excluding regions of the system matrix (Figure 5.9) that exhibit overlapping orders. Figure 5.10a illustrates the peaks at relevant wavenumbers/wavelengths and their corresponding cavity length(s). This is accomplished by identifying the peaks in each row (cavity length) of Figure 5.9 and excluding regions where there is not precisely one peak above 10% of the maximum value. Consequently, the third order is entirely absent since it completely overlaps with the second order. Additionally, the overlap between the first and second orders results in no remapping for cavity lengths between 7.8 µm and 9.1 µm.

Figure 5.10b displays a remapped interferogram of a butane-containing gas cell placed in front of a 150°C black body emitter. The exitance of the black body, scaled by the FTIR transmittance spectrum of the sample, is overlaid in blue. The figure demonstrates good agreement between the remapped interferogram and the exitance spectrum. Furthermore, the second order has a higher spectral resolution, as anticipated. However, the second order only applies to a narrow spectral range compared to the first transmission order due to the overlap between orders.

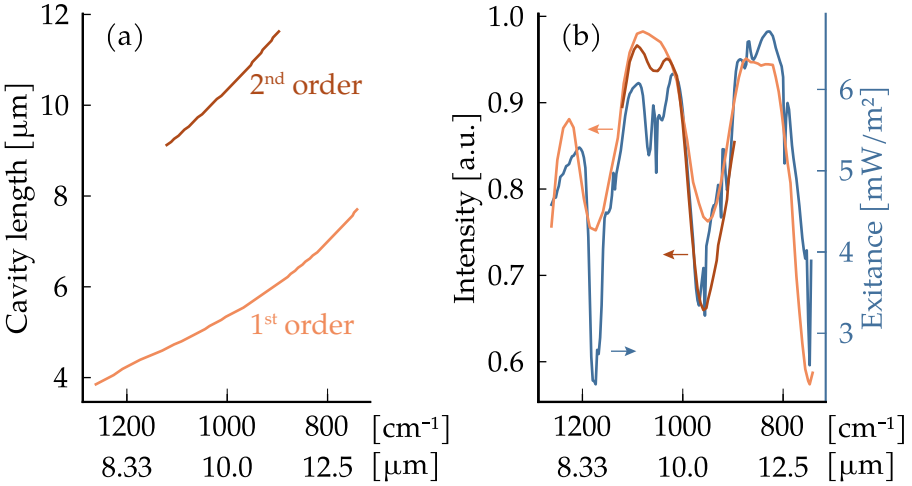

Figure 5.10: (a) Remapped cavity length to wavenumbers/wavelengths. The remapping is done by finding the peak position (measured in wavenumbers) of each row (cavity length) in Figure 5.9. Rows with multiple peaks above 10 % of the maximum value are excluded. (b) Remapped interferogram of butane based on (a). The transmission of the black body exitance spectrum is indicated in green.

The interferograms are normalized between 0 and 1 before remapping. Firstly, the offset is removed, setting the minimum value to 0. Secondly, each point in the interferogram is scaled by the sum of the corresponding row in the system matrix, as defined by Eq. (5.36). Finally, the scaled interferogram is normalized to a maximum of 1.

$$\boldsymbol{\psi}_{\text{scaled}} = \boldsymbol{\psi} \oslash (\boldsymbol{\mathcal{A}}\mathbf{1}) \tag{5.36}$$

This scaling compensates for the spectral shape introduced by the SFPI. However, the compensation is not perfect, and its limitations become particularly apparent at the leading edge of the interferogram, where the first transmission order is introduced. In this region, the transmission values are small relative to the rest of the system matrix, making the scaling more sensitive to numerical instability (i.e., division by small values). If the signal is smooth, the residual noise introduced by this scaling can also be observed (Figure 5.11).

As the remapping process does not scale the interferograms to align with the exitance of the input spectrum, the use of an error metric such as the MSE is not appropriate or meaningful in this context. Instead, the

Pearson correlation coefficient, ρ_{corr}, measures the correlation between two signals. This scale-invariant metric quantifies whether the signals rise and fall together (positive correlation) regardless of their absolute magnitudes. The Pearson correlation coefficient is defined as the ratio of the covariance of the two variables to the product of their standard deviations, as expressed in Eq. (5.37):

$$\rho_{\text{corr}} = \frac{\sum_{i=1}^{N}(x_i - \bar{x})(y_i - \bar{y})}{\sqrt{\sum_{i=1}^{N}(x_i - \bar{x})^2 \sum_{i=1}^{N}(y_i - \bar{y})^2}} \tag{5.37}$$

Here, x_i and y_i represent individual elements of two vectors of length N, and $\bar{x}$ and $\bar{y}$ denote the mean values of their respective vectors. ρ_{corr} is calculated between the remapped interferograms and corresponding exitance spectra. For the entire data set, the average is $\bar{\rho}_{\text{corr}} = 0.61$ for the first order and $\bar{\rho}_{\text{corr}} = 0.66$ for the second order with standard deviations of $\text{std}(\rho_{\text{corr}}) = 0.38$ and $\text{std}(\rho_{\text{corr}}) = 0.42$, respectively. Due to the large size of the dataset, the remapped interferograms and Pearson correlation coefficients for all measurements are available for viewing at https://madsnibe.com/HSTI/images/pearsons.pdf.

Although this method of interpreting the interferograms is straightforward and produces relatively satisfactory results, it does not take full advantage of the enhanced spectral resolution provided by the higher

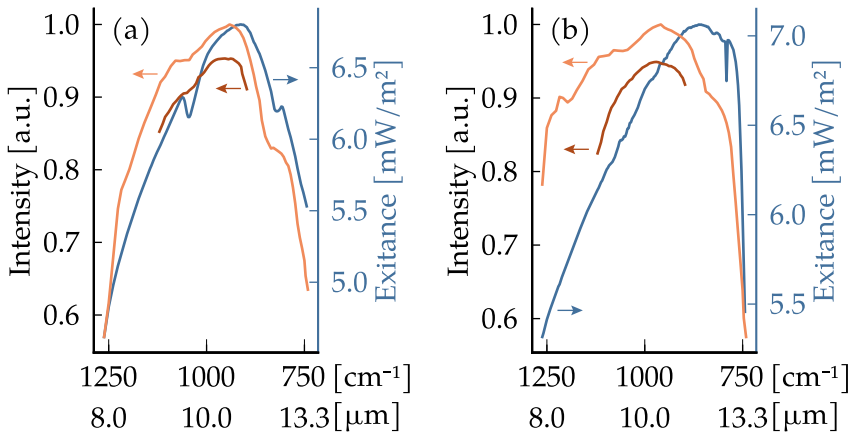

Figure 5.11: Remapped interferograms of the gas cell containing (a) air after NO exposure and (b) CO_2 in front of a 150 °C black body.

transmission orders. In the subsequent sections, the reconstruction is formulated as an inverse problem and is addressed using a variety of approaches.

5.3.3 Solving for the Incident Spectrum Explicitly

As in previous analyses, Eq. (5.3) is rewritten into an $\mathbf{Ax} = \mathbf{b}$ problem. The variables are defined as follows:

$$\mathbf{A} = \boldsymbol{\mathcal{A}} \tag{5.38}$$

$$\mathbf{x} = \mathbf{m}_{\mathbf{BB},\boldsymbol{\lambda}} \circ \boldsymbol{t}_{\mathbf{s}} + \mathbf{m}_{\mathbf{env},\boldsymbol{\lambda}} \circ \boldsymbol{r}_{\mathbf{s}} \tag{5.39}$$

$$\mathbf{b} = \boldsymbol{\psi} - (\mathbf{m}_{\mathbf{d},\boldsymbol{\lambda}} \circ_{\mathrm{r}} \boldsymbol{\mathcal{R}}_{\mathbf{SFPI}} - \mathbf{m}_{\mathbf{d},\boldsymbol{\lambda}})\,\mathbf{s} \tag{5.40}$$

Here, while $\mathbf{x}$ is the variable to be reconstructed, the presented expression is used as the ground truth for evaluating the reconstructions. Additionally, the interferograms $\boldsymbol{\psi}$ have been baseline-corrected such that their first element equals zero. The same solution as presented in Eq. (5.17) is used to solve for $\mathbf{x}$:

$$\mathbf{X} = \left(\mathbf{A}^\top \mathbf{A} + \gamma \boldsymbol{\mathcal{M}}^\top \boldsymbol{\mathcal{M}}\right)^{-1} \mathbf{A}^\top \mathbf{B} \tag{5.41}$$

$$\mathbf{B} = \begin{bmatrix} \mathbf{b}_{\mathbf{acetone}} & \mathbf{b}_{\mathbf{NH3}} & \cdots & \mathbf{b}_{\mathbf{toluene}} \end{bmatrix}$$

In this context, $\mathbf{B}$ is a matrix where each column represents a processed interferogram, and the columns of $\mathbf{X}$ contain the reconstructions of the incident spectra. Figure 5.12 presents the explicit solution for the reconstructions of butane (Figure 5.12a) and CO_2 (Figure 5.12b). The regularization parameter has been set to $\gamma = 10^{12}$. The ground truth (GT) is calculated using Eq. (5.39). The root mean square error (RMSE) is computed as the square root of the MSE, as defined in Eq. (5.42):

$$\mathrm{RMSE}(\mathbf{y}, \hat{\mathbf{y}}) = \sqrt{\frac{1}{n} \sum_{i=1}^{n} (y_i - \hat{y}_i)^2} \tag{5.42}$$

The RMSE is, in this case, only calculated within the spectral range of 1288 cm^{-1} to 659 cm^{-1}, corresponding to the range where the detector response exceeds 10% of its maximum. The reconstruction (R) exhibits instability as it approaches this spectral range as it has to compensate

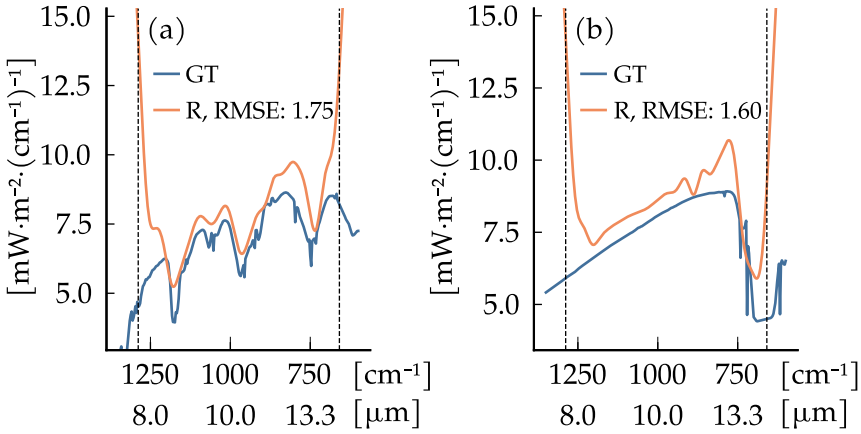

Figure 5.12: Spectral exitance for (a) butane and (b) CO_2-containing gas cells placed in front of a 150 °C blackbody emitter. "GT" indicates the ground truth, which is the incident spectrum based on FTIR transmittance and reflectance spectra. The RMSE of the reconstruction (R) is calculated only between 1288 cm^{-1} and 659 cm^{-1}, where the detector response exceeds 10%, as indicated by vertical dashed lines.

for the low response. While the overall shape of the reconstructions is in good agreement with the GT, it struggles with smooth signals, as evident from Figure 5.12b, where ringing can also be observed. If the regularization parameter is lowered, the solutions will oscillate even more, and details are lost if it is raised. Reconstructions for the entire dataset are available at `https://madsnibe.com/HSTI/images/explicit_solve_all_specs.pdf`. The mean RMSE of the entire data set is 2.02 $mW/m^2/cm^{-1}$ with a standard deviation of 0.67 $mW/m^2/cm^{-1}$. In general, the reconstructions overestimate the exitance spectrum. A possible explanation could be that the emissivity of the detector itself is not unity, as it is otherwise implied in Eq. (5.40). Another possible course could be the offset ζ is not included in the reconstructions, and thus, there are some unknown detector parameters that are not accounted for.

5.3.4 Nonnegative Matrix Factorization

The reconstruction problem is inherently underdetermined, implying the existence of infinitely many potential solutions. Consequently, the primary challenge lies in constraining the algorithms to converge toward physically plausible solutions that align with the desired characteristics.

The first-order derivative regularization employed thus far represents one approach to promote solutions that are more stable, and exhibit reduced oscillatory behavior. An alternative methodology involves constraining the solution to be a superposition of constituent sub-signals, which can be either predefined by the user or derived through model training [49, 50]. One example is Nonnegative Matrix Factorization (NMF) which aims to decompose a given nonnegative signal(s) into a dictionary containing atoms (signal components) in its columns and a matrix of coefficients as described by Eq. (5.43). All components involved in this decomposition are constrained to be nonnegative, as implied by the name. This constraint is appropriate because the signal being reconstructed is inherently nonnegative, allowing it to be expressed as a sum of other nonnegative signals.

$$\hat{\mathbf{X}} = \mathbf{W}\mathbf{H} \approx \mathbf{X} \tag{5.43}$$

Here, $\hat{\mathbf{X}} \in \mathbb{R}^{N \times J}$, where N denotes the number of features and J the number of samples, represents the decomposed signal approximating the true signals contained in the columns of $\mathbf{X}$. The matrix $\mathbf{W} \in \mathbb{R}^{N \times K}$ serves as the dictionary, with K components. The columns of $\mathbf{W}$, referred to as atoms, can be interpreted as the building blocks of the signal,

Algorithm 3 Accelerated Nonnegative Matrix Factorization (NMF)

Initialize $\mathbf{W}$ and $\mathbf{H}$ with random numbers
$\mathbf{V} \leftarrow \mathbf{W}$ and $\mathbf{J} \leftarrow \mathbf{H}$
for $k = 1, 2, \ldots, k_{\max}$ **do**
  $\mu_{\mathbf{W}} \leftarrow 1/\|\mathbf{H}\mathbf{H}^\top\|$
  $\nabla_{\mathbf{W}} \leftarrow \mathbf{W}\mathbf{H}\mathbf{H}^\top - \mathbf{X}\mathbf{H}^\top$
  $\mathbf{W}_{\mathbf{old}} \leftarrow \mathbf{W}$
  $\mathbf{W} \leftarrow \mathrm{proj}_+ [\mathbf{V} - \mu_{\mathbf{W}} \cdot \nabla_{\mathbf{W}}]$
  $\mathbf{V} \leftarrow \mathbf{W} + \frac{k}{k+3}(\mathbf{W} - \mathbf{W}_{\mathbf{old}})$
  $\mu_{\mathbf{H}} \leftarrow 1/\|\mathbf{W}^\top\mathbf{W}\|_F$
  $\nabla_{\mathbf{H}} \leftarrow \mathbf{W}^\top\mathbf{W}\mathbf{H} - \mathbf{W}^\top\mathbf{X}$
  $\mathbf{H}_{\mathbf{old}} \leftarrow \mathbf{H}$
  $\mathbf{H} \leftarrow \mathrm{proj}_+ [\mathbf{J} - \mu_{\mathbf{H}} \cdot \nabla_{\mathbf{H}}]$
  $\mathbf{J} \leftarrow \mathbf{H} + \frac{k}{k+3}(\mathbf{H} - \mathbf{H}_{\mathbf{old}})$
end for
return $\mathbf{W}, \mathbf{H}$

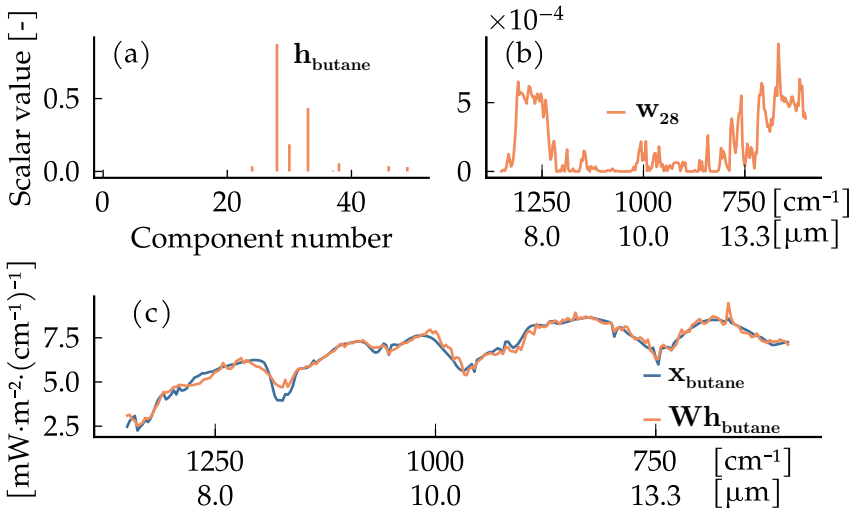

Figure 5.13: NMF calculated using Algorithm 3 with $k_{\max}$ =100,000 iterations and $K = 50$ atoms. (a) show the coefficients related to butane. (b) is the 28th atom of $\mathbf{W}$, which is the most prominent in the case of reconstruction of the butane spectrum as presented in (c). The reconstruction (NOT based on SFPI interferogram) has an RMSE 0.25 mW/m^2/cm^{-1}.

while the matrix $\mathbf{H} \in \mathbb{R}^{K \times J}$ contains the coefficients for each atom in its columns. Consequently, the minimization problem in Eq. (5.5) can be reformulated as

$$\arg\min_{\hat{\mathbf{H}}} \frac{1}{2} \|\mathbf{B} - \boldsymbol{\mathcal{A}}\mathbf{W}\hat{\mathbf{H}}\|_2^2 \tag{5.44}$$

The estimated signal can then be reconstructed using $\hat{\mathbf{X}} = \mathbf{W}\hat{\mathbf{H}}$. Prior to addressing the inverse problem, the following sections will focus on the decomposition of the real signals in $\mathbf{X}$ into a dictionary and a coefficient matrix.

The decomposition itself can be formulated as a minimization problem:

$$\arg\min_{\mathbf{W},\mathbf{H}} \frac{1}{2} \|\mathbf{X} - \mathbf{W}\mathbf{H}\|_F^2 \quad \text{s.t.} \quad \mathbf{W}, \mathbf{H} \geq \mathbf{0} \tag{5.45}$$

This problem will be solved using a gradient descent scheme analogous to that presented in Algorithm 1. Since the minimization involves both

$\mathbf{W}$ and $\mathbf{H}$, the gradients are be computed with respect to both variables:

$$\nabla_{\mathbf{W}} \frac{1}{2} \|\mathbf{X} - \mathbf{W}\mathbf{H}\|_F^2 = \mathbf{W}\mathbf{H}\mathbf{H}^\top - \mathbf{X}\mathbf{H}^\top \tag{5.46}$$

$$\nabla_{\mathbf{H}} \frac{1}{2} \|\mathbf{X} - \mathbf{W}\mathbf{H}\|_F^2 = \mathbf{W}^\top\mathbf{W}\mathbf{H} - \mathbf{W}^\top\mathbf{X} \tag{5.47}$$

Since both terms are updated during each iteration of the algorithm, the step size must also be computed for each iteration, as outlined in Algorithm 3 (step 4 and step 9). Note that the step size here has been reduced to half the maximum allowed step size presented in Eq. (5.21) to further enhance stability. Furthermore, this represents an accelerated descent scheme in terms of both variables. The notation in Algorithm 3 has been adjusted slightly to align with practical implementations, such as in Python, and to minimize notational clutter. Specifically, the iteration numbers, traditionally expressed as superscripts (k), are omitted to simplify the representation of variables.

Performing Algorithm 3 on $\mathbf{X}$ yields the results presented in Figure 5.13. In this case, $\mathbf{W}$ is initialized with 50 atoms, and the algorithm is executed for 100,000 iterations. The reconstructed butane spectrum (Figure 5.13c) achieves an RMSE of 0.25 $\mathrm{mW/m^2/cm^{-1}}$; however, the reconstruction is noticeably noisy. This noise can be attributed to the noisy nature of the atoms, as illustrated in Figure 5.13b. To address this issue, the update scheme is modified to incorporate smoothing regularization on the atoms of $\mathbf{W}$.

Smoothness Regularization

Adding the same regularization terms as used in Eqs. (5.15) and (5.16) ($\frac{1}{2}\gamma\|\mathbf{M}\mathbf{W}\|_F^2$) to the cost function, changes only the gradient of $\mathbf{W}$ and its step size $\mu_{\mathbf{W}}$. The new gradient is presented in Eq. (5.48).

$$\begin{aligned} &\nabla_{\mathbf{W}} \frac{1}{2} \left(\|\mathbf{X} - \mathbf{W}\mathbf{H}\|_F^2 + \frac{1}{2}\gamma\|\mathbf{M}\mathbf{W}\|_F^2 \right) \\ &= \mathbf{W}\mathbf{H}\mathbf{H}^\top - \mathbf{X}\mathbf{H}^\top + \gamma\mathbf{M}^\top\mathbf{M}\mathbf{W} \end{aligned} \tag{5.48}$$

The modified AGD algorithm incorporating smoothness regularization is detailed in Algorithm 4, with the result of 50,000 iterations presented

Algorithm 4 NMF with regularization on $\mathbf{W}$

Initialize $\mathbf{W}$ and $\mathbf{H}$ with random numbers
$\mathbf{V} \leftarrow \mathbf{W}$ and $\mathbf{J} \leftarrow \mathbf{H}$
for $k = 1, 2, \ldots, k_{\max}$ **do**
  $\mu_{\mathbf{W}} \leftarrow 1/\left(\|\mathbf{H}\mathbf{H}^\top\|_F + \gamma\|\mathbf{M}^\top\mathbf{M}\|_F\right)$
  $\nabla_{\mathbf{W}} \leftarrow \mathbf{W}\mathbf{H}\mathbf{H}^\top - \mathbf{X}\mathbf{H}^\top + \gamma\mathbf{M}^\top\mathbf{M}\mathbf{W}$
  $\mathbf{W}_{\mathbf{old}} \leftarrow \mathbf{W}$
  $\mathbf{W} \leftarrow \mathrm{proj}_+\left[\mathbf{V} - \mu_{\mathbf{W}} \cdot \nabla_{\mathbf{W}}\right]$
  $\mathbf{V} \leftarrow \mathbf{W} + \frac{k}{k+3}(\mathbf{W} - \mathbf{W}_{\mathbf{old}})$
  $\mu_{\mathbf{H}} \leftarrow 1/\|\mathbf{W}^\top\mathbf{W}\|_F$
  $\nabla_{\mathbf{H}} \leftarrow \mathbf{W}^\top\mathbf{W}\mathbf{H} - \mathbf{W}^\top\mathbf{X}$
  $\mathbf{H}_{\mathbf{old}} \leftarrow \mathbf{H}$
  $\mathbf{H} \leftarrow \mathrm{proj}_+\left[\mathbf{J} - \mu_{\mathbf{H}} \cdot \nabla_{\mathbf{H}}\right]$
  $\mathbf{J} \leftarrow \mathbf{H} + \frac{k}{k+3}(\mathbf{H} - \mathbf{H}_{\mathbf{old}})$
end for
return $\mathbf{W}, \mathbf{H}$

in Figure 5.14. The inclusion of the smoothness regularization yields visibly smoother atoms (Figure 5.14b) compared to the unregularized counterpart. Similarly, the reconstructed signal demonstrates enhanced smoothness (Figure 5.14c). An RMSE of 0.23 $\mathrm{mW/m^2/cm^{-1}}$ is achieved, requiring only half the iterations needed in the unregularized scenario.

User Defined Dictionary

Larger datasets have the potential to yield a more comprehensive and representative set of atoms. For cameras intended for specific applications, the dictionary could be tailored to meet those particular requirements. However, such tailoring introduces the risk of overfitting, where the model may learn to associate specific features in the interferograms with high-resolution spectral features that are not genuinely resolvable. To mitigate this risk, the dictionary is determined independently to ensure it only contains information that is physically resolvable by the SFPI. This approach also eliminates the need to divide the data into training and validation subsets, simplifying the process. Consequently, utilizing a user-defined dictionary ensures that reconstructions are broadly applicable across a wide range of applications.

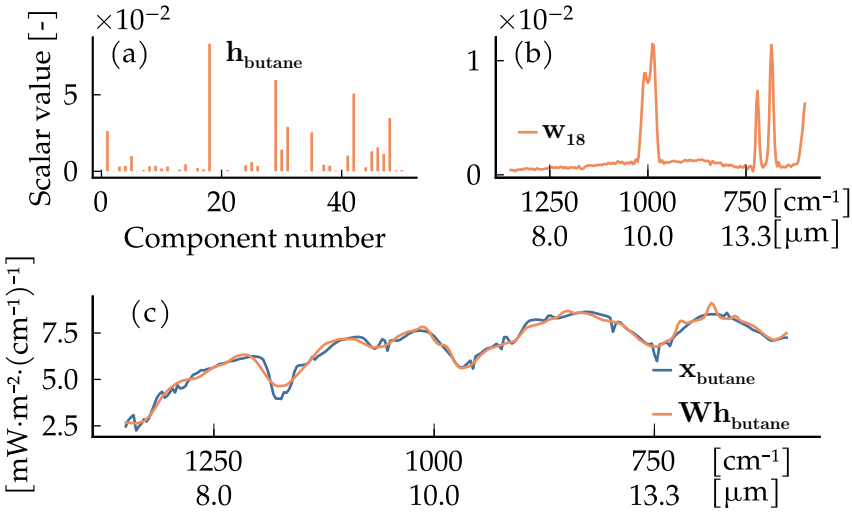

Figure 5.14: NMF calculated using Algorithm 4 with $k_{\max}$ =50,000 iterations and $K = 50$ atoms. Smoothness regularization is applied to the columns of $\mathbf{W}$ with a regularization parameter of $\gamma = 1$. (a) Displays the coefficients corresponding to butane. (b) Represents the 18th atom of $\mathbf{W}$, which significantly contributes to the reconstruction of the butane spectrum shown in (c). The reconstruction (NOT based on SFPI interferogram) of the butane spectrum achieves an RMSE of 0.23 $\mathrm{mW/m^2/cm^{-1}}$.

The system matrix $\boldsymbol{\mathcal{A}}$ (Figure 5.9) defines the relationship between the cavity length of the SFPI and the wavenumber of the incident radiation. Each row of $\boldsymbol{\mathcal{A}}$ represents the distribution of wavenumbers associated with the recorded signal at a specific cavity length. Consequently, the spectra reaching the detector can be expressed as a superposition of the SFPI transmittance spectra. Based on this, the new dictionary is constructed as $\mathbf{W} = \boldsymbol{\mathcal{A}}^\top$. However, no signal is observed before a cavity length of approximately 3.9 µm. To account for this, the first 13 columns of the dictionary are removed. Furthermore, the signal often includes contributions from blackbody emissions. To address this, 128 blackbody spectra (Eq. (2.41)) corresponding to temperatures ranging from 200 °K to 400 °K are incorporated as additional atoms in the dictionary. Lastly, each atom in the dictionary is normalized to have a unit norm ($\|\mathbf{w}_k\|_2 = 1$ for all k). The complete dictionary is presented in Figure 5.15.

Reconstructions using the custom dictionary are performed as shown in Algorithm 5. In this AGD framework, only $\mathbf{H}$ is optimized while

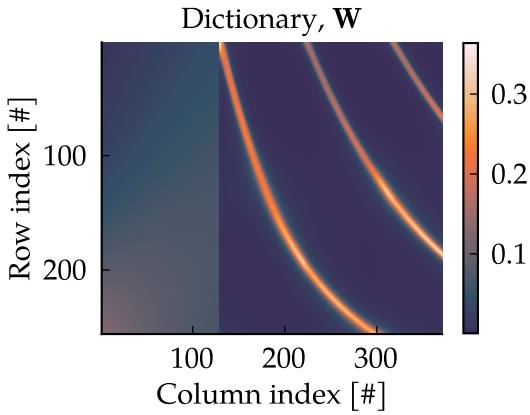

Figure 5.15: Dictionary containing 371 atoms, 128 of which are blackbody exitance spectra with temperatures ranging from 200 K to 400 K. The remaining atoms are the rows of the system matrix, $\boldsymbol{\mathcal{A}}$, with the rows below 3.9 µm cavity length removed due to insufficient signal. All atoms have been normalized to have unit norm.

Algorithm 5 AGD with regularization on $\mathbf{H}$ for NMF

Initialize $\mathbf{H}$ with random numbers
$\mathbf{J} \leftarrow \mathbf{H}$
for $k = 1, 2, \ldots, k_{\max}$ **do**
    $\mu_{\mathbf{H}} \leftarrow 1/\left(\|\mathbf{W}^\top\mathbf{W}\|_F + \gamma\|\mathbf{M}^\top\mathbf{M}\|_F\right)$
    $\nabla_{\mathbf{H}} \leftarrow \mathbf{W}^\top\mathbf{W}\mathbf{H} - \mathbf{W}^\top\mathbf{X} + \gamma\mathbf{M}^\top\mathbf{M}\mathbf{H}$
    $\mathbf{H}_{\mathbf{old}} \leftarrow \mathbf{H}$
    $\mathbf{H} \leftarrow \mathrm{proj}_+[\mathbf{J} - \mu_{\mathbf{H}} \cdot \nabla_{\mathbf{H}}]$
    $\mathbf{J} \leftarrow \mathbf{H} + \frac{k}{k+3}(\mathbf{H} - \mathbf{H}_{\mathbf{old}})$
end for
return H

keeping $\mathbf{W}$ fixed. Smoothness regularization is applied to $\mathbf{H}$ due to the inherent correlation between the atoms. Abrupt variations in $\mathbf{H}$ are unlikely, as spectral features typically require contributions from multiple neighboring atoms for accurate representation.

The reconstruction of butane is shown in Figure 5.16. This reconstruction represents the best achievable reconstruction for the SFPI, as the dictionary atoms are directly derived from the SFPI transmission profile at various cavity lengths. Thus, the reconstructions primarily capture

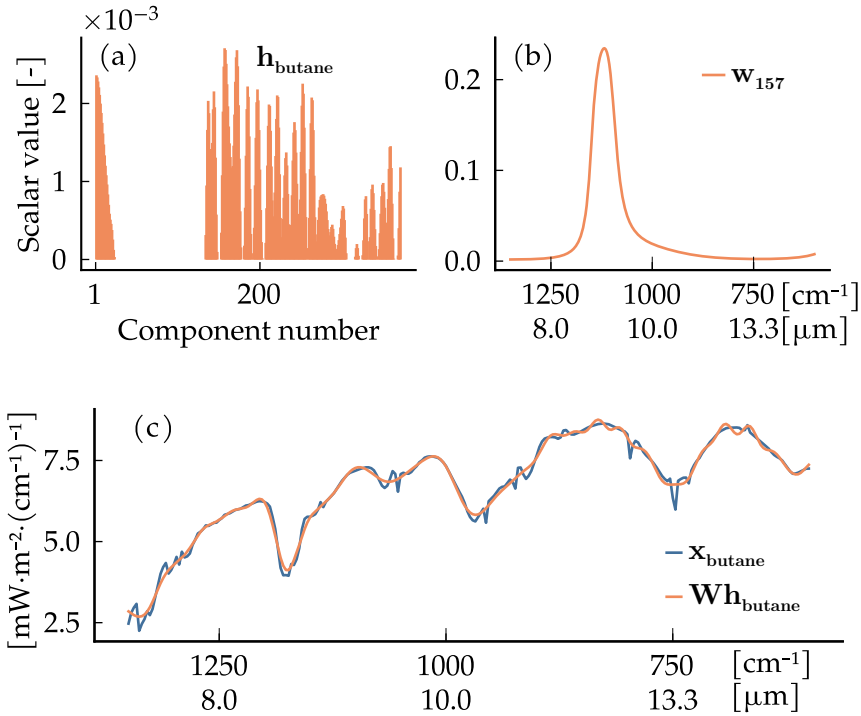

Figure 5.16: Reconstruction (NOT based on SFPI interferogram) of butane exitance spectrum based on Algorithm 5 using 1000 iterations and $\gamma = 10^{-1}$. (a) show the coefficients corresponding to the butane reconstruction, with the most contributing atom displayed in (b). The reconstruction itself is shown in (c) and achieves an RMSE = 0.14 mW/m^2/cm^{-1}.

the broader features of the original spectrum, reflecting the resolution limitations imposed by the SFPI.

Reconstruction From Interferograms

The reconstructions of the SFPI interferograms are now performed using the dictionary presented in Figure 5.15. To solve for $\hat{\mathbf{H}}$ in Eq. (5.44), the approach detailed in Algorithm 5 is applied. However, $\mathbf{W}$ is combined with the system matrix as $\hat{\mathbf{W}} = \boldsymbol{\mathcal{A}}\mathbf{W}$. Additionally, $\mathbf{B}$ is used in place of $\mathbf{X}$ in the algorithm. The solution to the minimization problem is presented in Figure 5.17a, where $\hat{\mathbf{h}}_{\mathbf{butane}}$ is a single coefficient vector from $\hat{\mathbf{H}}$.

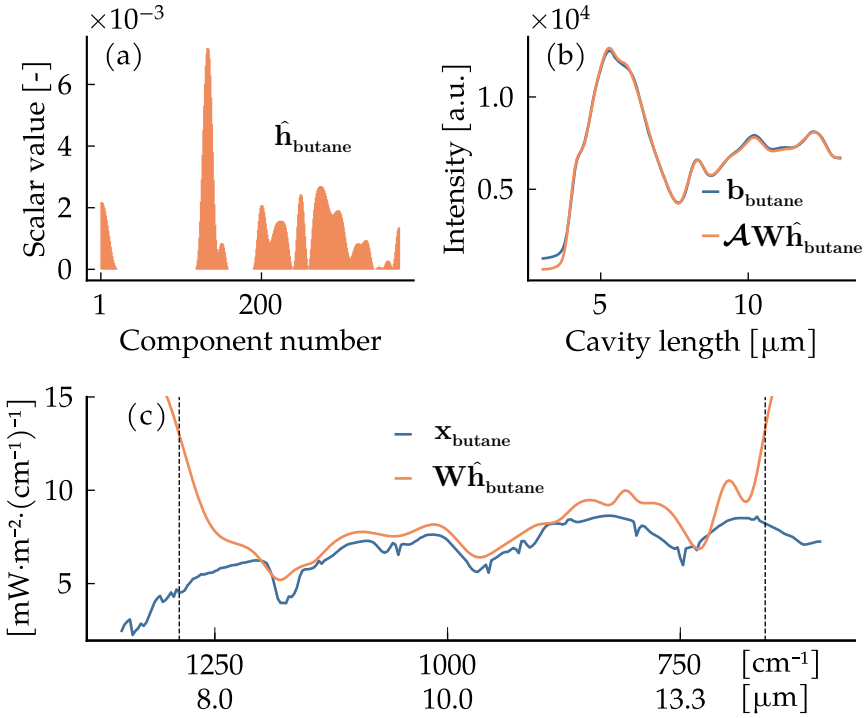

Figure 5.17: Spectral reconstruction of butane based on SFPI interferograms using Algorithm 5 with 100,000 iterations and $\gamma = 10^{11}$. The RMSE of the interferogram reconstruction (c) is 179, while the RMSE of the exitance spectrum (c) is 1.67 mW/m^2/cm^{-1}. (a) shows the coefficients solved during the reconstruction.

Interferogram reconstruction is expressed as $\hat{\mathbf{W}}\hat{\mathbf{h}}_{\text{butane}} = \boldsymbol{\mathcal{A}}\mathbf{W}\hat{\mathbf{h}}_{\text{butane}}$, and the result is presented in Figure 5.17b, achieving an RMSE of 179. Similarly, the reconstruction of the incident spectrum is given by $\hat{\mathbf{x}}_{\text{butane}} = \mathbf{W}\hat{\mathbf{h}}_{\text{butane}}$, as shown in Figure 5.17c, with an RMSE of 1.67 mW/m^2/cm^{-1}. The RMSE in both cases is calculated only within the range marked by the two vertical lines, which indicate the spectral region where the detector's sensitivity exceeds 10%. Reconstructions of the entire data set are available here `https://madsnibe.com/HSTI/images/all_reconstructions.pdf` with an average RMSE of 1.88 mW/m^2/cm^{-1} and a standard deviation of 0.57 mW/m^2/cm^{-1}.

The interferogram reconstruction in Figure 5.17b shows good agreement across most cavity lengths, with discrepancies at shorter lengths likely

due to limited SFPI transmission. The lack of radiometric calibration and the detector's temperature resolution of 0.3 K may also contribute to variations in the spectral reconstruction (Figure 5.17c).

Spectral reconstructions exhibit increasing estimates at the edges of the detector's sensitive range, marked by vertical lines in Figure 5.17c. This behavior also observed in the explicit solution (Figure 5.12), is attributed to overcompensation when system matrix entries diminish in magnitude.

5.3.5 Sensitivity to Spectral Misalignment

One challenge associated with the hyperspectral LWIR imager is that the absolute cavity length remains unknown without an external spectral reference. The significance of accurately estimating the absolute cav-

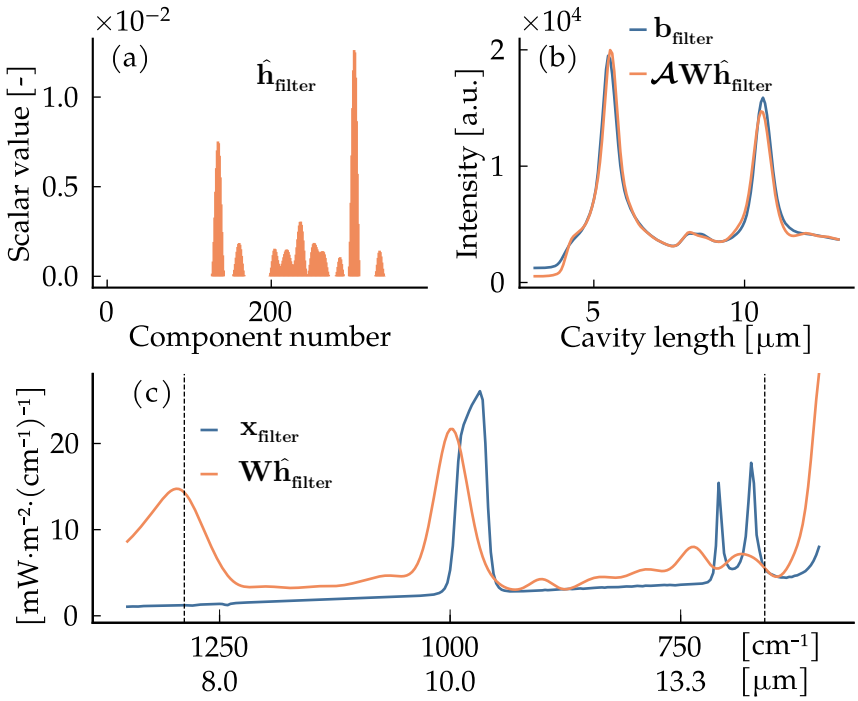

Figure 5.18: Reconstruction of the exitance spectrum for a 10.225 μm bandpass filter with a 300 °C blackbody emitter. Algorithm 5 was used with 100,000 iterations and $\gamma = 10^{11}$, offsetting cavity lengths in $\mathcal{A}$ by 200 nm. (a) Atom coefficients for reconstructing the interferogram in (b), RMSE = 284. (c) Incident spectrum reconstruction, RMSE = 5.34 mW/m^2/cm^{-1}.

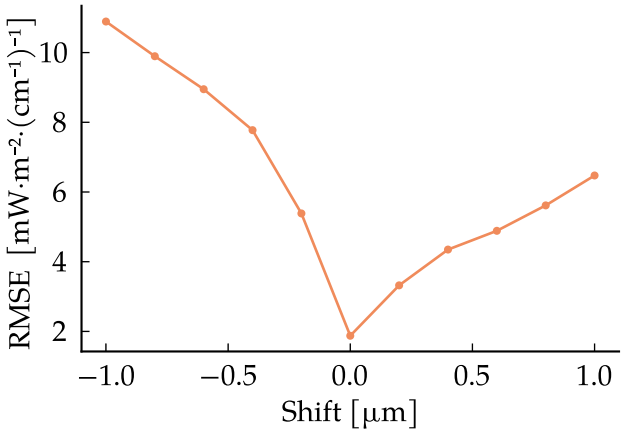

Figure 5.19: Mean RMSE of reconstructions across the entire dataset performed using the AGD shown in Algorithm 5 with 50,000 iterations and $\gamma = 10^{11}$. The reconstructions have been made with different offsets in the cavity lengths used when calculating the system matrix $\boldsymbol{\mathcal{A}}$.

ity length is demonstrated in Figure 5.18. Here, the spectral exitance spectrum of a 10.225 μm bandpass filter is reconstructed using a system matrix in which the cavity lengths are offset by 200 nm shorter than the values used previously in this section. The interferogram reconstruction in Figure 5.18b still exhibits excellent agreement, with an RMSE of 284 compared to 283 for the non-offset reconstruction. However, a substantial difference arises in the reconstruction of the exitance spectrum (Figure 5.18a). The RMSE of the non-offset reconstruction is 2.43 $\mathrm{mW/m^2/cm^{-1}}$, whereas the reconstruction using the offset system matrix yields a significantly higher RMSE of 5.34 $\mathrm{mW/m^2/cm^{-1}}$.

Even a small error in the calibration of the cavity length can result in a significant increase in reconstruction error. Figure 5.19 illustrates how the mean reconstruction error for the entire dataset varies with different offsets in the cavity lengths used to compute the system matrix $\boldsymbol{\mathcal{A}}$. The results reveal that the reconstruction error increases more rapidly for negative offsets than for positive ones. This behavior aligns with the dispersion relations (Eqs. (4.37) and (4.38)), which indicate that the spectral shift is more sensitive to shorter cavity lengths. These findings demonstrate that a miscalibration of only 100 nm can more than double the RMSE of the reconstructions.

5.4 Summary

Various linear algebra techniques have been employed to both predict the output of the HSC given a known input and to infer the input spectrum based on the recorded interferograms. Blackbody transmission measurements were conducted for various samples across different blackbody temperatures. Utilizing a mathematical model describing the radiative transfer between the HSC and the observed scene, it was possible to estimate the spectral sensitivity of the detector (and the objective lens). By combining this spectral response with GMM simulations, a system matrix was constructed, enabling the estimation of interferograms from a given spectral input.

Furthermore, different methods for converting recorded interferograms into wavenumber spectra have been explored. The most effective approach has been NMF, where a dictionary comprising blackbody exitance spectra and SFPI transmittance spectra has demonstrated the capability to accurately reconstruct incident spectra from measured interferograms. However, there is still room for improvement, and especially uncertainty in the known cavity length has proven to affect the reconstructions dramatically.

III Practical Applications

6 Plastic Classification 149

6.1 Introduction to Hyperspectral Imaging of Plastics 150
6.2 Materials and Methods 151
6.3 Results and Discussion 159
6.4 Conclusions 168

7 Analysis of Diffusion Flames 169

7.1 Introduction to Flame Imaging and Spectroscopy 170
7.2 Materials and Methods 171
7.3 Results and Discussion 176
7.4 Conclusions 183

8 Various Preliminary Studies 185

8.1 Combination of Incidence Spectra 186
8.2 Relationship Between Absorbance and Interferogram Intensity 187
8.3 Imaging Reflections 189
8.4 Imaging Minerals 197
8.5 Applications' summary 208

6. Plastic Classification

This chapter presents the work conducted on the classification of plastics using a hyperspectral LWIR imager. The findings of this work are documented in two publications: *Classification of commercial plastics using hyperspectral long wave infrared emission imaging* [3] and *Classification of black plastic types by hyperspectral imaging based on long-wave infrared emission spectroscopy* [4]. Since the methodologies of the two studies are largely similar, their results are combined in this chapter, with explicit indications of any methodological differences.

In both studies, various plastic samples heated to 60 °C were imaged using the hyperspectral camera. The first set of samples included the following range of commercial plastic types: polyoxymethylene (POM), poly(vinylidene difluoride) (PVDF), poly(vinyl chloride) (PVC), polystyrene (PS), polypropylene (PP), poly(methyl methacrylate) (PMMA), poly(ethylene terephthalate) (PET), polyetheretherketone (PEEK), polycarbonate (PC), polyamide 12 (PA12), high-density polyethylene (HDPE), and poly(acrylonitrile-butadiene-styrene) (ABS). These samples consisted of both colored (not black) and natural plastics.

The second study focused on the classification of black plastics, which posed additional challenges due to the presence of carbon black. The black plastic samples included PS, poly(styrene-co-acrylonitrile) (SAN), PMMA, POM, polyamide 6 (PA6), PVC, polyethylene (PE), polyamide 6,6 (PA66), and PET. Despite the increased difficulty associated with the black body signal contribution from the carbon black, most plastic types in both studies were successfully distinguished from one another.

6.1 Introduction to Hyperspectral Imaging of Plastics

Plastic is omnipresent in modern society, with applications spanning nearly all industries and sectors. Over the last two decades, global plastic production has more than doubled, reaching approximately 400 megatonnes annually [51]. This surge in plastic use has led to significant environmental challenges, as large quantities are mismanaged. Only about 10% of plastics are recycled, while an estimated 22% are disposed of in unregulated dump sites or released into the environment [52, 53]. Recycling plastics effectively requires a material purity exceeding 95% [54], a threshold that is often difficult to achieve due to inadequate recycling infrastructure and poor consumer practices [55].

Various spectroscopic techniques have demonstrated the capability to differentiate between polymer types, typically operating in the visible and near-infrared regions to estimate absorption spectra based on reflected light [56, 57]. However, the presence of carbon black additives in black plastics leads to increased light absorption across the entire spectrum, significantly reducing the intensity of reflected signals [58]. Longer wavelengths, such as those in the mid-wave infrared (MWIR) and LWIR regions, have shown promise for distinguishing polymer types despite the presence of carbon black. Nevertheless, many of these studies rely on single-point FTIR measurements, which are impractical for industrial-scale applications [59, 60].

The results presented in the following sections explore the potential of LWIR hyperspectral imaging for polymer classification. By employing an imaging-based approach, it becomes feasible to analyze multiple plastic samples simultaneously, enabling inline measurements, which is a requirement for industrial-scale plastic sorting. Two sample sets are examined: the first consists of various commercial plastics that are not colored black, referred to as *non-black* plastics, while the second comprises exclusively *black* plastic samples.

6.2 Materials and Methods

6.2.1 Samples and Experimental Setup

The plastic samples investigated represent many common commercial types. Non-black plastics (1–13) are shown in Table 6.1 and Figure 6.1, while black plastics (14–25) are found in Table 6.2 and Figure 6.2.

Table 6.1: List of non-black plastic samples used, including their type, abbreviation, trade name, and supplier.

Plastic Type	ID	Trade Name	Supplier
Polyethylene	1 HDPE	PE 100	SIMONA
Polypropylene	2 PP	240-CA12	INEOS
Poly(vinyl chloride)	3 PVC	PVC-U	GEHR
Poly(vinylidene difluoride)	4 PVDF	PVDF	GEHR
Polyoxymethylene	5 POM N	Ertacetal C	Mitsubishi
Polyoxymethylene	6 POM B	Ertacetal C	Mitsubishi
Polyetheretherketone	7 PEEK	Ketron PEEK 1000	Mitsubishi
Poly(acrylonitrile-butadienestyrene)	8 ABS	Terluran GP35	INEOS
Poly(methyl methacrylate)	9 PMMA	Setacryl 1000	Madreperla
Polycarbonate	10 PC	Makrolon 2652	Covestro
Poly(ethylene terephthalate)	11 PET	CB-602	UltraPurge
Polyamide 12	12 PA12	PA 12-TR	GEHR
Polystyrene	13 PS	CD cover	–

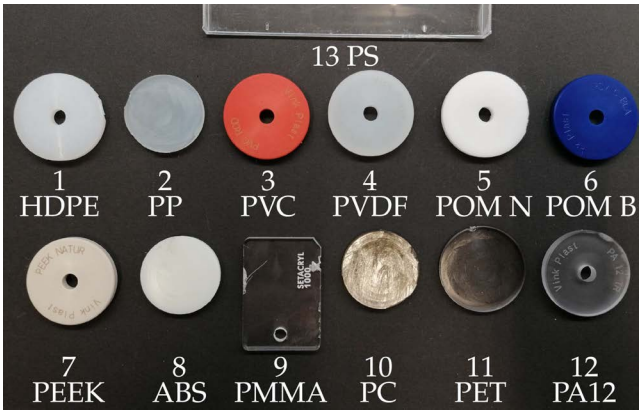

Figure 6.1: Photograph of colored plastic samples corresponding to Table 6.1. Adapted from [56].

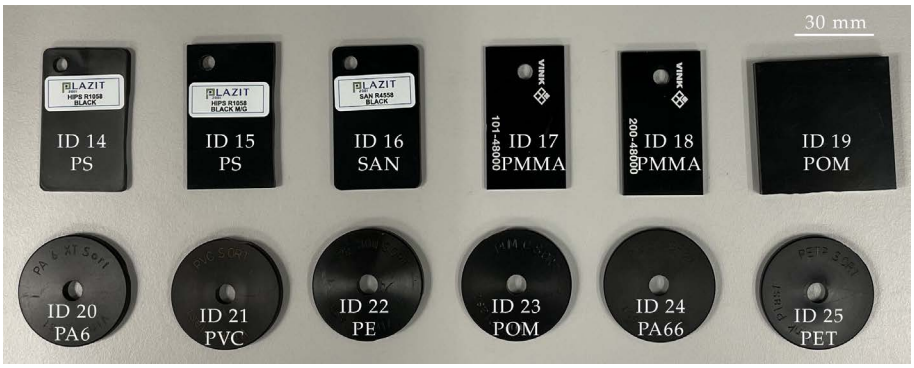

Figure 6.2: Photograph of black plastic samples corresponding to Table 6.2. Adapted from [4].

Table 6.2: List of black plastic samples used, including their type, abbreviation, trade name, and supplier. [a]Contains 30% glass fibers.

Plastic Type	ID	Trade Name	Supplier
Polystyrene	14 PS	R1058-Black	Plazit-Polygal
Polystyrene	15 PS	R1058-Black-MG	Plazit-Polygal
Poly(styrene-co-acrylonitrile)	16 SAN	R4558-Black	Plazit-Polygal
Poly(methyl methacrylate)	17 PMMA	101–48,000	Vink
Poly(methyl methacrylate)	18 PMMA	200–48,000	Vink
Polyoxymethylene	19 POM	SustarinC-Black	Röchling
Polyamide 6	20 PA6	PA6XTSort	Vink
Poly(vinyl chloride)	21 PVC	PVCSort	Vink
Polyethylene	22 PE	PE300Sort	Vink
Polyoxymethylene	23 POM	POMCSort	Vink
Polyamide 6,6[a]	24 PA66	PA66-GF30	Vink
Poly(ethylene terephthalate)	25 PET	PETPSort	Vink

A schematic representation of the experimental setup is shown in Figure 6.3. The setup includes the hyperspectral imager positioned above a small aluminum oven. The oven features an aluminum baseplate (dimensions: 90 × 90 × 20 mm) with two heaters (diameter: Ø10 mm, length: 70 mm, power: 250 W). The temperature of the baseplate is regulated via a PID controller in conjunction with a K-type thermocouple embedded directly within the baseplate. The oven chamber is constructed from a hollow aluminum cylinder (inner diameter: Ø50 mm, height: 45 mm) and is sealed at the top with a ZnSe window that has an anti-reflective coating (diameter: Ø50.8 mm, thickness: 5 mm). A secondary K-type

thermocouple is installed through the oven wall, positioned 20 mm above the baseplate, to monitor the internal temperature. Samples are placed directly on the baseplate, and the oven chamber is lowered over them to minimize air currents. The oven temperature is set to 60 °C, and samples are left to thermally equilibrate for at least 20 minutes.

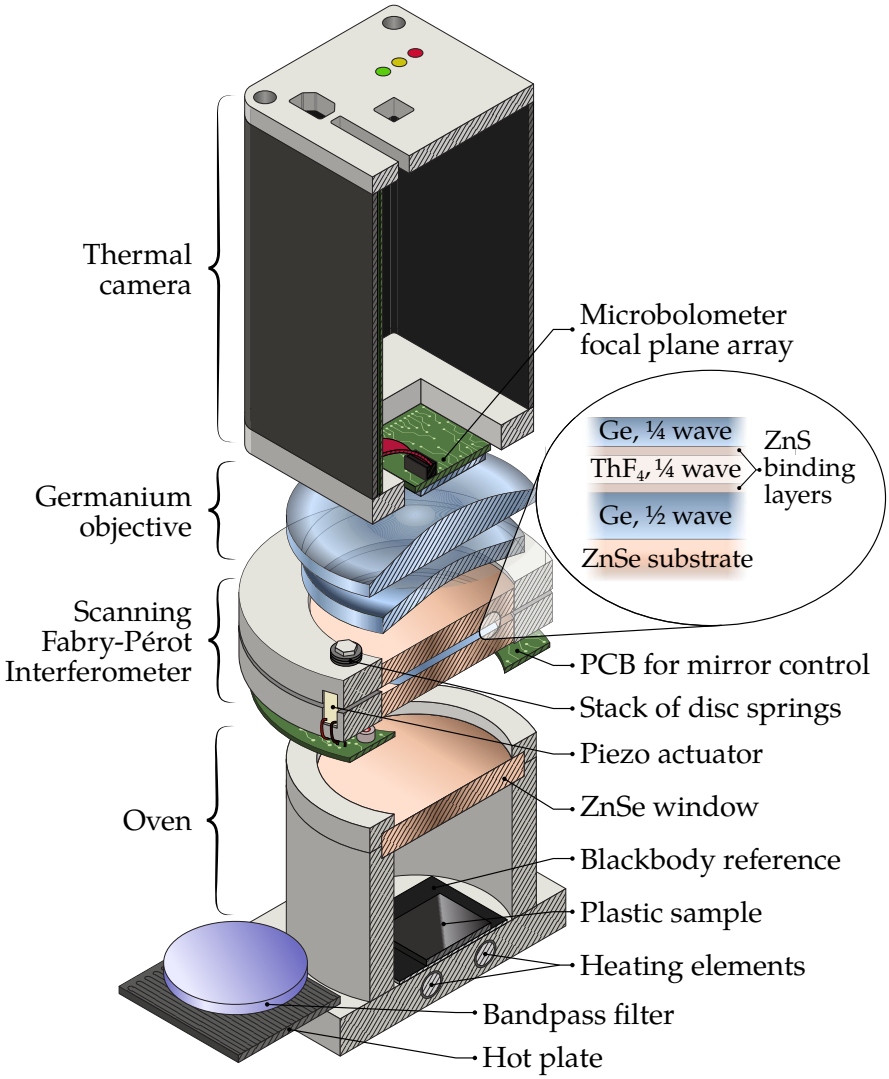

Figure 6.3: Schematic representation of experimental setup used to image various plastic samples heated to 60 °C. Adapted from [4].

Differences in Setups for the two Sample Sets

The primary difference between the experimental setups for hyperspectral imaging of black and non-black plastics lies in the external spectral reference used to calibrate the cavity length for the interferograms. In both cases, laser diode interferograms are utilized to estimate cavity expansion (Figure 3.5.3). For black plastics, the external reference is an 8.226 µm (1216 cm^{-1}) bandpass filter (Andover Corporation, USA) placed above an 80 °C hotplate (Figure 6.3). For non-black plastics, a piece of POM N (11.2 mm × 11.0 mm × 5.9 mm) is used as the spectral reference, positioned adjacent to the sample under investigation.

A blackbody reference sample is included to preprocess the acquired hyperspectral data cubes to minimize the contribution of the blackbody signal from the samples themselves. For non-black plastics, the blackbody reference is a stainless steel sample coated with Ultra Black™ ($\varepsilon > 0.93$, 3–30 µm, Acktar, IL), measuring 14.3 mm × 12.6 mm × 0.75 mm, and is placed next to the POM N reference and the sample. For black plastics, a larger blackbody reference (50 × 50 mm) is placed between the baseplate and the sample, ensuring that the reference remains visible within the frame.

Some black plastic samples could not fit within the oven chamber. For the rectangular samples (Figure 6.2), the oven was placed directly on top, resting on the sample. This setup leaves a small air gap between the baseplate and the oven wall. However, as the oven is sealed at the top, convection currents through the oven are prevented. This configuration introduces a temperature gradient between the samples' center and perimeter due to exposure to outside air at the edges. Nonetheless, this is not considered problematic since only the central region of the sample, far from the edges, is analyzed.

PCA is used to classify both the black and non-black plastic datasets. The non-black plastics dataset includes 13 distinct labels corresponding to each sample, with POM being the only duplicated polymer type. The black plastic dataset contains two instances of PS, PMMA, and POM, which are grouped under their respective polymer labels during the classification process.

6.2.2 Data Processing

The complete sequence of processing steps, from the raw data cube to the final classification, is outlined in the flowchart shown in Figure 6.4. Note that the spectral calibration described in [4] occurs prior to the preprocessing steps, specifically between the 'Crop image' and 'Baseline correction' stages. While it is possible to perform spectral calibration later in the workflow without impacting the outcome, the remaining processing steps remain identical.

The following list describes the processing steps before calculating the PCA model in further detail:

1. Baseline correction is performed on all interferograms as described in Eq. (2.70).
2. Blackbody correction is applied by calculating the difference to blackbody reference: $\psi'_{x,y} = \psi_{\boldsymbol{BB}} - \psi_{x,y}$, where $\psi_{x,y}$ represents the interferogram at pixel (x, y) and $\psi_{\boldsymbol{BB}}$ is the mean interferogram of the blackbody reference sample (30×30 pixels for the black plastics and 40×40 pixels for the non-black plastics).
3. Savitzky-Golay filtering (section 2.5) is applied to each interferogram with a window size of 5 samples, a first-order polynomial, and a first-order derivative.
4. SNV: Standard normal variate normalization is applied to each interferogram as described in Eq. (2.75).
5. Extract nine interferograms: For each sample, nine interferograms are extracted by averaging over a region of 10×10 pixels for the non-black plastics and 18×18 pixels for the black plastics

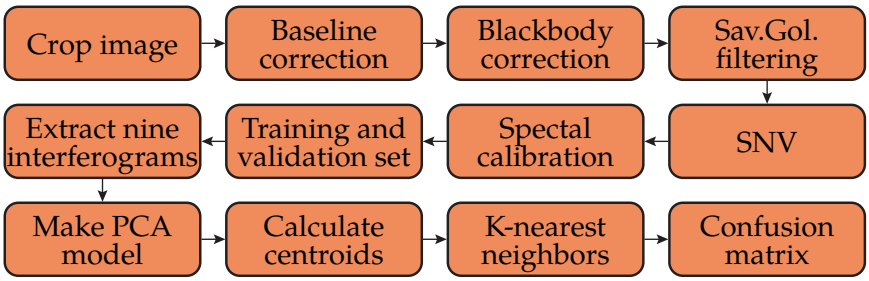

Figure 6.4: Flowchart describing the data processing from raw data cube to material classification. Adapted from [4].

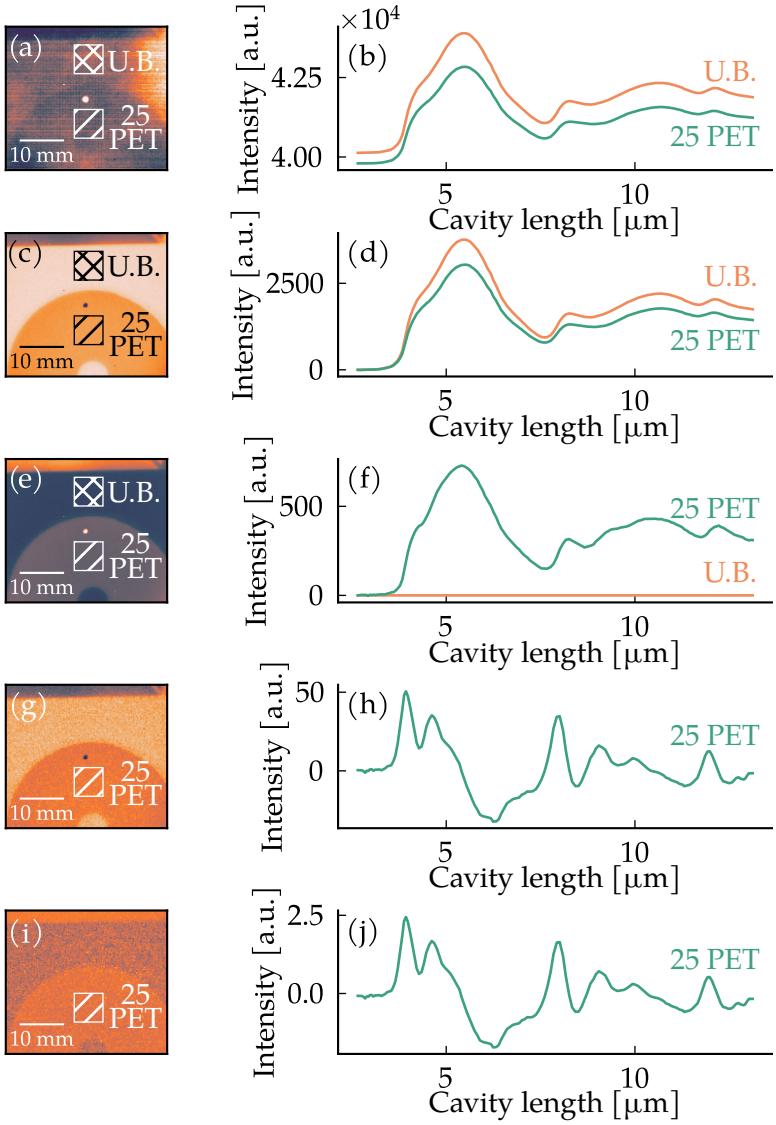

Figure 6.5: (a), (c), (e), (g), and (i): Images at a cavity length of 6.0 µm from the data cube showing '25 PET' at various preprocessing stages. (b), (d), (f), (h), and (j): Mean interferograms from 40×40-pixel regions. U.B. denotes 'Ultra Black™' (blackbody reference). Stages: (a) raw data (cropped), (c) baselined (Eq. (2.70)), (e) difference to U.B., (g) Savitzky-Golay filtered, (i) SNV normalized (Eq. (2.75)). Adapted from [4].

Figure 6.5 illustrates the effects of each preprocessing step applied to the black '25 PET' sample. The same processing steps are applied to the non-black data set as well. In Figure 6.5a, the sample is nearly indistinguishable from the Ultra Black™ blackbody reference. This is a known limitation of the microbolometer since manufacturing tolerances result in slight pixel-to-pixel variations in radiation response, causing differing outputs under identical irradiation conditions. This issue is partially addressed during the baselining step (Figure 6.5c and d), where all interferograms are shifted to start at zero. The integrated transmittance across the detector's spectral range at the mirrors' initial position is below 0.6%, enabling its use as a dark frame. However, this adjustment does not correct for differences in pixel responsivity (i.e., the change in signal per unit change in incident flux), which requires NUC calibration.

Subtle spectral features are enhanced by subtracting each pixel's interferogram from the Ultra Black™ reference (Figure 6.5e and f) and further amplified using a Savitzky-Golay filter with a first-order derivative (Figure 6.5g and h). While this filter accentuates details, it introduces spatial noise, which is largely mitigated by averaging across pixels. SNV is then applied to standardize interferograms and reduce intensity differences (Figure 6.5i and j). Averaged interferograms from 54×54-pixels for all samples are shown in Figure 6.14a, displaying the same characteristic peaks as the non-black dataset, marked by vertical lines.

Interpolation Along Spectral Axis

All data cubes must share a common spectral axis since the classification relies on PCA (section 2.6). Consequently, a new unified spectral axis describing the cavity length must be computed. The interpolation limits are determined by the data cube with the longest initial cavity length (cavity length at the first spectral channel) and the shortest final cavity length (cavity length at the last spectral channel). The number of equidistant interpolation points is set by the data cube with the fewest spectral channels. For the black plastics, the interpolation is performed over 155 channels spanning cavity lengths from 2.8 μm to 13.0 μm. For the non-black plastics, interpolation is applied using 141 channels spanning cavity lengths from 2.9 μm to 13.1 μm.

6.2.3 Classification Method

Plastic samples are classified using a PCA model. Each sample is imaged twice, with the sample removed and repositioned in the oven between captures. One image is assigned to the training set, while the other is included in the validation set. The PCA model is computed using the training set, and the number of principal components (PCs) included in the model is determined based on the scree plot, where the elbow point identifies the optimal number of PCs. The centroids for each sample (computed as the average of the nine mean interferograms) are calculated for the training set. The validation set is projected onto the same loadings derived from the training set, and each projected interferogram is assigned a class label based on its nearest centroid from the training set (K-nearest neighbors).

The model's performance is assessed using the accuracy metric, which quantifies the proportion of correct predictions relative to the total number of predictions, as defined in Eq. (6.1).

$$\mathscr{A} = \frac{\mathrm{TP}}{\mathrm{TP} + \mathrm{FP} + \mathrm{TN} + \mathrm{FN}} \tag{6.1}$$

Here, TP denotes the number of true positives, FP the number of false positives, and TN and FN represent the number of true negatives and false negatives, respectively.

6.3 Results and Discussion

The results are organized based on the two datasets: black plastics and non-black plastics. Certain results are presented only once, as they are similar for both datasets. For instance, spectral calibration and data preprocessing (Figure 6.7 and Figure 6.5) produce the same effects across both datasets, and therefore, only one set of results is displayed. Additionally, some aspects of the discussion apply to both datasets, resulting in a degree of overlap in their presentation.

6.3.1 Non-black Plastics

Spectral Calibration

Figure 6.6a illustrates a slice (42nd spectral channel). The mean interferogram extracted from the POM spectral reference sample is shown in Figure 6.6b, derived from a hatched square region (40×40 pixels). Figure 6.5 illustrates the effects of intermediate processing steps using the black plastics dataset, with similar effects observed for the non-black dataset. In Figure 6.6b, the apex of the third peak is located, and a skewed Gaussian function is fitted using five neighboring samples on each side, as indicated by the shaded region. The peak of the fitted function is identified at step 417.

PET interferograms from the training and test sets, extracted from a 30×30-pixel region, are shown both before (Figure 6.7a) and after spec-

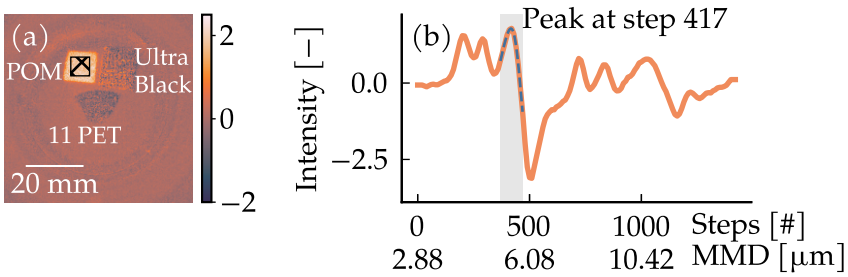

Figure 6.6: (a) Slice of the data cube at step 420, with the hatched 40×40-pixel square indicating the region used to calculate the mean interferogram of POM, shown in (b). The maximum of the interferogram is identified at approximately step 420, and a skewed Gaussian is fitted using five neighboring points on either side of the peak. The peak of the fit is located at step 417. Adapted from [3].

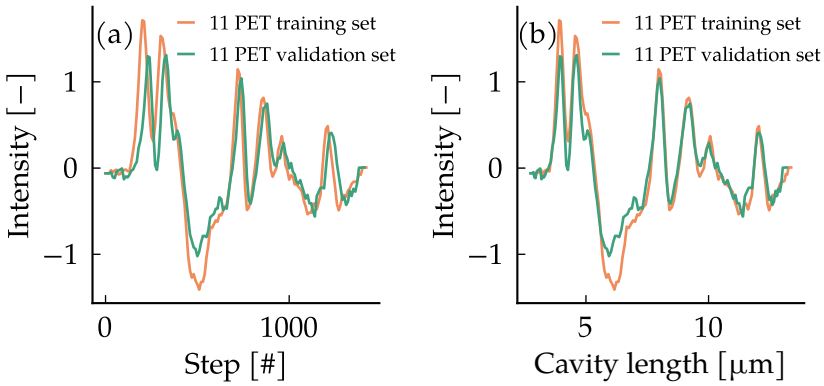

Figure 6.7: (a) Mean interferograms extracted from a 30×30-pixel region in two separate data cubes of the '11 PET' sample (training and validation set). (b) Corresponding data with calibrated cavity lengths. Adapted from [3].

tral calibration (Figure 6.7b). Before calibration, the apex of the first peak is located at step 200 for the training set and step 230 for the validation set, indicating a shift of approximately 30 steps (3 spectral channels), corresponding to ≈ 2% of the total range. Following calibration (Figure 6.7b), the peaks align within 0.04 μm, corresponding to a shift of ≈ 0.4% of the total range, underlining the importance of the spectral calibration.

Sample Prediction

PCA was applied to the training set, and the projection onto PC 2 and PC 3 is shown in Figure 6.8a. PC 1 is omitted as it primarily separates the POM samples from the rest of the dataset, making it challenging to discern the clustering of other materials. The significance of POM is further highlighted by the loading of PC 1 (Figure 6.9b), which closely resembles the POM interferograms and is attributed 75.13 % of the variance. Nine components are included in the PCA model based on the elbow point in the scree plot and collectively describe 96.12 % of the variance (Figure 6.8b).

PC 3 primarily distinguishes PET from the other samples, as evidenced by the score plot (Figure 6.8a) and the loadings (Figure 6.9b). The three vertical lines in Figure 6.9 mark the positions of characteristic peaks at cavity lengths of 4.0 μm, 8.1 μm, and 12.1 μm. These peaks arise from the first-order derivative included in the Savitzky-Golay filter,

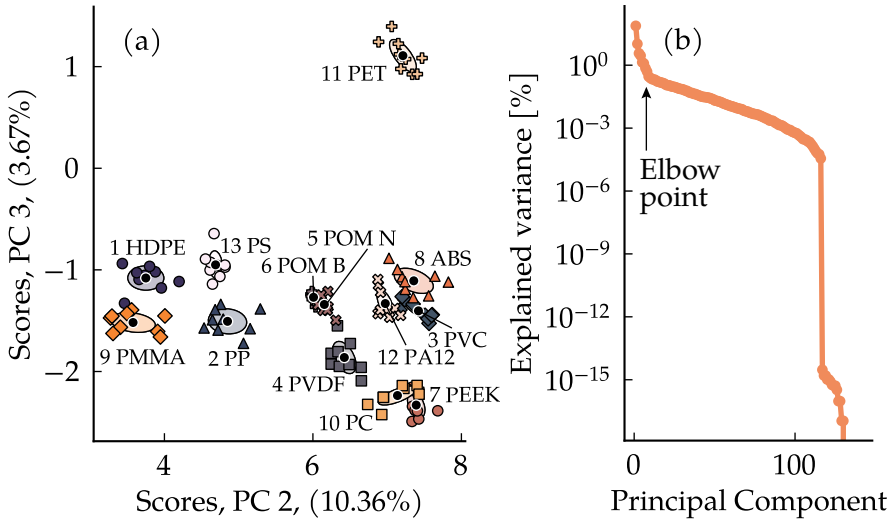

Figure 6.8: (a) Projection of the training set onto PC 2 and PC 3 of the PCA model. Black circles denote the centroids of each plastic sample, while confidence ellipses represent one standard deviation. The percentages in brackets indicate the explained variance of PC 2 and PC 3, respectively. (b) Explained variance of all principal components of the PCA model. An elbow point is located at PC 9. Adapted from [4].

which emphasizes regions with steep slopes caused by the rising edge of the detector's spectral response. The alignment of these peaks at approximately half-integer multiples of 8 µm corresponds to the steepest slope in the detector response (Figure 5.7) and indicates the introduction of new SFPI transmission orders.

PC 2 exploits the positions of these peaks to differentiate between interferograms. Specifically, interferograms with peaks shifted toward shorter cavity lengths exhibit stronger correlations than those with peaks shifted toward longer cavity lengths. Higher-order components primarily capture high-frequency features in the signals, which are often attributed to noise. As a result, assigning specific spectral features to individual material types in these components becomes increasingly challenging.

K-nearest neighbors was used to classify interferograms from the validation set after projection onto the first nine principal components of the training set. The classification results, shown in a normalized confusion

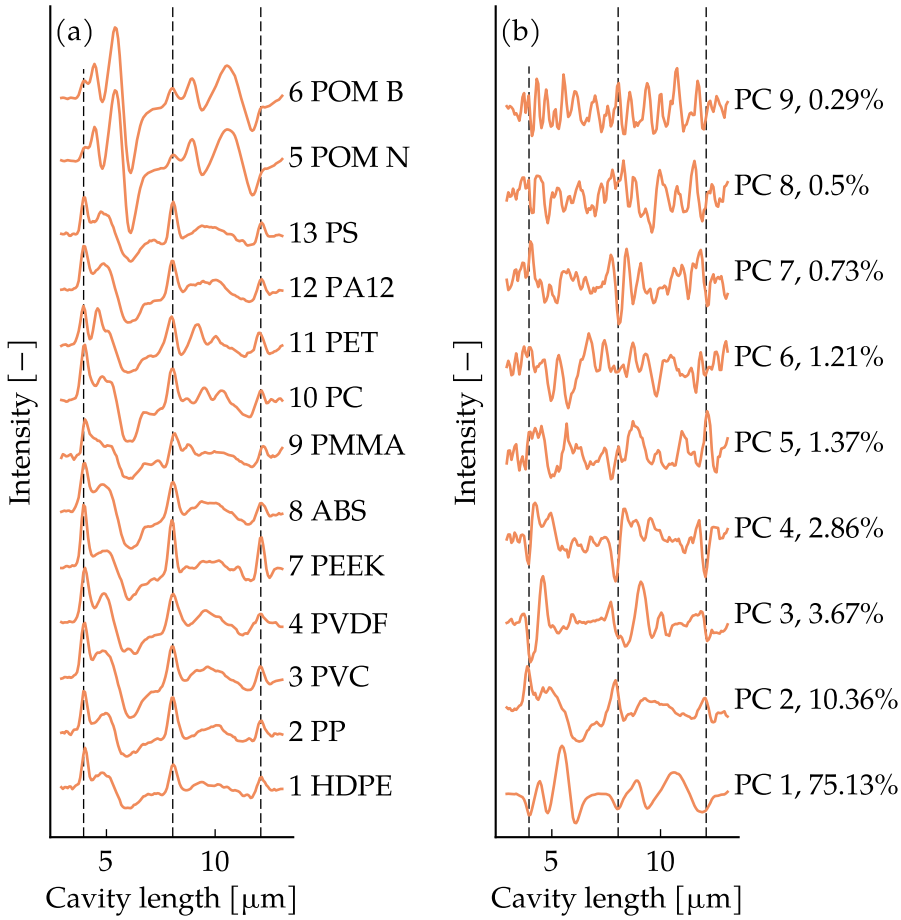

Figure 6.9: (a) Averaged interferograms for all plastic samples, computed from 30×30-pixel regions across training and test datasets. Interferograms are intensity-shifted for clarity, with dashed lines at cavity lengths of 4.0 μm, 8.1 μm, and 12.1 μm marking key peaks. (b) The first nine PCA loadings with corresponding explained variances. Adapted from [3].

matrix (Figure 6.10), indicate an accuracy of $\mathscr{A} = 88.9\,\%$. Most samples were correctly classified, except for '1 HDPE,' '5 POM N,' and '8 ABS.' Specifically, '1 HDPE' was misclassified once as '13 PS,' while '8 ABS' was misclassified twice as '3 PVC' and five times as '12 PA12.' These errors likely result from the similarity of their interferograms, as seen in Figure 6.9a, where residual differences after blackbody subtraction may introduce misclassification.

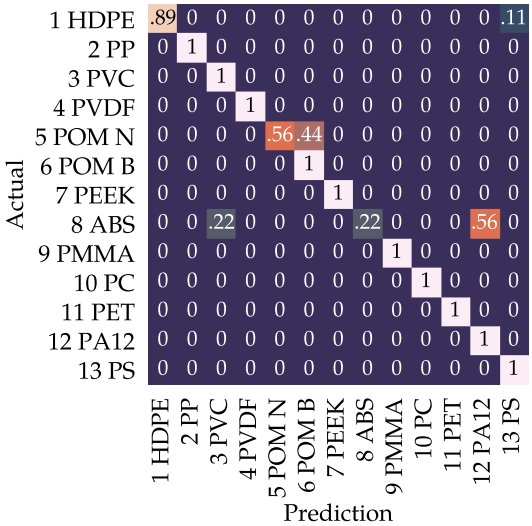

Figure 6.10: Normalized confusion matrix for validation set predictions using k-nearest neighbors based on the nine selected PCs from the PCA model. Adapted from [3].

Additionally, '5 POM N' was misclassified as '6 POM B' four times, which is expected since both samples are made of POM and are only differentiated by their pigmentation. The pigment concentration, ranging from 0.2% to 4% by mass, does not significantly impact the LWIR emission spectrum.

What Makes POM so Distinct?

Absorption and emission spectra of materials are described by Kirchhoff's law of thermal radiation (Equation 2.64). In emission measurements, blackbody (or graybody) radiation often dominates, masking weaker spectral features. These features can be enhanced by computing the difference relative to a blackbody reference. However, significant differences between the sample's emissivity and that of the blackbody can leave residual graybody signals leading to low SNR, which may still obscure the remaining spectral features, as demonstrated in Figure 6.11b.

Emission spectroscopy was conducted on the '5 POM N' and '2 PP' samples using a Bruker VERTEX 70(v) FTIR spectrometer equipped with an A540 emission adapter by application scientist Gerd Riedel from Bruker. The spectral excitance spectra presented in Figure 6.11a were calculated

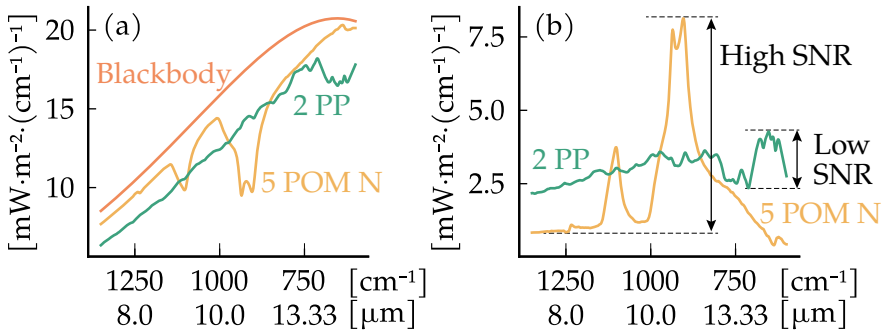

Figure 6.11: (a) Spectral exitance measurements of 5 POM N and 2 PP, derived from FTIR emissivity data and a theoretical 60°C blackbody spectrum. (b) Difference between the exitance spectra and the blackbody spectrum for each sample. Adapted from supporting information from [3].

by multiplying the measured emissivities by a theoretical blackbody spectrum at 60 °C. Although the Acktar Ultra Black™ does not have a perfectly constant emissivity like an ideal black or graybody, its emissivity exceeds 0.97, making it a suitable blackbody substitute [61]. The difference between the exitance spectra and the theoretical blackbody is shown in Figure 6.11b, mirroring the preprocessing step applied to interferograms. The '5 POM N' sample exhibits more pronounced spectral variations than the '2 PP' sample, showing a higher noise floor due to larger emissivity differences relative to the blackbody reference. As a consequence, the SNR of the POM signal is comparatively higher, and POM was therefore selected as the spectral reference.

6.3.2 Black Plastics

Polymer Type Prediction

The PCA model is then trained on the interferograms extracted from the training set, and their projection is seen in Figure 6.12b. Just as in the case of the non-black plastics, PC 1 is dominated by the POM signals, making it difficult to make out the clustering of the other samples. PC 3 is again used to distinguish PET from the other samples (Figure 6.14b).

The model achieved an accuracy of $\mathscr{A} = 73.1$ %, with the corresponding confusion matrix shown in Figure 6.12a. Without pooling by polymer type, accuracy drops to $\mathscr{A} = 57.4$ %, as samples of the same polymer exhibit highly similar spectral features.

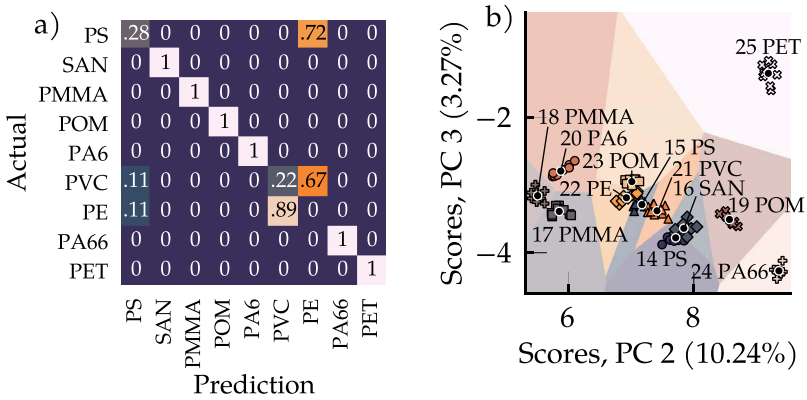

Figure 6.12: (a) Normalized confusion matrix for polymer classification in the black plastic dataset, with pooled PS, PMMA, and POM labels. (b) The training set projection onto PC 2 and PC 3, showing explained variance (in parentheses) and sample centroids (black circles). Adapted from [4].

The spectral dissimilarity between samples can be quantified using the Euclidean distance between the centroids of the training set (Figure 6.13). The distances between centroids reveal that the POM samples are notably distinct, with average distances of 63.1% and 86.7% for '19 POM' and '23 POM', respectively. In contrast, the shortest distances are observed between '15 PS', '21 PVC', and '22 PE', with average distances of

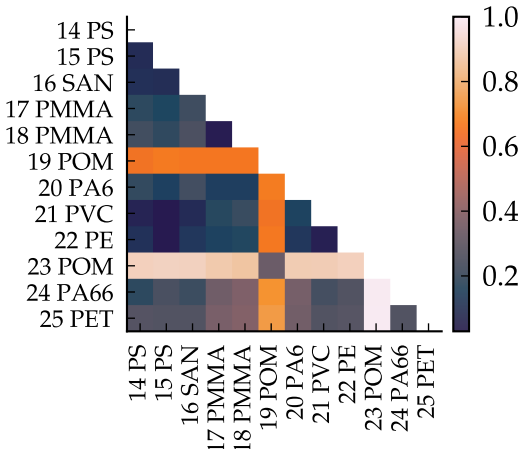

Figure 6.13: Euclidian distance calculated between each centroid of the training set. Distances have been normalized with respect to the largest distance. Adapted from [4].

25.2%, 25.0%, and 25.3%, respectively. These polymer types are also the only ones misclassified, likely due to residual signals obscuring spectral features after blackbody correction, as seen in the non-black plastic dataset.

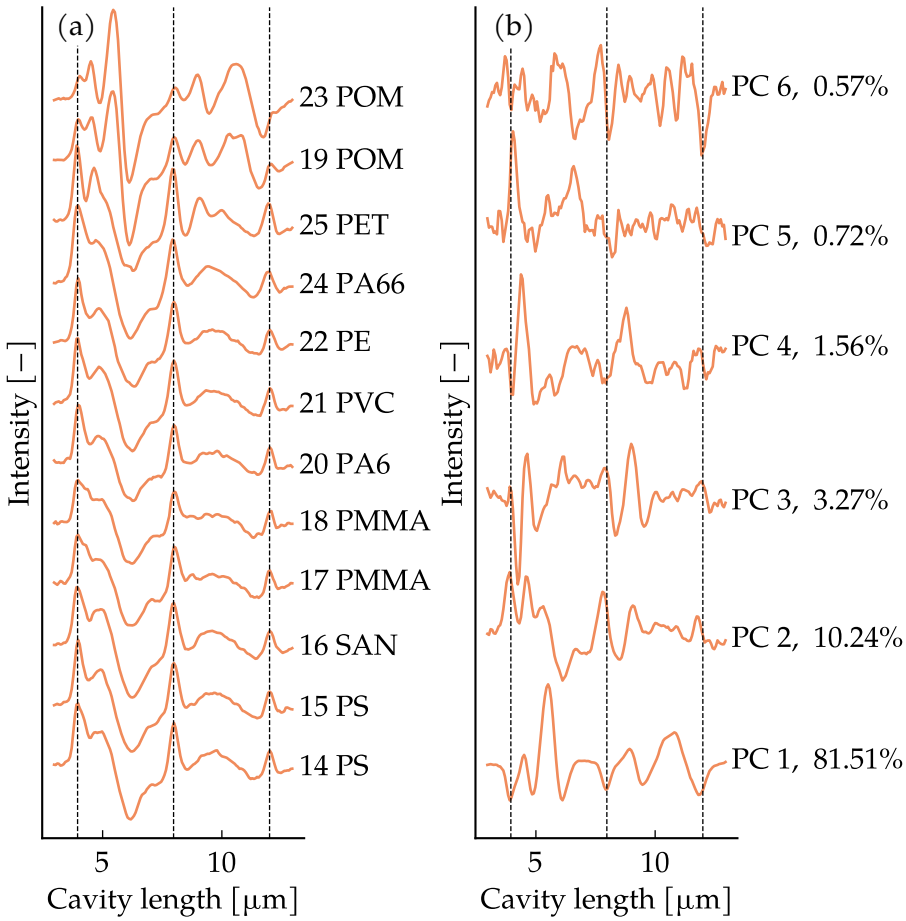

Figure 6.14: (a) Average interferograms sampled across a 54×54-pixel area for each of the black plastic samples. (b) The loadings that are included in the PCA model. Percentages indicate the explained variance of the respective components. Both interferograms and loadings have been offset for clarity.

6.3.3 Industrial Implications

One significant limitation of using this hyperspectral imager in industrial applications is its data acquisition speed, which is generally too slow for processes involving conveyor belts. Enhancing the detector frame rate to 120 Hz and improving the control electronics for the cavity mirrors could reduce acquisition time to approximately 1 second. While this remains relatively slow for high-speed industrial processes, it demonstrates the potential of the LWIR regime and microbolometer detectors for distinguishing between different types of plastics. Alternative techniques such as push-broom hyperspectral imaging may be more suitable for applications requiring higher throughput.

Another challenge is the need to heat samples when utilizing emission spectra for classification. Since the microbolometer measures the *net* heat transfer between itself and the sample, an alternative solution could involve either cooling or heating the detector. However, heating the detector increases Johnson noise, reducing the SNR [7]. Other studies have explored heating samples to measure differences in heating and cooling rates [62, 63]. While effective, this approach is energy-intensive and time-consuming and depends on the thermal mass and emissivity of the samples.

Reflectance spectroscopy may present a viable alternative to sample heating. Instead of analyzing emission spectra, an external light source can be used to measure the reflectance spectra of samples. Assuming negligible transmittance and that the reflected signal is significantly stronger than sample emissions, absorbance spectra could be inferred from the reflectance measurements. Although this method has not been explored further, it could eliminate the need for thermal equilibration of samples, offering a potentially faster approach. However, the non-flat geometry of plastic waste introduces variations in reflection angles, which may lead to challenges with specular reflections. These reflections could result in significant variations in signal intensity, as specular highlights appear considerably brighter than other regions of the plastic. Consequently, diffuse lighting conditions are likely required to mitigate these effects. Furthermore, the influence of contaminants such as dirt and water within the waste stream has not been examined, and these factors may adversely affect both emission and reflectance measurements.

6.4 Conclusions

The LWIR HSC has successfully differentiated various types of polymers, both with and without carbon black additives. Classification of the datasets (black and non-black) was performed using k-nearest neighbors in combination with PCA. For the non-black dataset, the classification accuracy achieved was $\mathscr{A} = 88.9\%$, with misclassification only occurring for '8 ABS' and '1 HDPE'. This misclassification is attributed to the low emissivity of these samples, resulting in significant residual errors that obscure the spectral signal after blackbody correction.

For the black plastic dataset, the classification accuracy was $\mathscr{A} = 73.1\%$, indicating that the presence of carbon black within the polymer matrix impacts performance in the LWIR range, leading to lower accuracy compared to the non-black dataset. Nonetheless, the results demonstrate that most polymer types can still be effectively classified, with POM and PET exhibiting particularly distinct spectral characteristics.

The results highlight the potential of this technique, even with minimal preprocessing and the use of simple, well-established classification methods. While more advanced machine-learning algorithms could further enhance performance, this study underscores the efficacy of the hyperspectral LWIR imager for polymer classification in its current form.

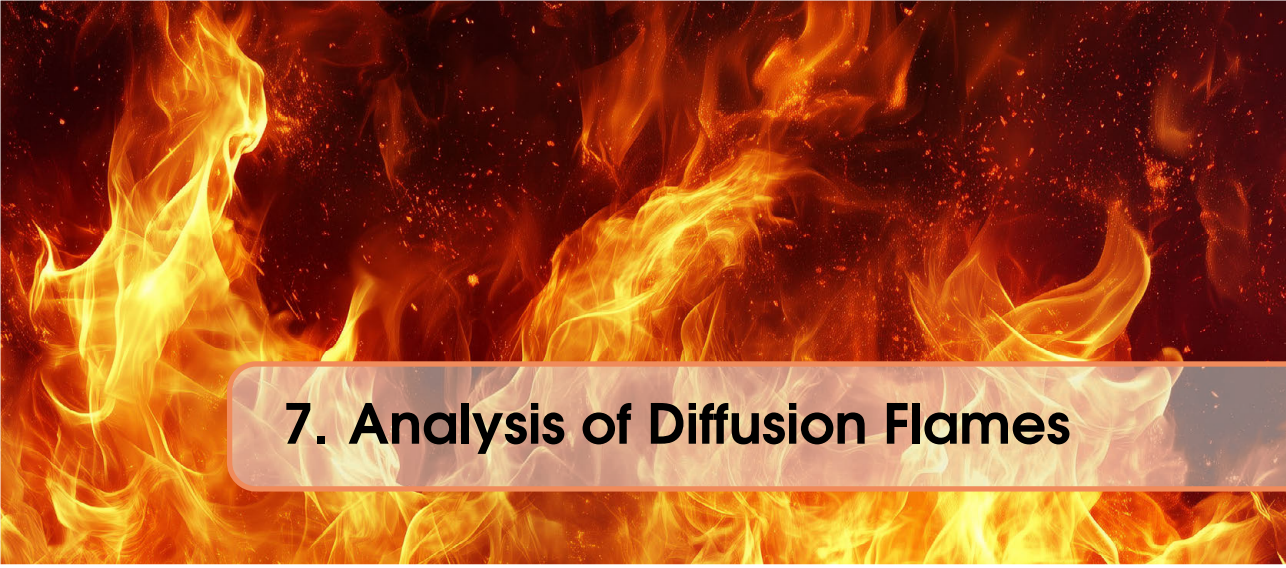

7. Analysis of Diffusion Flames

This chapter presents the results obtained using the LWIR HSC to analyze flames of various pure hydrocarbon fuels (methane, ethane, propane, butane, acetylene, and ethylene) and hydrogen in a diffusion regime where oxygen and fuel are not premixed. Hyperspectral data cubes were employed to identify distinct reaction zones within the flames and characterize intermediate combustion products. It was observed that all tested hydrocarbons produced ethylene as an intermediate product except methane and acetylene. Significant differences between most fuels were identified using the Pearson correlation coefficient for comparison. Hydrogen exhibited unique spectral characteristics, as the dominant observable features were associated with water vapor. This enabled finer rotational and vibrational transitions of water vapor in the LWIR regime to be resolved. Additionally, the absence of CO_2 spectral features in hydrogen flames provided a spectral profile distinct from the hydrocarbons.

These findings have been documented in a manuscript submitted to *Applied Spectroscopy* on January 11, 2025. Both the manuscript and accompanying supporting information are included in Appendix E.

7.1 Introduction to Flame Imaging and Spectroscopy

Flame imaging is a crucial diagnostic tool in fire sciences, providing insights into flame structure and behavior [64, 65]. Thermal cameras, widely used in fire safety, detect emitted radiation independent of lighting conditions, enabling localization of hot spots and analysis of fire dynamics [66, 67]. Conventional thermal cameras operate in the LWIR range, but they integrate over the spectral range, losing valuable spectral information crucial for chemical identification.

Combustion-relevant molecules predominantly reflect, absorb, and emit radiation within the IR region (1–1000 µm) due to vibrational and rotational transitions. This makes IR cameras highly effective for selective probing of gas-phase, particulate, and hot surface materials with high sensitivity [68]. The fundamental vibrational modes of molecules are predominantly found in the MWIR region, and the LWIR region is primarily associated with deformation bands [69].

Although the LWIR range is not ideal for detailed chemical identification, LWIR cameras are particularly advantageous for remote sensing applications due to their affordability, availability, and widespread use in fire testing facilities compared to the more expensive, cooled MCT detectors required for MWIR imaging. However, conventional LWIR cameras lack the spectral resolution needed for chemical differentiation. While much of the literature on flame spectroscopy focuses on single-point measurements [70, 71, 72], hyperspectral imaging has shown promise for flame analysis and its application in the LWIR region remains unexplored [73, 74].

A cost-effective hyperspectral imaging system can be realized by combining a microbolometer-based LWIR camera with an SFPI. This approach provides spatially resolved hyperspectral data, enabling the identification of reaction zones within flames based on their spectral profiles. This study focuses on stable diffusion flames fueled by methane, ethane, propane, butane, acetylene, ethylene, and hydrogen.

7.2 Materials and Methods

7.2.1 Experimental Setup

The seven different fuel gases used in this study are listed in Table 7.1. Laminar, self-sustained flames were generated by igniting a manually regulated gas flow. The gases were supplied from pressurized canisters connected via approximately 1-meter-long tubes (Ø4 mm, PFA) to a blunt-tip needle (Ø0.8 mm, length 23 mm, B. Braun Melsungen AG, DE). Fuel and air were mixed at the needle exit (<0.1 mm) to produce flames ranging from 5 to 10 cm in height. To ensure stable combustion, air currents were minimized by turning off ventilation and limiting other activities in the laboratory. These precautions allowed for approximately steady flames during the 8-second acquisition period required to capture a hyperspectral image. All experiments were conducted within a two-hour window under controlled ambient conditions.

Table 7.1: List of fuels used for diffusion flame analysis.

Fuel type	Manufacturer	Purity (%)
Methane (CH_4)	Messer CANGas, DE	99.995
Ethane (C_2H_6)	Messer CANGas, DE	99.95
Propane (C_3H_8)	Messer CANGas, DE	99.95
Butane (C_4H_{10})	Guilbert Express, FR	N.A.
Acetylene (C_2H_2)	Linde, DK	>98.5
Ethylene (C_2H_4)	GHC Gerling Holz & Co., DE	99.9
Hydrogen (H_2)	Messer CANGas, DE	99.999

The experimental setup is depicted in Figure 7.1. The hyperspectral LWIR imager was positioned approximately 40 cm from the flame emerging from the needle. At this distance, each pixel samples an approximately 24 mm^2 area of the image plane. A long-wave pass filter with a 50% cut-on wavelength at 8.51 µm (1174.5 cm^{-1}, Andover Corporation, USA) was placed directly in front of the SFPI, and its transmittance spectrum is presented in the inset. The longwave pass filter was necessary to subdue water vapor emissions around 1250 cm^{-1} (Figure 7.5c). Additionally, a bandpass filter with a central wavelength of 10.26 µm (975 cm^{-1}) and an FWHM of 0.35 µm (34 cm^{-1}, Andover Corporation, USA) was positioned adjacent to the flame, in front of a hot plate maintained at

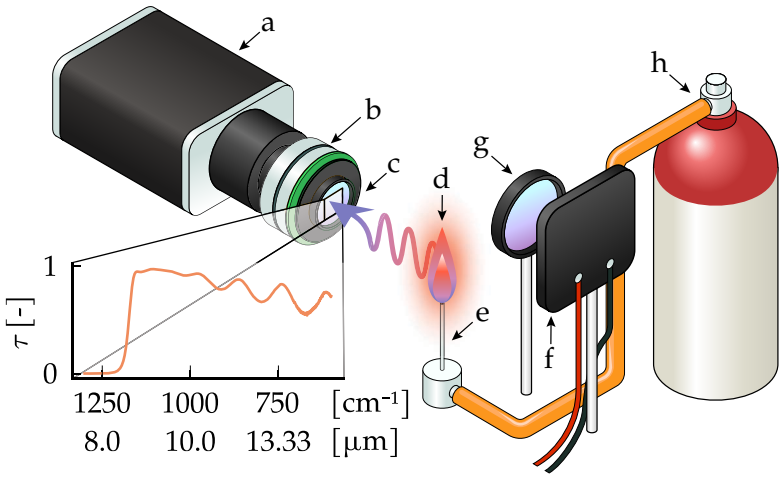

Figure 7.1: Schematic of the hyperspectral LWIR imager integrated into the experimental setup (not to scale). The system comprises the following components: a: a thermal camera, b: an SFPI, c: an 8.51 μm long-wave pass filter, d: a flame, e: a blunt-tip needle, f: a hot plate maintained at 80 °C, g: a 10.26 μm bandpass filter, and h: gas canister with regulator valve. The insert shows the transmittance profile of the long-wave pass filter (c).

80 °C. This filter is the external spectral reference to estimate the absolute cavity length.

7.2.2 Data Processing

A hyperspectral image was acquired for each fuel, and the only preprocessing of the data cubes before further analysis is baselining (Eq. (2.70)) and compensation of the spectral shift caused by varying incidence angles as described in section 4.4.

Regions of interest (ROIs) were selected based on the observed reaction zones within the flame (Figure 7.2a). ROI I, located near the flame base (8×40 pixels); ROI II, positioned within the luminous inner cone of the flame, if present (15×40 pixels, or 15×20 pixels for propane); and ROI III, situated above the flame in the outer non-luminous cone (25×40 pixels); ROI IV, bandpass filter placed in front of 80 °C hotplate used for spectral alignment (50×50 pixels). A mean interferogram is extracted from each ROI as depicted in Figure 7.2b. Shaded areas around each interferogram indicate one standard deviation.

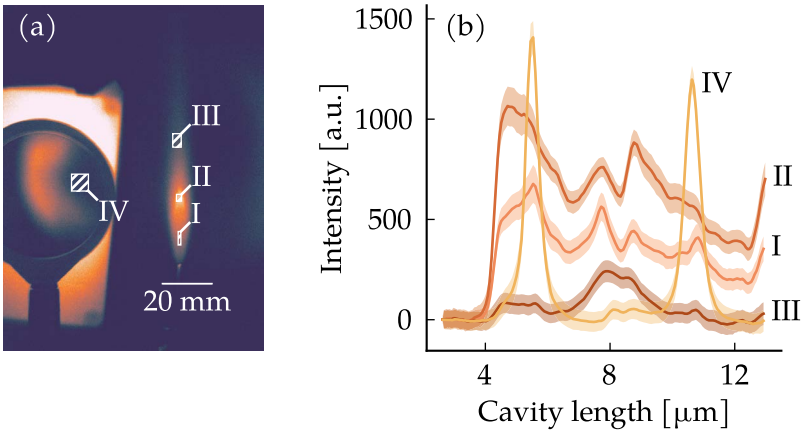

Figure 7.2: (a) Image form data cube showing propane frame at 8.8 μm cavity length. The four ROIs used to extract mean interferograms are overlayed in white. (b) Mean interferograms extracted from the regions depicted in (a). Shaded areas correspond to one standard deviation.

The selection of ROIs was based on the observation that different regions of the flames exhibited distinct spectral profiles and intensities. This observation is further supported by K-means clustering, which partitions data into k clusters by grouping points with similar characteristics based on their proximity to cluster centroids. In this study, $k = 4$ was used to segment the flames into three regions and a background (Figure 7.3). Notably, butane, acetylene, and ethylene exhibit a pronounced hot spot in the center of the flame, which further analysis attributes primarily to blackbody radiation from soot particles. While other fuels are also segmented into three regions, the central hot spot is less prominent.

Spectral Calibration

The spectral axes of the resulting data cubes were measured in terms of cavity length, calibrated using laser diode interferograms and the interferogram of the bandpass filter, as detailed in Figure 3.5.3. They must share a common spectral axis to enable direct comparison between data cubes. However, the nth channel of two different data cubes does not necessarily correspond to the same cavity length. This is illustrated in Figure 7.4, where the bandpass filter interferograms are shown as a function of spectral channel (Figure 7.4a) and cavity length (Figure 7.4b).

To standardize the spectral axes across data cubes, interpolation is re-

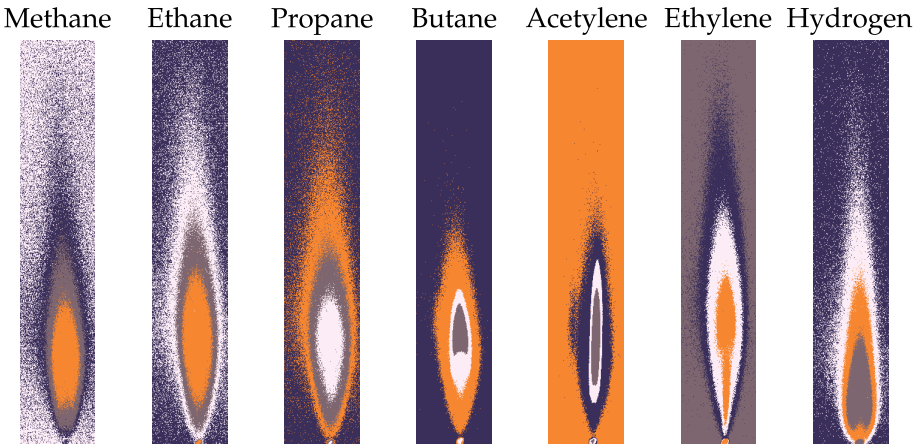

Figure 7.3: K-means clustering was applied to segment flames into four regions based on the interferogram associated with each pixel in the hyperspectral images. The colors assigned to each cluster are random, meaning that the same color across different data cubes may not consistently represent similar areas of the images (such as the background).

quired to align channel numbers with the same cavity lengths for all cubes. The interpolation range is determined by the longest initial cavity length (cavity length at the first channel) and the shortest final cavity length (cavity length at the last channel). The number of interpolation points is dictated by the data cube with the fewest channels, which in this case is 148. Direct comparisons can be performed once all data cubes are resampled to a common spectral axis.

The remapping technique described in subsection 5.3.2 was applied to associate the interferograms with their corresponding wavenumbers. However, the rescaling step outlined in Equation 5.36 was omitted in this case. Peak positions were then extracted from the remapped interferograms for further analysis.

Analysis Methods

To quantify the similarity between the extracted flame regions from each ROI, the Pearson correlation coefficient (ρ_{corr}) is employed, as defined in Eq. (5.37). $\rho_{\text{corr}} = 1$ indicates perfect correlation, $\rho_{\text{corr}} > 0.8$ is considered high correlation, and $\rho_{\text{corr}} < 0.5$ is regarded as low correlation. The entire interferograms (not the remapped versions) are used for the correlation analysis since valuable information is contained within the

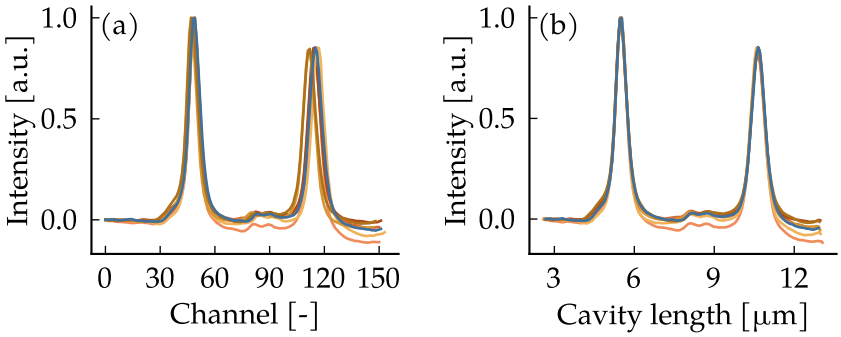

Figure 7.4: Mean bandpass filter interferograms extracted from each data cube (ROI IV). (a) Interferograms are shown as a function of channel number, while (b) presents the same data calibrated to cavity length.

overlapping tranmission orders.

For a more qualitative analysis, PCA is applied (section 2.6). Firstly, all data cubes are combined into one large data cube containing all seven flames, and SNV is applied to each pixel (Eq. (2.75)). PCA is then applied first to separate the flames from the background, enhancing the visibility and distinction of the flame regions. PCA is then applied a second time, and the resulting density scatter plot of the scores is analyzed to identify areas within and across multiple flames that correlate strongly and regions that exhibit significant differences.

7.3 Results and Discussion

7.3.1 Spectral Analysis of Hydrogen Flame

The images and interferograms (raw and remapped) for all flames are extensive and have therefore been included in the supporting information of the main paper, found on page 298. The extracted and remapped interferogram from ROI I of the hydrogen flame is shown in Figure 7.5a and Figure 7.5b. The superior spectral resolution of the second transmission order is evident, as four distinct spectral peaks at 1016 cm^{-1}, 964 cm^{-1}, 904 cm^{-1}, and 858 cm^{-1} can be resolved. In contrast, only the 964 cm^{-1} peak is discernible in the first order.

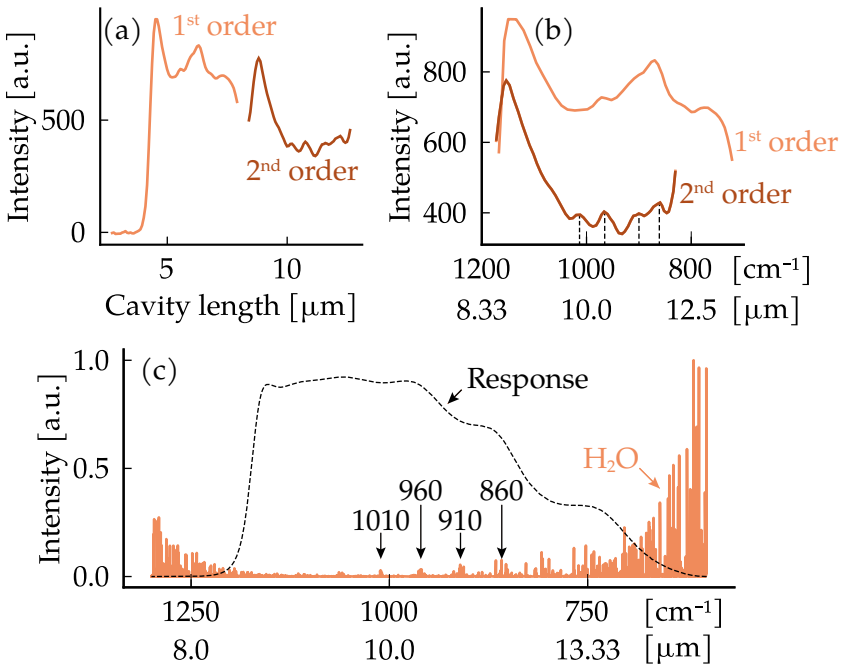

Figure 7.5: (a) Mean interferogram from ROI I of the hydrogen flame. Colors indicate the orders shown in the remapped interferogram in (b). (c) Normalized absorption spectrum of water vapor at elevated temperatures (1000K). The absorption spectrum is calculated using the HITRAN Application Programming Interface [75]. The combined response of the detector and the long-wave pass filter has been overlaid. The four peaks in the second-order remapped interferogram (Figure 7.5a) have been annotated.

Water is the only combustion product of hydrogen, and typically, it does not affect spectral measurements with the hyperspectral LWIR imager noticeably. However, its absorption features become detectable at elevated temperatures in the flame. The four peaks observed in the second transmission order (Figure 7.5b) are also found in the high-temperature absorption spectrum of water (Figure 7.5c). The reason that the peak locations do not precisely match is because of the limited spectral resolution of the SFPI ($\approx 40\ \mathrm{cm}^{-1}$).

7.3.2 Analysis of Regions of Interest

Peaks are identified in all remapped interferograms and summarized in the band assignment diagram in Figure 7.6. It highlights the spectral fingerprints exhibited by each flame across all three ROIs.

ROI I, situated near the base of the flame, is anticipated to exhibit the emission spectrum of the fuel or its early decomposition products before combustion. For ethane, an absorption band at 830 cm^{-1} (C–H bending) is expected based on its FTIR absorption spectrum [76]. The remapped interferogram lacks this band but exhibits a peak at 970 cm^{-1} which is consistently detected within ROI I for all tested hydrocarbons, with the exception of methane and acetylene. This feature is likely associated with ethylene (C–H wagging) near the flame base, aligning with previous studies documenting ethylene as a primary decomposition product in alkane combustion [77]. However, the strong signal from ethylene may mask weaker contributions from other combustion intermediates. These observations suggest that combustion reactions initiate very close to the flame base.

ROI II, located near the middle of the flame, shows that most flames, except methane and hydrogen, exhibit a distinct bright spot. Such luminous regions typically indicate soot formation, which results from incomplete combustion. Governed by flame temperature, soot particles emit significant blackbody radiation, contributing prominently to the emission signal [78]. This phenomenon is particularly pronounced in butane and acetylene flames whose interferograms closely resemble a blackbody spectrum. The increased blackbody radiation in these cases is likely due to the lower purity of the industrial-grade gases used. Based on the interferograms measured in ROI II, these findings differentiate between sooty and clean flames.

ROI III, located above the flame, is expected to primarily contain combustion products such as CO_2 and H_2O. This is supported by the presence of a peak observed for all hydrocarbon flames near a cavity length of 7.9 µm, corresponding to the bending mode of CO_2 within the 670–720 cm^{-1} absorption band [76]. Notably, this peak is absent in the hydrogen flame interferograms, which instead display distinct water vapor peaks, reflecting the absence of CO_2 as a combustion byproduct. Additionally, all flame interferograms exhibit distinct peaks or shoulders in ROIs II and III near cavity lengths of 4.7 µm and 8.7 µm (corresponding to 1132 cm^{-1} in the remapped interferograms), as well as a rising slope at longer cavity lengths (around 13 µm). These features are attributed to water vapor emissions, which are not filtered by the long-wave pass filter.

7.3.3 Pearson Correlation Coefficient Analysis

ρ_{corr} is calculated for all fuel combinations within each ROI and presented in Figure 7.7. ROIs I and II exhibit the most significant spectral differences among the analyzed fuel gases. In ROI I, the overall average ρ_{corr} is 0.82. Methane, ethylene, and hydrogen are the most dissimilar, with average ρ_{corr} values of 0.71, 0.70, and 0.82, respectively. Methane's distinctiveness primarily arises from the absence of peaks at cavity lengths of 5.6 µm and 10.8 µm (corresponding to 970 cm^{-1} in the remapped interferogram). These features, attributed to ethylene, are also absent in the hydrogen interferograms, which explains the relatively low correlation ($\rho = 0.65$) between ethylene and hydrogen. In contrast, ethane, propane, and butane demonstrate high spectral similarity, with average ρ_{corr} values of 0.90, 0.89, and 0.88, respectively.

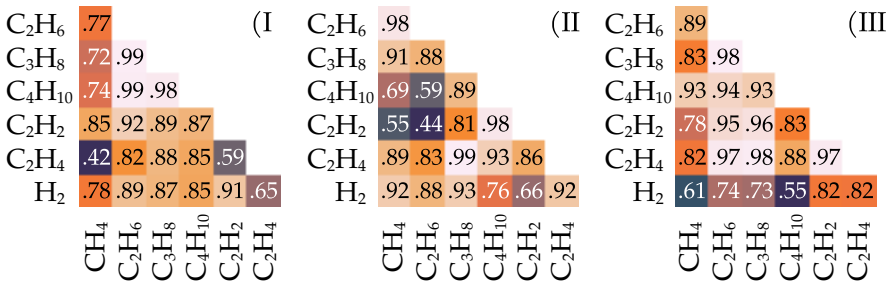

Figure 7.7: Pearson correlation coefficients calculated between flame interferograms sampled at ROIs I, II, and III, as shown in Figure 7.2a.

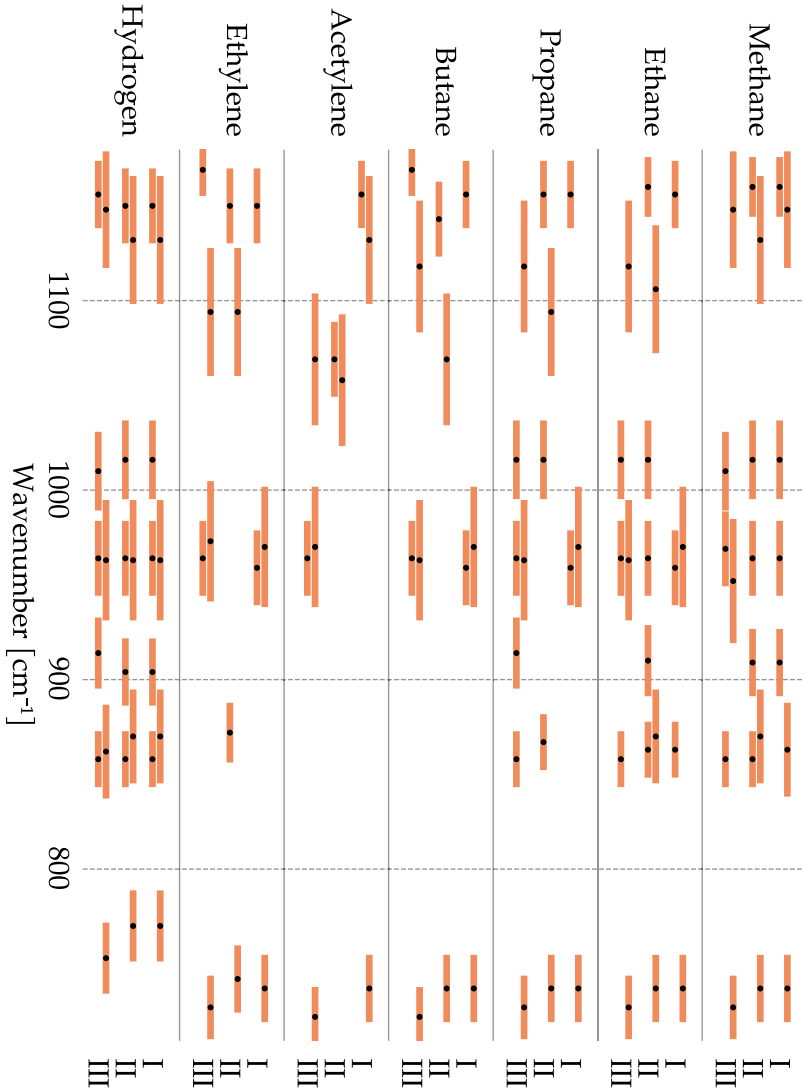

Figure 7.6: Spectral features extracted from remapped flame interferograms are presented with peak locations indicated by black dots. The bar widths represent the resolution of the SFPI at each wavenumber (Figure 4.17). Three flame ROIs are depicted, each represented by two bars: the upper bar corresponds to the first transmission order, while the lower bar corresponds to the second transmission order.

The most considerable blackbody contributions were observed in ROI II. Notably, the interferograms of butane and acetylene exhibit significant blackbody contributions, resulting in lower average ρ_{corr} values of 0.81 and 0.72, respectively. ROI III exhibits the highest correlations since combustion reaction products are expected to be the primary ones. Across all hydrocarbons, the average ρ_{corr} is 0.91. This suggests that above the flame, the dominant species are H_2O and CO_2, while in the case of hydrogen, only H_2O is present, yielding the lowest average ρ_{corr} of 0.71.

7.3.4 Principal Component Analysis

PCA allows for the simultaneous analysis of differences and similarities across all flames. However, the background contributes significantly to the overall signal and is removed using PC 1, as shown in Figure 7.8a. PC 1 effectively separates the background from the flame, enabling the exclusion of background pixels. After this step, the isolated flame is depicted in Figure 7.8b. PCA is then reapplied to the filtered portion of the data cube, as shown in Figure 7.9.

Figure 7.9 reveals that some background pixels remain unfiltered, al-

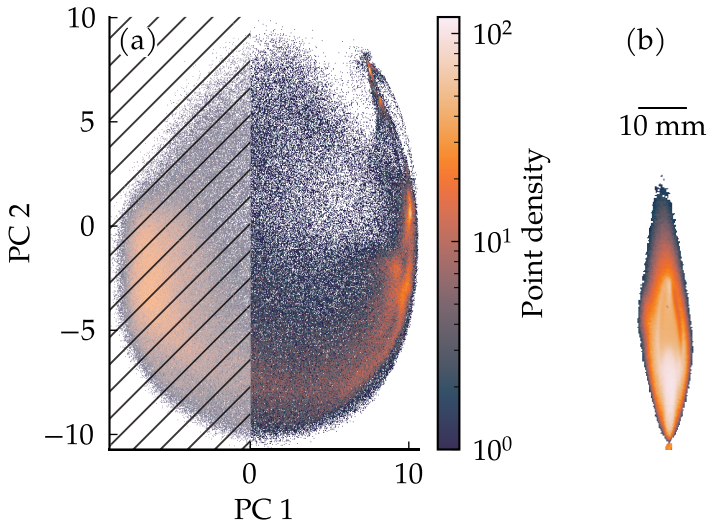

Figure 7.8: (a) Density scatter plot of the first two PCs, with the hatched area indicating excluded data. (b) PC 1 of propane, excluding pixels within the hatched area in (a).

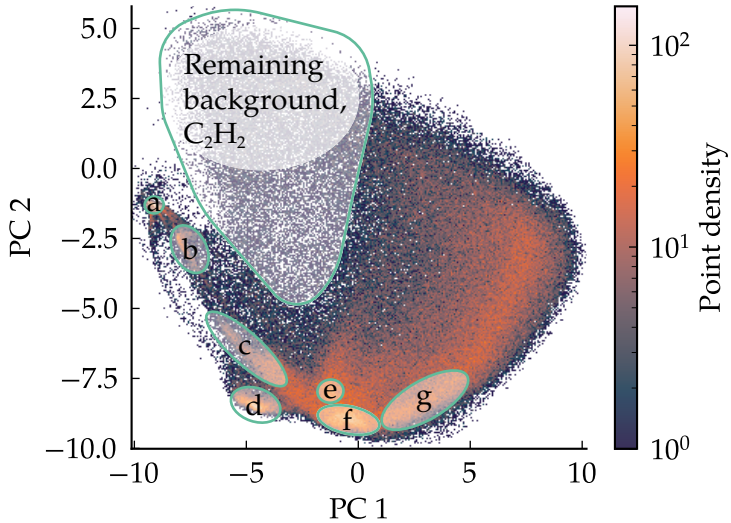

Figure 7.9: Density scatter plot of PC 1 and PC 2 scores on PCA calculated after removing background as shown in Figure 7.8. a: Acetylene signal, b: blackbody signal, c: ethylene signal, d: hydrogen signal, e: methane, f: areas between hot spots in flames, g: upper parts of ethylene containing flames.

though these are exclusively associated with the acetylene flame, as indicated. Distinct hot spots are now discernible, labeled from 'a' to 'g', illustrating how various flames and flame regions are separated in PCA space. Based on PC 1 and PC 2 alone, several features can be distinguished: (a) the acetylene signal from ROI II; (b) blackbody emissions from flames, excluding acetylene; (c) ethylene signals from flames where ethylene is present as an intermediate combustion product; (d) hot water vapor emissions from the hydrogen flame; (e) the methane flame, primarily from ROI I; (f) intermediate regions between hot spots in ROIs I and II; and (g) the upper portions of flames containing ethylene (between ROIs II and III).

Figure 7.10a illustrates the explained variance for each PC in the PCA model. A steep drop-off is observed for the first five PCs, accounting for 66.7% of the total variance. However, 54 PCs are required to capture 90% of the variance. This indicates substantial flame variability that few PCs cannot effectively capture. This variability may be attributed to minor turbulence within the flames or the continuous chemical reactions occurring along the flame front, leading to dynamic changes in species

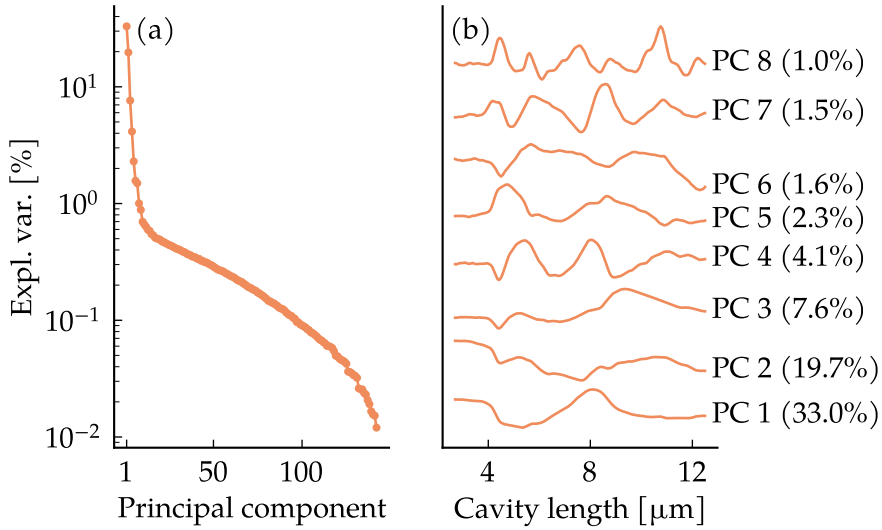

Figure 7.10: (a) Scree plot showing the explained variance of each principal component. (b) The first eight principal components. The percentages indicated in the parentheses indicate the explained variance of that component. Graphs have been offset for clarity.

concentrations and corresponding spectral profiles along the flame's length. The variation could also be attributed to the 8-second acquisition time for capturing the data cube.

Figure 7.10b presents the loadings for the eight most significant PCs, highlighting their contribution to distinguishing different signals. PC 1 strongly correlates with the CO_2 signal observed at the top of hydrocarbon flames (ROI III). In contrast, blackbody emissions from butane and acetylene flames are strongly anti-correlated with PC 1. Notably, PC 4 and PC 8 strongly correlate with the ethylene signal, while water vapor emissions from hydrogen flames appear to be inversely correlated with PC 2 and PC 4.

The Pearson correlation analysis and PCA emphasize the value of spatial information provided by a hyperspectral *imager*, which captures spectral variations across flame regions that single-point measurements cannot resolve. Radiometric calibration could enable temperature mapping and species concentration estimates, while shorter acquisition times would enhance temporal resolution, allowing analysis of turbulent flames.

7.4 Conclusions

Hyperspectral LWIR images of flames from seven gaseous fuels (methane, ethane, propane, butane, ethylene, acetylene, and hydrogen) were obtained using the HSC. Three distinct reaction zones within the flames were identified, each characterized by unique spectral signatures. Ethylene was consistently detected as an intermediate combustion product for all tested hydrocarbons except methane and acetylene. Additionally, multiple rotational and vibrational water vapor transitions were observed across all samples, accompanied by significant contributions from CO_2 emissions in the hydrocarbon flames.

This study demonstrates the effectiveness of hyperspectral LWIR imaging, developed from an ordinary thermal camera, for flame characterization. The combination of high spatial resolution and detailed spectral information provides a deeper understanding of flame dynamics, enabling the identification of reaction zones and spectral features that are beyond the scope of traditional single-point measurements.

8. Various Preliminary Studies

This chapter presents several smaller studies conducted during the PhD project. These include some incomplete results that nonetheless provide valuable insights into the operation of the hyperspectral imager and its application in the analysis of various materials. The chapter begins with a discussion on the mathematical treatment of interferograms when combining them, in contrast to conventional FTIR-acquired spectra. This is followed by an examination of the relationship between interferogram intensity and the concentration of gases or solutions. Subsequently, application examples are presented, illustrating the use of the imager to analyze different types of minerals and gases, as well as the effects on interferograms when the subjects are colder than the detector.

8.1 Combination of Incidence Spectra

In transmission spectroscopy, the combined transmission spectrum of multiple samples can typically be calculated by taking the element-wise product of the transmission spectra of the individual samples. However, in the case of the interferograms recorded by the HSC, each data point represents a weighted sum of transmitted wavelengths across the detector's sensitive range. Consequently, the relationship between the transmission spectra and the interferograms is more complex and requires detailed analysis, which is presented below.

Here, the transmission spectra of K distinct samples are considered. The combined transmission spectrum is expressed as the element-wise product of the individual transmission spectra, given by:

$$\boldsymbol{\phi} = \boldsymbol{t}^{(1)} \circ \boldsymbol{t}^{(2)} \circ \cdots \circ \boldsymbol{t}^{(K)} = \prod_{i=1}^{K} \boldsymbol{t}^{(i)} \tag{8.1}$$

The interferogram recorded by the HSC, $\boldsymbol{\psi}$, is the dot product of $\boldsymbol{t}$ and the system matrix $\boldsymbol{\mathcal{A}}$. To simplify, consider a single sample where the interferogram is expressed as:

$$\boldsymbol{\psi}^{(1)} = \boldsymbol{\mathcal{A}}\boldsymbol{t}^{(1)} = \begin{bmatrix} a_{1,1}t_1^{(1)} + a_{1,2}t_2^{(1)} & \cdots & +a_{1,N}t_N^{(1)} \\ a_{2,1}t_1^{(1)} + a_{2,2}t_2^{(1)} & \cdots & +a_{2,N}t_N^{(1)} \\ \vdots & \cdots & \vdots \\ a_{M,1}t_1^{(1)} + a_{M,2}t_2^{(1)} & \cdots & +a_{M,N}t_N^{(1)} \end{bmatrix} \tag{8.2}$$

Now, consider the case of two samples. The combined interferogram is given by:

$$\boldsymbol{\psi}^{(1+2)} = \boldsymbol{\mathcal{A}}\boldsymbol{\phi} = \begin{bmatrix} a_{1,1}t_1^{(1)}t_1^{(2)} & \cdots & +a_{1,N}t_N^{(1)}t_N^{(2)} \\ a_{2,1}t_1^{(1)}t_1^{(2)} & \cdots & +a_{2,N}t_N^{(1)}t_N^{(2)} \\ \vdots & \cdots & \vdots \\ a_{M,1}t_1^{(1)}t_1^{(2)} & \cdots & +a_{M,N}t_N^{(1)}t_N^{(2)} \end{bmatrix} \tag{8.3}$$

Thus, $\boldsymbol{\psi}^{(1)} + \boldsymbol{\psi}^{(2)} \neq \boldsymbol{\psi}^{(1)}\boldsymbol{\psi}^{(2)} \neq \boldsymbol{\psi}^{(1+2)}$ meaning that it is not possible to combine the interferograms directly in a linear manner.

8.2 Relationship Between Absorbance and Interferogram Intensity

Transmission spectroscopy is commonly employed to infer the concentrations of solutions based on their absorbance spectra. Since interferograms do not follow additive or multiplicative rules when combining transmittance spectra of different absorptive species, it is of particular interest to examine how variations in concentration influence interferograms. The relationship between absorbance A' and concentration c' is governed by Beer's Law, as expressed in Eq. (8.4) [79]:

$$A' = \alpha' l c' \tag{8.4}$$

where α' represents the absorptivity (not to be confused with the absorptance $\alpha = 1 - 10^{-A'}$), and l denotes the path length through the absorbing medium. The relationship between transmittance and absorbance is given in Eq. (8.5):

$$\mathcal{T} = 10^{-A'} \tag{8.5}$$

Equation Eq. (8.5) is applied to convert an FTIR transmittance spectrum of ammonium vapor into an absorbance spectrum, as shown in Figure 8.1. The concentration of the ammonium vapor is not explicitly known and is assumed to be 100% for subsequent calculations. Using Eqs. (8.4) and (8.5), transmittance spectra are computed for six concentrations ranging from 3.1% to 100%.

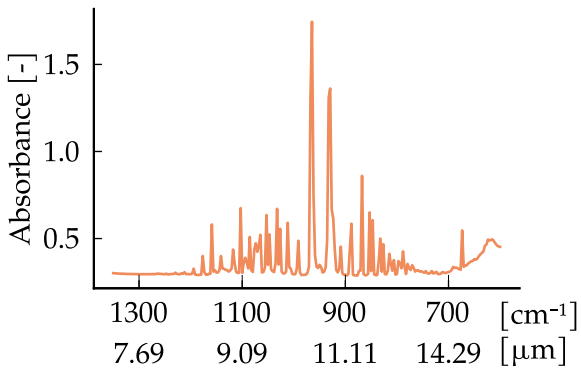

Figure 8.1: Absorbance spectrum of ammonia vapor, converted from an FTIR transmittance measurement. The vapor concentration is unknown.

The computed transmittance spectra are then utilized to estimate the interferograms via Eq. (5.32), with the results presented in Figure 8.2a. Plotting the interferogram intensity at a cavity length of 10.9 µm against the concentration yields an R^2 value of 0.97 for the linear fit (Figure 8.2b). When the same interferograms are plotted using a logarithmic y-axis (Figure 8.2c), the corresponding plot of logarithmic intensities versus concentration results in an R^2 value of 0.998 (Figure 8.2d). This demonstrates that while not perfect, the linear relationship between concentration and interferogram intensities is more closely preserved when working with logarithmic intensities, similar to traditional transmission spectroscopy techniques.

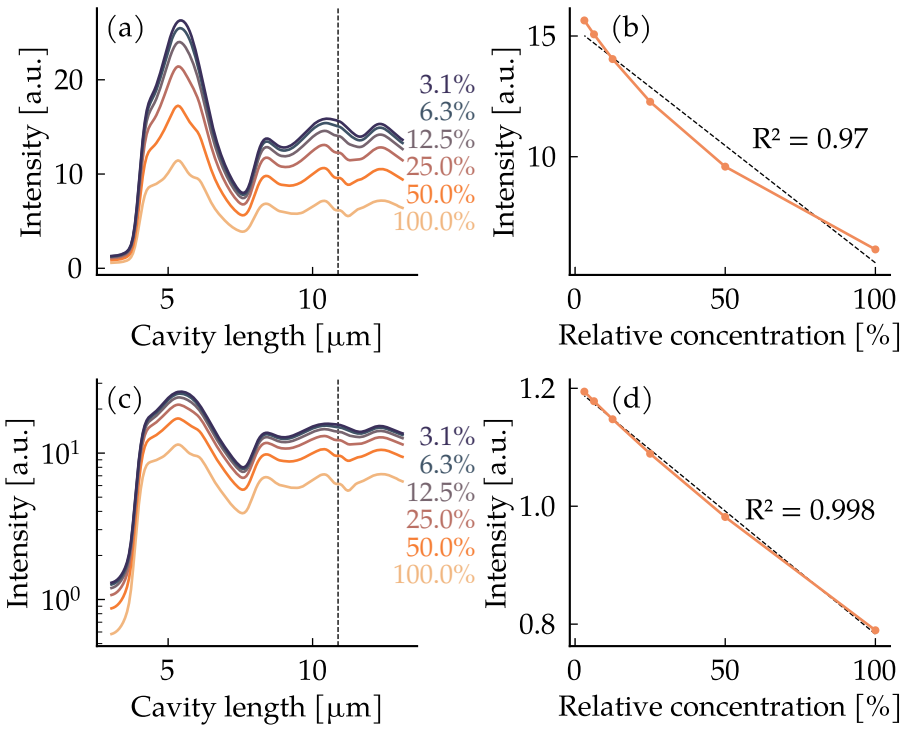

Figure 8.2: (a) Interferograms for different concentrations of ammonia vapor, with percentages indicating relative concentrations and corresponding color codes. (b) Interferogram intensity at a cavity length of 10.9 µm (dashed line in (a)), with a linear fit. (c) Same interferograms as in (a), but displayed with logarithmic intensities, using the same color scheme. (d) Logarithmic intensities at 10.9 µm cavity length (dashed line in (c)), with a linear fit.

8.3 Imaging Reflections

One proposed modification to the experimental method for plastic classification involved analyzing the reflected signals of samples instead of their emission signals (subsection 6.3.3). This section presents preliminary studies investigating reflection signals — not on plastics, but on sapphire (Ø: 30 mm) and fused silica (Ø: 50 mm) substrates. These experiments provided valuable insights into how the imager acts when measuring subjects that are colder than the detector itself.

8.3.1 Experimental Setup

The experimental setup is illustrated in Figure 8.3a. The samples were stacked to ensure the same reflection angle. Figure 8.3b shows a cropped image of a data cube showing a heating lamp reflection in the surface of the fused silica and sapphire samples. Various light sources were used for reflection, including a heat lamp, a hotplate with a glass top, and a

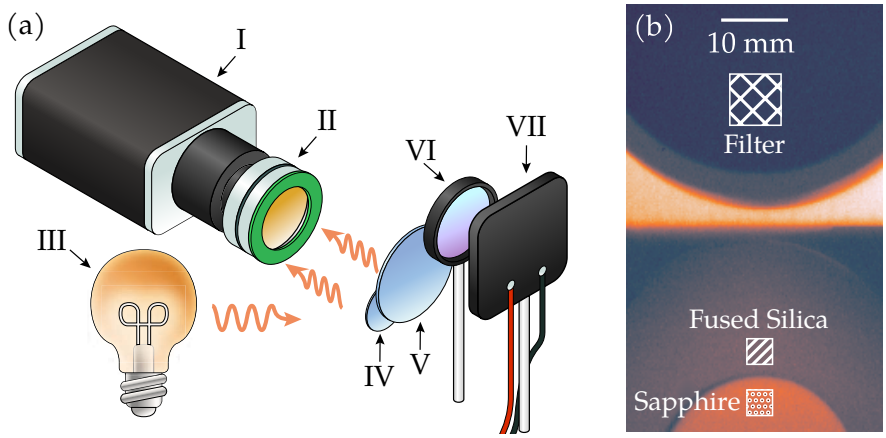

Figure 8.3: (a) Experimental setup for investigating reflection signals. The setup includes: (I) a thermal camera, paired with (II) an SFPI positioned in front of it; (III) a reflection source, which may consist of a heat lamp, hot plate, metal container filled with liquid nitrogen, or ambient room light; (IV) a sapphire substrate; (V) a fused silica substrate; and (VI) an 8.226 µm central wavelength bandpass filter placed in front of (VII) a hot plate, used for spectral alignment of the measurements. (b) A cropped data cube highlighting the regions used to extract average interferograms. For the bandpass filter, a 30×30-pixel region is sampled, while 15×15-pixel regions are analyzed for the sapphire and fused silica samples.

stainless steel container filled with liquid nitrogen (LN). The LN-filled container was included to assess whether reflections colder than the substrate could be detected. The surface temperature of the container was not directly measurable, as the K-type thermocouple provided no readings below −150 °C. For the purpose of this analysis, the container surface temperature is assumed to be −150 °C, even though the temperature of LN is −196 °C.

The substrate temperatures were also varied. Measurements were conducted with the samples at ambient temperature (21 °C), heated to 80 °C, and after immersion in LN. An 8.226 µm bandpass filter (Andover Corporation, US) placed in front of an 80 °C hotplate was used for spectral alignment of the data cubes. The only preprocessing done the the data cubes was baselining (Eq. (2.70)).

8.3.2 Results and Discussion

Reflections of Samples at Ambient Temperature

The interferograms averaged from 15×15-pixel regions of fused silica (Figure 8.4a) and sapphire (Figure 8.4b) reveal distinct differences between the materials. For the fused silica, peaks at cavity lengths of 4.6 µm and 9.1 µm are observed, while sapphire shows peaks at 6.4 µm and 12.1 µm. Using Eq. (5.32) and Figure 5.10a, these peaks can be attributed to spectral features at approximately 1125 cm^{-1} for fused silica and 875 cm^{-1} for sapphire, consistent with literature findings [80, 81].

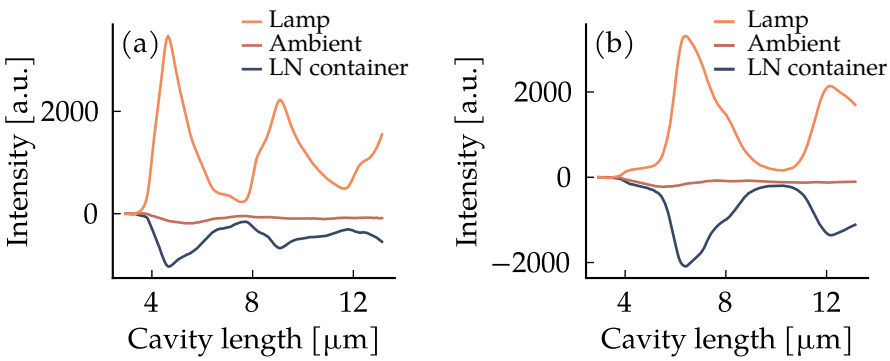

Figure 8.4: Interferograms of reflectance signal in (a) fused silica and (b) sapphire. LN is an abbreviation for liquid nitrogen.

Fused silica is mostly opaque at wavenumbers below 1500 cm^{-1}, where it primarily absorbs, except for a prominent reflection peak around 1125 cm^{-1}. This reflection peak is what is detected in the interferogram. In contrast, sapphire exhibits low reflectance at wavenumbers above 900 cm^{-1}, below which its reflectance rapidly increases to near unity, extending to approximately 600 cm^{-1}. This abrupt change in reflectance accounts for the rising slope seen in the sapphire interferograms (Figure 8.4b). The trough near a cavity length of 9 µm is caused by the lack of reflection signals at wavenumbers above 900 cm^{-1}, which also explains the reduced signal strength at the beginning of the first transmission order (below 5.4 µm cavity length).

The reflection of the lamp produces a strong positive signal, as intuitively expected. The reflection of the ambient environment is relatively weak, making it difficult to distinguish between fused silica and sapphire under these conditions. Additionally, most of the reflected signal here is negative, indicating that the samples and the environment are at a lower temperature than the detector (approximately 21 °C versus approximately 30 °C of the detector). Interestingly, and maybe unintuitively, the reflection from the LN-filled container creates an almost perfect inverted mirror image of the lamp's reflection, reflected across the zero line. The negative signal indicates that the net radiant flux is negative relative to the initial position of the SFPI.

If the sample's reflectance were unity, the camera would capture the source's radiation directly. However, the reflectance of the samples is less than unity, and their transmittance in the LWIR region is nearly zero. This implies that any light not reflected is absorbed. Consequently, in regions where the reflection signal is minimal, the camera effectively images a sample resembling a graybody at approximately 21 °C. This explains why, in areas of low sample reflectance, the reflections of both the lamp and the LN-filled container converge toward the interferogram of the ambient reflection.

Reflections of Samples at 80 °C

The sample temperature was increased to 80 °C by mounting the samples on a hot plate. To replace the heat lamp reflection, a hot plate with a glass top was used, allowing for temperature control. However, a thermocouple was not used to validate the actual temperatures of the

hot plate or the samples. Consequently, the temperatures reported in Figure 8.5 are based solely on the hot plate's settings.

Reflection interferograms for both samples are shown in Figure 8.5, with reflection temperatures ranging from −150 °C to 150 °C. Additionally, the emission interferogram of the hot plate set to 150 °C is included. The hot plate is not a perfect blackbody, evident from features such as the shoulder at a cavity length of 4.6 µm. The hot plate interferogram has been normalized to the highest intensity reflection.

Notably, the regions of low reflection (Figure 8.5) correspond to the cavity lengths where the interferogram intensities align across all reflection temperatures. Specifically, this occurs at 7.6 µm and 11.7 µm for fused silica, and below 5.4 µm and at 10.2 µm for sapphire. This alignment arises because, in these ranges, the detected signal primarily consists of emitted light from the samples, which is maintained at a constant temperature of approximately 80 °C, resulting in similar interferogram intensities across reflection temperatures.

The spectral profiles of both samples vary as the temperature of the reflection source changes, altering the ratio of emitted to reflected radiation. Notably, sapphire (Figure 8.5b) exhibits a shift toward longer

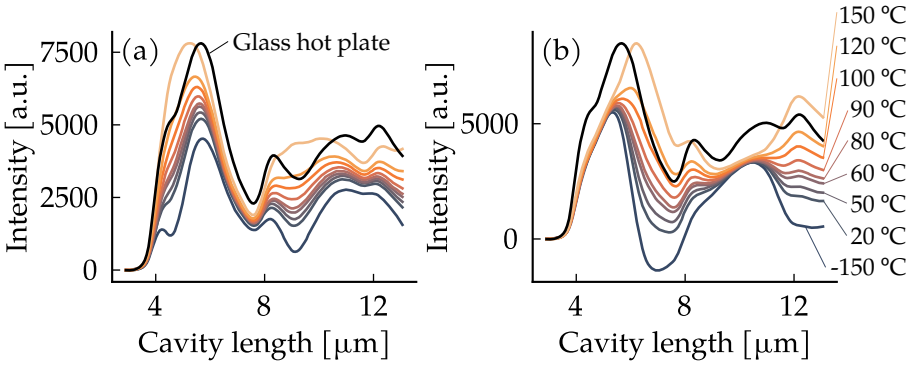

Figure 8.5: (a) fused silica and (b) sapphire, both heated to 80 °C with reflections of a glass hot plate set to different temperatures as indicated by the temperatures in (b). To reach a temperature ≈ −150 °, a metal container filled with liquid nitrogen was used instead. The same color legend is used in both (a) and (b). The black interferogram is a direct measurement of the 150 °C glass hot plate normalized to the highest value of the reflection signal in (a) and (b), respectively.

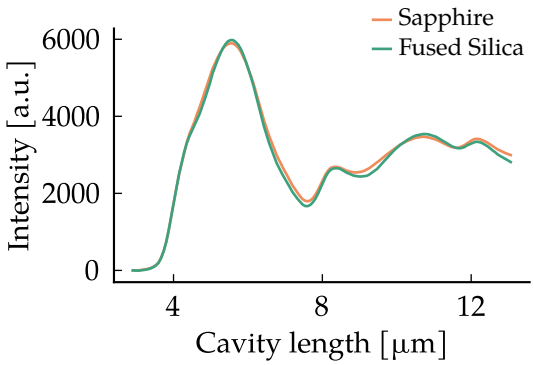

Figure 8.6: Interferograms of glass hot plate set to 90 °C reflected off sapphire and fused silica heated to 80 °C. The same interferograms can be found in Figure 8.5.

cavity lengths as the emitter temperature increases, causing the interferograms to resemble the reflection signal shown in Figure 8.4b. Interestingly, when the temperature of the reflection source matches that of the samples, there is minimal difference between the interferograms of the sapphire and fused silica samples (Figure 8.6).

This scenario also highlights a discrepancy between the two hot plates used in the setup. The glass hot plate in the reflection source had to be set to 90 °C to match the temperature of the samples on another hot plate set to 80 °C. When the temperature of the samples and the reflection source are equal, the reflected and emitted signals become balanced. Since the samples have negligible transmittance, any light not reflected is absorbed and thus also emitted. As a result, both samples appear to behave as blackbodies, with the reflected and emitted contributions to the signal in equilibrium.

An interesting study involves examining how the reflected signal is influenced by a reflection source with a distinct spectral signature. To investigate this, a gas cell filled with ethylene was placed between the glass hot plate and the sapphire and fused silica samples, ensuring that the radiation reflected off the samples passed through the gas. The results of these measurements are shown in Figure 8.7, alongside the transmission interferogram of the ethylene gas cell placed in front of the glass hot plate.

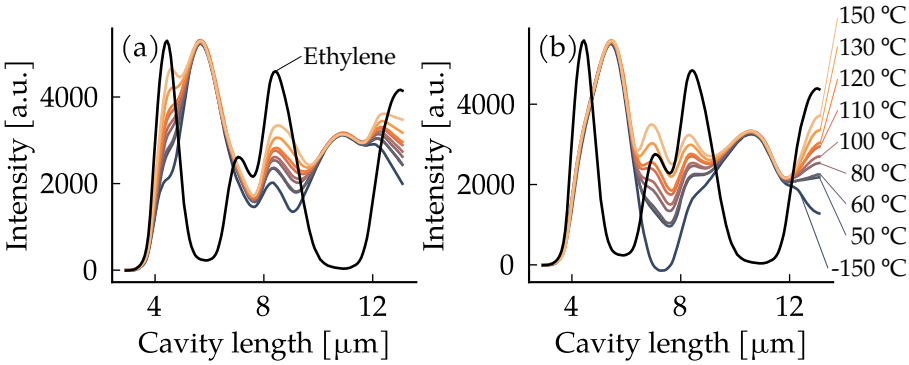

Figure 8.7: (a) fused silica and (b) sapphire, both heated to 80 °C with reflections of an ethylene gas cell in front of a glass hot plate set to different temperatures as indicated by the temperatures in (b). To reach a temperature ≈ -150 °, a metal container filled with liquid nitrogen was used instead. The same color legend is used in both (a) and (b). The black interferogram is a direct measurement of the ethylene gas cell in front of the 150 °C glass hot plate normalized to the highest value of the reflection signal in (a) and (b), respectively.

The results clearly demonstrate that in regions where ethylene absorbs nearly all radiation, the recorded signal remains constant regardless of the glass hot plate's temperature. In these regions, the hyperspectral imager detects only the emission signal from the samples. This behavior is observed in the bands centered at approximately 5.8 μm and 10.8 μm cavity lengths. Outside these absorption bands, the reflected interferograms vary with changes in the reflection source temperature, provided the samples are reflective within those regions. For instance, fused silica at 7.6 μm and sapphire below 5.4 μm cavity lengths exhibit low reflectance, and consequently, changes in the reflected source temperature do not affect the signal in these regions.

Reflections of Samples at -196 °C

To complete the reflection studies, the samples were cooled using LN to observe how the reflections appear when the emission signal from the samples is minimal. The interferograms shown in Figure 8.8 illustrate the results of this experiment and reveal that, as long as the samples exhibit some absorptivity (Figure 8.4), the interferogram intensity remains very low. Only in regions where the samples have the highest reflectance do the interferograms of the heat lamp and ambient reflections approach

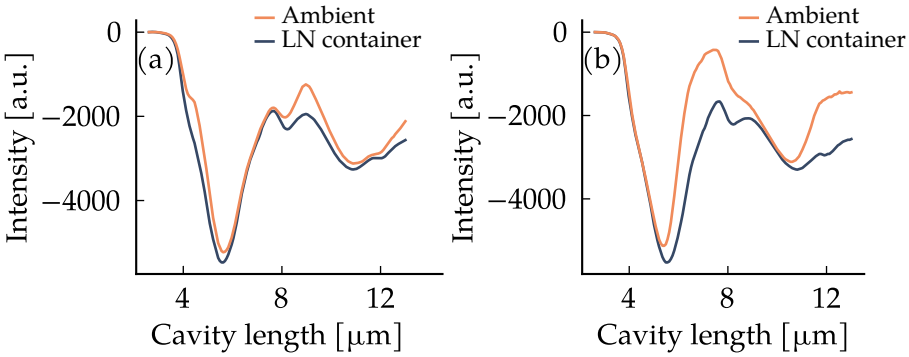

Figure 8.8: Interferograms of reflectance signal in (a) fused silica and (b) sapphire, both submerged in liquid nitrogen (LN). The interferograms represent 40×40-pixel averages.

an intensity close to zero, as seen most prominently with sapphire in Figure 8.8b.

Measurements with reflections from the heat lamp were also performed, but these signals appear to closely overlap with the reflection signal of the background emissions ("Ambient" in Figure 8.8). This could suggest that the reflection angle of the heat source was insufficient for the camera to capture it effectively, as the heat lamp's signal should be significantly stronger, given that the reflection is the primary contributor to the signal, and should look similar to Figure 8.4. Alternatively, it is possible that the detector's response is not entirely linear across the range; however, the signals do not show evidence of saturation. Given more time, it would have been interesting to perform the measurement again to clarify

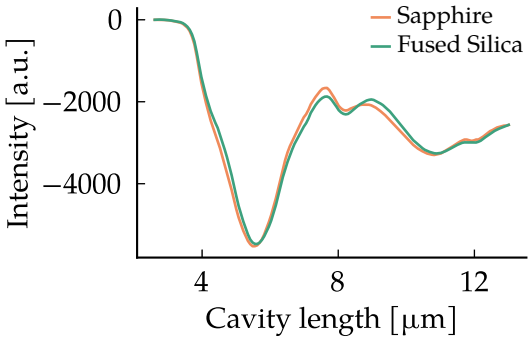

Figure 8.9: Intererograms of the LN container reflection presented in Figure 8.8.

whether this was a physical effect or a mistake in the experimental setup.

Finally, when the radiation from the LN-filled container is reflected off the samples, the detected signal shows minimal variation, as depicted in Figure 8.9. This result mirrors the findings presented in Figure 8.6, indicating that for reflections from broadband sources, the surface temperatures of the samples and the emitter must differ to effectively distinguish between them.

These experiments demonstrate that the spectral signature of illumination sources significantly influences the recorded signal. By selecting sources with specific spectral profiles, it is possible to isolate the signal contributions from the subject's emission and the source's reflection, as shown in the ethylene measurements. Furthermore, since the detector is sensitive to LWIR radiation, replacing heat sources with those colder than the detector does not eliminate reflections; rather, it reverses the direction of radiative transfer. As a result, the HSC records an inverted interferogram compared to a hot source. Expectedly, when there is no flux difference between objects in the scene, reflection sources, and the detector, the signal is minimal, preventing material differentiation.

8.4 Imaging Minerals

Many minerals exhibit distinct spectral signatures in the LWIR regime. This section presents preliminary studies on reflection measurements conducted on a variety of mineral samples, emission measurements of gemstones (including diamonds), and a hyperspectral image of a limestone cliff face containing flint stone deposits.

8.4.1 Imaging Mineral Samples

Hyperspectral images of 21 mineral samples were acquired. Figure 8.10 shows a single frame from the data cube, with a mask applied to exclude the background, ensuring that only the mineral samples are analyzed. The analyzed samples include magnetite, tourmaline, apatite, pyroxene, quartz, ilmenite, serpentine, epidote, biotite, feldspar, galena, pyrite, calcite, mica, plagioclase, garnet (two samples), sphalerite, chalcopyrite, fluorite, and hornblende. The samples were placed on a table, with the hyperspectral imager positioned 75 cm directly above and two halogen lamps angled at approximately 60°relative to vertical to illuminate the samples. Due to the angle and the non-uniform surfaces of the samples, specular reflections were not achieved uniformly across all samples, leading to unequal signal contributions.

No spectral reference was used for these measurements; thus, only rela-

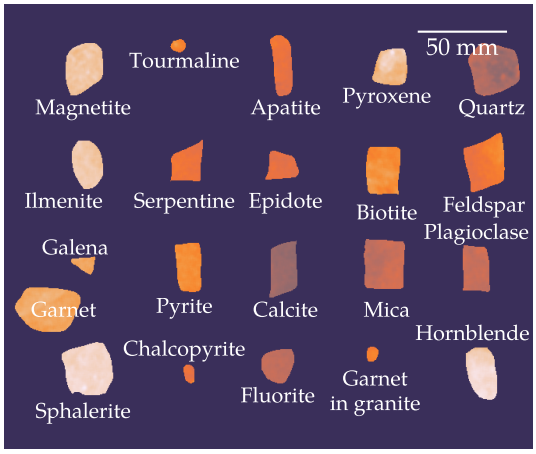

Figure 8.10: Mineral samples with the background excluded using masking.

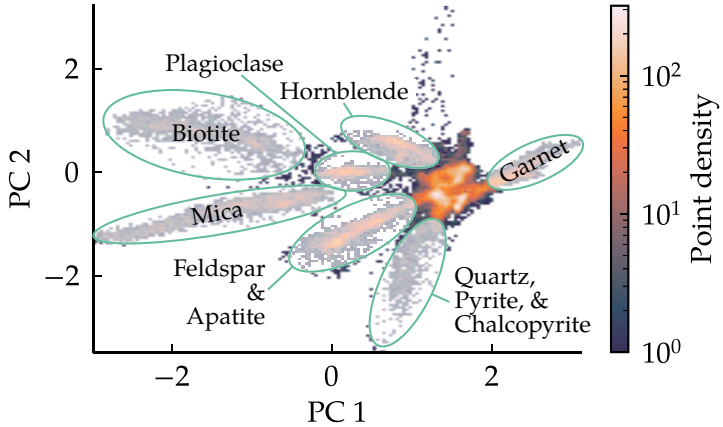

Figure 8.11: Density scatter plot of PC 1 and PC 2 scores for the mineral samples (Figure 8.10). Annotated clusters indicate specific minerals.

tive cavity expansion was derived from the laser diode interferograms. Consequently, it was not possible to correct for angular spectral shifts since the absolute cavity length was unknown.

Apart from masking the background, the only preprocessing applied was SNV normalization. Subsequently, PCA was performed, and the density scatter plot of the PC 1 and PC 2 scores is shown in Figure 8.11. Distinct clusters corresponding to specific minerals are evident, as annotated in the figure. A blackbody reference sample, as used in the plastic experiments (chapter 6), could enhance spectral detail extraction. However, it remains uncertain whether all minerals possess distinguishing spectral features in the LWIR regime. It should also be noted that since the absolute cavity length is unknown, it is not possible to compensate for the angular spectral shift (section 4.4).

The PCA scree plot (Figure 8.12a) reveals an elbow point at the seventh component. The loadings of the first seven PCs are shown in Figure 8.12b, where the first two components indicate that the clustering in Figure 8.11 is primarily influenced by the locations of the first and second peaks in the interferograms.

K-means clustering was applied to the first seven PCs using $k = 21$ clusters, with the resulting class labels shown in Figure 8.13. The colors indicate the class assigned to each pixel.

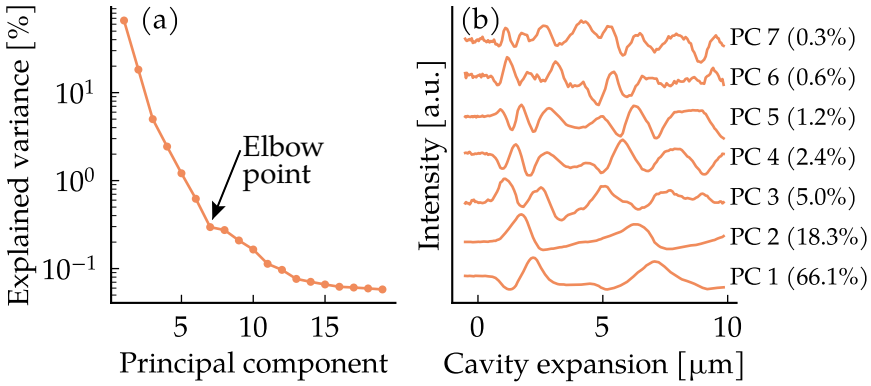

Figure 8.12: (a) Scree plot showing the explained variance of the PCA model, with an elbow point at PC 7. (b) Loadings of the first seven PCs.

The results reveal that not all minerals could be uniquely classified. For instance, magnetite, tourmaline, galena, and ilmenite were grouped into a single cluster, likely due to minimal or no spectral differences. Similarly, serpentine and epidote were clustered together. Conversely, samples such as garnet, pyroxene, biotite, mica, quartz, and feldspar were assigned multiple class labels, which may reflect chemical variations within the minerals or the influence of differing reflection angles from the multifaceted surfaces of the crystals.

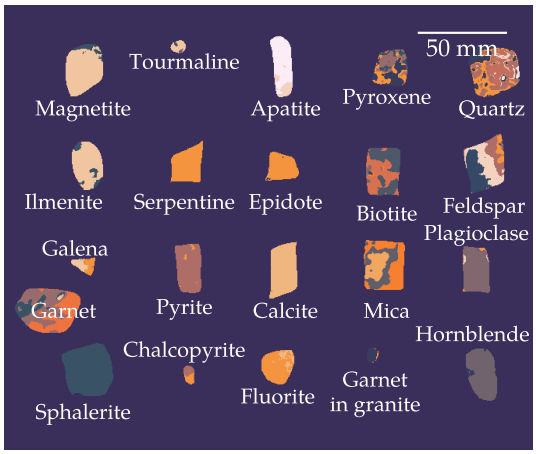

Figure 8.13: K-means clustering based on the first seven PCs, with $k = 21$ clusters. Colors correspond to the assigned class labels.

Reflectance FTIR measurements of the samples were not conducted, making it challenging to determine the exact spectra entering the camera or to assess which samples could theoretically be distinguished. Further studies are needed to optimize lighting angles and configurations to enhance the detection of reflected signals. Employing a more diffuse light source could also reduce angle dependence, simplifying the analysis of signals from samples with multifaceted surfaces.

8.4.2 Imaging Gemstones

This section presents measurements of gemstones heated to 100 °C on a hotplate. The experiments were conducted by colleague Anders L. Jørgensen in collaboration with DSEF German Gem Lab. A list of the gemstones analyzed in this study is provided in Table 8.1. The Type IaAB diamond is a natural diamond with a relatively high nitrogen content, often giving it a yellow tint, as shown in Figure 8.14. In contrast, the Type IIa diamond is a naturally occurring diamond with very low nitrogen content, making it significantly more transparent.

The data processing steps included compensation for angular spectral shift, baselining as presented in Eq. (2.70), blackbody compensation as described in subsection 6.2.2, and SNV normalization. The blackbody reference was a piece of aluminum coated with Surrey Nanosystems Vantablack [82]. A mask was applied to exclude the background, isolating the gemstones for analysis. The mean interferograms for each gemstone are shown in Figure 8.17 (page 204).

PCA was performed on the masked data cube, and the score plot for PC 1 and PC 2 is presented in Figure 8.16. The results indicate that all but quartz and GGG (Gadolinium Gallium Garnet), as well as HPHT (High-

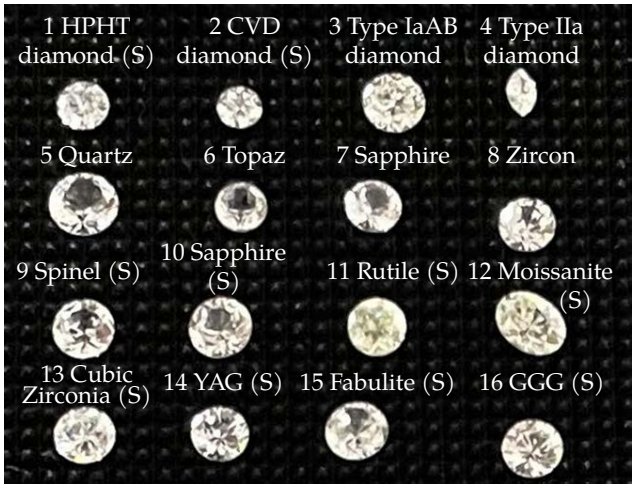

Figure 8.14: Color image of the gemstones used in this study with IDs and names indicated. The gemstones are placed on an anodized aluminum block with a pyramid texture (dots in the image) and heated to 100 °C.

Table 8.1: List of gemstones analyzed in this study. (S) indicates synthetic gemstones. Abbreviations: HPHT: High-Pressure High-Temperature; CVD: Chemical Vapor Deposition; YAG: Yttrium Aluminum Garnet; GGG: Gadolinium Gallium Garnet. A color image of the gemstones is shown in Figure 8.14.

ID	Gemstone Type	ID	Gemstone Type
1	HPHT diamond (S)	9	Spinel (S)
2	CVD diamond (S)	10	Sapphire (S)
3	Type IaAB diamond	11	Rutile (S)
4	Type IIa diamond	12	Moissanite (S)
5	Quartz	13	Cubic Zirconia (S)
6	Topaz	14	YAG (S)
7	Sapphire diamond	15	Fabulite (S)
8	Zircon diamond	16	GGG (S)

Pressure High-Temperature), CVD (Chemical Vapor Deposition), and Type IIa diamonds, form distinct clusters even using just the first two PCs. This is further supported by the scree plot in Figure 8.15a, where the first two PCs explain 79.8% of the variance in the data. The similarity among HPHT, CVD, and Type IIa diamonds is unsurprising, as these are diamonds with low impurity levels. However, using the sixth PC (Figure 8.15b), it is possible to distinguish the natural Type IIa diamond from the synthetic ones (HPHT and CVD diamonds). The type IaAB diamond contains nitrogen impurities in the form of pairs and clusters

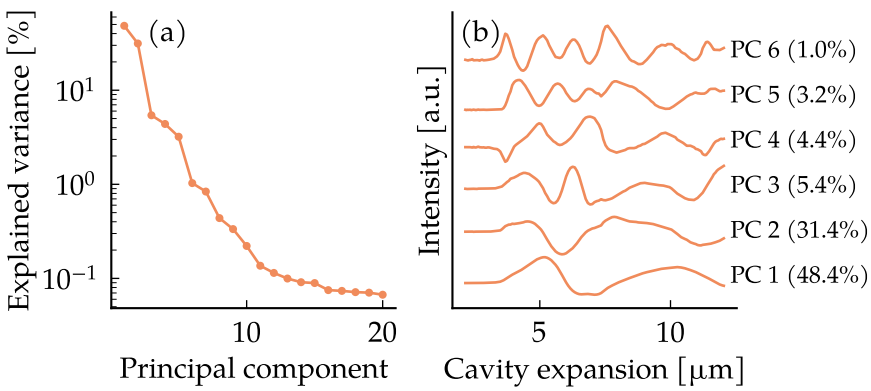

Figure 8.15: (a) Scree plot showing the explained variance of the first 20 PCs. (b) Loadings of the first six PCs for the PCA model of the gemstones.

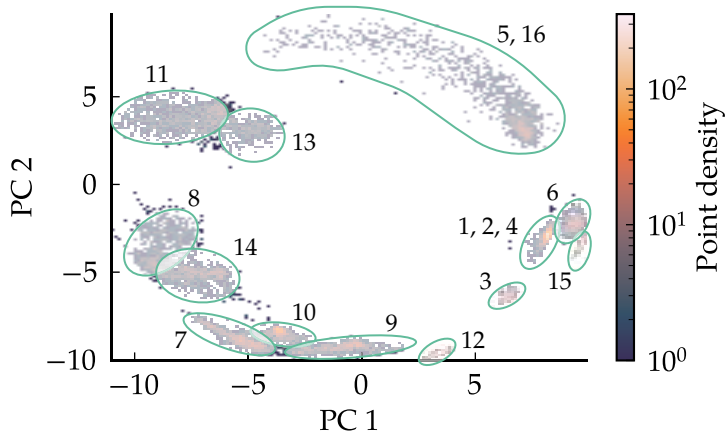

Figure 8.16: Density scatter plot of PC 1 and PC 2 scores for the gemstones. The numbers correspond to the IDs in Table 8.1.

of four nitrogen atoms, resulting in absorption bands at approximately 1282 cm^{-1} and 1136 cm^{-1} [83], which enable its separation from other diamonds (Figure 8.16).

Other clusters are challenging to explain based solely on chemical composition. The overlapping spectral orders mean that complex spectra with multiple features arising from different chemical species are difficult to interpret due to interferogram overlap. The only grouping where chemical composition aligns is the clustering of the two sapphire gemstones and the spinel, which all contain aluminum oxide.

Unfortunately, no absorption or emission FTIR spectra were recorded for the analyzed gemstones, making it difficult to establish reliable reference data for comparison. Additional studies, including FTIR measurements, would be valuable for validating these findings. Both the emission measurements of gemstones presented here and the reflectance measurements of minerals in subsection 8.4.1 highlight the potential of LWIR hyperspectral imaging for mineral differentiation in a laboratory setting. These results demonstrate how the spatial resolution of an imaging-based approach significantly increases throughput compared to single-point techniques such as transmittance or reflectance FTIR. In the following section, the HSC is applied in a field setting where environmental conditions are considerably less controlled.

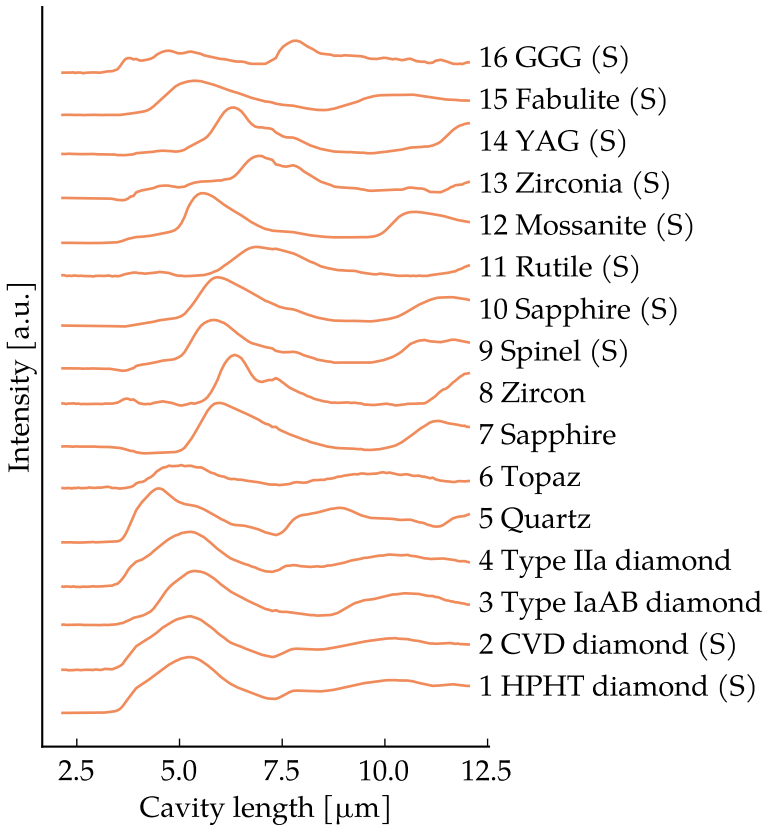

Figure 8.17: Mean interferograms of the emission signal for each gemstone heated to 100 °C. The interferograms are SNV normalized and offset for clarity.

8.4.3 Imaging Cliff Face

The last application example demonstrates the HSC applied in the field at the Boesdal limestone quarry to image a limestone cliff face containing flint stone sediments (Figure 8.18). Since no spectral reference was brought to the site, only the relative expansion of the SFPI cavity was derived from the laser diode interferograms. Additionally, no scale bar is provided due to the unknown distance to the cliff face and the uncertain size of its features.

Figure 8.19a displays an image from the hyperspectral data cube acquired at a relative cavity expansion of 2.1 µm. Only SNV normalization was applied to the data cube. While little detail is visible in this band, applying PCA and visualizing the scores of PC 4 reveal the flint stone sediments as distinct dark bands across the image (Figure 8.19b).

The scree plot in Figure 8.20a indicates that a large number of components are required to describe the signal, suggesting that the scene is either spectrally complex or affected by noise. Additionally, the data show evidence of non-parallel SFPI mirrors, which could cause spectral offsets in interferograms across the image plane. Such offsets may result in identical materials appearing as different interferograms, thereby requiring additional PCs to describe them.

Figure 8.18: Color image of the hyperspectral imager directed at the limestone cliff face.

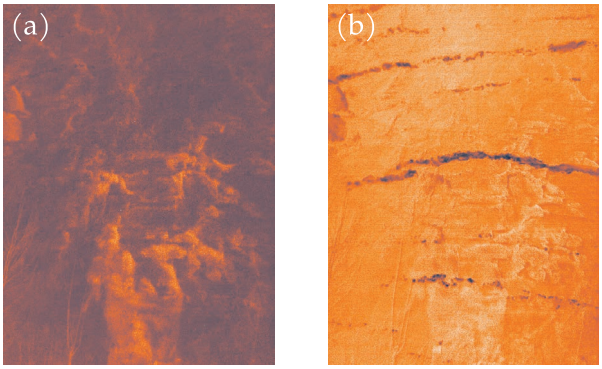

Figure 8.19: (a) Image of the limestone cliff face from the hyperspectral data cube after an SFPI cavity expansion of 2.1 µm. (b) PC 4 score image highlighting flint stone sediments.

The PC 4 score image (Figure 8.19b) reveals that the flint sediments score low in PC 4, indicating they are anti-correlated with the peaks observed in the PC 4 loadings (Figure 8.20b). Two peaks, separated by 4.3 µm cavity length, likely correspond to absorption bands at approximately 1165 cm^{-1} and 1074 cm^{-1} (8.3 µm and 9.3 µm wavelengths), which are attributed to Si-O stretching in flint stone [84]. However, without knowledge of the absolute SFPI cavity length and reference measurements, this attribution remains uncertain.

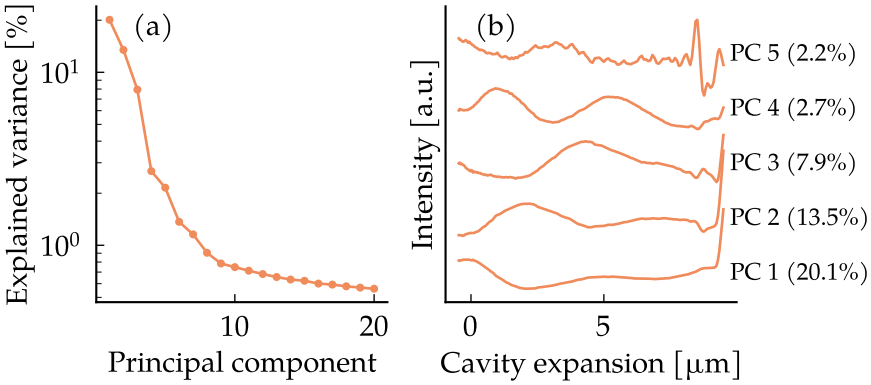

Figure 8.20: (a) Scree plot showing the explained variance of the first 20 PCs. (b) Loadings of the first five PCs.

The steep peaks at the end of the loadings for the first three PCs (Figure 8.20b) are caused by the sudden appearance of sunlight during the latter part of the data cube acquisition, which increased the reflection signal intensity at the end of the interferograms.

The measurements conducted on various minerals presented here demonstrate the potential of hyperspectral LWIR imaging for mineral analysis and characterization. Many minerals exhibit distinct spectral signatures, enabling classification. In a controlled laboratory setting, lighting conditions and sample temperatures can be precisely regulated. Even in field conditions, usable results can be obtained despite varying illumination. Notably, even in the absence of direct sunlight, ambient sky illumination provides sufficient contrast to differentiate flint from limestone based on their reflectance signals.

8.5 Applications' summary

This chapter has outlined several potential applications of the hyperspectral LWIR imager. Promising results have been obtained in distinguishing polymer types based on their emission spectra, even in their black form. However, classification using emission signals requires the samples to reach a sufficient temperature to achieve an adequate SNR. As an alternative, reflectance measurements have been proposed, though their feasibility for plastic samples remains untested. It might also not be the best fit for black plastics due to the absorption of carbon black.

Minerals have successfully been differentiated using unsupervised classification based on reflection measurements, though specular reflections are highly sensitive to the illumination incidence angle. It has been demonstrated that material identification is possible regardless of whether the reflection source is hot or cold, provided a flux difference exists between the detector and the scene. Selecting an illumination source with a specific spectral signature could further enable the separation of reflectance and emission features of a given material.

The HSC has also been employed to identify reaction zones within stable diffusion flames, revealing that different flame regions correspond to distinct intermediate reactions in the combustion of hydrocarbon gases. Further studies could focus on quantifying species concentrations, determining heat release rates, and measuring flame temperatures.

Another promising application not explored in this thesis is gas leak detection. Preliminary results indicate that ammonia and methane leaks can be identified, though achieving sufficient contrast between the gas and background remains a challenge for reliable detection. Future research is planned in this direction.

Expanding access to the HSC may further accelerate innovation, enabling researchers to explore applications beyond those considered here. Broad adoption of this novel technology could lead to new and unforeseen advancements.

IV Summary and Outlook

9. Summary and Outlook

After 211 pages describing a hyperspectral LWIR imager, this section provides a summary and evaluation of the project's progress. The primary objective has been to enhance the understanding of the imager's functionality and to develop a mathematical framework for modeling its performance. Central to the imager's hyperspectral capabilities is the SFPI, whose operation is critical for understanding the relationship between incident radiation and the camera's output.

GMM was employed to model the relationship between the wavelength of the incident light, the cavity length of the SFPI, and its transmittance. This approach enabled the estimation of the wavelength distribution transmitted to the detector at various cavity lengths. The detector's spectral response was determined by combining the GMM transmittance calculations with transmittance measurements of various materials. This spectral response, integrated with the GMM transmittance, enabled the formulation of a system matrix that accurately relates a given incident spectrum to the interferograms recorded by the camera.

While estimating the interferogram output from the camera based on an incident spectrum is relatively straightforward, solving the inverse problem has proven more challenging. This difficulty arises from the underdetermined nature of the problem and the SFPI's ability to transmit multiple transmission orders at the same cavity length. As a result, the signal measured at a given cavity length can originate from two vastly different wavelengths, complicating spectral reconstruction. By employing an NMF approach, it has been possible to reconstruct incident spectra from measured interferograms. However, significant room remains for

improvement, particularly regarding errors introduced by inaccuracies in the cavity length estimation, which can result in substantial reconstruction errors. Further development is also needed in the mathematical modeling of the light incident on the detector, specifically in accounting for the radiation emitted by the detector and its reflection off the SFPI. This also includes getting a deeper understanding of the detector output concerning how it responds to changes in its own temperature.

Efforts are underway to address the need for an external spectral reference to determine the cavity length of the SFPI. The proposed solution combines broadband LEDs with spectrometers and utilizes FFT to determine the cavity length based on the spectrometer output. This approach provides a reliable method for improving spectral reconstruction and standardizing hyperspectral data cubes, ensuring that images are captured at consistent cavity lengths across multiple acquisitions.

A secondary goal of the project was to explore potential applications of this technology. One notable achievement was successfully classifying black plastic samples, traditionally challenging for reflection-based spectral imagers. The LWIR emission signal of samples heated to 60 °C was found to be less influenced by carbon black additives, which are otherwise known to obscure the spectral characteristics of the polymer matrix.

Additionally, the imaging of combustion processes yielded highly promising results. Flames from hydrocarbon and hydrogen fuels were analyzed, leveraging the spatial resolution of the imager to identify distinct reaction regions within the flames. Furthermore, it was possible to differentiate between the two fuel types based on their spectral profiles.

Mineral analysis represents another promising application area for the HSC. Studies have demonstrated that many types of minerals can be effectively distinguished in the LWIR regime, both through emission and reflection. However, further research is required to explore this technique's limitations, particularly when applied to larger-scale subjects such as entire cliff faces. In such cases, lighting conditions pose significant challenges, and identifying the most suitable approaches for these scenarios warrants additional investigation.

The recorded interferograms of materials are significantly influenced by

the lighting conditions. Since the HSC operates in the LWIR domain, even reflections from relatively cold objects can provide spectral information about the material in which the reflection occurs. The selection of the light source could potentially be optimized to extract information on both the emissivity and reflectance of a sample within the same interferogram.

In conclusion, this work has established a foundation for further advancements in developing the hyperspectral imager, bringing it closer to a finalized product nearly ready for initial deployment. Hyperspectral imaging in the LWIR regime remains a relatively novel field, and broader adoption of this technology will undoubtedly drive its progression and uncover new applications beyond those currently envisioned. The findings presented in this thesis demonstrate the imager's potential for diverse applications across various industries and research fields, with many more possibilities likely to emerge in the future.

Closing Remarks

Working with the LWIR HSC over the past three years has been a rewarding, challenging, and, at times, truly enjoyable experience. It has provided an opportunity to explore diverse fields, refine technical skills, and collaborate with a range of inspiring people. While progress is sometimes difficult to perceive in the midst of day-to-day work, looking back, it is evident that the project has come a long way. The HSC now performs significantly better, thanks to both hardware and software improvements. Moreover, a deeper understanding of the system allows for more effective data utilization, expanding the range of possible applications for the imager.

Although the imager is not yet fully complete — if such a state even exists — it has reached a level where it is much closer to being placed in the hands of others who will undoubtedly explore new and exciting use cases beyond what I had originally envisioned. I look forward to seeing where the project progresses from here, particularly as more researchers and engineers apply the HSC to their own studies.

Whether you have read this thesis from start to finish (in which case, I admire your perseverance) or simply turned to this page out of curiosity, thank you for your time and interest in this work. I hope it has provided valuable insights into the capabilities of hyperspectral imaging in the LWIR domain.

V Appendices

A Conference Proceedings: A hyperspectral thermal imager based on a low order scanning Fabry-Pérot interferometer 217

B Paper: Classification of commercial plastics using hyperspectral long wave infrared emission imaging 229

C Paper: Classification of black plastic types by hyperspectral imaging based on long-wave infrared emission spectroscopy 239

D Manuscript: Long-wave infrared hyperspectral imager based on a scanning Fabry-Pérot interferometer 249

E Manuscript: Signatures of Flames by Long-Wave Infrared Hyperspectral Imaging . . 273

F Digital PID Controller for SFPI 325

G Generalized Matrix Method Python Function 329

H Python GUI: Hyperspectral Viewer 341

I Posters 347

I.1 International Association for Spectral Imaging 2022 348

I.2 SPIE Defence and Commercial Sensing 2024 . . . 349

I.3 International Association for Spectral Imaging 2024 350

A. Conference Proceedings: A hyperspectral thermal imager based on a low order scanning Fabry-Pérot interferometer

This section introduces the paper *A hyperspectral thermal imager based on a low-order scanning Fabry-Pérot interferometer*, published alongside the poster (section I.2) for the SPIE Defence + Commercial Sensing 2024 conference [85]. The proceeding outlines the hyperspectral LWIR imager's operating principle, detailing the cavity length's calibration, the estimation of interferograms using the system matrix and FTIR measurements, and the explicit solution of the inverse problem to estimate the incident spectrum.

A hyperspectral thermal imager based on a low order scanning Fabry-Pérot interferometer

Mads Nibe Larsen*[a,b], Anders Løcthe Jørgensen[b], Victor Petrunin[b] Jakob Kjelstrup-Hansen[a], Bjarke Jørgensen[b]
[a]NanoSYD, Mads Clausen Institute, University of Southern Denmark, 6400 Sønderborg, Denmark;
[b]Newtec Engineering A/S, 5230 Odense, Denmark

ABSTRACT

This work describes a novel hyperspectral imaging system for the long-wave infrared domain. Being a spectral scanner, it is more versatile compared to single-point and push-broom techniques, which require relative movement between instrument and sample to acquire an image. The imager is equipped with a 1024×768-pixel uncooled microbolometer sensor, which is sensitive to wavelengths in the range from 8 to 14 µm. A scanning Fabry-Pérot interferometer is placed in front of the collecting optics. The distance between its two mirrors determines the distribution of wavelengths entering the system. By capturing images at different mirror separation distances, a hyperspectral data cube is formed. The spectral information provided in such a hyperspectral data cube can i.a. be used for material classification, as here demonstrated with an example of different gemstones.

Keywords: Long-wave infrared imaging, hyperspectral imaging, thermal camera, scanning Fabry-Pérot interferometer

1. INTRODUCTION

Hyperspectral imaging is an emerging technique which has proved to be a powerful and flexible tool with many applications across several industries. In many cases, the imaging systems are tailored towards the visible and near infrared (VIS/NIR) part of the electromagnetic spectrum, where the instruments are used to i.a. perform sensory analyses of foods [1], estimate nutrient content of soils [2], and monitoring wood moisture content [3]. Traditional spectral methods have relied on single-point measurements, offering high spectral resolution but often requiring lengthy acquisition times to capture spatial information, if any at all. However, imaging systems now enable simultaneous acquisition of spectral information at multiple points in space, significantly reducing acquisition time.

Recently, the ability to also detect the short-wave infrared (SWIR) part of the spectrum has improved the performance of the technique significantly and broadened the number of applications even further. This has e.g. made it possible to classify different kinds of plastics [4], to detection of apple scab disease [5], and to estimate degree of polymerization in cotton fabrics [6] to name a few. Additionally, in the long-wave infrared (LWIR) regime, the fundamental vibrational states of many different materials can be observed enabling applications such as remote sensing of minerals [7] and gaseous plumes [8]. The LWIR range of the electromagnetic spectrum is also often associated with thermal radiation which is why most thermal cameras operate in this region.

However, the selection of hyperspectral imagers becomes more limited when extending beyond the SWIR into the LWIR regime. To the authors knowledge at the time of writing, the only commercially available solution is the *Hyper-Cam LW*, *Hyper-Cam Airborne Mini* and *Hyper-Cam Mini xLW* by Telops [9]. These are hyperspectral imagers utilizing a Michelson interferometry akin to Fourier Transform Infrared (FTIR) spectrometers. The spectral resolution of these cameras reaches 0.25 cm^{-1} and the spectral range is 7.4 – 12.5 µm wavelengths. Despite the high performance, these cameras are characterized by their heavy weight (24 kg) and high cost due to the utilization of bandgap Mercury-Cadmium-Telluride (MCT) detectors which require cryogenic cooling.

*mani@newtec.dk

Image Sensing Technologies: Materials, Devices, Systems, and Applications XI, edited by Nibir K. Dhar, Achyut K. Dutta, Sachidananda R. Babu, Proc. of SPIE Vol. 13030, 130300E · © 2024 SPIE · 0277-786X · doi: 10.1117/12.3013384

In this work, a novel hyperspectral imaging system tailored towards the LWIR regime is presented. The imaging system combines a Scanning Fabry-Pérot Interferometer (SFPI) and a thermal camera equipped with a microbolometer sensor which is sensitive to wavelengths ranging from 8 to 14 µm and a spatial resolution of 1024×768-pixels. The adoption of a microbolometer sensor eliminates the need for cryogenic cooling, resulting in a lighter and more cost-effective solution compared to MCT-based alternatives. It is presented how the SFPI is controlled as well as how the acquired data can be interpreted and used to material segregation. It has previously been shown how the same camera system can be used for material classification and subsequent temperature determination [10], while the focus of this work is on the instrument itself.

2. OVERVIEW OF HYPERSPECTRAL IMAGING SYSTEM

The hyperspectral thermal camera consists of three parts as illustrated in Fig. 1: I) A microbolometer equipped thermal camera II) germanium (Ge) lenses, and III) a scanning Fabry-Pérot interferometer.

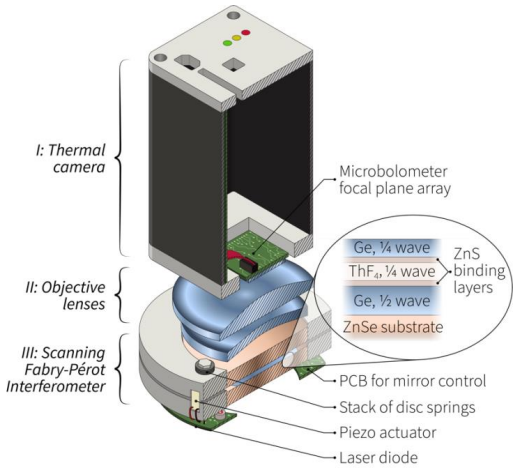

Figure 1. Illustration of hyperspectral thermal camera (not to scale).

2.1 Thermal camera

The QT5022 camera (QTechnology, DK) is fitted with a 1024×768 pixel microbolometer sensor, Pico1024Gen2™ (Lynred, USA). The sensor is sensitive to wavelengths in the range from 8 – 14 µm.

2.2 Objective lenses

Two germanium lenses (Ophir Optronics Ltd., IL) are used to focus the incoming light onto the sensor. The front element is a Ø40.4 mm aspheric lens with an effective focal length of ≈ 135 mm, while the second lens is a Ø54 mm spherical lens with a focal length of ≈ 45 mm. In combination, the two lenses have an effective focal length of 35 mm, and their position can be controlled electronically to adjust focus.

2.3 Scanning Fabry-Pérot Interferometer

The hyperspectral capabilities of the imaging system are provided by a scanning Fabry-Pérot interferometer (SFPI) placed in the front of the objective lenses. It consists of two partially transmitting mirrors made from zinc selenide (ZnSe) substrates (Ø50.8 mm, thickness: 5 mm). A three-layer dielectric coating (Ø43 mm, centered) has been deposited on each of the substrates and is comprised of 1.311 µm germanium (Ge), 1.981 µm thorium tetrafluoride (ThF_4) followed by another 0.655 µm Ge. 100 Å binding layers of zinc sulfide (ZnS) are deposited between Ge and ThF_4 layers and have negligible influence of the optical characteristics of the mirrors. In the wavelength range where the sensor is sensitive (8 – 14 µm), the mirrors have an average reflectance of ≈ 84% as depicted in Fig. 2.

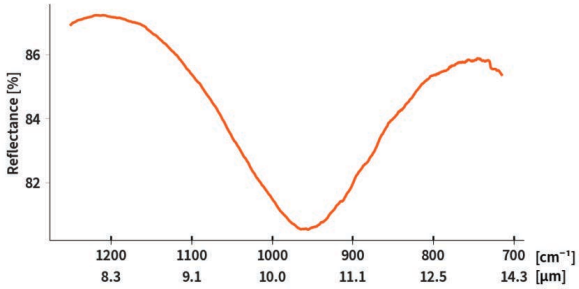

Figure 2. Reflectance of a single SFPI mirror in the wavelength range from 8 – 14 µm

The SFPI functions as a variable bandpass filter, where the mirror-to-mirror distance (MMD) determines the distribution of transmitted wavelengths. For an idealized SFPI, the transmission, τ, is described by the Airy function (Eq. 1).

$$\tau = \frac{1}{1 + \mathrm{F}\sin^2\frac{\delta}{2}}, \quad F = \frac{4r}{(1-r)^2}, \quad \delta = \frac{4\pi d\cos\theta}{\lambda} \tag{1}$$

Here, F is the coefficient of finesse, r is the mirror reflectance, which is assumed to be equal for both mirrors, d is the MMD, λ is the wavelength, and θ is the angle of incidence. From Eq. (1), it is evident that the maximum transmission occurs at:

$$2d\cos\theta = m\lambda = \frac{m}{k}, \quad m = 1, 2, 3 \ldots \tag{2}$$

where m is referred to as the transmission order and $= 1/\lambda k$ is the wavenumber. Since the mirrors are comprised of dielectric stacks, the electric field can propagate inside the layers. The reflection therefore does not necessarily occur at the top surface of the mirrors but rather, the "plane of reflection" shifts with changing wavelengths. To account for this, instead of using the Airy function from Eq. (1) to calculate the relationship between transmission, wavelength and MMD, the Generalized Matrix Method (GMM – also sometimes referred to as the Transfer Matrix Method, TMM) [11] is employed instead. Using GMM, it is possible to calculate the electric field at any position inside the mirrors and by extension, the reflectance and transmission for any combination of wavelength and MMD. This is achieved by calculating the reflection and transmission at each interface between the dielectric layers as well as accounting for the accumulated phase as the light propagates through each layer. Fig. 3 is denoted as the transmission matrix and depicts the transmission of the SFPI for relevant combinations of MMD and wavelength calculated from GMM.

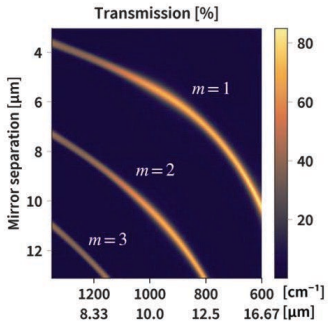

Figure 3. Transmission of the SFPI for relevant combinations of mirror separations and wavelengths/wave numbers calculated using GMM. The first three transmission orders (m's) are indicated.

Mirror control

Each of the mirrors are mounted in its own half of a stainless-steel fixture which is held together by three bolts mounted at 120° intervals around the perimeter. Each bolt also passes through a stack of four disc-springs (outer diameter: Ø12.5 mm, force: 673 N, Sodemann Industrifjedre A/S, DK). The bolts are tightened onto the springs providing a load of ≈ 400 N. Three piezo actuators (PK2FMP2, force: 673 N, max expansion: 11.2 µm, Thorlabs, USA) are mounted at 120° intervals in-between the two halves of the flange. By applying a voltage (0 – 75 V) to these piezo actuators, the two halves of the flanges and hereby the two mirrors are forced apart, hereby changing the MMD. By ramping the voltage, the MMD gradually increases from ≈ 3 µm to ≈ 13 µm. To ensure that the three actuators displace the mirrors by an equal amount, i.e. keep the mirrors mutually parallel, three pairs of photo and laser diodes (660 nm nominal wavelength) are placed on a printed circuit board (PCB) mounted in front of the SFPI. The reflected laser light is used to monitor the relative displacement of the mirrors as described in more detail below. Approximately 143 images are captured while sweeping across the achievable MMD range, forming the data cube containing 768×1024×143 data points (width×height×depth).

During an imaging sweep, the voltage across the piezo actuators is increased from 0 V to 75 V causing them to expand. However, the expansion of all actuators is not equal due to manufacturing/material tolerances and non-linearities of the piezos. It is paramount for the performance of the SFPI that the mirrors remain parallel throughout the sweep. This is achieved using three laser diodes which shine into the cavity through the uncoated region of the mirrors. As the MMD changes, the light undergoes alternating constructive and destructive interference which is monitored by photo diodes placed next to the laser diodes (Fig. 4). From the resulting interferograms it is possible to keep track of how far the given part of the mirror has moved. Since the same voltage does not correspond to the same expansion for all actuators, the sweep is divided into 1500 individual steps, each associated with a set of voltages for the individual actuators. 9 learning sweeps are performed where the expansion of each actuator is monitored, and the voltages adjusted to ensure that the phase difference between the interferograms is maintained throughout the sweep (Fig. 4c). The number of steps in each sweep is lowered to accommodate the fact that the range of motion is not equal across the actuators. This way, the actuator with the shortest expansion determines the maximum expansion achievable with the SFPI.

As mentioned, the interferograms from the laser diode reflections can be used keep track of the relative displacement of the mirrors. The light undergoes constructive interference whenever

$$d = \frac{m}{2}\frac{\lambda_{\text{diode}}}{\cos\theta}, \quad m = 1, 2, 3 \ldots \tag{3}$$

where λ_{diode} is the wavelength of the laser diode, θ is the angle of incidence of the laser light relative to the optical axis of the system. The nominal wavelength of the laser diodes is 660 nm, but the exact wavelength may differ from that.

Furthermore, the angle of incidence of the laser light is also unknown and the effective wavelength is therefore introduced as

$$\lambda_{eff} = \frac{\lambda_{\text{diode}}}{\cos\theta} \tag{4}$$

This has been experimentally determined to be $\lambda_{eff} = 680$ nm. In the laser interferogram, the transition from a peak to a neighboring trough thus corresponds to a change in MMD of 680 nm /4 = 170 nm.

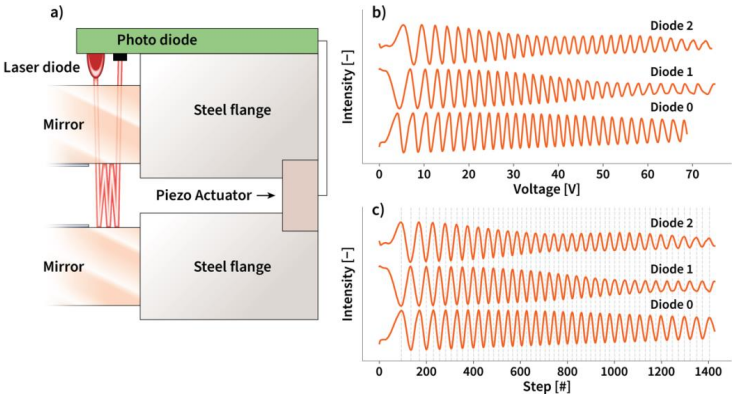

Figure 4. a) Schematic drawing of how light is reflected inside the SFPI cavity, and the intensity of the reflected light is monitored by a photo diode placed next to the laser diode. Three photo/laser diode pairs are placed around the perimeter of the mirrors giving rise to the interferograms presented in b). c) The sweep is divided into steps which ensure that the phase difference between all three diodes is maintained throughout the sweep.

The relationship between the step numbers and the relative displacement is found by fitting a 3rd order polynomial to the position of the peaks and troughs (Fig. 4c), as displayed in Fig. 5a. Here, the vertical distance between each point is 170 nm corresponding to $\lambda_{eff}/4$. A 3rd order polynomial is chosen for the fit to compensate for the nonlinearity and hysteresis of the piezo actuators. However, this still only give the *relative* displacement of the mirrors which is an inherent drawback of using a monochromatic light source. To get the absolute MMD, the relative displacement axis (y-axis in Fig. 5a) must be offset to an appropriate starting position. This requires a reference sample with known spectral features which always occur at the same MMD. For the results presented here, that reference sample is a bandpass filter with a central wavelength of 8.226 µm (1216 cm^{-1}) (Andover Corporation, USA). When a hyperspectral image is captured, this filter is always present in the same part of the frame (away from the sample under investigation) making it possible to align the spectral axes across multiple images. The interferogram of the filter is extracted (Fig. 5b) and show three distinct transmission orders. The position of the 2nd transmission order corresponds to an absolute MMD of 8.38 µm and all relative MMD axes are offset to match this. 8.38 µm is determined based on the transmission spectrum of the filter as well as the SFPI itself in a similar fashion as to what will be explained in section 3.

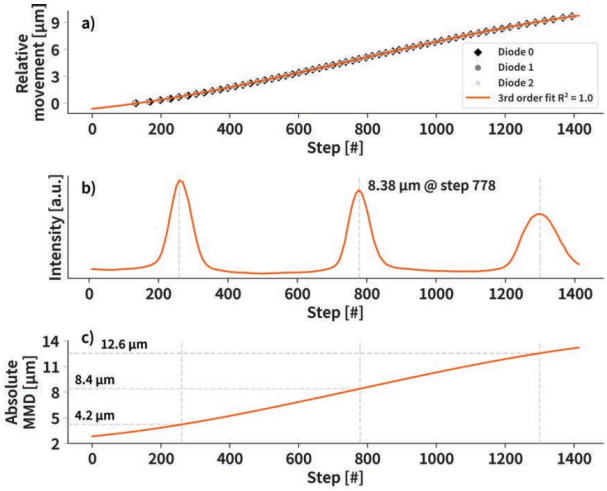

Figure 5. a) Relationship between relative displacement of SFPI mirrors and the step #. Each point corresponds to either a peak or a through in the laser interferograms displayed in Fig. 4c and have been plotted with a vertical distance between neighboring points of $\frac{\lambda_{eff}}{4} = 170$ nm. A third order polynomial has been fitted to estimate the mirror displacement at every step. b) Extracted interferogram of bandpass filter. The position of the central transmission order is used to align the spectral axes across multiple hyperspectral images. The position of the peak (measured in steps) will always correspond to an absolute MMD of 8.38 µm, and the MMD fit is offset accordingly as shown in c).

3. PREDICTING INTERFEROGRAM FROM INPUT SPECTRUM

The "spectra" that make up the hyperspectral images are denoted as "interferograms" since the spectral corresponds to MMD and *not* in wavelength. As mentioned, the SFPI acts as a variable bandpass filter, which means that for a given MMD, the incident light is filtered according to the given transmission profile as presented in Fig. 3. This filtration can be viewed as a multiplication of the incident spectrum with the given row of the transmission matrix. This is illustrated for an example of a methanol transmission spectrum in Fig. 6. Methanol vapor has been transferred to a gas cell with ZnSe windows using a nitrogen bubbler. The incident spectrum (Fig. 6a) is multiplied with the transmission profile of the SFPI at five different MMDs resulting in the spectra presented in Fig. 6b. Notice how the spectra of MMD = 4 µm, 8 µm, and 12 µm all have a peak at ≈ 1250 cm^{-1} - one for each of the transmission orders as illustrated in Fig. 3. The same spectral feature can therefore show up multiple times in the recorded interferogram as it is also illustrated in Fig. 5b where a single transmission peak at 1216 cm^{-1} occurs at MMDs of 4.2 µm, 8.4 µm, 12.6 µm. This matches the transmission criterion stated in Eq. (2) where the separation between the MMD peak positions should be equal to half the wavelength.

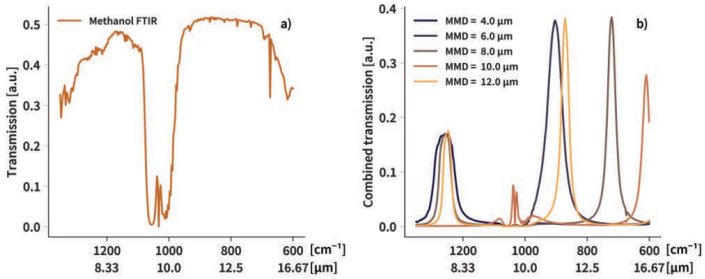

Figure 6. a) FTIR transmission spectrum of methanol vapor in a gas cell measured with a Perkin Elmer Spectrum 65 FT-IR Spectrometer with 1 cm^{-1} resolution. b) Transmission spectra of the methanol spectrum from a) after it has passed through the SFPI at different MMDs.

The camera itself does not distinguish between the wavelengths and therefore only captures a weighted sum of the transmission spectrum at any given MMD. The weighted sum refers to the spectral response of the sensor itself, which has been applied to the system matrix (Fig. 3.) and presented in Fig. 7a. From this it is possible to predict the interferograms of a given input spectrum. Let the weighted system matrix be denoted as $\boldsymbol{A}$ and let the input spectrum be denoted as $\boldsymbol{x}$. The recorded interferogram can then be calculated as

$$\hat{\boldsymbol{b}} = \boldsymbol{A}\boldsymbol{x} \tag{5}$$

Given a setup, where the gas cell containing methanol vapor is placed in front of a 150 ºC black body radiator (CS1050-100, HGH Infrared Systems, FR) it is possible to predict the recorded interferogram. Firstly let $B(T,\lambda)$ denote the spectral exitance of a theoretical black body.

$$B(T,k) = 2\pi hc^2k^3\frac{1}{\exp\left\{\frac{hck}{k_BT}\right\}-1} \tag{6}$$

Here, h, c, and k_B are the Planck constant, the speed of light, and the Boltzmann constant respectively while T is the temperature of the black body. The input signal at a given wavenumber is then defined as

$$x_{methanol}(k) = \tau_{methanol}(k)B(150ºC,k), \tag{7}$$

where $\tau_{methanol}$ is the FTIR transmission spectrum of the methanol vapor as depicted in Fig. 6a. From this, the interferogram is predicted and presented in Fig. 7b. This is compared to the measured interferogram, which is extracted from a 40×40-pixel area of the hyperspectral image. To compare the two, the relative root mean square error (RRMSE) is used.

$$\text{RRMSE} = \sqrt{\frac{\frac{1}{n}\sum_{i=1}^{n}\left(\hat{b}_i - b_i\right)^2}{\sum_{i=1}^{n} b_i^2}} \tag{8}$$

Here, b_i is the ith element of the measured interferogram containing n elements. Using this method, the RRMSE is 0.26% indicating good agreement between prediction and measurement. Possible sources of error come from the GMM calculations which do not take losses into account nor broadening and phase shifts from imperfect layer transitions. Also, the exact film thicknesses may deviate slightly across the diameter of the mirrors. Furthermore, the sensor response is estimated based on several measurements of different materials and is therefore also associated with an error. Finally, the experimental black body was last calibrated in June 2014 and may therefore not be living up to spec.

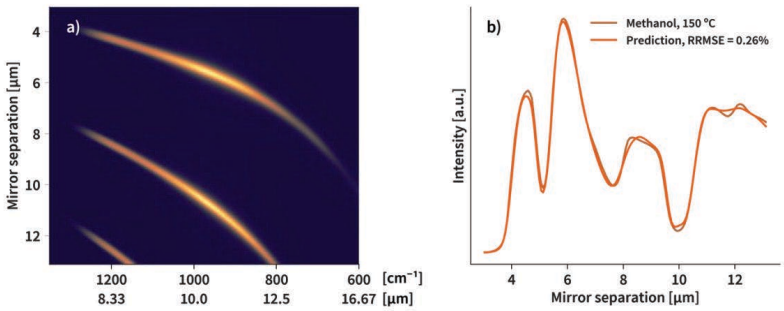

Figure 7. a) System matrix. The same transmission matrix as presented in Fig. 3, but now scaled with the response of the microbolometer sensor. b) Predicted interferogram of methanol based on the transmission spectrum illustrated in Fig. 6a shown along with the actual measurement of the same gas cell.

4. PREDICTING INPUT SPECTRUM FROM MEASURED INTERFEROGRAM

It is also possible to estimate the input spectrum based on the recorded interferogram. The system is under-determined and finding the right solution among the infinite possibilities is non-trivial. Eq. (5) can be rearranged to solve for $\boldsymbol{x}$, as well as introducing the regularization term $\gamma\boldsymbol{M}$. The estimation of $\boldsymbol{x}$ is denoted as:

$$\hat{\boldsymbol{x}} = (\boldsymbol{A}^T\boldsymbol{A} + \gamma\boldsymbol{M})^{-1}\boldsymbol{A}^T\boldsymbol{b} \tag{9}$$

Here $\boldsymbol{M}$ is introduced to encourage the solution to be smooth and has the form of

$$\boldsymbol{M} = \begin{bmatrix} 2 & -1 & 0 & 0 & 0 & \cdots \\ -1 & 2 & -1 & 0 & 0 & \cdots \\ 0 & -1 & 2 & -1 & 0 & \cdots \\ \vdots & \ddots & \ddots & \ddots & \ddots & \ddots \\ \cdots & 0 & 0 & -1 & 2 & -1 \\ \cdots & 0 & 0 & 0 & -1 & 2 \end{bmatrix} \tag{10}$$

γ is the regularization parameter which controls the impact of $\boldsymbol{M}$ on the overall solution. Using Eq. (9) it is possible to estimate the incident spectrum as it is presented in Fig. 8. Here, the RRMSE is 1.34 % which also indicates a good fit between $\hat{\boldsymbol{x}}$ and $\boldsymbol{x}$, however some deviations are observed along the smooth part of the spectrum. These oscillations can be suppressed by increasing γ, but that comes at the cost of the ability to resolve the sharp edges of the absorption band (950 – 1100 cm^{-1}).

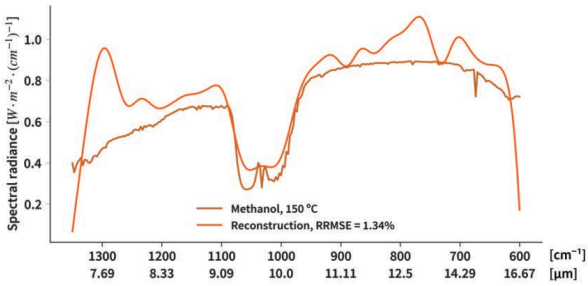

Figure 8. Reconstructed input signal based on the measured interferogram from Fig. 7b. The reconstruction is compared against the FTIR transmission spectrum of the methanol vapor from Fig. 6a multiplied with the spectral exitance of a 150 ºC black body as stated in Eq. (7).

5. DISTINGUISHING BETWEEN GEMSTONES USING HYPERSPECTRAL LWIR IMAGINNG

The interferograms of the hyperspectral images can also be used to differentiate between the objects in the scene. In this example, 16 different gemstones have been placed on a 100 ºC hot plate and imaged using the hyperspectral camera (Fig. 9). The samples consist of a variety of both synthetic and natural gemstones. To the naked eye, the gemstones are all transparent and similar in appearance (Fig. 9a). A hyperspectral image has been captured and Principal Component Analysis (PCA) has been performed along the spectral axis. Clustering is observed when the 2nd and 3rd principal components (PCs) are plotted together as depicted in the density scatter plot (Fig. 9b). Here, some of the most distinct clusters have been marked and identified with corresponding gemstones. Using the first 11 PCs, a k-means clustering algorithm has been employed to divide the image into 21 different clusters (Fig. 9c). Some of the clusters are designated to the background, and several of the gemstones are assigned more than one cluster. The signal recorded by the camera is a mixture of transmitted light from the hot plate, reflected light from the environment as well as emission from the heated gemstones. The multiple sources of light combined with the many facets of the gemstone lead to interferograms of the same material looking distinctly different, as it is also indicated by the clustering. Some pairs of gemstones cannot be separated using this clustering technique. These are the HPHT and CVD diamonds, YAG and Zircon, Natural sapphire and spinel, as well as Cubic Zirconia and Rutile.

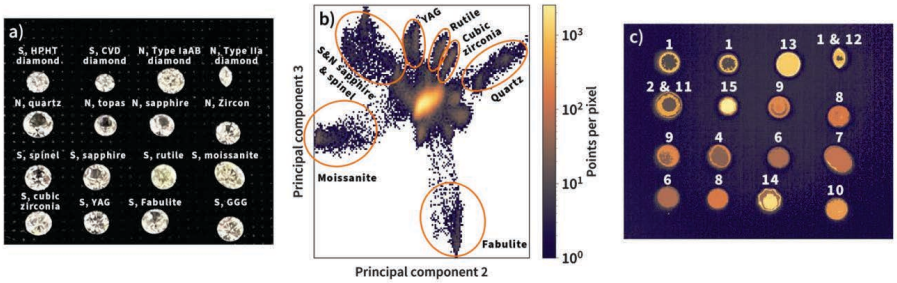

Figure 9. a) RGB color image of the 16 different gemstones. "S" and "N" refer to "synthetic" and "natural" respectively. The other abbreviations are HPHT: High Pressure High Temperature, CVD: Chemical Vapor Deposition, YAG: Yttrium Aluminum Garnet, and GGG: Gadolinium-Gallium-Garnet. b) Density scatter plot of the 2nd and 3rd principal components. A couple of the outstanding gemstones have been marked and labeled. c) Based on the first 11 components of the PCA models, K-means have been used to divide the image into 21 clusters. Here the main labels associated with each gemstone have been indicated. The numbers are chosen arbitrarily and could have been any form of symbol used to distinguish the clusters from each other.

6. SUMMARY AND CONCLUSIONS

This work has described a novel hyperspectral camera sensitive to wavelength in the range 8 – 14 µm. It combines a microbolometer-equipped thermal camera with an SFPI. The SFPI consists of two semitransparent mirrors and the distance between them dictates the transmitted wavelengths. The mirror separation is controlled by piezo actuators, which are used to drive the mirrors apart while the hyperspectral data cube is acquired. To ensure that the mirrors remain mutually parallel throughout the acquisition, the reflected light of three laser diodes is monitored. As the mirrors move apart, the reflected light undergoes alternating constructive and destructive interference, and the mutual phase difference between the signals are kept constant. From the reflected light it is possible to infer, how far the mirrors have traveled, and with the use of an external spectral reference, it is possible to determine the absolute MMD at each frame in the data cube. The spectral axis of the data cube corresponds to the MMD and not wavelength nor wavenumber. It is possible to convert from this representation and back into the wavelength domain by solving an under-determined inverse problem. From this it is possible to estimate the combination of wavelength which give rise to the recorded interferogram. Finally, it has been shown how multiple samples can be evaluated and distinguished simultaneously in an example where 16 gemstones have been imaged. Utilizing PCA and K-means clustering, all but four pairs of gemstones have been successfully distinguished.

7. ACKNOWLEDGEMENTS

The authors would like to thank Stefan Müller and DSEF German Gem Lab for providing gemstones for imaging and showing us hospitality during our visit to their laboratories. Financial support has been provided by the Innovation Fond Denmark (grant no: 1044-00116B).

REFERENCES

[1] G. Özdoğan, X. Lin, and D.-W. Sun, "Rapid and noninvasive sensory analyses of food products by hyperspectral imaging: Recent application developments," *Trends Food Sci. Technol.*, vol. 111, pp. 151–165, May 2021, doi: 10.1016/j.tifs.2021.02.044.

[2] S. Eshkabilov, A. Lee, X. Sun, C. W. Lee, and H. Simsek, "Hyperspectral imaging techniques for rapid detection of nutrient content of hydroponically grown lettuce cultivars," *Comput. Electron. Agric.*, vol. 181, p. 105968, Feb. 2021, doi: 10.1016/j.compag.2020.105968.

[3] H. Kobori *et al.*, "Applicability of Vis-NIR hyperspectral imaging for monitoring wood moisture content (MC)," *hfsg*, vol. 67, no. 3, pp. 307–314, Apr. 2013, doi: 10.1515/hf-2012-0054.

[4] M. L. Henriksen, C. B. Karlsen, P. Klarskov, and M. Hinge, "Plastic classification via in-line hyperspectral camera analysis and unsupervised machine learning," *Vib. Spectrosc.*, vol. 118, p. 103329, Jan. 2022, doi: 10.1016/j.vibspec.2021.103329.

[5] N. Gorretta, M. Nouri, A. Herrero, A. Gowen, and J.-M. Roger, "Early detection of the fungal disease 'apple scab' using SWIR hyperspectral imaging," in *2019 10th Workshop on Hyperspectral Imaging and Signal Processing: Evolution in Remote Sensing (WHISPERS)*, Amsterdam, Netherlands: IEEE, Sep. 2019, pp. 1–4. doi: 10.1109/WHISPERS.2019.8921066.

[6] E. Mahlamäki, I. Schlapp-Hackl, M. Rissanen, M. Hummel, and M. Mäkelä, "Discriminating the viscoelastic properties of cellulose textile fibers for recycling," *Resour. Conserv. Recycl.*, vol. 193, p. 106984, Jun. 2023, doi: 10.1016/j.resconrec.2023.106984.

[7] G. Notesco, V. Kopačková, P. Rojík, G. Schwartz, I. Livne, and E. Dor, "Mineral Classification of Land Surface Using Multispectral LWIR and Hyperspectral SWIR Remote-Sensing Data. A Case Study over the Sokolov Lignite Open-Pit Mines, the Czech Republic," *Remote Sens.*, vol. 6, no. 8, pp. 7005–7025, Jul. 2014, doi: 10.3390/rs6087005.

[8] E. Agassi, E. Hirsch, M. Chamberland, M.-A. Gagnon, and H. Eichstaedt, "Detection of gaseous plumes in airborne hyperspectral imagery," presented at the SPIE Defense + Security, A. W. Fountain, Ed., Baltimore, Maryland, United States, May 2016, p. 98240U. doi: 10.1117/12.2222142.

[9] telops, "Hyperspectral IR Cameras," Telops. Accessed: Aug. 23, 2021. [Online]. Available: https://www.telops.com/products/hyperspectral-ir-cameras/hyperspectral-cameras

[10] A. L. Jørgensen, M. N. Larsen, V. Petrunin, J. Kjelstrup-Hansen, and B. Jørgensen, "Surface temperature determination using long range thermal emission spectroscopy based on a first order scanning Fabry-Pérot interferometer," *Opt. Express*, vol. 30, no. 2, p. 2186, Jan. 2022, doi: 10.1364/OE.441798.

[11] E. Centurioni, "Generalized matrix method for calculation of internal light energy flux in mixed coherent and incoherent multilayers," *Appl. Opt.*, vol. 44, no. 35, p. 7532, Dec. 2005, doi: 10.1364/AO.44.007532.

B. Paper: Classification of commercial plastics using hyperspectral long wave infrared emission imaging

This section presents the paper *Classification of commercial plastics using hyperspectral long wave infrared emission imaging* published in Spectrochimica Acta Part A: Molecular and Biomolecular Spectroscopy [3]. This paper describes how the long-wave imager can distinguish between common plastic types based on their emission spectra.

Spectrochimica Acta Part A: Molecular and Biomolecular Spectroscopy 329 (2025) 125501

Contents lists available at ScienceDirect

Spectrochimica Acta Part A:
Molecular and Biomolecular Spectroscopy

journal homepage: www.journals.elsevier.com/spectrochimica-acta-part-a-molecular-and-biomolecular-spectroscopy

Classification of commercial plastics using hyperspectral long wave infrared emission imaging

Mads Nibe Larsen [a,b,c], Anders Løchte Jørgensen [b], Martin Lahn Henriksen [c], Victor Petrunin [b], Jakob Kjelstrup-Hansen [a], Bjarke Jørgensen [b], Mogens Hinge [c,*]

[a] NanoSYD, Mads Clausen Institute, University of Southern Denmark, 6400 Sønderborg, Denmark
[b] Newtec Engineering A/S, 5230 Odense, Denmark
[c] Plastic and Polymer Engineering, Department of Biological and Chemical Engineering, Aarhus University, 8200 Aarhus N, Denmark

HIGHLIGHTS

- A novel emission hyperspectral camera system is developed.
- Plastic classification is possible using low order Fabry-Pérot interferometry.
- Via hypercube data processing it is possible to classify the plastic types.
- Principal component analysis and k-nearest neighbours is applied for data treatment.

GRAPHICAL ABSTRACT

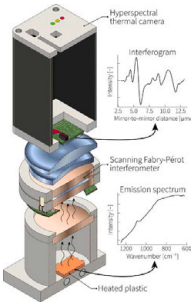

ARTICLE INFO

Keywords:
Hyperspectral imaging
Fabry-Pérot interferometry
Thermography
Plastics classification
Principal component analysis

ABSTRACT

The long wave infrared regime of the electromagnetic spectrum has been used to identify and classify different types of plastics. This work presents an early-stage version of an industrial hyperspectral camera, which is based on a low-order scanning Fabry-Pérot interferometer and is sensitive to radiation with wavelengths from 8 μm to 15 μm. As a demonstration, the setup is used to record interferograms and distinguish between twelve types of common plastics heated to 60 °C. The plastic identification is based on a nine-component principal component analysis model combined with k-nearest neighbors. The resulting model shows a micro precision of 90 % and a macro specificity of 99 %, being able to classify all tested plastic types except ABS.

* Corresponding author.
E-mail address: hinge@bce.au.dk (M. Hinge).

https://doi.org/10.1016/j.saa.2024.125501
Received 9 September 2024; Received in revised form 20 November 2024; Accepted 25 November 2024
Available online 27 November 2024
1386-1425/© 2024 The Author(s). Published by Elsevier B.V. This is an open access article under the CC BY license (http://creativecommons.org/licenses/by/4.0/).

1. Introduction

Plastics have for a long time been applied in almost all applications and sectors. However, only 8.3 % of plastics [1] are returned to the plastic circular economy [2–5]. Moreover, poor waste management has resulted in plastic pollution of our ecosystems [6–12]. There are several challenges in plastic recycling, such as underdeveloped waste management, poor consumer behavior, complex materials (multi-material items), etc. [13,14]. Furthermore, household collected waste plastics comprised of a complex mixture of sizes, materials, contaminants, etc. For most industrial production (of high-value products), the recycled plastic must have material purity of 95+ % [15]. Thus, to live up to the industrial demands, additional sorting of unwanted (or wanted) plastic waste is needed to bridge the plastic waste stream and the industrial demands.

Spectroscopic methods utilizing the mid wave and long wave infrared (MWIR and LWIR) regimes have previously been used to distinguish between different types of colored plastics [16,17]. However, these techniques generally rely on time-consuming single-point laboratory measurements. During industrial processing, this is impractical, and techniques with non-contact spectrum acquisition without sample manipulation are needed. Multi- and hyperspectral imaging techniques are generally comparatively easy to integrate in an industrial context, but the specificity is not on par with the point measurement methods. These imaging techniques are usually operating in reflection mode within the visible and near-infrared part of the spectrum. In general, black plastics (recycled or not) are challenging for the traditional reflection and transmission based hyperspectral methods applied for plastic type identification due to the vast light absorbance of carbon black [16,18].

As an alternative, infrared thermography, which is an *emission* imaging technique operating in the LWIR regime (8–15 μm), has shown promising results. The technique has been deployed to distinguish between different types of plastics by observing their heating and/or cooling rates [19,20]. In these studies, grayscale thermograms of plastics are evaluated during the heating and/or cooling of the samples over a time span of ≈1.5 min. Their results therefore rely on the physical characteristics of the samples, such as mass, heat capacity, and emissivity. It will, however, be possible to obtain spectral information if the wavelengths in their emission spectra could be separated. A potential solution is to employ a scanning Fabry-Pérot interferometer (SFPI). A SFPI consists of two partially transmitting mirrors that function as a variable bandpass filter, and the distribution of transmitted wavelengths depends on the mirror-to-mirror distance (MMD). The mirror displacement of a SFPI is in the order of micrometers compared to e.g., Michelson interferometers, which displace the mirror in the order of centimeters. The general approach of using the Fourier transform to convert interferograms into wavenumbers can, unfortunately, not be applied at the small mirror displacement of the SFPI. Thus, the SFPI output is normally an interferogram. Despite only covering a few transmission orders, the interferograms can still be applied to obtain material information [21]. Further, the small form factor of a SFPI reduces the cost of the optical system. Thus, a potential approach could be to combine a thermal camera with a SFPI, enabling hyperspectral imaging that can separate the incident light into discrete bands.

This study attempts to classify common plastic types based on recorded interferograms of their emission spectra. A novel hyperspectral camera is constructed by combining a low-order SFPI and a thermal camera with a microbolometer sensor. Interferograms of each plastic are obtained and calibrated prior to classifying the plastics using principal component analysis and k-nearest neighbors algorithm.

2. Materials and methods

2.1. Materials

The 13 different plastic types measuring approximately 10 mm × 10 mm × 4 mm are applied as received and are listed in Table 1. The data has previously been characterized [22] and is available online [23]. Further, a sample of poly(oxymethylene) (POM) (11.2 mm × 11.0 mm × 5.9 mm) and a sample of stainless steel coated with Ultra Black™ (14.3 mm × 12.6 mm × 0.75 mm, emissivity: $\varepsilon > 0.93$, 3–30 μm, Acktar IL) are used as received as spectral and black body references respectively.

2.2. Experimental setup

The setup for the spectral emission measurements consists of (I) an oven, (II) a scanning Fabry-Pérot interferometer, (III) two objective lenses, and (IV) a thermal camera equipped with a microbolometer sensor. The setup is illustrated in Fig. 1.

(I) Oven:

The oven consists of an aluminum baseplate (90 × 90 × 20 mm) with two embedded heaters (Ø10 mm, length: 70 mm, voltage: 220 V ac, power: 250 W, RS Components, DK). The temperature is controlled by a PID controller (Inkbird, CH) using a thermocouple (K-type) mounted directly into the base plate. The oven chamber is made from a hollow aluminum cylinder (inner diameter: Ø50 mm, height: 45 mm), and the top is fitted with a zinc selenide (ZnSe) window (Ø50.8 mm, thickness: 5 mm). Another thermocouple (K-type) is mounted through the oven wall, 20 mm from the base plate. Samples are placed directly onto the baseplate before the oven chamber is placed around it.

(II) Scanning Fabry-Pérot Interferometer

The SFPI consists of two semi-transparent mirrors, each comprised of a ZnSe substrate (Ø50.8 mm, thickness: 5 mm) on which a mirror coating (Ø43 mm, centered) is deposited. The mirror coating is a three-layer stack consisting of 1.311 μm germanium (Ge), 1.981 μm thorium tetrafluoride (ThF_4), and another 0.655 μm Ge. 100 Å zinc sulfide (ZnS) films are used as binding layers between the Ge and ThF_4 layers (these binding layers have negligible influence on the optical mirror properties). This film configuration reflects ≈84 % in the wavelength range from 8 μm to 15 μm, as shown in supporting information, Fig. S1.1 (SI S1.1). Thus, the resulting in the Full Width Half Maximum (FWHM) of each of the first three transmission orders is $\lambda^{(1)}_{FWHM} = 408 \pm 83$ nm, $\lambda^{(2)}_{FWHM} = 280 \pm 41$ nm, and $\lambda^{(3)}_{FWHM} = 154 \pm 17$ nm. The mirrors are mounted in individual stainless-steel fixtures held together by three nuts

Table 1
Plastic identification, type, trade name, and supplier for the materials included in this study. For POM, B = blue and N = natural.

ID	Plastic type	Name	Supplier
POM B	Polyoxymethylene	Ertacetal C	Mitsubishi
POM N	Polyoxymethylene	Ertacetal C	Mitsubishi
PVDF	Poly(vinylidene difluoride)	PVDF	GEHR
PVC	Poly(vinyl chloride)	PVC-U	GEHR
PS	Polystyrene	CD cover	–
PP	Polypropylene	240-CA12	INEOS
PMMA	Poly(methyl methacrylate)	Setacryl 1000	Madreperla
PET	Poly(ethylene therphalate)	CB-602	UltraPurge
PEEK	Polyetheretherketone	Ketron PEEK 1000	Mitsubishi
PC	Polycarbonate	Makrolon 2652	Covestro
PA12	Polyamide 12	PA 12-TR	GEHR
HDPE	Polyethylene	PE 100	SIMONA
ABS	Poly(acrylonitrile-butadienestyrene)	Terluran GP35	INEOS

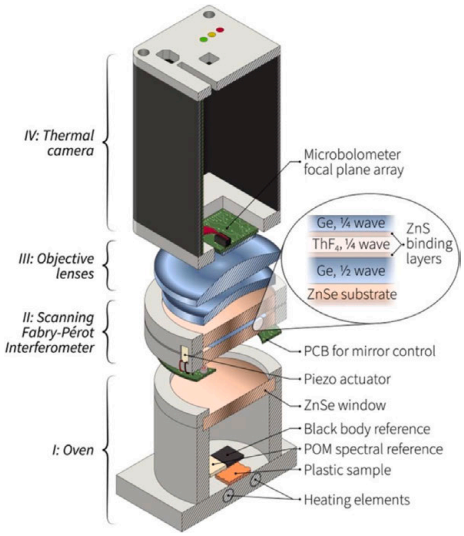

Fig. 1. Schematic representation of hyperspectral thermal camera as part of the experimental setup (not to scale) with a spectral range from 8 μm to 15 μm.

and bolts placed around the perimeter of the fixture, separated by 120°. Each bolt also passes through a stack of four disc springs (outer diameter: Ø12.5 mm, force: 673 N, Sodemann Industrifjedre A/S, DK), and the nuts are tightened to provide a load of ≈400 N to each stack. Three piezo actuators (PK2FMP2, force: 673 N, maximum expansion: 11.2 μm, Thorlabs, USA) are mounted between the two halves of the fixture at 120° intervals to control the mirror-to-mirror distance (MMD) from ≈3 μm to ≈13 μm. Three 655 nm (nominal value) laser diodes are mounted in 120° intervals around the perimeter of a printed circuit board (PCB) placed in front of the SFPI and are shining into the interferometer cavity (Fig. SI S3.1). Parallel movement of the mirrors is assured by maintaining a constant phase difference between the laser interferograms (measured by photodiodes). To maintain a constant phase difference between the three interferograms during the acquisition of the data cube, nine initial sweeps are performed to calibrate the actuators' expansion. In this process, the mirror sweep is split into ≈1420 steps. After the calibration sweeps, a final sweep is performed where an image is acquired at every 10th step, resulting in a data cube containing ≈143 channels.

(III) Objective lenses

A two-lens germanium objective with an effective focal length of 35 mm and an aperture of f/1 (Ophir Optronics Solutions Ltd., IL) is used to focus the transmitted light from the SFPI onto the sensor. The lenses are kept in a housing, and their position can be electronically controlled using a piezo inchworm driven linear actuator to achieve focus.

(IV) Thermal camera

The thermal camera is a QT5022 camera platform (QTechnology, DK) equipped with a 1024 × 768 pixel microbolometer sensor (Pico1024Gen2™, Lynred, FR), which is sensitive in the wavelength range from 8 μm to 15 μm.

2.3. Data processing

The flow chart presented in Fig. 2 lists the processing steps from acquiring the data cubes to the final classification.

2.3.1. Data cube acquisition

The oven is preheated to 60 °C and loaded with ≈0.5 g of the sample in the middle of the chamber. Additionally, POM and Ultrablack are placed in the oven as references for spectral and blackbody calibration, respectively. Samples are left to thermally equilibrate for at least 20 min before the data cube is acquired.

Each data cube has spatial dimensions of 1024 × 768 pixels, equivalent to 169.8 mm × 127.3 mm in the object plane with a 0.17 mm resolution in both directions. The resulting interferograms contains 141–146 channels depending on the starting position of the mirrors. Thus, MMDs spanning 2.8 μm–13.1 μm are covered.

2.3.2. Preprocessing

The data cube is cropped to the centermost 400 × 400 pixels, giving a sub-data cube excluding irrelevant periphery data (Fig. 3a). Baseline correction is performed by subtracting the first spectral channel from all channels in the data cube, which ensures that all interferograms are shifted to start at zero. The average (40 × 40 pixels) interferogram of the blackbody reference (I_{BB}) is extracted and applied as intensity calibration using Eq. (1):

$$I_f(x,y) = I_{BB} - I_i(x,y) \tag{1}$$

where $I_i(x,y)$ and $I_f(x,y)$ are the interferograms at pixel (x,y) before and after intensity calibration, respectively. Subsequently, a Savitzky-Golay filter ($n = 5$, 1st degree polynomial, 1st order derivative) is applied to the spectral dimension before applying standard normal variate (SNV) to the spectral dimension following Eq. (2).

$$I_{SNV}(x,y) = \frac{I(x,y) - \bar{I}(x,y)}{\sigma_I(x,y)} \tag{2}$$

Here, $I(x,y)$ is the interferogram at pixel (x,y), $\bar{I}(x,y)$ is its mean, and $\sigma_I(x,y)$ is its standard deviation.

The effect of averaging the pixels is evaluated based on the signal-to-noise ratio (SNR) of the PET interferograms. In this work, SNR is defined as the ratio between the amplitude of the MMD interval [7.5:8.5] μm (B-band) and the standard deviation of the interval [2.9:3.5] μm (A-band) as stated by Eq. (3) and illustrated in Fig. 4.

$$SNR = \frac{\max(I_B) - \min(I_B)}{\mathrm{STD}(I_A)} \tag{3}$$

2.3.3. Calibrating the spectral axis of the data cubes

The spectral axis associated with each data cube is defined in terms of the MMD, *not* wavelength. POM is used as a spectral reference, enabling relative comparisons between data cubes. The POM interferogram is averaged from a 40 × 40-pixel area, and the position of the third peak apex is used as a reference for aligning the spectral axes of all data cubes. The true position of this apex can lie between sampling points (every 10th step), and it is therefore estimated by fitting a skewed Gaussian with a resolution of 1 step to the 11 closest data points. Subsequently, a 3rd-order polynomial is fitted to the position of peaks and troughs (measured in steps) of the 655 nm laser diode interferograms. Thereby step numbers become associated with the relative displacement of the mirrors (Fig. SI S3.2). Finally, the MMD axis is defined by shifting the relative mirror separation to align the position of the third POM apex with 5.41 μm.

Data cubes must share the same spectral axis to enable evaluation across data cubes. The lower bound of the range is determined by the largest starting MMD (MMD at the 1st spectral channel) across all data cubes. Similarly, the upper bound is determined by the smallest ending

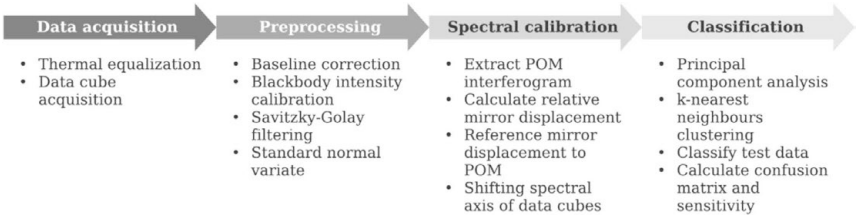

Fig. 2. Flow chart of processing steps from data cube acquisition to material classification using k-nearest neighbors.

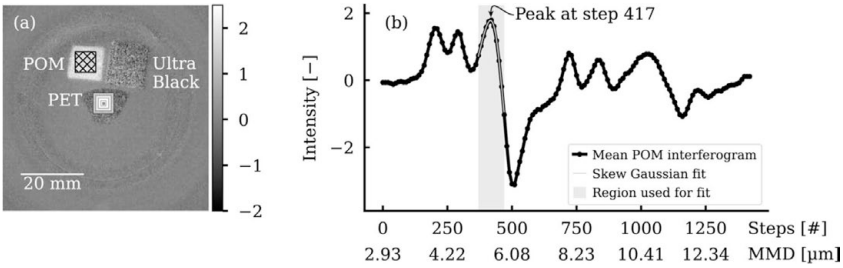

Fig. 3. (a) Slice of data cube at step 420. The hatched 40 × 40 pixel square marks the region from which the mean interferogram of POM is calculated and presented in (b). The interferogram maximum is identified at step ≈420, and using the five neighboring points on each side, it is fitted to a skewed Gaussian. The concentric squares are applied for examination averaging of interferograms.

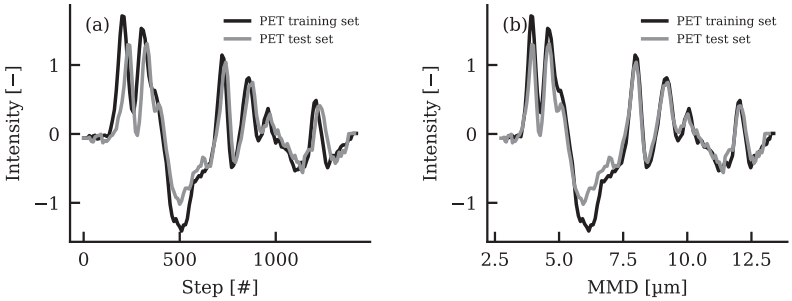

Fig. 4. (a) Mean interferograms of 30 × 30 pixel from two different data cubes of the PET sample. (b) Data with calibrated MMD axis.

MMD (MMD at the final spectral channel) across all data cubes. The sampling points must correspond to the same MMDs, and the interferograms are therefore linearly interpolated between two adjacent data points. This results in all data cubes having the same number of data points at the same MMD with equal spacing.

2.3.4. Classification method

Data cubes from training and testing have been acquired over several days (43 days). Two separate data cube areas captured of each sample and the samples have been reintroduced into the measurement setup between measurements. The data cubes for training were randomly chosen and the other corresponding data cube was applied for testing. Nine interferograms, each an average of 10 × 10 pixels, are extracted from each plastic sample. This results in a total of 117 interferograms for both training and test set.

A PCA model is made based on the training set by first calculating the covariance matrix of the interferograms and subsequently calculating its eigenvalues and eigenvectors. The eigenvectors are often referred to as the loadings of the PCA model, and the eigenvalues are used to calculate the explained variance, var_i, of each principal component (PC) using Eq. (4).

$$\mathrm{var}_i = \frac{\lambda_i}{\sum_{n=1}^{N} \lambda_n} \tag{4}$$

Here, λ_i is the ith out of N eigenvalues.

For classification, the k-nearest neighbor algorithm (k = 13; one for each plastic sample) is subsequently used on the projections of the training set onto the PCs of the PCA model. The nine interferograms of each material are projected onto PCs, and the centroid of each material

cluster is calculated. Classification of the test set is done by projecting each interferogram onto the PCs and calculating the closest centroid. The number of PCs included in the model is determined by the elbow point of the scree plot (Fig. SI S5.1), showing the explained variance of each PC. The micro precision (η) of the predictions is calculated as the ratio of true positives (TP) and the total number of predictions as given in Eq. (5)

$$\eta = \frac{TP}{\sum (TP + FP)} \tag{5}$$

where FP is the total number of false positives. The results of all model predictions are summarized in a confusion matrix. The macro specificity (κ) is averaged across the entire model following Eq. (6)

$$\kappa = \frac{1}{N} \sum_{i=1}^{N} \frac{TN_i}{TN_i + FP_i} \tag{6}$$

Here TN denotes the number of true negatives, while $N = 13$ represents the total number of plastic samples. The subscripts indicate that specificity must be computed separately for each individual class before determining the overall average.

3. Results

Fig. 3a shows the data processing of a PET data cube, with the mean interferogram extracted from the POM spectral reference sample presented in Fig. 3b. Interferograms of intermediate processing steps can be found in Fig. SI S8.1.

The hatched square in Fig. 3a indicates from where the mean interferogram of POM has been extracted and presented in Fig. 3b. Here, the third peak apex is located, and a skewed Gaussian is fitted based on the five neighboring samples on each side as indicated by the shaded region. The peak of the fit is identified at step 417.

The PET interferograms from the training and test sets are extracted from a 30 × 30 pixel region and presented in Fig. 4 before (Fig. 4a) and after spectral calibration (Fig. 4b).

From Fig. 4a, before calibration, the first peak apex is at step 200 for the training set and at 230 for the test set. The two interferograms are off by ≈30 steps (i.e., 3 channels) relative to each other, corresponding to a shift of ≈2 % of the total range. However, after calibration (Fig. 4b), the same peaks are within 0.04 μm of each other, corresponding to a shift of ≈0.4 % of the total range.

The effect on SNR of averaging the interferograms of PET across several pixels is presented in Fig. 5. Each interferogram is sampled from areas ranging from 1 × 1 to 40 × 40 pixels as indicated by the concentric squares in Fig. 3a.

The interferograms presented in Fig. 5 clearly illustrate that the SNR

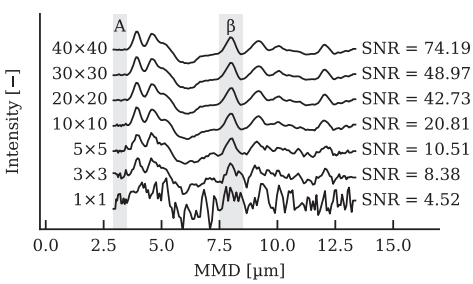

Fig. 5. Mean interferograms sampled across progressively larger areas of 1 × 1, 3 × 3, 5 × 5, 10 × 10, 20 × 20, 30 × 30, and 40 × 40 pixels as indicated by the concentric squares in Fig. 3a. The SNR of each interferogram has been calculated using Eq. (3) using the A and B bands.

for a single pixel is too low (SNR: 4.52), and additionally show that clear interferogram features are visible when 100 pixels or more are averaged (SNR: 20.81).

The average (across both test and training set) interpolated interferograms are presented in Fig. 6a and have 141 data points with MMDs ranging from 2.93 to 13.08 μm. Nine PCs are chosen to be included in the model based on the elbow point of the scree plot (Fig. SI S5.1). The loadings of these nine PCs are presented in Fig. 6b.

Almost all interferograms in Fig. 6a share prominent bands at MMD = 3.95 μm, 8.05 μm, and 12.10 μm as indicated by dashed lines marking the transitions between transmission orders as the MMD increases. The first nine PCs explain an accumulated 96.1 % of the total variance of the training set, with their individual importance indicated next to each loading in Fig. 6b.

The projection of the training set onto PC 2 and PC 3 is presented in Fig. 7a.

Fig. 7 illustrates PC 2 and PC 3 (as PC 1 is dominated by POM), making the visual assessment of the individual clusters clear. The black stars (★) indicate the cluster centroids, and the ellipses indicate one standard deviation from the centroid. The interferograms of the test set are classified, and the result is presented in the normalized confusion matrix in Fig. 8.

All materials are perfectly classified besides ABS, HDPE, and POM (Fig. 8). The misclassification between POM B (0.44) and POM N (0.56) is expected as these have similar emission interferograms. However, only 22 % of the ABS is correctly classified, and it is seen that ABS is not making tight clusters, which therefore overlaps with PA12, ABS, and PVC. Hence, minor changes in noise level and calibration could result in poor ABS prediction. A single HDPE sample is incorrectly classified as PS. η of the model is calculated to 90 % and κ to 99 %.

4. Discussion

4.1. Signal processing

Absorption and emission spectra of a material are related by Kirchhoff's law of thermal radiation. The resulting graybody emission dominates the measurements and hides weak spectral features. The spectral features are thus developed by simulations measurement of a blackbody reference and calculating the difference between the plastics and blackbody interferograms. This emphasizes the minute spectral features in the emission interferograms. It is a challenge if the sample's emissivity deviates strongly from the blackbody's emissivity leaving significant residual graybody emission signal, as exemplified by Fig. SI S9.1. POM N exhibits significant fluctuations in its emission spectrum and after blackbody correction, resulting in strong spectral features (Fig. SI S9.1b). While PP shows smaller spectral features and a higher baseline value after correction due to relatively large residual blackbody signal.

After graybody emission correction, the interferograms show three characteristic peaks at MMD = 3.95 μm, 8.05 μm, and 12.10 μm (dashed lines in Fig. 6a). The MMD of these peaks are associated with half-integer multiples of the lower bound of the microbolometer's sensitivity (wavelength ≈ 8 μm). These overlapping transmission order peaks have a relatively strong intensity masking potential spectral information at these MMDs. Additionally, as the SFPI is swept across three transmission orders (8 – 15 μm), which all contain the same spectral features but at different MMDs. Thus, the overlapping of transmission orders and the three dominating peaks hamper the translation from MMD to wavelengths. Even though it is expected that the interferograms would reflect the emission from specific chemical functionalities, it has not been possible to uniquely assign functional groups to the individual bands in the interferograms.

The variability in material emissivities results in differences in emitted radiation, which consequently affect the measured interferogram intensities. This is corrected by SNV normalization of the

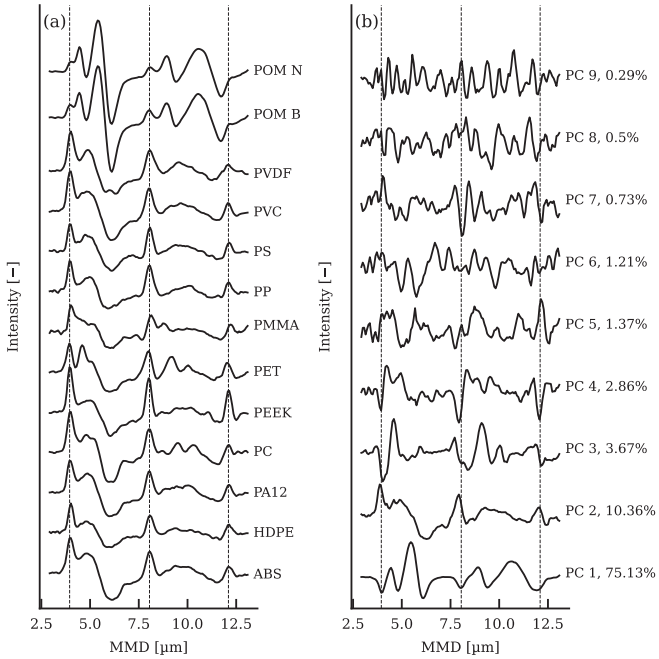

Fig. 6. (a) Mean interferograms of all plastic samples averaged across both training and test data (30 × 30 pixels, from both sets). The interferograms have been intensity-shifted for visual clarity. Dashed lines (MMD = 3.95 μm, 8.05 μm, and 12.10 μm) indicate the characteristic interferogram peaks. (b) The first nine loadings of the PCA model, along with their individually explained variances.

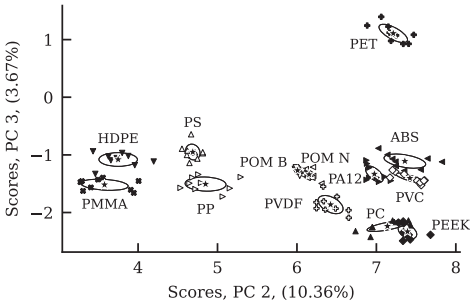

Fig. 7. Projection of training set onto PC 2 and PC 3 of the PCA model. The centroids of each plastic sample are indicated by black stars, and the confidence ellipses indicate one standard deviation. The values in brackets indicate the explained variance of PC 2 and PC 3, respectively.

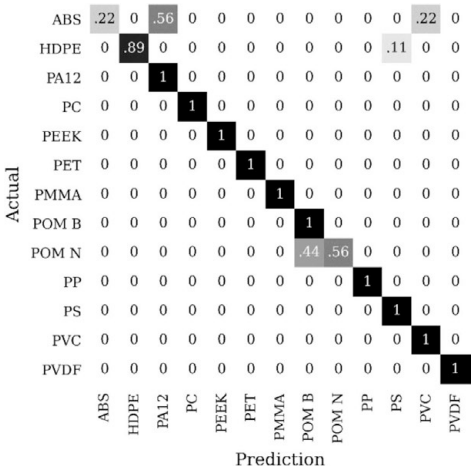

Fig. 8. The normalized confusion matrix for the prediction of the test set based on k-nearest neighbors of the selected 9 PCs from the PCA model.

interferograms. This normalization minimizes variabilities caused by large intensity differences and ensures the best variance maximization for the subsequent dimension reduction via PCA. Thus, this correction enables plastic material distinction based on their interferograms. Currently, only the relative mirror displacement can be derived from the interferograms of the monochromatic laser diodes and not the absolute MMD, thus necessitating spectral calibration. When calibrating the

interferograms, it is preferable to avoid selecting one of the three peaks arising from sweeping the SFPI across the transmission orders (e.g., MMD at 3.95 μm), as this will result in an equipment-dependent reference point. This will challenge cross-system comparison. The interferograms are therefore aligned to a spectral feature of POM as it shows a distinct interferogram and strong signal intensity (Fig. 6a). The highest intensity in the POM interferograms is the third apex (Fig. 3a) which was defined to MMD = 5.41 μm. The minimum intensity (MMD ≈ 6 μm) would give an equally strong reference point. However, it would demand more data manipulations to apply the Gaussian fitting procedure. Clearly, selecting an apex in any other material would work equally well to give an external material reference. Defining an external reference point will not solve the issue of having a varying number of spectral channels in each data cube. During the alignment sweeps, mirror alignment is optimized by successively adjusting the potentials applied across the piezo actuators. These potentials are dependent on the initial position of the mirrors and the SFPI temperature. As a result, different data cubes may have a different number of channels. Thus, adjusting the number of channels across the data cubes is achieved by the procedure described in Section 2.3.3. Further, the external reference point will not ensure exact MMD alignments. Thus, linear interpolation between MMDs is used to obtain data cubes with the same number of spectral channels. It is clear from Fig. 4 that employing an external reference and aligning MMD decreases the data cubes misalignment by almost a decade.

Generally, two interferograms of the same material lie within two standard deviations of the average. Closer examination of the interferograms (Fig. SI S2.1a – S2.13a) reveals variations between corresponding data sets, e.g., PVC at MMDs between 8.5 μm and 11.5 μm. It is challenging to determine whether the signal variations are noise or actual spectral features. Several interferograms are available from each plastic sample as a single pixel corresponds to a spatial area of 0.17 × 0.17 mm (0.03 mm^2). Averaging a 3 × 3 pixel (0.26 mm^2) doubles the SNR. More detailed spectral features become visible, and the improvement in SNR diminishes when exceeding 20 × 20 pixels (11.56 mm^2) (Fig. 5). Though the SNR improves with larger averaging areas, it is also important to examine how signal averaging affects the performance of the material prediction models.

4.2. Material prediction

The performance of the classification model improves with larger sampling areas (Figs. S7.1–S7.4) as the SNR is raised. For example, sampling 3 × 3 (0.26 mm^2) or 5 × 5 (0.72 mm^2) pixels results in η of 74.5 % and 84.2 %, respectively and κ of 97.9 % and 98.7 % respectively. Industrial plastic flakes are normally above 5 × 5 mm (25 mm^2), and averaging multiple (100+) interferograms from a single plastic flake will be possible (with the present setup), ensuring good classification.

Examining the PCA model loadings reveals how the different plastics are classified (Fig. 6b). PC 1 distinguishes POM from the rest and is responsible for 75 % of the variance due to the strong spectral features in the POM interferograms (Fig. 6b). The loadings of PC 2 mostly evaluate variations in the position of the three overlapping transmission order peaks and their shift to towards shorter MMDs (3.9 μm, 7.9 μm, and 12.0 μm). This causes PMMA and HDPE to score low as their three characteristic peaks are shifted towards longer MMDs. This indicated that these plastics have spectral features positioned close to the artifacts from the overlapping transmission orders. PET is almost exclusively distinguished using PC 3, as it shares the same bands at 9.2 μm and 10.0 μm. PVDF scores high on PC 4 partly due to its peak at MMD ≈ 6.0 μm and trough at MMD ≈ 11.2 μm. With higher-order components, the captured detail becomes smaller as the explained variance decreases, and the PCs describe finer features and become more dominated by noise. Thus, the same components are used to describe multiple materials simultaneously, and it becomes challenging to designate which loadings distinguish which materials.

The classification performs well (η = 89.7 %, κ = 99.1 %), however, ABS, HDPE, and POM N are misclassified in some instances (Fig. 8). The ABS interferograms are misclassified seven out of nine times, classifying them as either PA12 or PVC, and HDPE is classified as PS in one case. Fig. 6a depicts minute differences between the ABS and HDPE interferograms. A plausible explanation is the residual signal after blackbody correction. It was examined if excluding the strong influence of POM would enhance the predictive power of the remaining plastics. When excluding POM then PC 1 explains 40.1 % of the variance, and the cumulative explained variance of the nine PCs is 86.4 % compared to 96.1 % when including POM. This indicates that the smaller spectral variations are weighted higher and the η of the model without POM is 90.1 % while it is 89.7 % when both POM samples were included. The minute reduction in η is ascribed to the misclassifications between the two POM samples. Furthermore, excluding POM from the model leads to a worse classification of PA12, which is misclassified twice as ABS. The correct prediction of ABS increases by one as it is misclassified as PA12 one time fewer than the model including POM. The model classified POM N as POM B four out of nine times, as expected since both samples are POM. This shows that pigmentation (conc. ≈ 0.2–4 % by mass) has minimal influence on the spectral features in emission spectroscopy, implying that the technique might be suitable for classifying colored or even black plastics.

4.3. Industrial challenges/relevance/implications

The data processing (PCA and k-nearest neighbors) is mostly linear matrix operations which are performed quickly (in orders of μs or faster). This means that data processing is not a limiting factor when considering the industrial potential of emission spectroscopy. However, sample heating and data acquisition time are the main limitations of employing this camera in industrial settings. To acquire one data cube, nine alignment sweeps are performed prior to the actual data acquisition sweep, each sweep taking ≈35 s. It is anticipated that the initial alignment sweeps can be performed at the beginning, followed by continuous data cube acquisitions. Further, optimization of the electronics could enable the microbolometer sensor to reach a refresh rate of 60 Hz, reducing the data cube acquisition time to ≈2 s. However, this is still too slow for most industrial applications, and thus, a reduced interferogram resolution might be necessary. The second industrial challenge is heating samples prior to measurement. Heating elements have previously been deployed at conveyors [24], but a more practical approach might be to cool the microbolometer sensor. Employing Peltier cooling to obtain the temperature difference might be a solution. In this study, the temperature difference of ≈32 °C could thus be archived without heating the samples.

Although several optimization steps are to be undertaken, this work clearly shows that it is possible to discriminate different plastic materials based on recorded interferograms of their thermal emission spectra via hyperspectral imaging. Hence, the task of industrialization of this technology is highly relevant to undertake.

5. Conclusion

Hyperspectral imaging sensitive to wavelength between 8 and 15 μm using a scanning Fabry-Pérot interferometer as a variable bandpass filter could classify most of the thirteen investigated plastic samples. The proposed spectral calibration method enables comparison between data cubes despite their different spectral axes. The PCA model successfully reduced the dimensionality of the data cubes of 141 spectral channels to 9 principal components. Hence, classification was demonstrated using down to 3 × 3 pixels (0.26 mm^2), though larger areas (10 × 10 pixels) improve the micro precision to 90 % and macro specificity to 99 %. The classified samples were a mixture of natural and colored industrial plastics. This simple classification model shows that the developed camera system can be applied to distinguish between many common

types of plastic.

Further exploration of this new technique could include studies of black plastics. Moreover, the reduction of acquisition time and the required sample temperature are important focus points for the industrialization of the technology.

Declaration of competing interest

The authors declare that they have no known competing financial interests or personal relationships that could have appeared to influence the work reported in this paper.

Acknowledgments

The authors thank the Innovation Fond Denmark (grant no: 1044-00116B) and the Innovation Fond Denmark (grant no: 0177-00035B), Aarhus University, Dansk Affaldsminimering, Vestforbrænding, and Plastix for financial support under the Re-Plast project. The authors would further thank Gerd Riedel (Bruker Optics, DE) for recording the emission FTIR spectra in Fig. SI S9.1.

Appendix A. Supplementary data

Supplementary data to this article can be found online at https://doi.org/10.1016/j.saa.2024.125501.

Data availability

Data will be made available on request.

References

[1] Plastics - the facts, Plastics Europe, 2022.
[2] I. Auken, Danmark uden affald, Miljø- og Fødevareministeriet, 2023.
[3] F. Besenbacher, Advisory Board for cirkulær økonomi - anbefalinger til regeringen, Miljø Og Fødevareministeriet (2017).
[4] G. Leone, J. M. T. I. Borràs, E. D. V. Martín, The new plastics economy: rethinking the future of plastics & catalysing action, Ellen MacArthur Found, 68, 2017.
[5] S.A. Veltzé, C. Fischer, S. Hirsbak, Miljøets fodspor nr. 5 - affald, Miljøstyrelsen, 5, 2019.
[6] D.K.A. Barnes, A. Walters, L. Gonçalves, Macroplastics at sea around Antarctica, Mar. Environ. Res. 70 (2) (2010) 250–252, https://doi.org/10.1016/j.marenvres.2010.05.006.
[7] A.S. Colferai, R.P. Silva-Filho, A.M. Martins, L. Bugoni, Distribution pattern of anthropogenic marine debris along the gastrointestinal tract of green turtles (Chelonia mydas) as implications for rehabilitation, Mar. Pollut. Bull. 119 (1) (2017) 231–237, https://doi.org/10.1016/j.marpolbul.2017.03.053.
[8] P.L. Corcoran, M.C. Biesinger, M. Grifi, Plastics and beaches: a degrading relationship, Mar. Pollut. Bull. 58 (1) (2009) 80–84, https://doi.org/10.1016/j.marpolbul.2008.08.022.
[9] E. Martinez, K. Maamaatuaiahutapu, V. Taillandier, Floating marine debris surface drift: Convergence and accumulation toward the South Pacific subtropical gyre, Mar. Pollut. Bull. 58 (9) (2009) 1347–1355, https://doi.org/10.1016/j.marpolbul.2009.04.022.
[10] P.G. Ryan, C.J. Moore, J.A. van Franeker, C.L. Moloney, Monitoring the abundance of plastic debris in the marine environment, Philos. Trans. R. Soc. B Biol. Sci. 364 (1526) (Jul. 2009) 1999–2012, https://doi.org/10.1098/rstb.2008.0207.
[11] Sustainable plastics strategy, SUSCHEM, Dec. 2020.
[12] R.C. Thompson, et al., Lost at sea: where is all the plastic? Science 304 (5672) (2004) 838, https://doi.org/10.1126/science.1094559.
[13] A European strategy for plastics in a circular economy, European Comission, 2018.
[14] P.H. Andersen et al., The new plastics economy, 2019.
[15] M. Tsakona, L. Rucevska, Baseline report on plastic waste, Basel Convention (2020).
[16] O. Rozenstein, E. Puckrin, J. Adamowski, Development of a new approach based on midwave infrared spectroscopy for post-consumer black plastic waste sorting in the recycling industry, Waste Manag. 68 (2017) 38–44, https://doi.org/10.1016/j.wasman.2017.07.023.
[17] A. Vázquez-Guardado, M. Money, N. McKinney, D. Chanda, Multi-spectral infrared spectroscopy for robust plastic identification, Appl. Opt. 54 (24) (2015) 7396, https://doi.org/10.1364/AO.54.007396.
[18] C. Signoret, A.-S. Caro-Bretelle, J.-M. Lopez-Cuesta, P. Ienny, D. Perrin, Alterations of plastics spectra in MIR and the potential impacts on identification towards recycling, Resour. Conserv. Recycl. 161 (2020) 104980, https://doi.org/10.1016/j.resconrec.2020.104980.
[19] J. Colwill, A. Simeone, O. Gould, E. Woolley, C. Mulvenna, Energy-efficient systems for the sensing and separation of mixed polymers, Proc. CIRP 62 (2017) 512–517, https://doi.org/10.1016/j.procir.2016.06.116.
[20] M. Kedzierski, E. Geslain, M.L. Pedrotti, J.-F. Ghiglione, S. Bruzaud, Pre-detection of microplastics using active thermography, Chemosphere 262 (2021) 127648, https://doi.org/10.1016/j.chemosphere.2020.127648.
[21] A.L. Jørgensen, M.N. Larsen, V. Petrunin, J. Kjelstrup-Hansen, B. Jørgensen, Surface temperature determination using long range thermal emission spectroscopy based on a first order scanning Fabry-Pérot interferometer, Opt. Exp. 30 (2) (2022) 2186, https://doi.org/10.1364/OE.441798.
[22] M.L. Henriksen, C.B. Karlsen, P. Klarskov, M. Hinge, Plastic classification via in-line hyperspectral camera analysis and unsupervised machine learning, Vib. Spectrosc. 118 (2022) 103329, https://doi.org/10.1016/j.vibspec.2021.103329.
[23] Re-plast.dk - Database, Nov. 25, 2020. <https://re-plast.dk/> (Accessed May 19, 2023).
[24] P. Meinlschmidt, V. Maergner, Thermographic techniques and adapted algorithms for automatic detection of foreign bodies in food, Presented at the AeroSense 2003, K. E. Cramer and X. P. Maldague, Eds., Orlando, FL, Apr. 2003, p. 168. doi: 10.1117/12.488701.

C. Paper: Classification of black plastic types by hyperspectral imaging based on long-wave infrared emission spectroscopy

This section presents the paper titled *Classification of black plastic types by hyperspectral imaging based on long-wave infrared emission spectroscopy*, published in Polymer Testing [4]. This paper uses a similar methodology as in *Classification of commercial plastics using hyperspectral long wave infrared emission imaging*. Still, this time, the plastics have been colored using carbon black, which traditional imaging techniques have difficulty distinguishing.

Polymer Testing 141 (2024) 108629

Contents lists available at ScienceDirect

Polymer Testing

journal homepage: www.elsevier.com/locate/polytest

Classification of black plastic types by hyperspectral imaging based on long-wave infrared emission spectroscopy

Mads Nibe Larsen [a,b], Anders Løchte Jørgensen [b], Victor Petrunin [b], Jakob Kjelstrup-Hansen [a], Bjarke Jørgensen [b], Mogens Hinge [c,*]

[a] NanoSYD, Mads Clausen Institute, University of Southern Denmark, 6400, Sønderborg, Denmark
[b] Newtec Engineering A/S, 5230, Odense, Denmark
[c] Plastic and Polymer Engineering, Department of Biological and Chemical Engineering, Aarhus University, 8200, Aarhus N, Denmark

ARTICLE INFO

Keywords:
Hyperspectral imaging
Fabry-pérot interferometry
Thermography
Classification of black plastics
Principal component analysis

ABSTRACT

Identification of black plastics poses a significant challenge in recycling due to the absorptive nature of carbon black additives. This work introduces a method where hyperspectral imaging in the long-wave infrared regime is used to distinguish between twelve samples of commercially available black plastics encompassing nine distinct polymer types. The spectral scanner comprises a scanning Fabry-Pérot interferometer and a thermal camera based on an uncooled microbolometer detector sensitive to wavelengths from 8 μm to 15 μm. A principal component model is combined with k-nearest neighbors to differentiate between plastic samples in hyperspectral images. The model successfully classifies five (PET, POM, PMMA, PA6, and PA66) out of nine black polymers, and the overall accuracy of the model is $A = 73.1$ %.

1. Introduction

Plastics have become ubiquitous across all industries and sectors of modern society due to its high versatility, low cost, and convenience. Plastic production has more than doubled in the past two decades, with global production reaching 400 megatonnes in 2022, but unfortunately, only about 10 % is recycled [1]. Furthermore, poor waste management results in around 22 % of the plastic being disposed of in unregulated dumpsites, burned in open pits, or leaked into the ecosystem leading to contamination [2–8]. This is caused by poor consumer behavior and underdeveloped recycling infrastructure. Household plastic waste consists of a mix of different materials, sizes, shapes, additives, and contaminants [9,10]. All this makes it difficult to obtain the >95 % material purity required for recycling of high-quality products [11].

Optical imaging and spectroscopic methods have previously been shown to be able to differentiate between various types of plastics and are already employed for plastic identification. These methods operate in various parts of the electromagnetic spectrum, such as X-ray [12], ultra-violet (UV) [13], visible (VIS) [14], near-infrared (NIR, [wavelengths 850–1800 nm]) [15], and Terahertz [16]. These techniques employ either reflective or transmissive measurements of the plastic samples.

However, black dyed plastics challenge these techniques as the content of carbon black results in light absorption at all wavelengths [17–19]. X-rays penetrate plastics of any color, however, often results in poor spectroscopic contrast which is too low for plastic discrimination [17,20]. Exciting the black plastics with UV lasers enables laser-induced fluorescence in the range from 280 to 550 nm and was used for identification of black plastics (PS, PE and PP) with high accuracy [21]. Fourier Transform Infrared (FTIR) spectroscopy has also been shown to distinguish black plastics as it utilizes long-wave infrared (LWIR) wavelengths where the impact of carbon black is less severe [19,22]. The Mid-infrared (MIR) wavelengths have been utilized for identifying the plastic type in black plastics [23]. Additionally, an advanced camera technology which upconverts light to the NIR-Vis range has been applied to analyze mixed plastic waste [24]. However, for FTIR transmission measurements, the plastic samples must be tens of microns thin. Using FTIR in attenuated total reflectance (ATR) mode, the sample must be in direct contact with the crystal. As an alternative to transmission and reflection spectroscopy techniques thermographic methods in the LWIR spectral range can also distinguish between various types of plastics by observing differences in their heating/cooling rate [25]. However, black dyed plastics challenge these techniques as the content of carbon black results in light absorption at all wavelengths [26]. Fourier Transform

* Corresponding author.
E-mail address: hinge@bce.au.dk (M. Hinge).

https://doi.org/10.1016/j.polymertesting.2024.108629
Received 13 September 2024; Received in revised form 15 October 2024; Accepted 3 November 2024
Available online 7 November 2024
0142-9418/© 2024 The Authors. Published by Elsevier Ltd. This is an open access article under the CC BY license (http://creativecommons.org/licenses/by/4.0/).

Infrared (FTIR) spectroscopy has been shown to distinguish black plastics as it utilizes long-wave infrared (LWIR) wavelengths where the impact of carbon black is less severe [19,22]. However, for FTIR transmission measurements, the plastic samples must be tens of microns thin. Using FTIR in attenuated total reflectance (ATR) mode, the sample must be in direct contact with the crystal. Hence, these FTIR techniques are not feasible for plastic identification in an industrial setting where the plastics are transported via conveyor belts [27].

Thermographic methods in the LWIR spectral range can distinguish between various types of plastics by observing differences in their heating/cooling rate [25]. However, data processing requires a detailed understanding of sample heat capacity, mass, and emissivity to obtain accurate results. In the case of black plastics, the addition of a typically unknown concentration of carbon black to the polymer matrix increases the plastic's emissivity. Thus, the accurate physical properties are generally unknown, and only relative comparisons can be performed. However, the emission spectra are independent of geometry and carry material-specific information, and hyperspectral emission spectroscopy would enable classification of black plastics based on their polymer type.

In this study, a newly developed hyperspectral LWIR imager is attempted for differentiating among polymer types in twelve commercial black plastic samples. This method combines a low-order scanning Fabry-Pérot interferometer (SFPI) and a thermal camera based on an uncooled microbolometer detector. The obtained hyperspectral images are pre-processed by spectra averaging, Savitzky-Golay filtering, etc., and subsequently applied in a classification of the plastic types. After preprocessing, a principal component analysis (PCA) is applied for dimensionality reduction, and subsequent k-nearest neighbors is used to classify the black plastic samples.

2. Materials and methods

2.1. Materials

This study includes twelve black plastic samples (Table 1 and Fig. 1) with varying sizes and shapes, with side lengths/diameters of a few centimeters, and thicknesses ranging from 2.6 to 6.0 mm. Some samples are variations with the same polymer matrix (e.g. PMMA 101–48,000 and 200–48,000) giving nine distinct polymer types. The samples have been described in detail elsewhere [16].

2.2. Experimental setup

The experimental setup (illustrated in Fig. 2) consists of the hyperspectral imaging system positioned above a heating chamber (oven) where the plastic sample is placed. The hyperspectral camera consists of a scanning Fabry-Pérot interferometer, collecting germanium optics, and a microbolometer-equipped thermal camera. Furthermore, an IR bandpass filter with a central wavelength of 8.226 μm (1216 cm^{-1}) (Andover Corporation, USA) is fitted above an 80 °C hotplate (OpenBuilds USA) which is placed next to the oven.

The oven consists of a 90 × 90 × 20 mm aluminum baseplate with two 250 W heating elements (Ø10 × 70 mm, 220 V AC, RS Components, DK) and a hollow aluminum cylinder (inner diameter: Ø50 mm, height: 45 mm). The top of the oven is fitted with a zinc selenide (ZnSe) window (Ø50.8 × 5 mm) with an anti-reflective coating. A PID controller (Inkbird, CH) connected to the baseplate via a K-type thermocouple controls the oven temperature.

The scanning Fabry-Pérot interferometer is made from two ZnSe substrates (Ø50.8 × 5 mm), on each of which, a partially transparent dielectric thin-film mirror is deposited (Ø43 mm, centered). The thin-film stack comprises 1.311 μm germanium (Ge), 1.981 μm thorium tetrafluoride (ThF_4), and another 0.655 μm Ge. 100 Å zinc sulfide (ZnS) binding layers are deposited between the Ge and ThF_4 layers. This results in mirrors having an ≈ 84 % average reflectance in the wavelength range from 8 to 15 μm. Each of the mirrors is fixed in their own half of a stainless-steel fixture. The two halves are held together by three sets of nuts and bolts equally spaced around the fixture perimeter. A stack of four disc-springs (outer diameter: Ø12.5 mm, force: 673 N, Sodemann Industrifjedre A/S, DK) is placed between each bolt and the fixture to provide a restoring force when the two halves of the fixture are forced apart by three piezo actuators (PK2FMP2, force: 400 N, maximum expansion: 11.2 μm, Thorlabs, USA).

A germanium objective with an effective focal length of 35 mm and f/1 aperture (Ophir Optronics Solutions Ltd., IL) focuses the light onto the microbolometer sensor. It comprises a Ø35.2 mm aspheric front element with an effective focal length of ≈135 mm and a Ø52.3 mm spherical back element with a focal length of ≈45 mm. The focal plane can be adjusted electronically via a piezo inchworm linear actuator.

The thermal camera consists of an uncooled 1024 × 768-pixel microbolometer sensor (Pico1024Gen2™, Lynred, FR) fitted to a QT5022 camera platform (QTechnology, DK). The sensor is sensitive to wavelengths ranging from 8 μm to 15 μm.

2.3. Data flow and processing

Fig. 3 gives a visual overview of the entire data processing.

All data processing is performed in Python v.3.11 only including the NumPy package and each part of the data processing will be described in the following subsections.

2.4. Image acquisition

A black body reference sample (Ultra Black™ emissivity: $\varepsilon > 0.93$, 3–30 μm, Acktar, IL) is placed inside the oven directly on top of the aluminum baseplate heated to 60 °C. The sample under investigation is placed on top of the black body reference, still leaving parts uncovered. The sample is then left to thermally equilibrate for at least 30 min before a hyperspectral image is collected. For the rectangular samples, the oven chamber rests on top of the sample, introducing a minor airgap between the oven and the baseplate (see Fig. S1). When capturing a hyperspectral image, the MMD sweeps from ≈3 μm to ≈13 μm during which ≈150 images are acquired. An MMD sweep takes ≈10 s, during which the camera captures images as fast as possible. Hyperspectral image acquisition is repeated twice for all samples, giving a training and a validation data cube.

2.5. Spectral calibration and mirror alignment

A potential is applied to the piezo actuators to control the mirror-to-mirror distance (MMD). As the piezo actuators expand, the MMD increases up to ≈13 μm, and this sweep is discretized into 1500 "steps".

Table 1
Sample identification (ID), plastic type, abbreviation (Abbv.), trade name, and supplier are listed for the studied black plastic samples.

ID	Plastic type	Abbv.	Trade Name	Supplier
1	Polystyrene	PS	R1058-Black	Plazit-Polygal
2	Polystyrene	PS	R1058-Black-MG	Plazit-Polygal
3	Poly(styrene-co-acrylonitrile)	SAN	R4558-Black	Plazit-Polygal
4	Poly(methyl methacrylate)	PMMA	101–48,000	Vink
5	Poly(methyl methacrylate)	PMMA	200–48,000	Vink
6	Polyoxymethylene	POM	SustarinC-Black	Röchling
7	Polyamide 6	PA6	PA6XTSort	Vink
8	Poly(vinyl chloride)	PVC	PVCSort	Vink
9	Polyethylene	PE	PE300Sort	Vink
10	Polyoxymethylene	POM	POMCSort	Vink
11	Polyamide 6,6[a]	PA66	PA66-GF30	Vink
12	Poly(ethylene therphalate)	PET	PETPSort	Vink

[a] Contains 30 % glass fibers.

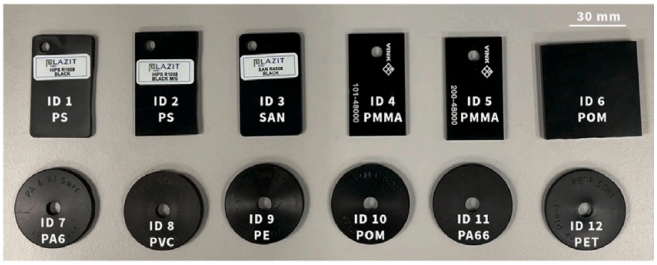

Fig. 1. Photograph of the investigated plastic samples. Details are given in the main text.

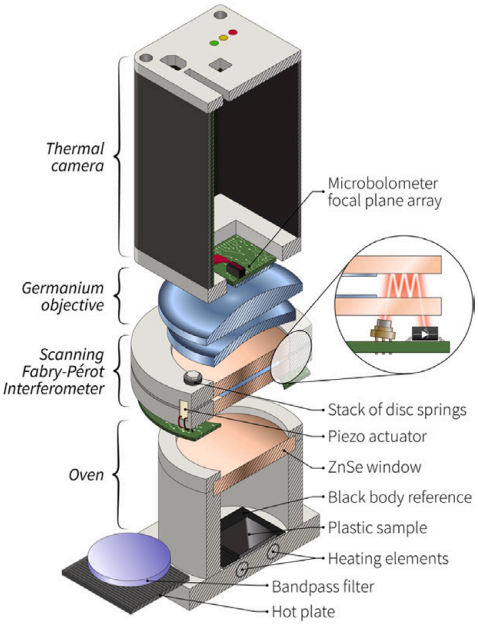

Fig. 2. Schematic representation of hyperspectral thermal camera as part of the experimental setup (not to scale). Insert shows the system for monitoring the MMD.

Initially, the same voltage is applied across all actuators. However, imperfections in the piezo actuators cause slightly different expansions. Preliminary calibrations sweeps are therefore performed and each "step" is associated with three potentials applied to the three actuators. During these sweeps, the displacement of the mirrors is monitored, and the potentials are adjusted accordingly in an iterative process ensuring the mirrors remain mutually parallel. A printed circuit board (PCB) with three laser diodes is mounted around the edge of the SFPI to monitor the this relative displacement. Laser beams from the three laser diodes are aimed at the uncoated part of the mirror cavity, and part of each beam is reflected back onto photodiodes located next to the laser diodes (Fig. 2 inset).

The displacement of the mirrors can be inferred from the laser diode interferograms via Eq. (1), which describes the condition for constructive interference.

$$MMD = \frac{m}{2}\frac{\lambda_{\text{diode}}}{\cos\theta} \quad m \in \{1, 2, 3, \ldots\} \tag{1}$$

Here, m is the transmission order, λ_{diode} is the laser diode wavelength, and θ is the angle of incidence between the laser beam and the mirror substrate. The exact angle of incidence is unknown, and an effective wavelength, $\lambda_{\text{eff}} = \lambda_{\text{diode}}/\cos\theta$ is introduced and can be substituted into Eq. (1). The displacement associated with moving from a constructive interference peak to the neighboring destructive interference trough is $\frac{\lambda_{\text{eff}}}{4} = 170$ nm. A 3rd order polynomial fit to the peak/trough locations makes it possible to relate each step with a physical displacement of the mirrors. The position of the first peak/trough (whichever comes first) defines a mirror displacement of 0 μm, and every subsequent peak/trough is associated with an MMD increase of 170 nm. To determine the absolute MMD, a 40 × 40-pixel average interferogram of the narrow bandpass filter is extracted. The second-order peak is known to be associated with an MMD of 8.4 μm, and the rest of the interferograms are offset accordingly.

The exact number of images (and corresponding MMD) recorded during a sweep can vary among sweeps. To enable comparisons, the data cubes are interpolated along their spectral dimension. The data cube with the fewest channels determines the number of interpolation points. The data cube with the largest initial MMD (i.e., MMD at the 1st channel) determines the lower end of the interpolation range. Similarly, the data cube with the smallest final MMD determines the upper bound of the interpolation range.

2.6. Data pre-processing

Obtained data cubes are baseline corrected by initially subtracting the first channel following Eq. (2).

$$I_1(x, y, z) = I_0(x, y, z) - I_0(x, y, 0) \tag{2}$$

Here, $I(x, y)$ is the interferogram found at pixel coordinates (x, y) and z refers to the zth entry along the spectral dimension. The indices refer to the data cube processing step, with subscript 0 indicating the raw data. A 30 × 30-pixel area of the black body reference sample is averaged, $I_{1,BB}$, and the data cube is then black body corrected by subtraction from the black body interferogram, following Eq. (3).

$$I_2(x, y, z) = I_{1,BB}(z) - I_1(x, y, z) \tag{3}$$

Subsequently, a Savitzky-Golay filter (5 samples, 1st degree polynomial, 1st order derivative) is applied, and the resulting interferograms are referred to as $I_3(x, y, z)$. Finally, standard normal variate (SNV) is applied along the spectral axis by Eq. (4).

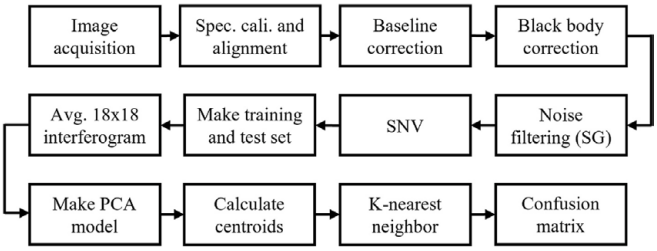

Fig. 3. Data processing flow chart from image acquisition to final classification. Where, Spec. cali.: Spectral calibration, SG: Savitzky-Golay filtering, SNV: standard normal variate, Avg.: average, and PCA: principal component analysis.

$$I_4(x,y,z) = \frac{I_3(x,y,z) - \bar{I}_3(x,y)}{\sigma_3(x,y)} \tag{4}$$

Here, $\bar{I}_3(x,y)$ is the mean and $\sigma_3(x,y)$ is the standard deviation of the interferogram at (x,y).

2.7. Classification method

Hyperspectral image acquisition was performed twice for all plastic samples, resulting in separate training and validation data cubes. Between each acquisition, the samples were repositioned, with up to a day between measurements. Nine sample areas of 18 × 18-pixel averages are extracted from each data cube. Subsequently, extracted interferograms from the training data set are combined into a single matrix, with each row corresponding to an interferogram, and principal component analysis (PCA) is applied. The explained variance associated with each principal component (PC) is calculated by Eq. (5) [28].

$$\mathrm{EV}_i = \frac{s_i^2}{\sum_{n=1}^{N} s_n^2} \tag{5}$$

where s_i is the ith out of N singular values of the data covariance matrix. The elbow point of the scree plot is used to determine the number of PCs to include in the model (Fig. 6). The centroid of the nine extracted interferograms projected onto the PCs is calculated for each of the twelve plastic samples.

After training, the validation data set of the plastic samples is projected onto the model and the class assigned to each projection is based on the closest centroid from the training set (k-nearest neighbors). To evaluate the model performance, the predictions are compiled in a normalized confusion matrix. The accuracy, A, of this classification is calculated as the ratio of true positives (TP) and the total number of predictions as given in Eq. (6)

$$A = \frac{TP}{TP + FP + TN + FN} \tag{6}$$

where FP is the total number of false positives, TN is the total number of true negatives, and FN is the total number of false negatives.

A confusion matrix is calculated to summarize the performance of the classification model. Rows corresponding to the actual class, and columns representing the predicted class. TP is located along the diagonal, indicating correct classifications, while FP and FN are placed off-diagonal indicating misclassifications. The rows are normalized to a sum of 1.

3. Results

3.1. Equipment alignment and data preprocessing

The laser diode interferograms are depicted in Fig. S2 as a function of applied actuator voltage, and in Fig. 4a as a function of step #. When the laser interferograms are depicted as a function of step #, the phase difference is maintained throughout the sweep as indicated by the dashed lines in Fig. 4a.

According to Eq. (1), the displacement from a peak to a trough in the laser diode interferogram (i.e., the distance between two adjacent lines in Fig. 4a) corresponds to 170 nm. To obtain an expression relating the relative mirror displacement and step #, a 3rd-order polynomial is fit ($R^2 = 0.99996$, Fig. S3a).

The average interferogram of the IR-bandpass filter is extracted from the data cube. The position of the second band is identified at step 778 (Fig. S3b) and is associated with an MMD of 8.4 μm. The relative displacement curve (Fig. S3a) is offset to align step 778 with an absolute MMD of 8.4 μm, resulting in the final MMD axis (Fig. 4b). The effect of the alignment procedure is demonstrated in Fig. S4, where two interferograms of the same PET sample are overlayed (after data preprocessing). Every data cube has 155 channels with MMDs spanning from 2.8 μm to 13.0 μm after calibration. The effects of the data processing procedure are depicted in Fig. 5. Here, both an image, as well as the extracted average interferograms of ID 12 PET and the Actar Ultra Black reference sample (black body), are presented at each stage of the procedure described in section 2.5.

The mean interferogram of each plastic sample from the training set has been extracted and displayed in Fig. 6.

All interferograms show common peaks at MMD = 3.95 μm, 7.98 μm, and 12.0 μm. Additionally, the POM samples stand out by having pronounced peaks at 4.5 μm and 5.4 μm MMD, which are replicated at 9.0 μm and 10.6 μm respectively. The PET interferogram also shows a distinctive peak at 4.6 μm MMD, which is replicated in the second order at 9.1 μm. A shoulder is also visible around 5.1 μm, which shows up again as a discrete peak at 10.0 μm.

Comparison of the rest of interferograms reveals a high degree of similarity, with minor differences observed in the shapes and positions of the peaks.

3.2. Plastic classification

The PCA model is calculated based on the training set, and the resulting scree plot which gives the explained variance of the PCs from Eq. (5) is shown in Fig. 7.

As indicated by the inset, an elbow point is identified at PC6, and thus, six PCs are included in the model. Together, the six PCs explain 97.9 % of the variance of the data set. The higher-order components, which contribute less to the variance, primarily explain the noise in the

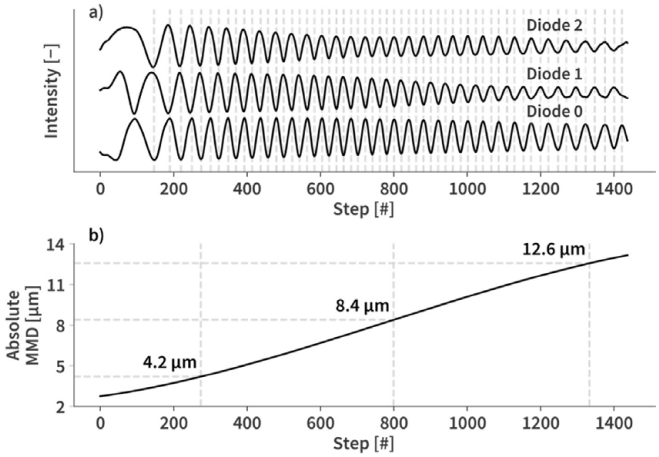

Fig. 4. **a)** The laser diode interferograms as a function of calibrated steps. Vertical lines illustrate the alignment between peaks and throughs. **b)** Absolute MMD as a function of steps. The horizontal lines refer to the locations of the three transmission orders of an 8.226 µm bandpass filter, which has been used in the calibration procedure (Fig. S3b).

signal. The loadings of the six included PCs are found in Fig. S5.

Interferograms from the validation data set are projected onto the loadings of the six included PCs. Fig. 8b shows the projections along PC2 and PC3, as PC1 mainly distinguishes POM from the other plastic types. The normalized confusion matrix summarizes the classifications of the test set interferograms (Fig. S6). The accuracy of the model (Eq. (6)) is calculated to $A = 57.4$ %. Several of the samples are of the same polymer type, and confusion among samples of the same polymer should, therefore, not necessarily be penalized. Upon pooling (ID 1 PS & ID 2 PS, ID 4 PMMA & ID 5 PMMA, and ID 6 POM & ID 10 POM) samples by polymer type, the accuracy increases to $A = 73.1$ % (Fig. 8a). Additional classification metrics are provided for each of the material classes and presented in Table S1 in section S5.

The Euclidian distance between centroids is a measure of how much the interferograms differ from each other (Fig. 9). The farther apart, the more different the interferograms. Here, the Euclidean distances between all samples are normalized to the largest distance in the set (which is between ID 10 POM and ID 12 PET).

The greatest distance is observed between ID 10 POM and ID 12 PET, indicating the most significant variation. The POM samples labeled ID 6 POM and ID 10 POM have the highest average distances to the other samples, measuring 0.63 and 0.86, respectively. Conversely, the sample with the shortest average distance to the other samples is ID 8 PVC with a distance of 0.25.

4. Discussion

4.1. The experimental setup

Employing a microbolometer detector demands that the difference in radiation power *received* and *emitted* by the detector is maximized, as the signal strength is proportional to the net radiation power transferred to the detector. The microbolometer detector employed in this work is uncooled, generating a need for sample heating to increase the received signal to a sufficient level. However, heating the samples is energy and time demanding. Thus, cooling or heating the detector might be a solution to increase the difference and thereby increase the signal strength. It is convenient to increase the sensor temperature, but this will also increase the noise equivalent power (NEP), thereby reducing the signal-to-noise ratio [29]. This implies that cooling the microbolometer detector would be beneficial for industrial settings (i.e. unheated plastics). It would also be faster since there is no need to wait for thermal equilibrium. However, in the current study, the temperature difference was obtained by heating the samples in the heating chamber. The heating chamber could not accommodate the rectangular samples, and minor air gaps along the mating sample surfaces might lower the sample temperature (Fig. S1). This was mitigated by extracting the mean interferograms from the middle of the heating chamber, and the oven top was sealed, minimizing convection currents. It can thus be assumed that the minor gaps have negligible effect on the mean interferograms.

To obtain useful interferograms, it is crucial that the mirrors remain mutually parallel throughout the sweeps. The phase difference between the three laser diode interferograms will change throughout the sweep if the same potential is applied to all actuators simultaneously (Fig. S2). The potential is individually set for each actuator to ensure that all three laser interferograms are in phase (or 180° out of phase). Thus, when depicted as a function of step #, the three interferograms are in phase throughout the sweep, indicating equal displacement of all parts of the mirror (Fig. 4a). It is possible to calculate their relative displacement from the laser diode interferograms. The angle between the mirror and the laser diodes is unknown, and the effective wavelength (λ_{eff}, Eq. (1)) is therefore determined based on hyperspectral images of the narrow bandpass filters. This effective wavelength is then used when calculating the relative mirror displacement (Fig. 4b). The relative displacement is offset based on the extracted interferogram of the bandpass filter, thus ensuring that all interferograms are spectrally aligned. Additionally, the maximum expansion for each actuator is different, and the total number of steps is set to accommodate the actuator with the smallest expansion. Due to the data acquisition scheme, the exact number of spectral channels in each data cube varies, and the exact MMD associated with each step is misaligned. Each data cube must, therefore, be interpolated to share a common spectral axis.

Initially, the mirrors are 2.97 µm apart, and the transmission of the SFPI is ≈ 0.6 % for wavelengths within the spectral range of the detector (8–15 µm). The first spectral channel thus effectively functions as a dark frame. The interferograms share the same three characteristic features at

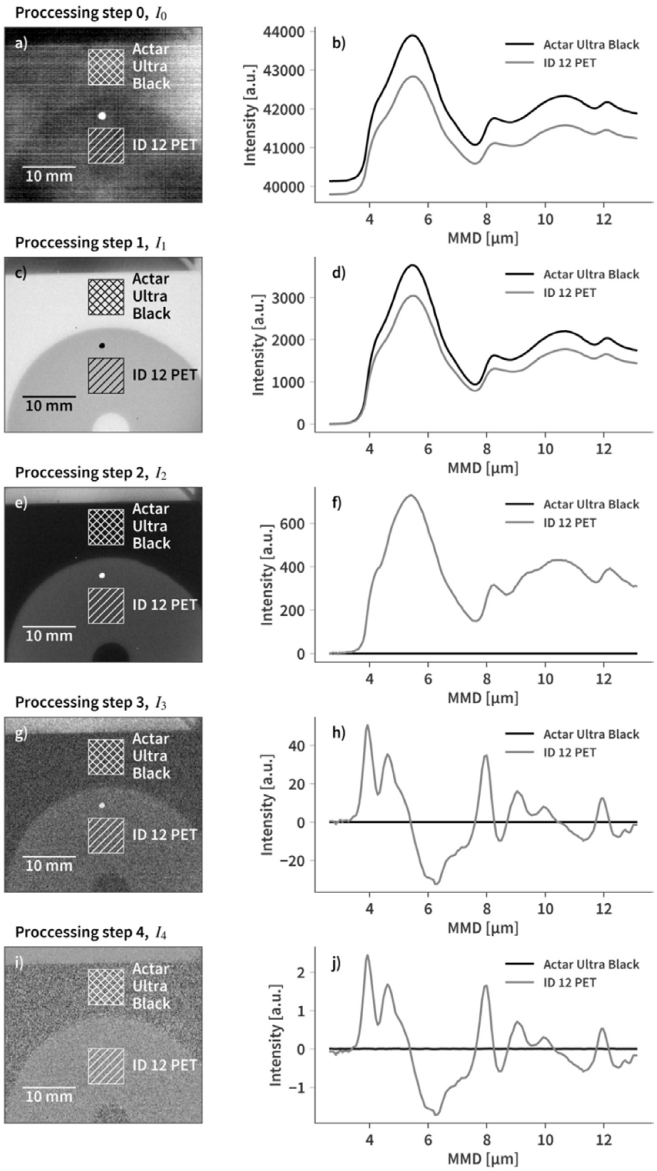

Fig. 5. a), c), e), g), and i): Images acquired at an MMD 6.0 μm from the data cubes at different preprocessing steps. b), d), f), h), and j): Mean interferogram extracted from 40 × 40-pixel areas of the data cube.

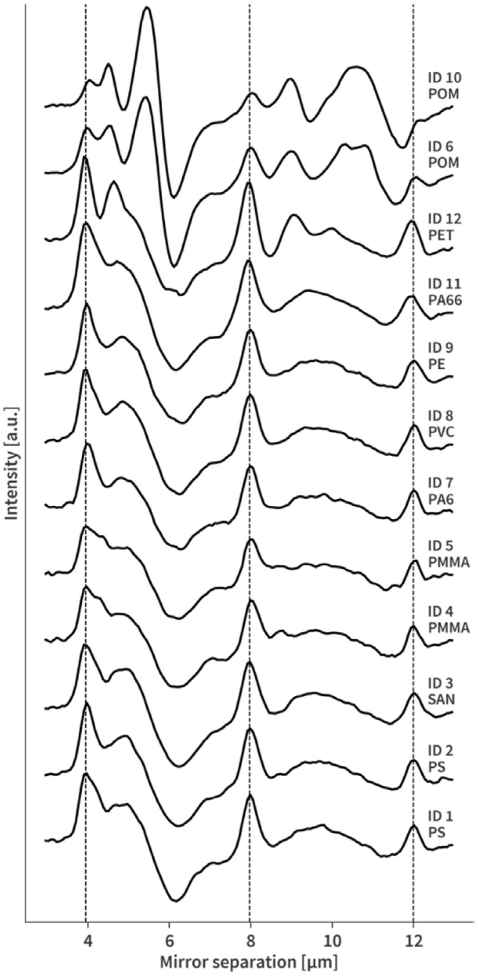

Fig. 6. The mean interferogram of plastics in the training set. Interferograms are offset for clarity. Vertical dashed lines are placed at MMD = 3.95 μm, 7.98 μm and 12.0 μm.

MMD = 3.95 μm, 7.98 μm, and 12.0 μm as the mirrors move apart. These features are caused by the introduction of the next transmission order of the SFPI. The microbolometer detector has a maximum sensitivity at 8 μm, and when the MMD is a multiple of 8/2 μm, an increase in the interferogram intensity is observed. Similarly, the signal decreases as transmission orders leave the sensitive region of the microbolometer (8–15 μm), however, the sensitivity drop-off is gradual compared to the onset.

4.2. Polymer type prediction

The differentiation of plastic samples based on raw data is impeded

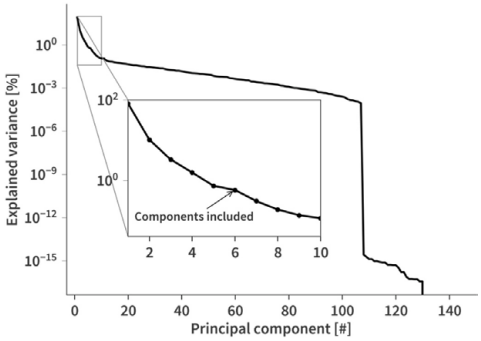

Fig. 7. Scree plot showing the contribution to the variance explained by each PC. The inset shows a zoom-in from PC1 to PC10.

by severe spatial noise (Fig. 5a and b). This spatial noise predominantly arises from the offset between pixels, which results from the manufacturing tolerances of the detector. All interferograms are ensured to have an initial intensity of 0 by subtracting the first spectral channel from the rest of the data cube. This effectively serves as a dark frame calibration as close to no light is let through in the mirrors' initial position. Although this approach visually enhances the images, discerning the material interferogram based on spectral features remains a challenge (Fig. 5c and d). These features can be enhanced by computing the difference between the black body reference sample and the interferograms at each material pixel. This reduces the influence of the black body signal, which is superimposed on the material interferograms. The resulting difference makes the finer spectral features discernible, such as the shoulder at 4.3 μm and 9.4 μm MMD (Fig. 5e and f). However, the reference sample has spectral features of its own [30] that affect the residual signal, but since the same reference and temperature are used for all samples, the effect is the same. If the emissivity contrast between the plastic and the reference sample is substantial, the spectral features become challenging to identify due to being obscured by a significant residual signal. Additional enhancement is obtained by applying a 1st-order derivative Savitzky-Golay filter, which noticeably accentuates the spectral features (Fig. 5g and h). However, this introduces additional spatial noise due to the difference in pixel responsivity from the manufacturing process. SNV is employed to standardize the interferograms with a mean of 0 and approximately the same scale. Finally, the impact of spatial noise illustrated in Fig. 5i is mitigated by sampling across 18 × 18-pixel areas in the subsequent classification step.

The classification of the samples resulted in an accuracy of 57.4 % for individual samples and 73.1 % when classifying based on polymer type. Certain polymers (e.g. POM, PET, PMMA) are more readily classifiable than others (Fig. 7a). Especially POM samples display notable differences as supported by the loadings, where PC1 aligns with the interferogram of POM and accounts for 81.5 % of the variance in the data (Fig. S5). Additionally, the large Euclidean distances between the POM samples and the rest of the samples further underscore this distinction (Fig. 9). Contrary, the shortest distances are observed for ID 2 PS, ID 8 PVC, and ID 9 PE with average distances of 25.2 %, 25.0 %, and 25.3 %, respectively. Their mutual distance from each other is 3.6 % on average, explaining why they are confused in classification. Common for all samples, which are confused with each other, is that their mutual distances are below 10 %.

The goal is to differentiate the samples based on their spectral properties rather than signal amplitude, which can be affected by the presence of carbon black additive. It is expected that carbon black plays a significant role in black body emission. Therefore, samples with higher

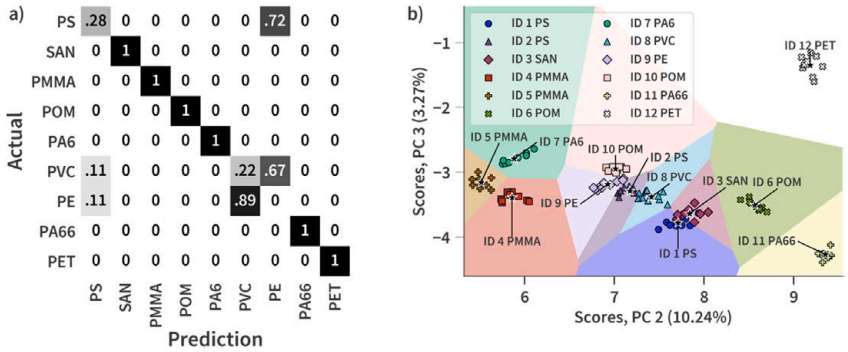

Fig. 8. The normalized confusion matrix displays the classification results for the validation set. Classification is based on the projections of the validation data, as shown in (b). The centroids of the training set are marked with (★). Each projected point from the validation set is classified using a k-nearest neighbor approach, where classification is determined by the closest centroid.

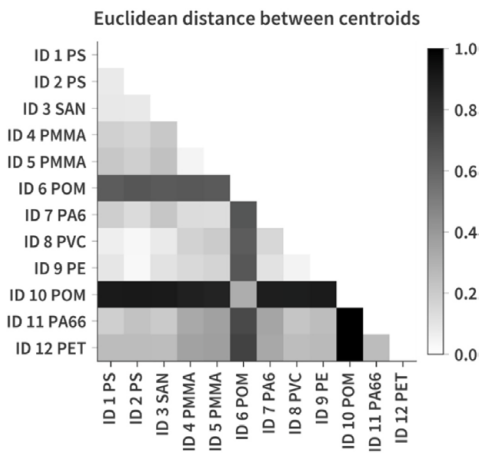

Fig. 9. Distances between each centroid of the training set normalized to the largest distance.

carbon black content may show stronger emission signals without a corresponding increase in spectral features. It is challenging to determine how the concentration of carbon black affects the emission spectrum and, consequently, the classification of polymers without having samples of the same polymer with increasing concentrations of carbon black. Additional research is needed to investigate if there is a threshold above which the concentration becomes too high to differentiate the polymers accurately.

The classification model demonstrates an accuracy of 73.1 % when evaluating polymer types. In addition, the results presented in Fig. 8a infer that LWIR hyperspectral imaging has the potential to differentiate between POM, PET, PMMA, and PA in their black forms. The model further distinguishes between PA6 and PA66 as reflected in their difference of 34.8 %. This is unexpected due to the chemical similarity between the two polymers. A plausible explanation is that the spectral separation is ascribed to the 30 % by mass glass in PA66. As with glass and carbon black, the effect of additives and fillers added to plastics needs further investigation.

4.3. Future work

The current classification method shows promise with the applied plastic samples. However, it also indicates that classification becomes more challenging if the emissivity mismatch between the sample and black body reference is too large. This leads to a large residual signal after intensity calibration, and the spectral features which are important for distinguishing materials thus becomes obscured. Furthermore, it is important to assess the model's generalizability across a larger sample set representing the same plastic types with different additives. Additionally, conducting tests to understand how various additives impact the classification performance will provide insights into the potential use of hyperspectral LWIR imaging for differentiating plastics. The results presented in this study indicate that the hyperspectral emission imager is capable of distinguishing between the black plastic types. However, for successful industrial implementation, equipment improvements are necessary. A primary limitation is the image acquisition time, which is ≈10 s per data cube; an interval too slow for conveyor belt applications. Although the applied microbolometer sensor can have a frame rate of 120 Hz and would necessitate modifications to the electronics design. This could enable a data cube acquisition time of ≈1 s, which might still be insufficient for industrial processes. Further reduction of the data cube acquisition time could be achieved by decreasing the number of spectral bands. Additionally, elevating the plastic sample temperature is time consuming and heating the samples during their conveyance could mitigate this issue. Another possibility involves cooling the sensor and thereby increasing the temperature differential between the samples and the detector. Though the demonstrated equipment and approach is to be further developed, the results clearly underline the vast potential of further exploration of hyperspectral imaging of emission spectra. This is a positive direction in solving the challenge with classification of black plastics where reflectance techniques fall short.

5. Conclusion

The results of the study indicate that several black plastic samples can be uniquely classified based on their emission spectra. It is further shown that hyperspectral emission imaging can be obtained by isolating the individual wavelengths with a scanning Fabry-Pérot interferometer (SFPI) and imaging the different wavelengths with a microbolometer

sensor in the long wavelength infrared spectral range (LWIR). The SFPI-based LWIR hyperspectral imager has been used to acquire emission measurements of twelve industrial plastic samples containing carbon black. The proposed spectral calibration procedure of the hyperspectral imager has proved capable of aligning spectral axes of different data cubes. The ≈70,000 interferograms were processed enabling direct comparisons among the polymer types. For increasing the signal to noise ratio 324 interferograms was average leaving 216 interferograms for further analysis. Applying a PCA model for dimensional reduction and subsequent classify via a k-nearest neighbors algorithm showed that five of the nine different polymer types was successfully identified with a accuracy of 73.1 %. The results show that PET, POM, PMMA, SAN, and PA can be clearly distinguished using the presented hyperspectral emission imager and methodology.

CRediT authorship contribution statement

Mads Nibe Larsen: Writing – review & editing, Writing – original draft, Visualization, Software, Methodology, Investigation, Formal analysis, Conceptualization. **Anders Løchte Jørgensen:** Writing – review & editing, Methodology. **Victor Petrunin:** Methodology. **Jakob Kjelstrup-Hansen:** Writing – review & editing, Supervision, Project administration, Funding acquisition. **Bjarke Jørgensen:** Writing – review & editing, Supervision, Project administration, Funding acquisition, Conceptualization. **Mogens Hinge:** Writing – review & editing, Supervision, Methodology, Funding acquisition, Conceptualization.

Declaration of competing interest

The authors declare the following financial interests/personal relationships which may be considered as potential competing interests:As a camera producer Newtec Engineering (i.e., Mads Nibe Larsen, Anders Løchte Jørgensen, Victor Petrunin, and Bjarke Jørgensen), declare interest in commercial exploitation of the work reported in this paper. Jakob Kjelstrup-Hansen, and Mogens Hinge declare to have no conflict of interest.

6 Acknowledgements

The authors would like to thank the Innovation Fond Denmark (grant no. 1044-00116B and 0177-00035B), Aarhus University, Dansk Affaldsminimering, Vestforbrænding, and Plastix for financial support under the Re-Plast project.

Appendix A. Supplementary data

Supplementary data to this article can be found online at https://doi.org/10.1016/j.polymertesting.2024.108629.

Data availability

Data will be made available on request.

References

[1] *Plastics – the Fast Facts 2023*; Plastics Europe, 2023.
[2] OECD, Global plastics outlook: economic drivers, environmental impacts and policy options, OECD, 2022, https://doi.org/10.1787/de747aef-en.
[3] D.K.A. Barnes, A. Walters, L. Gonçalves, Macroplastics at sea around Antarctica, Mar. Environ. Res. 70 (2) (2010) 250–252, https://doi.org/10.1016/j.marenvres.2010.05.006.
[4] P.L. Corcoran, M.C. Biesinger, M. Grifi, Plastics and beaches: a degrading relationship, Mar. Pollut. Bull. 58 (1) (2009) 80–84, https://doi.org/10.1016/j.marpolbul.2008.08.022.
[5] R.C. Thompson, Y. Olsen, R.P. Mitchell, A. Davis, S.J. Rowland, A.W.G. John, D. McGonigle, A.E. Russell, Lost at sea: where is all the plastic? Science 304 (5672) (2004) 838, https://doi.org/10.1126/science.1094559, 838.
[6] E. Martinez, K. Maamaatuaiahutapu, V. Taillandier, Floating marine debris surface drift: convergence and accumulation toward the south pacific subtropical gyre, Mar. Pollut. Bull. 58 (9) (2009) 1347–1355, https://doi.org/10.1016/j.marpolbul.2009.04.022.
[7] A.S. Colferai, R.P. Silva-Filho, A.M. Martins, L. Bugoni, Distribution pattern of anthropogenic marine debris along the gastrointestinal tract of green turtles (Chelonia mydas) as implications for rehabilitation, Mar. Pollut. Bull. 119 (1) (2017) 231–237, https://doi.org/10.1016/j.marpolbul.2017.03.053.
[8] P.G. Ryan, C.J. Moore, J.A. van Franeker, C.L. Moloney, Monitoring the abundance of plastic debris in the marine environment, Philos. Trans. R. Soc. B Biol. Sci. 364 (1526) (2009) 1999–2012, https://doi.org/10.1098/rstb.2008.0207.
[9] A European Strategy for Plastics in a Circular Economy, European Comission, 2018.
[10] P.H. Andersen, T. Duvold, B. Frølund, J. Lüneborg, K. Toft-Petersen, H. Vanthournout, C. Witte, The New Plastics Economy, 2019.
[11] M. Tsakona, L. Rucevska, *Baseline Report On Plastic Waste*; Basel Convention, 2020.
[12] S. Brunner, P. Fomin, Ch Kargel, Automated sorting of polymer flakes: fluorescence labeling and development of a measurement system prototype, Waste Manag. 38 (2015) 49–60, https://doi.org/10.1016/j.wasman.2014.12.006.
[13] E. Maris, A. Aoussat, E. Naffrechoux, D. Froelich, Polymer tracer detection systems with UV fluorescence spectrometry to improve product recyclability, Miner. Eng. 29 (2012) 77–88, https://doi.org/10.1016/j.mineng.2011.09.016.
[14] S.M. Safavi, H. Masoumi, S.S. Mirian, M. Tabrizchi, Sorting of polypropylene resins by color in MSW using visible reflectance spectroscopy, Waste Manag. 30 (11) (2010) 2216–2222, https://doi.org/10.1016/j.wasman.2010.06.023.
[15] M.L. Henriksen, C.B. Karlsen, P. Klarskov, M. Hinge, Plastic classification via in-line hyperspectral camera analysis and unsupervised machine learning, Vib. Spectrosc. 118 (2022) 103329, https://doi.org/10.1016/j.vibspec.2021.103329.
[16] P.P. Cielecki, M. Hardenberg, G. Amariei, M.L. Henriksen, M. Hinge, P. Klarskov, Identification of black plastics with Terahertz time-domain spectroscopy and machine learning, Sci. Rep. 13 (1) (2023) 22399, https://doi.org/10.1038/s41598-023-49765-z.
[17] S. Serranti, G. Bonifazi, Techniques for separation of plastic wastes, in: Use of Recycled Plastics in Eco-Efficient Concrete, Elsevier, 2019, pp. 9–37, https://doi.org/10.1016/B978-0-08-102676-2.00002-5.
[18] G. Bonifazi, G. Capobianco, S. Serranti, A hierarchical classification approach for recognition of low-density (LDPE) and high-density polyethylene (HDPE) in mixed plastic waste based on short-wave infrared (SWIR) hyperspectral imaging, Spectrochim. Acta. A. Mol. Biomol. Spectrosc. 198 (2018) 115–122, https://doi.org/10.1016/j.saa.2018.03.006.
[19] C. Signoret, A.-S. Caro-Bretelle, J.-M. Lopez-Cuesta, P. Ienny, D. Perrin, MIR spectral characterization of plastic to enable discrimination in an industrial recycling context: I. Specific case of styrenic polymers, Waste Manag. 95 (2019) 513–525, https://doi.org/10.1016/j.wasman.2019.05.050.
[20] C. Vrancken, P.J. Longhurst, S.T. Wagland, Critical review of real-time methods for solid waste characterisation: informing material recovery and fuel production, Waste Manag. 61 (2017) 40–57, https://doi.org/10.1016/j.wasman.2017.01.019.
[21] G. Bonifazi, G. Capobianco, P. Cucuzza, S. Serranti, V. Spizzichino, Black plastic waste classification by laser-induced fluorescence technique combined with machine learning approaches, Waste Biomass Valorization 15 (3) (2024) 1641–1652, https://doi.org/10.1007/s12649-023-02146-z.
[22] C. Signoret, A.-S. Caro-Bretelle, J.-M. Lopez-Cuesta, P. Ienny, D. Perrin, Alterations of plastics spectra in MIR and the potential impacts on identification towards recycling, Resour. Conserv. Recycl. 161 (2020) 104980, https://doi.org/10.1016/j.resconrec.2020.104980.
[23] O. Rozenstein, E. Puckrin, J. Adamowski, Development of a new approach based on midwave infrared spectroscopy for post-consumer black plastic waste sorting in the recycling industry, Waste Manag. 68 (2017) 38–44, https://doi.org/10.1016/j.wasman.2017.07.023.
[24] S. Zinchik, S. Jiang, S. Friis, F. Long, L. Høgstedt, V.M. Zavala, E. Bar-Ziv, Accurate characterization of mixed plastic waste using machine learning and fast infrared spectroscopy, ACS Sustain. Chem. Eng. 9 (42) (2021) 14143–14151, https://doi.org/10.1021/acssuschemeng.1c04281.
[25] J. Colwill, A. Simeone, O. Gould, E. Woolley, C. Mulvenna, Energy-efficient systems for the sensing and separation of mixed polymers, Procedia CIRP 62 (2017) 512–517, https://doi.org/10.1016/j.procir.2016.06.116.
[26] S.P. Gundupalli, S. Hait, A. Thakur, A review on automated sorting of source-separated municipal solid waste for recycling, Waste Manag. 60 (2017) 56–74, https://doi.org/10.1016/j.wasman.2016.09.015.
[27] J.-P. Lange, Managing plastic Waste—Sorting, recycling, disposal, and product redesign, ACS Sustain. Chem. Eng. 9 (47) (2021) 15722–15738, https://doi.org/10.1021/acssuschemeng.1c05013.
[28] R. Bro, A.K. Smilde, Principal component analysis, Anal. Methods 6 (9) (2014) 2812–2831, https://doi.org/10.1039/C3AY41907J.
[29] M. Vollmer, K.-P. Möllmann, *Infrared Thermal Imaging - Fundamentals Research And Applications, Section 2.2.3.3*, 2nd Reprint, Wiley-VCH Verlag GmbH & Co. KGaA, 2010.
[30] Ultra Black Coating for MWIR and LWIR Acktar Optical Black Coating. Acktar black coatings. https://acktar.com/product/ultra-black/(accessed 2024-June-25).

D. Manuscript: Long-wave infrared hyperspectral imager based on a scanning Fabry-Pérot interferometer

This section includes the manuscript *Long-wave infrared hyperspectral imager based on a scanning Fabry-Pérot interferometer*, which is under review at the AIP Publishing journal, Review of Scientific Instruments (submitted 04/10/2024). The manuscript gives an overview of the working principle of the hyperspectral long-wave infrared imager, including estimates of its spectral resolution and how spectra are converted into interferograms. This section contains both the manuscript itself and the accompanying supporting information.

Long-wave infrared hyperspectral imager based on a scanning Fabry-Pérot interferometer

Mads Nibe Larsen[†,‡], Anders Løchte Jørgensen[‡], Victor Petrunin[‡], Jakob Kjelstrup-Hansen[†,£,*], Bjarke Jørgensen[‡]

[†]NanoSYD, Mads Clausen Institute, University of Southern Denmark, 6400 Sønderborg, Denmark

[‡]Newtec Engineering A/S, 5230 Odense, Denmark

[£]SDU Climate Cluster, University of Southern Denmark, 5230 Odense, Denmark

* Corresponding author: jkh@mci.sdu.dk

ABSTRACT

This work presents a hyperspectral imager sensitive to radiation in the 1250 to 666 cm^{-1} wavenumber range (wavelengths between 8 and 15 µm). The system combines a low-order scanning Fabry-Pérot interferometer with a thermal camera utilizing a 1024×768-pixel uncooled microbolometer detector. The compact interferometer design enables a relatively small footprint, providing a spectral resolution between 26 cm^{-1} and 39 cm^{-1}, depending on the wavenumber. Transmission measurements of various substances are shown to produce distinct interferograms, facilitating material identification. Additionally, a generalized matrix method is used to estimate the relationship between physical cavity length and wavenumber of the incident light, enabling the prediction of interferogram shapes.

Keywords:

Fabry-Pérot interferometry, Hyperspectral imaging, Spectral scanner, Long-Wave-infrared imaging

1 INTRODUCTION

Hyperspectral imaging (HSI) captures detailed spectral information across a broad wavelength range, enabling material identification through unique spectral fingerprints. Unlike traditional imaging, which records in a few broad bands, HSI collects a complete spectrum at every point, making it valuable for fields such as plastic waste management[1–4], medical diagnostics[5–7], agriculture[8,9], and food safety[10–13]. While most HSI systems operate in the visible and near-infrared (VIS/NIR) regions, long-wave infrared (LWIR) imaging (8–14 µm) offers advantages for chemical analysis, thanks to its sensitivity to molecular vibrations in the spectral fingerprint region. Techniques like Fourier transform infrared (FTIR) spectroscopy, including methods such as attenuated total reflectance (ATR), are widely used but limited to single-point measurements, making hyperspectral image acquisition challenging.

Existing hyperspectral LWIR imagers such as the Specim FX120[14] (7.7 – 12.3 µm wavelenghts) is a line scanner, thus requiring relative movement between the sample and camera to capture spatial information. Another example is the Telops Hypercam LW[15] (7.7 – 11.8 µm), which is a Michelson interferometer based imaging system equipped with a focal plane array. These systems use mercury-cadmium-telluride (MCT) detectors, which offer high signal-to-noise ratio but are expensive and require cryogenic cooling, limiting practicality for widespread use.

This paper presents a prototype LWIR hyperspectral imager combining a low-order scanning Fabry-Pérot interferometer (SFPI) with a 1024×768-pixel uncooled microbolometer thermal camera. Operating in the 8–15 µm range with a spectral resolution of 26–39 cm^{-1}, the system offers a compact, cost-effective alternative to cryogenically cooled systems. Using the generalized matrix method (GMM), SFPI transmission is modelled to predict spectral data, with experimental results closely matching theoretical estimates, demonstrating the system's potential for material identification.

2 Long-wave infrared hyperspectral imager

The hyperspectral imaging system consists of three main parts (Fig. 1a): I: An SFPI; II: Germanium optics; III: A thermal camera.

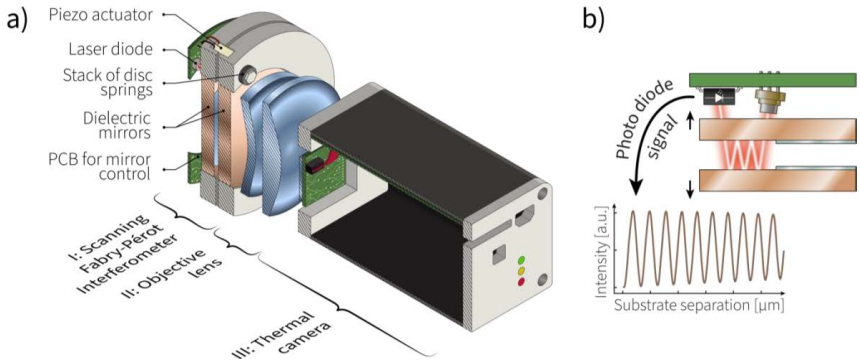

Figure 1: a) Schematic of hyperspectral imaging system (not to scale). b) Laser diode interferograms are recorded as the mirrors move apart.

The camera features a QT5022 camera platform (QTechnology, DK) equipped with a 1024×768-pixel microbolometer detector (Pico1024Gen2™, Lynred, USA) with a pixel pitch of 17 µm, which is sensitive to light in the range from 1250 to 666 cm^{-1} (8 – 15 µm wavelengths). It utilizes a germanium objective lens with an effective focal length of 35 mm and an aperture of f/1 (Ophir Optronics Solutions Ltd., IL) to focus the light onto the detector.

The hyperspectral capabilities are provided by the SFPI, which is placed directly in front of the objective lens. It comprises two custom-made, partially transmitting mirrors (Coherent Corp, USA), placed ~ 3 µm apart. Each mirror is made from a stack of dielectric coatings (Ø 43 mm centered) deposited on Zinc Selenide (ZnSe) substrates (Ø 50.8 mm, 5 mm thick). The layer composition of the mirror and antireflective coatings are presented in Tab. 1. This configuration results in a reflectance of 84 % within the spectral range of the camera (supporting information, Fig. S1.1). The physical cavity length (PCL) denotes the width of the airgap (distance between the two mirror coatings), and determines the distribution of transmitted wavelengths. By controlling the cavity length, the SFPI acts like a variable bandpass filter, and by capturing images at different cavity lengths, it is possible to construct a hyperspectral data cube containing 768×1024×160 data points (width×height×depth). The spectral dimension of the hyperspectral data cubes is referred to as interferograms, measured in PCL [µm] rather than wavelength [µm] or wavenumbers [cm^{-1}].

Table 1: Thicknesses of the dielectric layers in the mirror and anti-reflective coatings. Thicknesses are obtained using cross-sectional measurements of the mirrors by scanning electron microscopy (SEM). The arrow indicates direction from top to bottom.

Mirror material	Thickness [μm]
Ge	1.26
ZnS	0.02
ThF_4	1.79
ZnS	0.02
Ge	0.51
Total mirror thickness	3.60
ZnSe substrate	5000
AR material	
ThF_4	4.35
ZnSe	0.25
ThF_4	0.94
ZnSe	0.50
ThF_4	0.34
Total AR Thickness	6.38

Mirror control

Each mirror is mounted in one half of a custom-made stainless-steel fixture held together by three bolts spaced 120º apart. Three piezo actuators (PK2FMP2, 400 N force, 11.2 μm max expansion, 75 V max voltage, Thorlabs, USA) sit between the fixture halves, expanding to increase the PCL. Disc springs (Ø12.5 mm, 673 N) counteract the expansion, keeping the halves together. Voltage sweeps across the actuators adjust d from ~3 μm to ~13 μm for data cube acquisition.

To maintain mirror parallelism, three laser diodes (680 nm) shine light into an uncoated part of the cavity near each piezo actuator. Photodiodes monitor the reflected light, which alternates between constructive and destructive interference as the mirrors move (Fig. 1b). The condition for constructive interference is given in Eq. (1).

$$d_{substrate} = \frac{m}{2}\frac{\lambda}{n\cos\theta} = \frac{m}{2}\frac{1}{n\tilde{\nu}\cos\theta}, \quad m = 1, 2, 3 \ldots \tag{1}$$

$d_{subtrate}$ is distance between the two mirror substrates (not mirror coatings) and m is the transmission order, and n is the refractive index. The space between the two mirrors is filled with atmospheric air, and thus a refractive index of $n = 1$ is used. λ and $\tilde{\nu}$ are the wavelength and wavenumber respectively, and θ is the angle of incidence between the incident light and the mirror substrate. The cavity expansion is monitored using the interference fringes of the laser diodes, with 340 nm between consecutive peaks. An external spectral reference is used together with the interference fringes to calibrate the interferograms (spectral axis of data cube) in terms of the absolute PLC. The phase

difference between the three laser interferograms is kept constant to ensure uniform mirror displacement. Since each piezo responds differently, the sweep is divided into 1500 steps with unique voltages for each actuator, determined by calibration sweeps. The total steps are reduced to match the actuator with the least travel. A hyperspectral data cube is acquired in ~8 seconds, capturing ~160 images.

3 Simulating interferograms

The conversion of incident spectra to interferograms requires an understanding of the relationship between wavelength, PCL, and transmission. This is shown in Fig. 2a and determined using the generalized matrix method (details in Supporting Information, S2). The sensor response (Fig. 2b), estimated from experimental interferograms of various gases, is combined with the transmission matrix as per Eq. (2).

$$\mathbf{\Phi} = \mathbf{\Gamma} \circ_{\boldsymbol{r}} \boldsymbol{s} \tag{2}$$

Here, $\mathbf{\Phi}$ denotes the system matrix (Fig. 2c), $\mathbf{\Gamma}$ is the transmission matrix (Fig. 2a), and $\boldsymbol{s}$ is the normalized sensor response combined with the transmission of the germanium optics (Fig. 2b). $\circ_{\boldsymbol{r}}$ indicates the row-wise Hadamard product (each row of $\mathbf{\Gamma}$ is multiplied elementwise by $\mathbf{s}$).

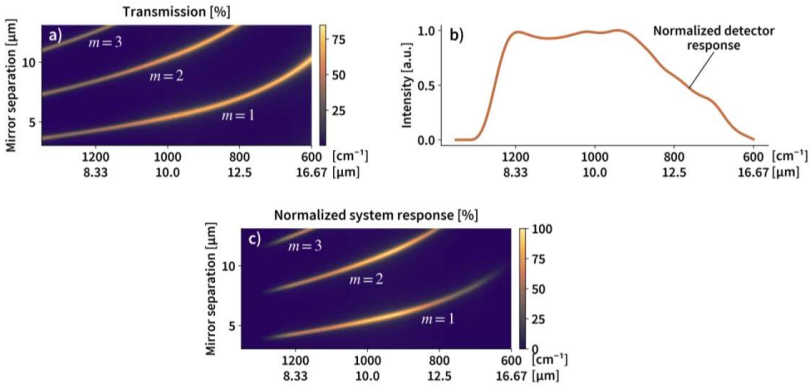

Figure 2: a) Transmission matrix showing the relationship between d, wavelength/wavenumber, and transmission through the SFPI. $m = 1, 2, 3$ indicates the transmission orders. b) Normalized response of detector and optics. c) Normalized system matrix showing the combined response of the SFPI depicted in a) and the response indicated in c).

Predicting interferograms from FTIR data

The system matrix can estimate the interferograms recorded by the hyperspectral camera. As shown in Fig. S3.1, a black body emitter (LS series 1050-100, Electro Optical Industries Inc., FR) emits

radiation, $\boldsymbol{m_{BB}}$, through a gas cell, where some light is absorbed, leaving the transmitted spectrum $\boldsymbol{x_t}$. The light then passes through the SFPI, where it's filtered based on d, and the remaining spectrum, $\boldsymbol{x_{SFPI}}$, is recorded by the camera.

$\boldsymbol{m_{BB}}$ is referred to as the black body spectral radiance [$Wm^{-2}Hz^{-1}$] and is defined based on Planck's law, Eq. (3)

$$\boldsymbol{m_{BB}}(T,\tilde{\nu}) = \frac{2hc^2\tilde{\nu}^3}{\exp\{hc\tilde{\nu}/k_BT\} - 1} \tag{3}$$

Here, h is Planck's constant, c is the speed of light in a vacuum, k_B is the Boltzmann constant, and T is the temperature of the emitter. The spectral profile of the light reaching the camera can be expressed by Eq. (4).

$$\boldsymbol{x_{SFPI}} = \boldsymbol{m_{BB}} \circ \boldsymbol{t_{gas}} \circ \boldsymbol{\Gamma}^{i,:} = \boldsymbol{x_t} \circ \boldsymbol{\Gamma}^{i,:} \tag{4}$$

$\boldsymbol{t_{gas}}$, is the transmission spectrum of the gas and $\boldsymbol{\Gamma}^{i,:}$ is the transmission of the SFPI at a given PCL. The superscript i refers to the relevant row of the transmittance matrix corresponding to a single cavity length, and ':' indicates that the entire row is used (all wavenumbers). "$\circ$" indicates elementwise multiplication (Hadamard product).

Eq. (5) models how the interferograms, $\boldsymbol{\psi}$, can be calculated based on the incoming light, and the system matrix.

$$\boldsymbol{\psi} = (\boldsymbol{\Gamma} \circ_r \boldsymbol{s}) \cdot \boldsymbol{x_t} = \boldsymbol{\Phi} \cdot \boldsymbol{x_t} \tag{5}$$

Fig. 3a illustrates how Eq. (5) is used to estimate the interferogram of methanol based on its black body transmission spectrum (Fig. 3b). Note that the measured and estimated interferograms have been normalized to values between 0 and 1. Additional comparisons between estimated and measured interferograms also express excellent agreement and are found in section S4.

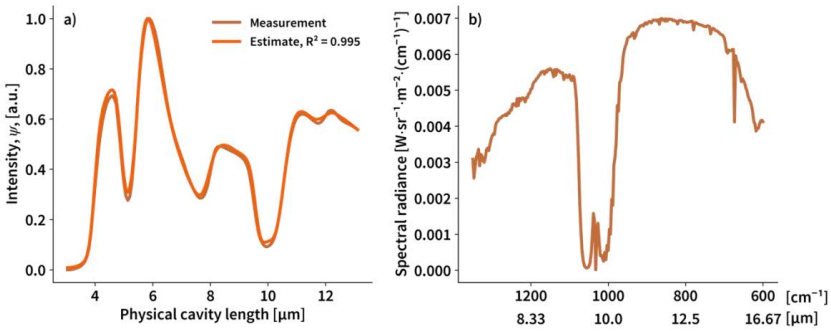

Figure 3: a) Measured and estimated interferograms of methanol vapor. The estimated interferogram is based on Eq. (5) and uses the spectral radiance of methanol vapor as depicted in b). Here, the transmission spectrum of the methanol vapor is measured using a Perkin Elmer Spectrum 65 FTIR spectrometer, which is multiplied by the spectral radiance of a 150 ºC black body as described by Eq. (3).

Estimate of spectral resolution

The full width half maximum (FWHM) of the SFPI transmission spectrum (a single row in Fig. 2c) serves as the resolution limit of the spectrometer. Fig. 4 illustrates the observed FWHMs for each of the visible transmission orders depicted in Fig. 2c. The improvement of resolution with lower wavenumbers is due to the increasing finesse of the cavity caused by higher mirror reflectivity (Fig. S1.1). Thus, the spectral resolution of the SFPI varies between 26 cm^{-1} and 39 cm^{-1} across the spectral range of the microbolometer detector.

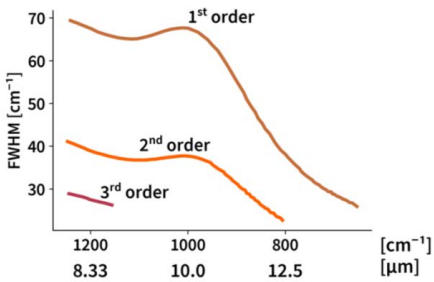

Figure 4: Spectral resolution derived from system matrix (Fig. 2c).

Polystyrene is used to examine the spectral resolution of the imager as it exhibits two transmission bands at 822 cm^{-1} and 865 cm^{-1}. These are barely distinguishable in the first transmission order (≈ 6.3 μm and 6.7 μm PCL) but separable in the second transmission order (≈ 12.1 μm and 12.8 μm

PCL), as illustrated in Fig. S5.1. This supports the validity of the resolutions estimate presented in Fig. 4. Measurements of additional samples covering the entire spectral range of the hyperspectral camera are needed to confirm the spectral resolution. However, the presented measurements of polystyrene show excellent agreement with the expected results.

Spectral aberrations due to Fabry-Pérot interferometer

A general issue with SFPIs is that their transmission profile varies with the incident angle of the light, as also described in Eq. (1). Light entering at oblique angles experiences higher wavenumbers, scaling the cavity length by $1/\cos\theta$. In this setup, light at the detector's edges arrives at a 17.3º angle, causing wavenumbers to be 4.7% higher than those at the center. Collimating optics could correct this but would reduce field of view and transmission. Alternatively, scaling the PCL for each pixel based on its position can account for this shift.

Unfortunately, is spectral broadening is introduced by the concave bending of the substrates of the specific mirrors employed in the SFPI. Compressive stress from the mirror coating causes the mirrors' center to be 300 nm farther apart than the edges, thus transmitting a broader spectrum at any given PCL. The influence of this effect changes with wavenumber and PCL and is described in further detail in the supporting information (S6). The maximum and minimum broadening are found in the first transmission order at PCLs of 9.8 µm and 3.6 µm with corresponding broadening of 16 cm^{-1} and 116 cm^{-1} respectively. This effect has been accounted for in the transmission and system matrices (Fig. 2a and 2c).

4 Summary and conclusions

The hyperspectral imager presented uses a low-order SFPI as a variable band-pass filter. The cavity distance increases from ~3 µm to ~13 µm in the span of 8 seconds, during which ~160 images are acquired, forming the data cube. GMM-based calculations predict the relationship between mirror separation and transmission, where higher orders improve spectral resolution. Spectral broadening from mirror bending is included directly in the calculations. Excellent correlation is found between transmission measurements of various materials and GMM based calculations. Future enhancements, such as integrating spectrometers for real-time mirror tracking, optimizing mirror coatings, and adding collimating optics, could improve accuracy and reduce post-processing.

5 Acknowledgements

The authors would like to thank the Innovation Fond Denmark (grant no: 1044-00116B) for providing financial support.

6 Author declarations

Declaration of interests

As a camera producer Newtec Engineering (i.e., Mads Nibe Larsen, Anders Løchte Jørgensen, Victor Petrunin, and Bjarke Jørgensen), declare interest in commercial exploitation of the work reported in this paper. Jakob Kjelstrup-Hansen declare to have no conflict of interest.

Ethics Approval

This research did not involve any human participants or animal subjects, and as such, no ethics approval was required.

Data availability statement

The data that support the findings of this study are available from the corresponding author upon reasonable request.

Author contributions

Mads Nibe Larsen (ORCID: 0000-0002-5412-6325): Conceptualization, Methodology, Investigation, Formal analysis, Software, Writing - Original Draft, Writing - Review & Editing, Visualization. Anders Løchte Jørgensen (ORCID: 0000-0001-9741-2025): Methodology, Review & Editing. Victor Petrunin (ORCID: 0009-0002-5960-9825): Methodology, Review & Editing. Jakob Kjelstrup-Hansen (ORCID: 0000-0003-4482-4979): Supervision, Funding acquisition, Project administration, Writing - Review & Editing. Bjarke Jørgensen (ORCID: 0000-0001-8559-9435): Conceptualization, Supervision, Funding acquisition, Project administration, Writing - Review & Editing.

7 REFERENCES

(1) Safavi, S. M. Sorting of Polypropylene Resins by Color in MSW Using Visible Reflectance Spectroscopy. *Waste Manag.* **2010**.
(2) Henriksen, M. L. Plastic Classification via In-Line Hyperspectral Camera Analysis and Unsupervised Machine Learning. *Vib. Spectrosc.* **2022**.
(3) Ghaffari, M. Systematic Reduction of Hyperspectral Images for High-Throughput Plastic Characterization. *Sci. Rep.* **2023**.
(4) Bonifazi, G. Fast and Effective Classification of Plastic Waste by Pushbroom Hyperspectral Sensor Coupled with Hierarchical Modelling and Variable Selection. **2023**.
(5) Holman, E. A. Expanding Hyperspectral Imaging Applications to the Clinical Scene: Non-Invasive, Label-Free Approaches for Early Diagnostics and Precision Medicine.
(6) Lu, G.; Fei, B. Medical Hyperspectral Imaging: A Review. *J. Biomed. Opt.* **2014**, *19*.
(7) A Review of the Medical Hyperspectral Imaging Systems and Unmixing Algorithms' in Biological Tissues. *Photodiagnosis Photodyn. Ther.* **2021**.
(8) Lu, B.; Dao, P. D.; Liu, J.; He, Y.; Shang, J. Recent Advances of Hyperspectral Imaging Technology and Applications in Agriculture. **2020**.
(9) Thomas, S. Benefits of Hyperspectral Imaging for Plant Disease Detection and Plant Protection: A Technical Perspective. **2018**.
(10) Patel, D.; Bhise, S.; Kapdi, S. S.; Bhatt, T. Non-Destructive Hyperspectral Imaging Technology to Assess the Quality and Safety of Food: A Review. *Food Prod. Process. Nutr.* **2024**, *6* (1), 69. https://doi.org/10.1186/s43014-024-00246-4.
(11) Ye, D.; Sun, L.; Tan, W.; Che, W.; Yang, M. Detecting and Classifying Minor Bruised Potato Based on Hyperspectral Imaging. *Chemom. Intell. Lab. Syst.* **2018**, *177*, 129–139. https://doi.org/10.1016/j.chemolab.2018.04.002.
(12) Ramos-Infante, S. J.; Suarez-Rubio, V.; Luri-Esplandiu, P.; Saiz-Abajo, M. J. Assessment Of Tomato Quality Characteristics Using Vis/Nir Hyperspectral Imaging And Chemometrics. In *2019 10th Workshop on Hyperspectral Imaging and Signal Processing: Evolution in Remote Sensing (WHISPERS)*; IEEE: Amsterdam, Netherlands, 2019; pp 1–5. https://doi.org/10.1109/WHISPERS.2019.8921170.
(13) Huang, M.; Kim, M. S.; Delwiche, S. R.; Chao, K.; Qin, J.; Mo, C.; Esquerre, C.; Zhu, Q. Quantitative Analysis of Melamine in Milk Powders Using Near-Infrared Hyperspectral Imaging and Band Ratio. *J. Food Eng.* **2016**, *181*, 10–19. https://doi.org/10.1016/j.jfoodeng.2016.02.017.
(14) Miko. *Specim FX120*. Specim. https://www.specim.com/products/specim-fx120/ (accessed 2024-09-18).
(15) *Hyperspectral Cameras - Telops Hyper-Cam & HC Airborne Mini*. Telops. https://www.telops.com/products/hyperspectral-cameras/ (accessed 2024-09-18).

Long-wave infrared hyperspectral imager based on a scanning Fabry-Pérot interferometer

Supporting information

Mads Nibe Larsen[†,‡], Anders Løchte Jørgensen[‡], Victor Petrunin[‡], Jakob Kjelstrup-Hansen[†,£,*], Bjarke Jørgensen[‡]

[†]NanoSYD, Mads Clausen Institute, University of Southern Denmark, 6400 Sønderborg, Denmark

[‡]Newtec Engineering A/S, 5230 Odense, Denmark

[£]SDU Climate Cluster, University of Southern Denmark, 5230 Odense, Denmark

* Corresponding author: jkh@mci.sdu.dk

S1 Reflectance of dielectric mirrors

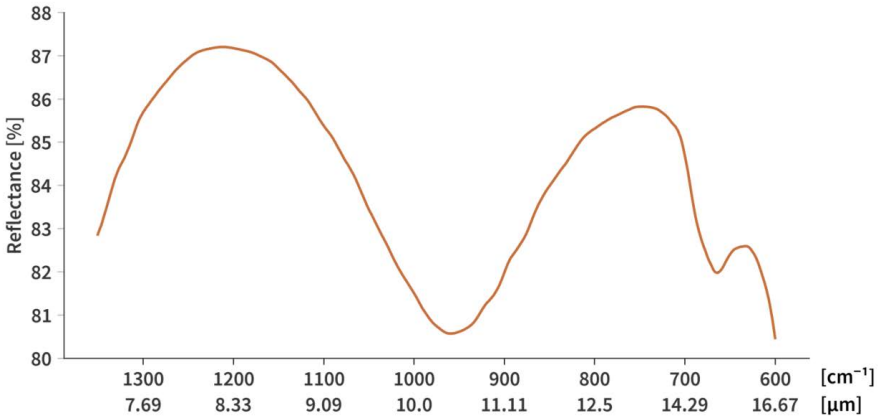

Figure S1.1: Reflectance of mirror used in the SFPI measured using specular reflectance FTIR spectroscopy on a Shimadzu IRAffinity-1 spectrometer.

S2 Estimating transmission through scanning Fabry-Perot interferometer

It is possible to estimate the transmission through the SFPI for any given combination of PCL and wavelength of the incident light. The Generalized Matrix Method (GMM) presented by Katsidis et al.[1] is a variation of the transfer matrix method (TMM), where it is possible to calculate the transmissive and reflective properties of a thin-film stack. In TMM, the Fresnel equations are used to calculate the amplitude of the electric field of a rightward and a leftward traveling wave on either side of an interface between two dielectrics (Fig. S2.1a). Relating the electric field, E, on either side of the interface between layer i and $i+1$ can be done as described in Eq. (S2.1).

$$\begin{bmatrix} E_{i,B}^{(r)} \\ E_{i,B}^{(l)} \end{bmatrix} = \frac{1}{t_{i\to i+1}} \begin{bmatrix} 1 & -r_{i+1\to i} \\ r_{i\to i+1} & t_{i\to i+1}t_{i+1\to i} - r_{i\to i+1}r_{i+1\to i} \end{bmatrix} \begin{bmatrix} E_{i+1,A}^{(r)} \\ E_{i+1,A}^{(l)} \end{bmatrix} = \boldsymbol{D}_{i\to i+1} \begin{bmatrix} E_{i+1,A}^{(r)} \\ E_{i+1,A}^{(l)} \end{bmatrix} \tag{S2.1}$$

Here, r and t are the complex reflection and transmission coefficients, respectively. The subscripts indicate firstly the layer of origin and finally the layer of destination (from and to). For the electric fields, the superscript (r) and (l) are used to represent the rightward and leftward moving waves respectively with subscript B and A indicates the interface's immediate left and right sides, respectively. $\boldsymbol{D}_{i\to i+1}$ is denoted the transmission matrix. To describe the accumulated phase as the light passes from one side of the layer to the other, the phase matrix $\boldsymbol{P}_i$ is introduced by Eq. (S2.2).

$$\begin{bmatrix} E_{i,B}^{(r)} \\ E_{i,B}^{(l)} \end{bmatrix} = \begin{bmatrix} \exp\{j2\pi n_i x\tilde{v}\} & 0 \\ 0 & \exp\{-j2\pi n_i x\tilde{v}\} \end{bmatrix} \begin{bmatrix} E_{i+1,A}^{(r)} \\ E_{i+1,A}^{(l)} \end{bmatrix} = \boldsymbol{P}_i \begin{bmatrix} E_{i+1,A}^{(r)} \\ E_{i+1,A}^{(l)} \end{bmatrix} \tag{S2.2}$$

Here, n_i is the complex index of refraction of the ith layer, x is the distance traveled inside the layer, and $\hat{v} = 1/\lambda$ is the wavenumber. In this work, wavenumbers are the preferred spectral unit to make comparisons with FTIR measurements easier. To describe the electric fields on either side of an N-layer stack, the transfer matrix $\boldsymbol{S}_{0\to N}$ is defined by Eq. (S2.3).

$$\begin{bmatrix} E_{0,B}^{(r)} \\ E_{0,B}^{(l)} \end{bmatrix} = \boldsymbol{D}_{0\to1}\left(\prod_{i=1}^{N-1} \boldsymbol{P}_i\, \boldsymbol{D}_{i\to i+1}\right)\begin{bmatrix} E_{N,A}^{(r)} \\ E_{N,A}^{(l)} \end{bmatrix} = \boldsymbol{S}_{0\to N}\begin{bmatrix} E_{N,A}^{(r)} \\ E_{N,A}^{(l)} \end{bmatrix} \tag{S2.3}$$

Finally, the transmittance is defined by Eq. (S2.4)

$$t_{0\to N} = \frac{E_{N,A}^{(r)}}{E_{0,B}^{(r)}} = \frac{1}{\boldsymbol{S}_{0\to N}[1,1]} \tag{S2.4}$$

It is then possible to calculate the transmittance spectrum by changing the wavenumber in Eq. (S2.2) and recalculating the transfer matrix.

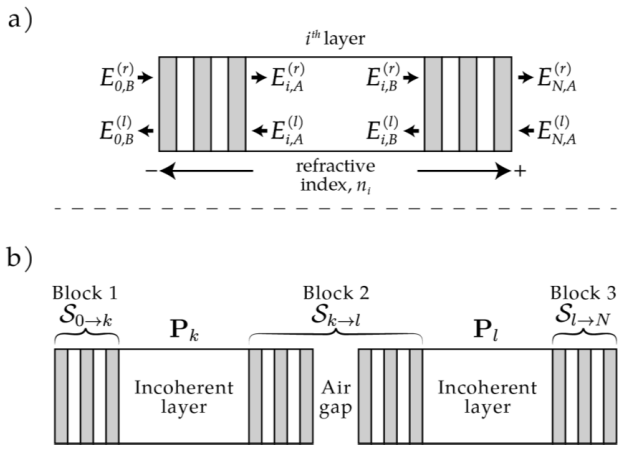

Figure S2.1: a) Thin film stack showing the electric field of the rightward and leftward moving waves on either side of each interface. b) Multiple film stacks with thick incoherent layers between. This specific case represents the two mirrors comprising the SFPI.

Including the 5 mm thick ZnSe substrates in the TMM calculations would lead to rapidly alternating constructive and destructive interference with a period of 0.42 cm^{-1} (From Eq. (1), refractive index of ZnSe $n = 2.4$). This is much finer than the best-case resolution of 26 cm^{-1} of the SFPI and should therefore be averaged out.

GMM allows for both partially and fully incoherent layers in the stack. The partially incoherent layers model the incoherence introduced by rough interfaces between layers and have *not* been included in these calculations. To include the fully coherent layers in the calculations, the stack is split up as indicated in Fig. S2.1b. When light travels through the thicker layers, the phase information is 'lost', and the layers of thin-film stacks are treated separately (Block 1, Block

2, and Block 3) from the incoherent layers placed at locations k and l. To 'remove' the phase information, the reflectance and transmission coefficients that make up the system matrices Eq. (S2.1) and (S2.3) are replaced with their square amplitudes. That means that the system matrix of Block 1 is now instead expressed by Eq. (S2.5).

$$\boldsymbol{S}_{0\to k}^{int} = \frac{1}{|t_{i\to k}|^2}\begin{bmatrix} 1 & -|r_{i+1\to i}|^2 \\ |r_{i\to i+1}|^2 & |t_{i\to i+1}t_{i+1\to i}|^2 - |r_{i\to i+1}r_{i+1\to i}|^2 \end{bmatrix} \tag{S2.5}$$

Similarly, the phase matrix of the incoherent layers is altered in a similar fashion

$$\boldsymbol{P}_{i}^{int} = \begin{bmatrix} |\exp\{j2\pi n_i d\tilde{\nu}\}|^2 & 0 \\ 0 & |\exp\{-j2\pi n_i d\tilde{\nu}\}|^2 \end{bmatrix} \tag{S2.6}$$

Effectively, the system matrix is calculated for each of the three blocks of thin-films separately, before the final system matrix for the entire SFPI (containing both coherent and incoherent layers) is calculated using Eq. (S2.7)

$$\boldsymbol{S}^{inco} = \boldsymbol{S}_{0\to k}^{int}\boldsymbol{P}_{\boldsymbol{k}}^{int}\boldsymbol{S}_{k\to l}^{int}\boldsymbol{P}_{\boldsymbol{l}}^{int}\boldsymbol{S}_{l\to N}^{int} \tag{S2.7}$$

Finally, the transmittance is calculated using Eq. (S2.8)

$$\Gamma = \frac{1}{\boldsymbol{S}^{inco}[1,1]} \tag{S2.8}$$

Using Eq. (S2.8) it is possible to calculate the transmittance at any combination of PCL and wavenumber. The transmittance matrix, $\boldsymbol{\Gamma}$, illustrates the relationship between transmittance, physical cavity length (PCL), and wavenumber (Fig. 2a). Each row in this matrix is the transmission spectrum of the SFPI at that given PCL corresponding to that row.

S3 Experimental setup

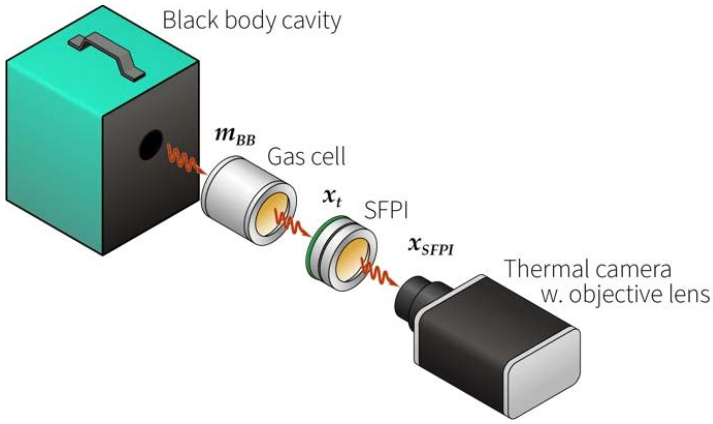

Figure S3.1: Schematic of the experimental setup. The light from a black body cavity passes through a gas cell containing either a gas or a vapor. The light then enters the SFPI and is filtered based on PCL, before finally entering the camera.

S4 Interferogram prediction

All spectral radiance spectra presented in this section have been measured using a Perkin Elmer Spectrum 65 FTIR spectrometer.

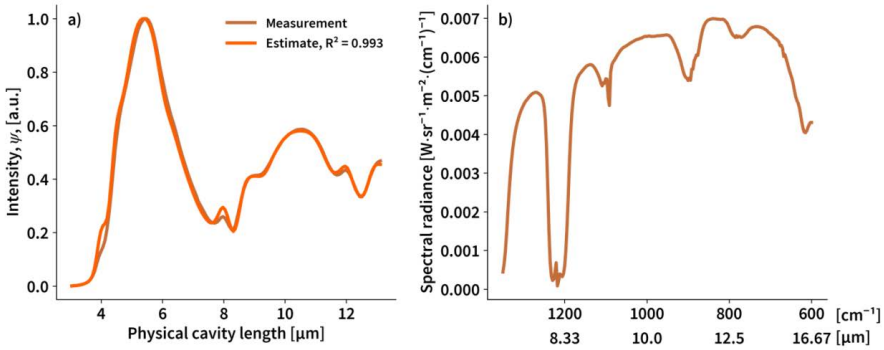

Figure S4.1: a) Measured and estimated interferograms of **acetone vapor**. The estimated interferogram is based on Eq. (5) and uses the spectral radiance of acetone vapor as depicted in b). Here, the transmission spectrum of the acetone vapor is multiplied by the spectral radiance of a 150 ºC black body as described by Eq. (3).

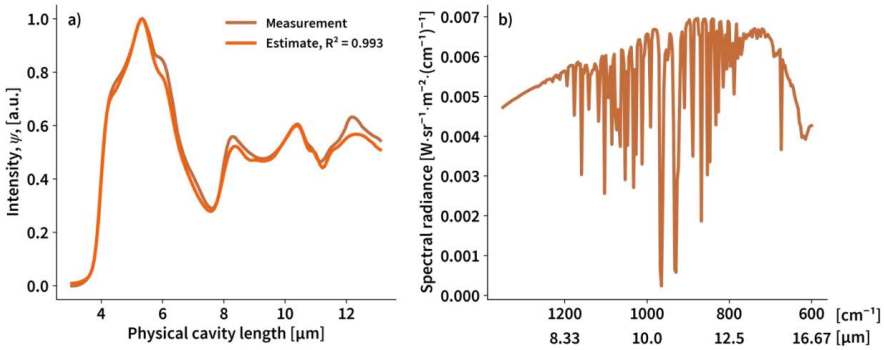

Figure S4.2: a) Measured and estimated interferograms of **ammonia**. The estimated interferogram is based on Eq. (5) and uses the spectral radiance of ammonia as depicted in b). Here, the transmission spectrum of the ammonia is multiplied by the spectral radiance of a 150 ºC black body as described by Eq. (3).

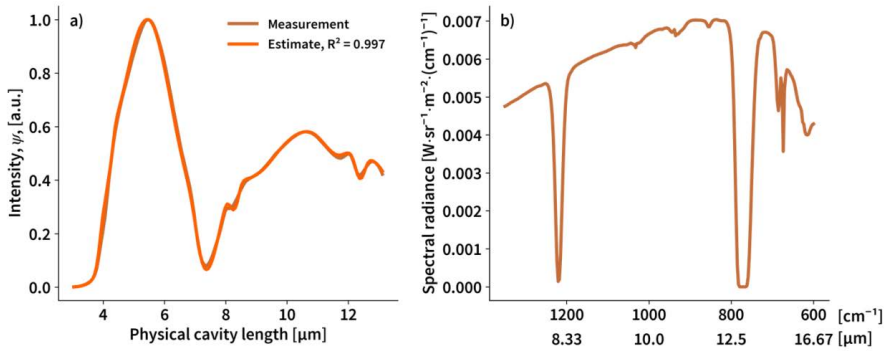

Figure S4.3: a) Measured and estimated interferograms of **chloroform**. The estimated interferogram is based on Eq. (5) and uses the spectral radiance of chloroform as depicted in b). Here, the transmission spectrum of the chloroform is multiplied by the spectral radiance of a 150 ºC black body as described by Eq. (3).

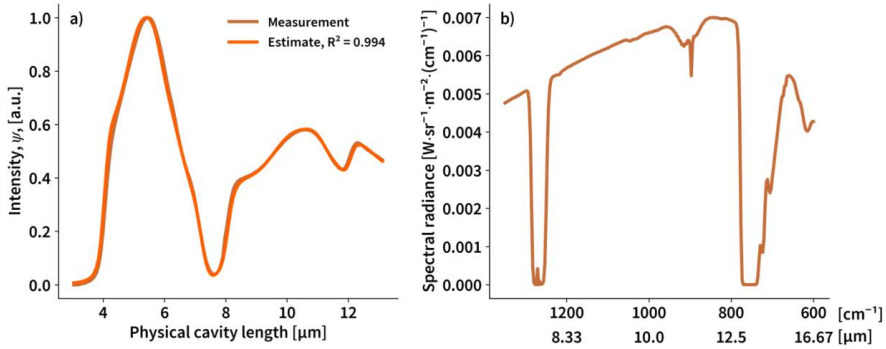

Figure S4.4: a) Measured and estimated interferograms of **dichloromethane**. The estimated interferogram is based on Eq. (5) and uses the spectral radiance of dichloromethane as depicted in b). Here, the transmission spectrum of the dichloromethane is multiplied by the spectral radiance of a 150 ºC black body as described by Eq. (3).

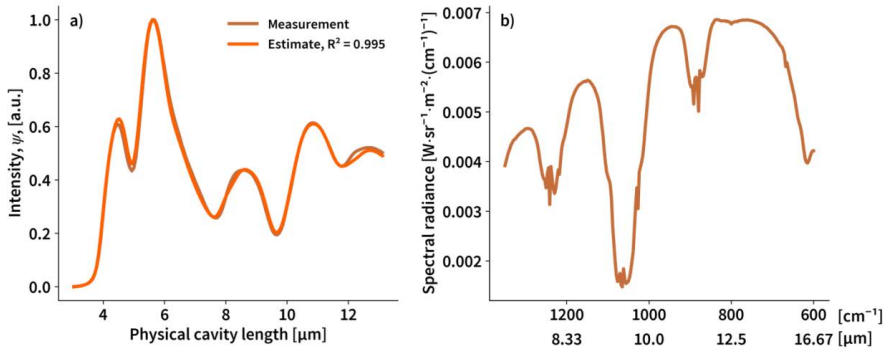

Figure S4.5: a) Measured and estimated interferograms of **ethanol vapor**. The estimated interferogram is based on Eq. (5) and uses the spectral radiance of ethanol vapor as depicted in b). Here, the transmission spectrum of the ethanol vapor is multiplied by the spectral radiance of a 150 ºC black body as described by Eq. (3).

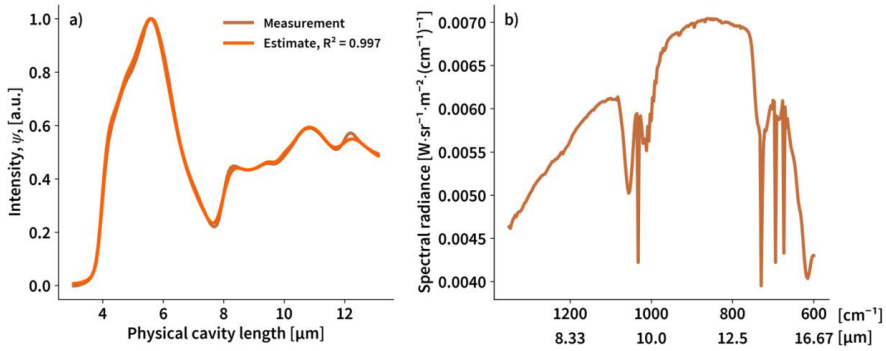

Figure S4.6: a) Measured and estimated interferograms of **toluene vapor**. The estimated interferogram is based on Eq. (5) and uses the spectral radiance of toluene vapor as depicted in b). Here, the transmission spectrum of the toluene vapor is multiplied by the spectral radiance of a 150 ºC black body as described by Eq. (3).

S5 Polystyrene interferograms

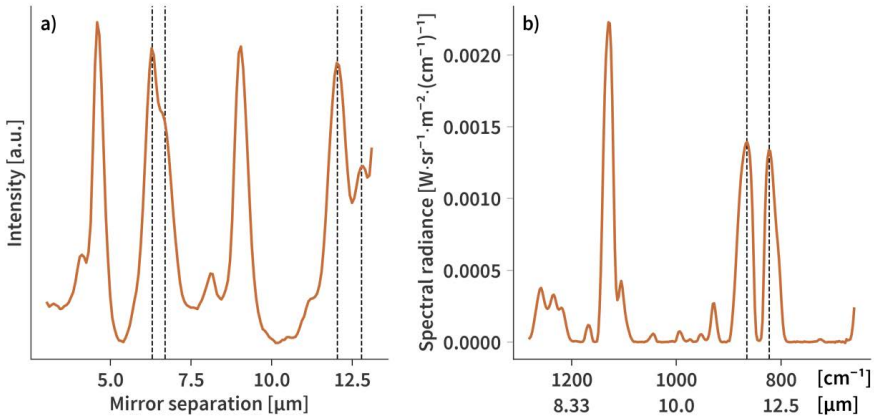

Figure S5.1: a) Averaged interferogram from hyperspectral image of polystyrene in front of a 150 ºC black body emitter. b) Transmission spectrum of the same polystyrene sample multiplied with the spectral radiance of a 150 ºC black body. Vertical lines in a) at 6.3 µm, 6.7 µm, 12.1 µm, and 12.8 µm PCL indicate the locations in the interferogram, where the two peaks indicated at 822 cm^{-1} and 865 cm^{-1} in b) in the first and second transmission orders, respectively.

S6 Broadening due to curved mirrors

Unfortunately, the compressive stresses in the mirror coatings cause the mirrors to be bent into a concave shape with the edges of the mirror coating being raised 150 nm above its center. This is not a general issue with SFPIs, but rather an artifact from the manufacturing procedure, which need to be accounted for in simulations. Now, a single PCL is no longer sufficient to describe the SFPI. Instead, the mirror is divided into nine concentric rings (Fig. S6.1b), each corresponding to an offset. A weighted average matrix is then computed, factoring in the non-uniform reflectivity and frequency-dependent broadening.

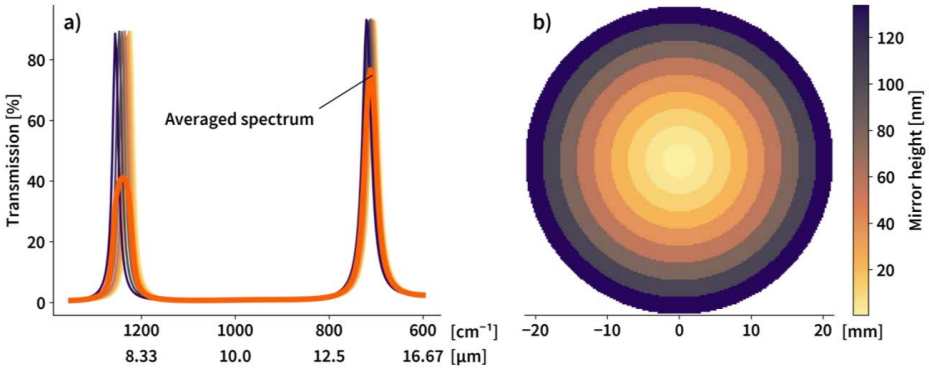

Figure 6.1: a) Transmission spectra for 8.1 µm physical cavity length at different parts of the mirrors. The colors correspond to the colored segments in b) indicating the height of the bent mirror. The thick, solid line in a) is the average of the transmission spectra, weighted based on their associated areas.

To calculate the broadening introduced by this effect, the difference in transmission wavenumber, $\Delta\tilde{\nu}$, is calculated for the center and the outermost ring as expressed by Eq. (S6.1) – (S6.3).

$$\tilde{\nu}_1 - \tilde{\nu}_2 = \frac{m}{2d'_1} - \frac{m}{2d'_2}, \qquad d'_2 > d'_1, \qquad \tilde{\nu}_1 > \tilde{\nu}_2 \tag{S6.1}$$

$$\Rightarrow \Delta\tilde{\nu} = \frac{m(d'_2 - d'_1)}{2d'_1 d'_2} \approx \frac{m\Delta d'}{2d'^2} \tag{S6.2}$$

$$\Rightarrow \frac{\Delta\tilde{\nu}}{\tilde{\nu}} = \frac{\Delta d'}{d'}, \qquad m = 2d'\tilde{\nu} \tag{S6.3}$$

Here, d'_1 and d'_2 represent the effective cavity length (ECL) of the SFPI measured at the edge and center of the mirror coating, respectively. The term "effective" is used because the plane of reflection does not necessarily coincide with the top surface of the mirror coating but rather lies within the coating itself. This shift is due to the phase change upon reflection, which becomes significant when the wavelengths are comparable in size to the cavity length, thereby influencing the transmission profile of the SFPI.

The magnitude of this effect varies with wavelength because the reflectivity of the mirror coatings is not uniform across the entire spectral range. By using GMM to compute the transmission matrix (Fig. 2a), the physical thicknesses of all layers of the SFPI are taken into account, making it straightforward to determine PCL. The ECL is essential for use in Equations (S6.1) through (S6.3), where it is assumed that the mirrors are perfectly reflective.

Nevertheless, an estimate of the broadening effect can be obtained using Equations (S6.1) through (S6.3). It is observed that both the maximum and minimum broadening occur within the first transmission order. By setting $\Delta d' = 300$ nm, the resulting broadening is calculated to range between 16 and 116 cm^{-1}

S7 References

(1) Katsidis, C. C.; Siapkas, D. I. General Transfer-Matrix Method for Optical Multilayer Systems with Coherent, Partially Coherent, and Incoherent Interference. *Appl. Opt.* **2002**, *41* (19), 3978. https://doi.org/10.1364/AO.41.003978.

E. Manuscript: Signatures of Flames by Long-Wave Infrared Hyperspectral Imaging

This section includes the manuscript *Signatures of Flames by Long-Wave Infrared Hyperspectral Imaging* submitted to *Applied Spectroscopy* on January 11, 2025. This manuscript demonstrates how the hyperspectral LWIR imager can detect and distinguish between reaction zones in simple diffusion flames of various hydrocarbon and hydrogen fuels. This section contains both the manuscript itself and the accompanying supporting information.

Signatures of Flames by Long-Wave Infrared Hyperspectral Imaging

Mads Nibe Larsen[†,‡], Iben Hansen-Bruhn[£], Anders Løchte Jørgensen[‡], Bjarke Jørgensen[‡], Jakob Kjelstrup-Hansen[†,*]

[†]NanoSYD, Mads Clausen Institute, University of Southern Denmark, 6400 Sønderborg, Denmark
[‡]Newtec Engineering A/S, 5230 Odense, Denmark.
[£]DBI - The Danish Institute of Fire and Security Technology, 2650 Hvidovre, Denmark.
*Corresponding author

ABSTRACT

Thermal cameras operating in the long-wave infrared (LWIR) spectral range (8-15 μm) are widely used for temperature inspection in fire sciences. This study explores the expansion of thermal imaging by coupling a standard thermal camera with a scanning Fabry-Pérot interferometer to achieve emission-based hyperspectral imaging. A hyperspectral camera system was developed that yields spatially resolved images of a flame in narrow spectral bands. The developed system offers a low-cost, portable solution for capturing both spatial and spectral data. The applicability was evaluated by measurement on diffusion flames of pure fuels such as hydrocarbons ranging from C_1 to C_4 or hydrogen. Despite the complexity and time-shifting nature of flames, the study demonstrates that hyperspectral data cubes captured in the LWIR spectral range can potentially differentiate among fuel signatures of flames, offering potential applications in fire diagnostics and remote fuel identification in complex fire scenarios. This hyperspectral longwave infrared imager offers the ability to analyze both the spatial and spectral dimensions of flames and provides a unique opportunity to develop new machine-learning diagnostic tools that can improve understanding of fire behavior and enhance fire safety in real-world applications.

Keywords:
Hyperspectral imaging, Fabry-Pérot, thermography, flame emission, LWIR spectroscopy.

1 INTRODUCTION

Flame imaging is an indispensable diagnostic tool in fire sciences, offering critical insights into flame anatomy and behavior. Fire safety engineers rely on visual documentation (i.e. photos and video recordings) from fire testing when assessing fire dynamics in complex construction setups involving heterogeneous materials [1],[2],[3]. Thermal imaging has emerged as a dependable tool when analyzing these fire scenarios. Since thermal cameras detect radiation emitted by the object itself, thermal cameras can be operated independent of lightning conditions and can localize hot spots even behind walls. Therefore, thermal cameras are widely adopted in fire sciences for identification of potential hazards, remote sensing of wildfires, early fire detection, fire severity assessment, and smoldering fires [4],[5],[6],[7]. Analyzing the visual characteristics of flames over a sequence of thermal images, e.g. contour, color intensity, luminosity, base width, flame height, and flickering frequency, contribute to a deeper understanding of the combustion processes. Conventionally, thermal energy from fires is detected by a focal plane array, translated to temperature by assuming blackbody Planck radiation [8], and converted to a greyscale image with brighter pixels corresponding to hotter areas. Detectors in conventional thermal cameras integrate radiation over the spectral range of 8–15 µm wavelength (wavenumbers between 1250 – 667 cm^{-1}), corresponding to the longwave infrared (LWIR) regime. This integration, however, results in the loss of valuable spectral information that could otherwise be utilized to infer critical physical parameters of the observed scene.

Since most combustion relevant molecules reflect, absorb, and emit radiation in the IR region (IR, 1-1000 µm) resulting from vibrational and rotational transitions, IR cameras enable selective probing of gas-phase, particulate, and hot surface contributions to the observed emissions with high sensitivity [9], [10]. While mid-wave infrared energy (MWIR, 3-5 µm) matches fundamental vibrational modes of molecules, LWIR is mainly associated with deformation bands. Chain alkanes exhibit C-H fundamental stretches around 3000 cm^{-1}, and deformation bands at 1350 cm^{-1} (C-H bending), 1150 cm^{-1} (combination of C-C stretch and skeletal vibration), 880 cm^{-1} (rocking), and 740 cm^{-1} (rocking) whereof the three last bands fall within the LWIR range [11]. Even though the LWIR detection range is not ideal for chemical identification purposes, LWIR cameras are highly suitable for remote sensing applications. Unlike MWIR cameras, which rely on ultrasensitive, cooled mercury-cadmium-telluride (MCT) detectors, LWIR cameras are more widely available, cost-effective with respect to

quality, and standard equipment in most fire testing facilities. A key challenge is that even though LWIR devices can act as sensors, conventional thermal cameras lack the spectral information needed for chemical identification.

A promising solution is to use cameras capable of hyperspectral imaging (HSI), which combines spatial and spectral information into data cubes. The data cubes consist of a two-dimensional thermal image (spatial dimensions x and y) with wavelength (λ) as the third dimension, enabling the simultaneous acquisition of spectral signatures. As each pixel in the image contains a spectrum, the dataset can be post-processed to extract detailed information on flame structure, composition, temperature gradients, and possibly reaction intermediates [12]. While many publications focus on flame emission spectroscopy [13],[14],[15], only few studies report on hyperspectral detection and imaging of fuel plumes and flames [16],[17],[18],[19],[20]. Of these, the majority applies NIR/SWIR (0.9-1.7 µm) and MWIR, for either solid-phase fuel identification or investigation of flames [21],[22],[23]. Furthermore, HSI has reached a level of maturity where rapid data acquisition and the computational power required for image processing are readily available. This advancement enables the simultaneous capture of spectral and temporal information, providing sufficient data for detailed flame analysis. [13],[24]. Thus, the upgrade of thermal cameras to hyperspectral systems, which integrate both spatial and spectral imaging of flames, offers significant potential for fire safety engineering by enabling simultaneous identification and real-time monitoring of combustion phenomena.

This study presents the expansion of a microbolometer-based thermal camera (LWIR, 8-15 µm) with a scanning Fabry-Pérot interferometer (SFPI), functioning as a variable bandpass filter. Together, they form a spectral imager that allows for the acquisition of hyperspectral data cubes without the need for relative movement between camera and subject unlike whisk- and push-broom techniques [25]. This hyperspectral LWIR imager provides a low-cost, portable solution for capturing spectral data on commonly available, uncooled microbolometer based thermal cameras. The combination of camera and SFPI has been previously demonstrated [26], [27],[28], [29], but the application of an SFPI-based LWIR system for flame signature analysis is, to the best of the authors' knowledge, unprecedented [8]. To assess the feasibility of LWIR hyperspectral flame imaging, hyperspectral data cubes were recorded on diffusion flames fueled by C_1 to C_4 hydrocarbons (methane, ethane, propane, butane, ethylene, acetylene) and hydrogen. Although far from representing practical fire scenarios, these laboratory flames serve

as a crucial starting point to validate the methodology for identifying contours and spectral signatures of dynamic emitting flames, prerequisites for real-world fire testing.

2 MATERIALS AND METHODS

2.1 Laboratory Flames

Seven different fuel gases were used: methane (Messer® CANGas, 99.995%, DE), ethane (Messer® CANGas, 99.95%, DE), propane (Messer® CANGas, 99.95%, DE,), butane (Guilbert Express, FR), acetylene (Linde, > 98.5%, DK), ethylene (GHC Gerling Holz & Co., 99.9%, DE), and hydrogen (Messer® CANgas, 99.999%, DE). Laminar, self-sustained flames were produced by ignition of a manually adjusted gas flow from a pressurized gas canister connected through ≈ 1 m tubes (Ø4 mm, PFA) to a blunt-tip needle (Ø0.8mm, length 23mm, B. Braun Melsungen AG, DE). Fuel and air were mixed just above the needle (<0.1 mm) to yield a flame of 5 -10 cm in height. Disturbances from air currents were minimized, and all experiments conducted within two hours at ambient conditions (temperature of 295 K, 55% relative humidity).

2.2 Experimental Setup

A thermal camera (QT5022, QTechnology, DK) equipped with an uncooled microbolometer detector array (Pico1024Gen2™, Lynred, France) was positioned ≈ 0.4 m from the center of the flame in line-of-sight as depicted in Fig. 1. The detector resolution was 1024×768 pixels with a pixel pitch of 17 µm and with sensitivity to wavelengths from 8 µm to 15 µm (1250 cm^{-1} to 667 cm^{-1}). The hyperspectral functionalities were provided by a scanning Fabry-Pérot interferometer (SFPI) placed 10 mm in front of the germanium lens objective (35 mm focal length, 1/f aperture, C-mount, Ophir Optronics Solutions Ltd., IL). With the focal plane distance being ≈ 0.4 m, each pixel corresponds to ≈ 4.9 mm both vertically and horizontally resulting in each pixel sampling an area of ≈ 24 mm^2. A long-wave pass filter (50% cut-on at 8.51 µm (1174.5 cm^{-1}), Andover Corporation, USA, transmission spectrum in Supporting Information (SI) Fig. S1.1) was placed directly in front of the SFPI. Additionally, a bandpass filter (10.26 µm (975 cm^{-1}), 0.35 µm (34 cm^{-1}) full width at half maximum (FWHM), Andover Corporation, USA, SI, Fig. S1.2) was placed next to the flame in front of a hot plate at 80 ºC used for spectral alignment.

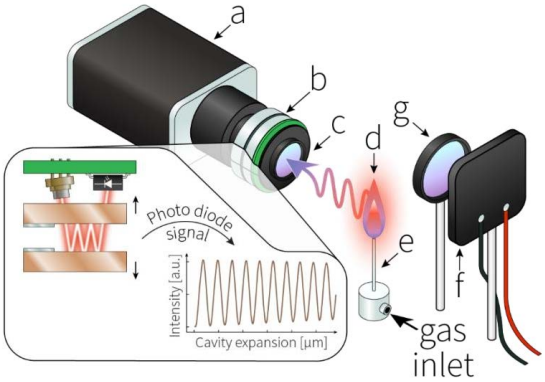

Figure 1: Schematic representation of hyperspectral LWIR imager in the experimental setup (not to scale). It consists of the following components: a) thermal camera, b) SFPI, c) 8.51 µm long-wave pass filter, d) flame, e) blunt-tip needle, f) hot plate set to 80 ºC, and g) 10.26 µm bandpass filter. The inset shows how light from laser diodes is reflected off the cavity, giving rise to laser diode interferograms.

2.2.1 Scanning Fabry-Pérot Interferometer

The SFPI functioned as a tunable band-pass filter, with its transmission profile set by the length of the cavity formed by two parallel, partially transparent mirrors (Coherent Corp, USA) with an 84% average reflectance over the 8–15 µm range. The mirror substrates had a diameter of Ø2" (50.8 mm), with a reflective coating of Ø43 mm centered on each substrate. Each mirror was placed in their own half of a stainless-steel flange. Three piezo actuators positioned 120º apart between the two halves were used to control the cavity length between ≈ 3 µm and ≈ 13 µm.

2.3 Data Acquisition

For each flame, a hyperspectral data cube (≈ 150 images, ≈ 250 MB data) was captured during the image acquisition sweep following four initial calibration sweeps. Each sweep lasts 16 s, corresponding to 8 s of increasing and decreasing cavity length, respectively. Interferograms from three laser diodes (λ_{eff} = 680 nm), reflected off an uncoated area of the SFPI cavity, were monitored for all sweeps (Fig. 1 insert). As cavity length increases, the laser light shows alternating constructive and destructive interference, as described by Eq. (1), where m is transmission order, d is cavity length, θ the light's incidence angle, λ wavelength, and $\tilde{\nu}$,the wavenumber. λ_{eff} is the 'effective wavelength' that takes the incidence angle into account.

$$d = \frac{m}{2}\lambda_{\text{eff}} = \frac{m}{2\tilde{\nu}\cos\theta}\ , \qquad m = 1, 2, 3 \ldots\ , \qquad \lambda_{\text{eff}} = \frac{\lambda}{\cos\theta} \tag{1}$$

The peak-to-peak distance of the laser interferograms thus corresponds to 340 nm (half the 680 nm wavelength). The interferograms are used to determine the expansion of the cavity, though it does not provide information about the absolute cavity length. To maintain parallel mirrors, a constant phase difference between the three laser interferograms ensured equal displacement across the mirror surfaces. The calibration sweeps determined the unique voltages for each piezo actuator to achieve a uniform sweep (parallel mirrors) and reduced the stroke length of the actuators to match the shortest of the three actuators. During the final image acquisition sweep, the camera captured images as quickly as possible, noting the corresponding actuator voltages, but not at fixed intervals. Thus, the total number of spectral channels in a data cube varied from 148 to 156.

2.4 Data Processing

The spectral axis of the data cubes describes the cavity length [μm] rather than wavelength. Thus, the 'spectrum' in each pixel of the data cube is referred to as an *interferogram*. It is possible to remap the interferogram onto a wavenumber/wavelength-dependent axis for easier interpretation, but some processing steps were performed initially as outlined below.

2.4.1 Offset Correction

To ensure that the intensity in each interferogram starts at zero, the offset is corrected by subtracting the first spectral channel from the data cube, as given in Eq. (2).

$$I_1(x, y) = I_0(x, y) - I_0(x, y, 0) \tag{2}$$

where $I_0(x, y)$ is the interferogram of the unprocessed data cube at pixel (x, y) and $I_0(x, y, 0)$ refers to the first channel of that pixel. The first channel is recorded when the mirrors are close together and < 0.6% of the incident light within the spectral range is transmitted. Hence, Eq. (2) corresponds to a type of *dark frame correction* which reduces the pixel offset noise associated with microbolometer detectors. The effect of offset correction is visually presented in SI, Fig. S2.1.

2.4.2 Spectral Shift Correction

From Eq. (1), the transmission wavelength depends on the angle of incidence. Consequently, the transmission wavelength is shorter at the detector edges than at its center. To achieve

uniform transmission wavelength across the detector, the interferogram axis must be adjusted by a factor of $\cos\theta$. The angular variation across the detector is calculated using Eq. (3).

$$\theta = \tan^{-1}\frac{r}{f} \tag{3}$$

Here, r is the distance from the detector center to the pixel, and f is the lens focal length (35 mm). At the region of interest (ROI, Fig. 2) furthest away from the detector's center, the scaling factor becomes $\cos\theta = 0.98$. This spectral shift correction is demonstrated in SI, Fig. S3.1, where a 60°C hotplate (monitored with a K-type thermocouple) filling the entire frame (a larger hotplate than what is used in the experimental setup presented in Fig. 1) was imaged through the 10.26 µm bandpass filter.

2.4.3 Spectral calibration

The interferogram of the 10.26 µm bandpass filter (averaged over a 50×50-pixel region from ROI IV in Fig. 2) is used to convert the spectral axis of the data cubes from channels to absolute cavity lengths. This filter serves as an external calibration reference, with two peaks corresponding to cavity lengths of 5.52 µm and 10.61 µm. The relative cavity expansion measured by the laser diodes is adjusted so that the first interferogram peak aligns with a cavity length of 5.52 µm. The impact of spectral alignment across data cubes is illustrated in SI, Fig. S4.1.

The peak positions of the bandpass filter were determined by computing the matrix-vector product of the system matrix (SI Fig. S5.1) and the transmission spectrum of the bandpass filter (SI Fig. S1.2). The system matrix links the cavity length, incident light wavelength, and the response of the imaging system using the generalized matrix method (GMM), which estimates the electric field distribution in the thin film stack [30]. Each row of the matrix corresponds to the transmission spectrum for a given cavity length, while each column represents the interferogram for a specific wavelength. The system matrix calculations incorporate the normalized spectral response of the detector and the long wave pass filter, accounting for the observed loss in intensity at shorter and longer wavelengths.

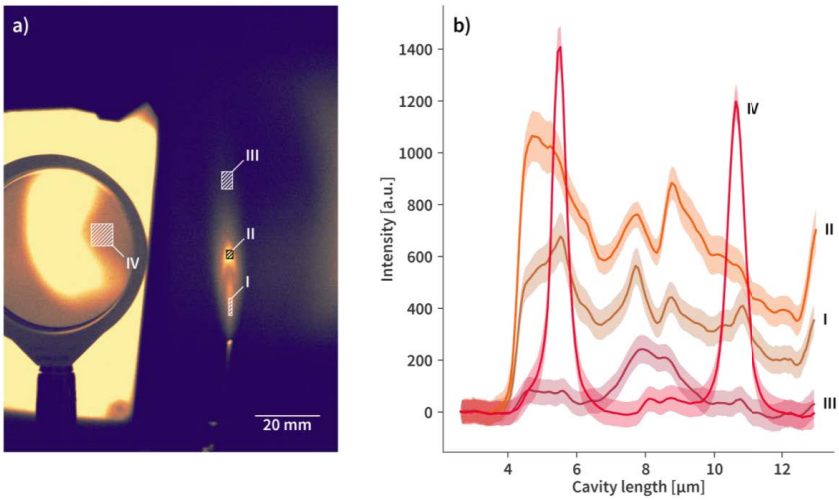

Figure 2: a) Channel of the data cube corresponding to a cavity length of 5.6 µm, showing a propane-air flame. Hatched areas represent ROIs I to IV where mean interferograms are extracted for data analysis. ± 1 standard deviation is indicated in a lighter shade. b) Mean interferograms (ROI I to IV) as a function of cavity length for the entire data cube.

2.4.4. Mean Interferogram Extraction in ROIs

Different parts of the flame have different spectral profiles as indicated by the clustering achieved using K-means and presented in SI Fig. S6.1. ROIs are selected as shown in Fig. 2a): *I* located close to the flame base (8×40 pixels), *II* located in the luminous inner cone (if present) of the flame (15×40 pixels, for propane 15×20 pixel), and *III* located above the flame in the outer non-luminous cone (25×40 pixels). Fig. 2a depicts measurements from channel 45 (corresponding cavity length of 5.6 µm) of a propane flame. The mean interferograms for propane flame ROIs are visualized in Fig. 2b. For all other flames, interferograms are found in SI, Fig. S7.1 to Fig. S7.7.

2.4.5 Interpolation of spectral axes

Due to variations in the spectral axes between data cubes (i.e., the cavity length corresponding to a given spectral band in one cube may differ from that of another). The data cube with the fewest spectral channels is used to determine the number of interpolation points, which are evenly distributed across the range defined by the maximum initial cavity length and the minimum cavity length of the final spectral channel across all data cubes. Thus, as the number

of spectral channels in each data cube varies, each data cube is interpolated to share a common spectral axis.

2.4.6 Remapping Cavity Lengths to Wavenumbers

The system matrix (SI Fig. S5.1) illustrates the multiple transmission orders by increased cavity lengths as predicted by Eq. (1). For certain cavity lengths, the detected light originates from multiple wavelengths, though it is still limited by the spectral range of the detector. To address this challenge, overlapping regions are excluded by disregarding cavity lengths where more than one peak exhibits a transmission greater than 15%. Consequently, the third transmission order is not visible in the translation between wavenumbers and cavity length (Fig. 3a) due to its overlap with the second order. Fig. 3b shows the interferogram of propane collected in ROI I mapped onto a wavelength/wavenumber axis. The same spectral feature ≈ 960 cm^{-1} is replicated in both the 1st and 2nd transmission order. Note that no additional scaling has been performed apart from the remapping of the axis to avoid edge effects, where compensating for the decreasing detector response could cause excessive amplification of the signal.

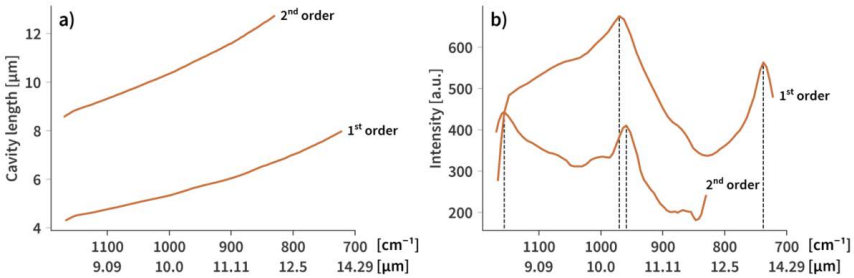

Figure 3: a) Relationship between cavity length and peak transmitted wavelength. b) Propane interferogram from ROI I remapped onto wavelength/wavenumber axis. Vertical, dashed lines indicate locations of extracted features.

The spectral resolution of the system is defined as the FWHM of each row in the system matrix (SI Fig. S5.1) and varies with both transmission order and wavelength as displayed in Fig. 4. Here, the same sections used for remapping in Fig. 3 are used and the resolution spans from 24 to 71 cm^{-1}. It should be noted that the rapid improvement in spectral resolution towards higher wavenumbers is caused by the long-wave pass filter.

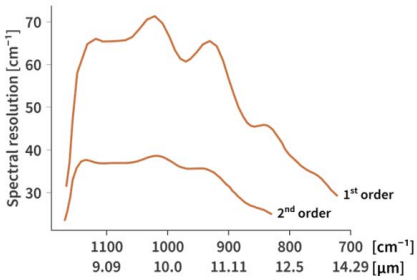

Figure 4: Spectral resolution of the hyperspectral image based on the FWHM derived from the system matrix in Fig. S5.1.

2.5 Flame Signatures

Wavenumbers associated with pronounced spectral features (exemplified by vertical, dashed lines in Fig. 3b) were extracted and tabulated for remapped flame interferograms in ROI I, II, and III for both first and second order transmissions. Reference spectra for fuel gas and combustion products (i.e. water (H_2O) and carbon dioxide (CO_2), downloaded from the HITRAN spectral database [31] or NIST Chemistry WebBook [32] respectively) were plotted with measured flame interferograms. Flame emission spectra from published peer-reviewed journal papers [33][34], free radicals present during combustion (OH·, C_2·, CH·, CO_2· etc.) [35], and the extensive tabulation of water lines [36],[37],[38] reported in the LWIR region were applied to aid interpretation of spectral features.

To investigate uniqueness of flame signatures, the Pearson correlation coefficient (ρ) was employed to assess the discrimination potential of measured flame interferograms. By utilizing the full interferograms (same processing except for remapping), ρ is a descriptor of similarities as defined in Eq. (4). ρ varies from [-1;1], where ρ=1 indicates perfect correlation, values above 0.8 implies a high correlation, and values below 0.5 are considered as low correlation.

$$\rho(I_a, I_b) = \frac{\mathrm{cov}(I_a, I_b)}{\sigma_{I_a}\sigma_{I_b}} \tag{4}$$

Here I_a and I_b are extracted interferograms, $cov(I_a, I_b)$ is their covariance, and σ_{I_a} and σ_{I_b} are their standard deviations.

3 RESULTS

Spectral features of all flames (C_1 to C_4 hydrocarbons and hydrogen), extracted from the remapped interferograms (SI, Fig. S7.8 – S7.14, depicted with reference spectra), are presented in Fig. 5. Black dots indicate peak locations, while the bar widths represent the resolution of the SFPI at the given wavenumber (Fig. 4). For each ROI, two lines of bars are presented: the top bar shows features extracted from the first transmission order, and the second bar represents features extracted from the second transmission order.

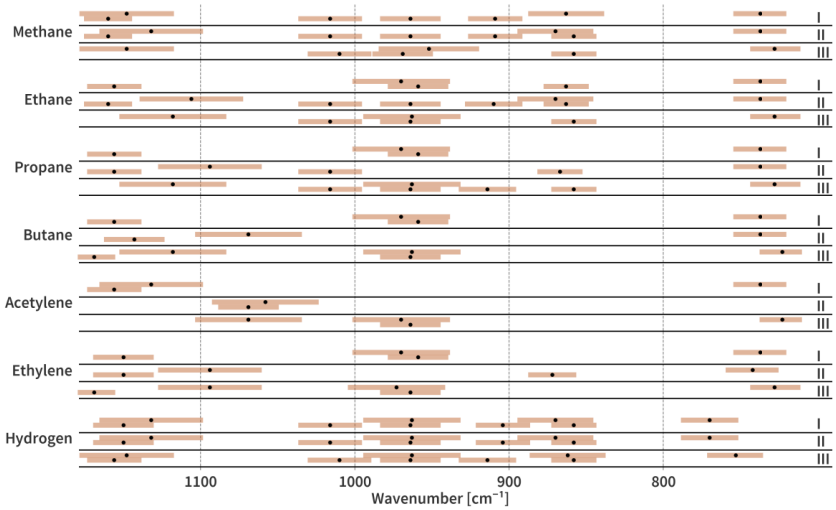

Figure 5: Spectral features from remapped flame interferograms. Peak locations are marked by black dots, and bar widths represent the resolution of the SFPI at each wavenumber. Three flame ROIs are shown with two lines of bars for each: the top bar corresponds to the first transmission order, and the lower bar to the second transmission order.

Figure 5 demonstrates that each flame exhibits distinct spectral fingerprints across all three ROIs. The butane and acetylene flame interferograms are notably differentiated by the absence of signals in the 900–800 cm^{-1} region, while hydrogen flames are characterized by a shifted pattern below 800 cm^{-1} across all ROIs. Remapped interferograms of alkanes with varying chain lengths (methane, ethane, propane, butane) reveal considerable similarities; however, methane flames can be identified by a unique band pattern above 1100 cm^{-1}, ethane and propane exhibit differing patterns in ROI II (1000–800 cm^{-1}), and butane lacks bands near 900 cm^{-1}. Furthermore, hydrocarbons of the same chain length but different chemical classes

(ethane, ethylene, acetylene) display distinct spectral differences across the entire range. Additionally, common feature for all fuels, except methane, acetylene, and hydrogen, is the presence of peaks near 970 cm^{-1}. These observations suggest the potential for discriminating flame signatures in the LWIR region, as supported by the data in SI Tab. S8.1, which compiles all extracted peak and shoulder locations.

To investigate the discrimination potential, the correlation charts derived from calculated Pearson coefficients are presented in Fig. 6 for ROIs I, II and III. When measured as average ρ, ROI III appears the most similar ROI regardless of fuel type in the combustion (I: 0.82, II: 0.82 and III: 0.85). Excluding hydrogen from ROI III, raises the average ρ to 0.91. This suggests that hydrogen flames could easily be distinguished from hydrocarbon flames by scanning only in ROI III. In ROI I, methane and ethylene are the most distinct gases (average ρ of 0.71 and 0.70) while in ROI II ethane and acetylene stand out (average ρ of 0.77 and 0.72). The lowest overall correlation coefficients are 0.43 (methane-ethylene), 0.44 (acetylene-ethane) and 0.55 (hydrogen-butane) for ROIs I, II and III, respectively. Altogether, the measured interferograms are significantly different, allowing to obtain a hydrocarbon signature.

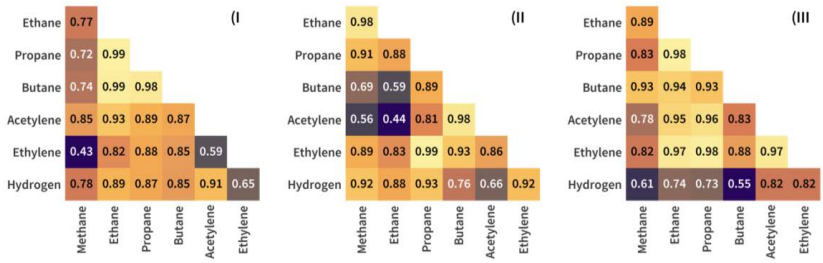

Figure 6: Pearson correlation coefficients between flame interferograms sampled at ROIs I, II, and III, as depicted in Fig. 2a. Darker shades represent lower values.

4 DISCUSSION

While controlled equivalence ratio of the flames might be appealing for scientific purposes, real-world fire scenarios involve diffusion flames that develop under ambient conditions. Emitted light from such flames arises from the combination of i) continuous blackbody radiation of particulate matter (e.g. soot, char, ash), ii) discrete emissions from rotational-vibrational transitions of gas molecules at high temperatures (primarily H_2O and CO_2), and iii) chemiluminescence resulting from the relaxation of electronically excited intermediate species [39], [40]. In the LWIR spectral range (8-15 μm), a densely packed rotational spectrum of water is expected below 1000 cm^{-1}, and with a decrease in the region 769-666 cm^{-1} due to atmospheric CO_2 absorption [36],[41]. For CO_2, a broad continuous band from 665 cm^{-1} to 700 cm^{-1} and a line at 721 cm^{-1} are expected [32], [42]. Spectral contributions from intermediate flame radicals (i.e. chemiluminescence) are however negligible as they predominantly occur in the ultraviolet or near-visible region. Further, the few emissions in LWIR region from OH· radicals and carbon monoxide (CO) are obscured by the stronger signals from CO_2 and H_2O [14]. However, any observations of fine structure in flame emission LWIR spectra captured by the hyperspectral LWIR imager, is constrained by the experimental setup including measurement conditions, instrumentation (i.e. detector resolution), and the data processing approach, which will be elaborated in this section.

4.1 Experimental Considerations

To minimize effects from atmospheric absorption, the optical path length for all experiments was below 0.5 m [43]. As the imaging system employs line-of-sight integration, each pixel accumulates signals from varying depths along the optical path. Hence, optically thick flames with higher concentration of emitting species increase the observed spectral intensity. ROI II was selected to represent the luminous zone, thus assuming the highest optical path length. As shown in Fig. 2b, spectral intensity ranks the ROIs (high to low): II > I > III, which was identical for all measured flames. The detected spectral intensity is, as expected, strongly influenced by the selected position of each ROI despite the balanced pixel areas (8-15-25 times 40 pixel in ROI I, II, III). Nevertheless, flame interferograms of all three ROI show the same curve features (Fig. 2b).

While methods for decoupling of optical path length and temperature effects were not explored in this study, efforts were made to ensure the reliability of experimental

measurements. Preliminary laboratory work on random test days demonstrated data consistency; however, for consistency all data were collected within a two-hour window to maintain comparable ambient conditions. Further, measures to reduce flame turbulence proved effective, enabling a stable flame throughout the 8-second duration required for acquisition of a hyperspectral data cube. Although this duration is insufficient for capturing flame dynamics, it provides a solid starting point for fire tests that typically span over 20 minutes and up to two hours.

In general, high resolution in the spectral, spatial, or temporal domains is desirable for capturing the full complexity of observed fire phenomena. As shown in Fig. 4, the spectral resolution varies non-linearly with wavenumber, spanning 40-70 cm^{-1} (m = 1) and 30-40 cm^{-1} (m = 2), respectively. Thus, extracted spectral features are reported as intervals, rather than as a single number to reflect uncertainties. A common criterion for resolving two peaks is for them to be separated by more than a FWHM. This condition, meaning no overlap between bands in Fig. 5 is met for all reported peaks. However, higher spectral resolution inherently narrows spectral bands, hereby reducing the amount of transmitted light and lowering the signal-to-noise ratio (SNR). Addressing this limitation would require the implementation of more sensitive detectors, such as MCT detectors. While capable of achieving higher sensitivity, these necessitate cryogenic cooling and significantly increase the overall system cost and complexity. Similarly, increased spatial resolution enhances the ability to resolve heterogeneous structures within the flame, such as localized reaction zones, while higher temporal resolution is essential for capturing rapid fluctuations and dynamic processes. However, high-resolution detectors come with trade-offs such as increased cost or reduction in sensitivity due to smaller pixel sizes. Although MCT detectors operate significantly faster than microbolometer detectors (microseconds versus milliseconds), their performance in this context would be constrained by the operational speed of the SFPI. MCT detectors can also be optimized for different spectral ranges, such as the MWIR. However, this would necessitate the development of new dielectric mirrors specifically designed for the targeted spectral range. Consequently, the microbolometer is deemed suitable for this application. Altogether, the quality of the data is inherently determined by the imaging system, with the spatial resolution primarily governed by the microbolometer detector, while the spectral and temporal resolution are dictated by the SFPI.

After acquiring the data, minimal data processing was applied to retain the integrity of the raw data, with offset correction being a critical step compensating for manufacturing tolerances inherent to microbolometer detectors. As illustrated in SI Fig. S2.1, the same image of propane is nearly indistinguishable before offset correction is applied, highlighting the importance of this preprocessing step. The need of an external spectral calibration target is demonstrated in SI Fig. S4.1a, showing that interferograms of the 10.26 µm bandpass filter (Fig. 1) from all data cubes are misaligned. However, after applying the spectral calibration procedure described in Section 2.4.3, the interferograms align, enabling direct comparisons between the data cubes (SI Fig. S4.1b). In summary, despite several experimental constraints and only basic data manipulations, repeatable spectral flame interferograms can be reliably obtained under ambient conditions; a critical prerequisite for developing an emission-based LWIR spectral database of flame signatures intended for statistical analysis or machine learning applications.

4.2 Signatures of Different Flame ROIs

ROI I, located near the base of the flame, is expected to exhibit the pure emission spectrum of fuel or early decomposition products prior to combustion. For ethane, an absorption band at 830 cm^{-1} (C-H bending) is anticipated based on its FTIR absorption spectrum (SI Figure S7.9). However, this band does not appear in the remapped interferogram (SI Figure S7.9); instead, a peak at 970 cm^{-1} is observed. Except for methane and acetylene, this 970 cm^{-1} peak is notably present in ROI I across all tested hydrocarbons. A plausible explanation is the presence of ethylene (C-H wagging) near the flame base. This finding aligns with literature where ethylene is documented as an early decomposition product in alkane combustion [44],[45]. Nevertheless, the substantial contribution of ethylene to the signal could potentially mask more subtle contributions from other combustion products. Altogether, these observations in ROI I supports the conclusion, that combustion reactions begin very close to the flame base.

Except for methane and hydrogen flames, a visually bright spot (ROI II) was observed in the flame center. Typically, a luminous flame center arises due to soot formation resulting from incomplete combustions. Governed by the flame temperature, carbon particulates burn brightly, thus manifesting as a significant blackbody contribution to the emission signal [46],[47]. This effect is particularly noticeable in the case of butane and acetylene (SI Fig. S7.4 and S7.5, ROI II), as the interferograms in ROI II closely resemble that of a blackbody (SI Fig. S11.1). These two gas samples are industrial-grade gases with a lower purity compared to the other gases analyzed. Consequently, the observed increase in blackbody radiation can likely be

attributed to the reduced purity of these samples. In this analysis, the acetylene interferogram is compared to a 150 °C blackbody spectrum. While the acetylene flame temperatures can exceed 2200 K depending on the fuel-to-air ratio [48], the blackbody spectrum highlights the expected spectral distribution and curve shape similarities in their emission profiles. The significantly higher flame temperature blueshifts the blackbody spectrum, explaining the steeper onset of the first and second order in SI Fig. S11.1. Hence, a clear distinction between sooty versus clean flames were detected in the measured flame interferograms for ROI II.

ROI III, located above the flame, is expected to contain remnants of combustion products (CO_2, H_2O). This is evidenced by a peak observed for all hydrocarbon gases at around 7.9 µm cavity length and assigned to bending mode of CO_2, with an absorption peak from 670 cm^{-1} to 720 cm^{-1} [32] (SI Fig. S12.1). Notably, this peak is absent in the interferograms extracted from hydrogen, which only shows the water vapor peaks due to the absence of CO_2 as a byproduct of its combustion. Further, all flame interferograms exhibit distinct peaks or shoulders in ROIs II and III at cavity lengths of approximately 4.7 µm and 8.7 µm (corresponding to 1132 cm^{-1} in the remapped interferogram), along with a rising slope towards the ends of the interferograms (around 13 µm). These features correspond to light at roughly 1150 cm^{-1} and are likely due to water vapor emissions. Water vapor has a strong absorption band just below the atmospheric window (around 1510 cm^{-1}), with the detector capturing the trailing edge of this feature [32]. While presence of water vapor is typically undetectable at room temperature, the elevated temperatures within the flame excite water molecules leading to notable increase in water emissions, rendering it observable by the detector. Additionally, hydrogen exhibits a peak at approximately 6.4 µm and 12.3 µm cavity length corresponding to light at 855 cm^{-1} (SI Fig. S7.14). Though not as pronounced, a similar feature is observed across all ROIs for hydrocarbon flames, but often disguised by the ethylene or blackbody interference and only visible as a shoulder. This is aligned with water emission lines predicted by [49] (SI Fig. S13.1) and is further supported by the observation of lines at 904 cm^{-1}, 964 cm^{-1}, and 1016 cm^{-1} (11.5 µm, 10.8 µm, and 10.2 µm cavity length, respectively) in the remapped hydrogen interferogram.

The analysis of the various ROIs reveals significant differences in spectral characteristics and intensity between distinct regions of the flame. K-means clustering was applied to the hyperspectral images, utilizing four clusters to segment talhe flames into distinct regions based on the interferogram at each pixel (SI, Fig. S8.1). This analysis demonstrates that the flames

can be segmented into specific regions in an unsupervised manner based on their spectral profiles. However, the spatial component of the hyperspectral data cubes has not been extensively incorporated into the present study. Previous research has utilized monochrome and RGB color images for detecting flame fronts [50] and texture for analysis [51]. Integrating spatial information into the analysis could facilitate the automatic identification of reaction zones within the flames.

4.3 Evaluation of Discrimination Potential by Pearson Correlation Analysis

Conventional spectroscopic analysis focuses on key feature extraction of the data set by selecting specific band regions to confirm or rule out presence of specific molecular species. While the simplest decoder for measured flame interferograms is comparison with theoretical bands expected for fuel molecules (SI, Tab. S9.1), no definite traces of fuel gas were identified in the data set (SI, Tab. S8.1). Whereas visual inspection of Fig. 5 reveals flame signatures and regions applicable (e.g. 900-800 cm^{-1}) for fuel identification, this approach does not fully utilize the multidimensional nature of the data set. To leverage the valuable information in light from overlapping orders and distinguish between various gas flames, the complete interferogram is instead utilized in the Pearson correlation coefficient analysis. The remapped interferograms primarily serve an interpretive tool as the Pearson correlation coefficient is not influenced by the amplitudes of the interferograms and only assesses their shapes. Another common approach for evaluating spectral similarity and differentiability is the application of principal component analysis (PCA). In this work, PCA was performed on the extracted averaged interferograms for each ROI, as presented in SI S10. PCA identifies the directions of maximum variance in the data, which can be used to analyze the relationship between the samples. Despite its utility, this study employs the Pearson correlation coefficient as the primary metric for spectral similarity due to its simplicity and ease of interpretation.

ROIs I and II are where the most significant differences among fuel gases are found. In ROI I, the overall average ρ is 0.82 (Fig. 6a and 6b). Methane, ethylene, and hydrogen emerge as the most dissimilar, with average ρ of 0.71, 0.70, and 0.82, respectively. Methane stands out, mainly because it lacks the peaks at 5.6 µm and 10.8 µm cavity length (corresponding to 970 cm^{-1} in remapped interferogram) (SI Fig. S7.1 and S7.8) – the same feature which originates from ethylene (SI Fig. S7.6 and S7.13). This feature is also missing from the hydrogen interferograms, which explains the relatively low $\rho = 0.65$ between ethylene and hydrogen.

Conversely, ethane, propane, and butane are aligned closely in shape, with average ρ of 0.90, 0.89, and 0.88, respectively.

In ROI II, the largest blackbody contributions were detected (as discussed in section 4.2) Notably, butane and acetylene exhibit considerable blackbody contribution makes the interferograms stand out, resulting in an average ρ of 0.81 and 0.72, respectively, which are the lowest in this ROI. The evidence that ROI III exclusively contains combustion reaction products (discussed in section 4.2) is reinforced by the high average Pearson correlation coefficient of 0.91 for all hydrocarbons. It is inferred that above the flame, primarily H_2O and CO_2 are present, while only H_2O is present in the case of hydrogen, with an average ρ of 0.71. Altogether, the preliminary correlation analysis on a data set of non-idealized flames demonstrates proof-on-concept, and that the introduced novel SFPI-upgraded low-cost thermal camera can potentially function as a basic flame spectrometer.

4.4 Perspectives

While SNR is inherently high for flames, one of the primary limitations of the current imaging system is the 8 seconds acquisition time for a data cube. The long acquisition time increases susceptibility to flame turbulence. However, this issue can be mitigated through software and hardware upgrades, potentially reducing the sampling time and improving data quality. The hyperspectral capabilities are derived from the SFPI and are largely independent of the detector, provided the detector is sensitive within the spectral range for which the mirrors are designed (8–15 µm). Consequently, the SFPI could be readily transferred to an alternative platform to achieve improved SNR and temporal resolution.

Another potential improvement involves performing a comprehensive radiometric calibration, enabling flame temperature estimation. Different fuels exhibit varying emissivities, implying that identical heat fluxes from two different fuels may originate from significantly different temperatures. If the system is capable of identifying the fuel type based on spectral signatures, it could subsequently apply a temperature model tailored to the detected fuel type. This approach would also facilitate the determination of temperatures in fuel mixtures, as the contributions from different fuel types vary depending on both their concentration and temperature.

5 CONCLUSION

This work demonstrates the potential of hyperspectral imaging as a diagnostic tool for fire safety sciences, providing new insights into the spectral behavior of hydrocarbon flames and enabling the rapid identification of fuel types.

In this study, hyperspectral images of flames from seven different gaseous fuels (methane, ethane, propane, butane, ethylene, acetylene, and hydrogen) were acquired using a hyperspectral LWIR imager, made by integrating a scanning Fabry-Pérot interferometer with a microbolometer-based thermal camera. Three distinct reaction zones within the flames were identified, each exhibiting unique spectral signatures. Ethylene was consistently observed as an intermediate combustion product for all tested hydrocarbons, except for methane and acetylene. Additionally, several rotational and vibrational transitions of water vapor were detected across all samples, alongside significant contributions from CO_2 emissions in all hydrocarbon flames.

This study successfully demonstrates the capabilities of hyperspectral LWIR imaging developed on top of an ordinary thermal camera for characterizing flames. The combination of high spatial resolution and detailed spectral information provides valuable insights, allowing for the identification of distinct reaction zones within the flame, beyond what is feasible with traditional single-point measurements.

6 CONFLICTS OF INTEREST

Newtec (i.e. MNL, ALJ, & BJ) declares interest in commercial exploitation of the work reported in this paper. IHB and JKH declare to have no conflicts of interest.

7 ACKNOWLEGDEMENTS

This work is partly funded by Innovation Fund Denmark (grant no. 1044-00116B).

8 CRediT

Mads Nibe Larsen (ORCID: 0000-0002-5412-6325): Conceptualization, Methodology, Investigation, Formal analysis, Investigation, Data curation, Software, Writing - Original Draft, Writing - Review & Editing, Visualization. **Iben Hansen-Bruhn** (ORCID: 0000–0002–5465–7484): Conceptualization, Methodology, Formal Analysis, Investigation, Writing – Review & Editing. **Anders Løchte Jørgensen** (ORCID: 0000-0001-9741-2025): Writing - Review & Editing. **Jakob Kjelstrup-Hansen** (ORCID: 0000-0003-4482-4979): Supervision, Funding acquisition, Project administration, Writing - Review & Editing. **Bjarke Jørgensen** (ORCID: 0000-0001-8559-9435): Conceptualization, Supervision, Funding acquisition, Project administration, Writing - Review & Editing.

9 REFERENCES

[1] Hernandez, R., & Ballester, J. (2008). Flame imaging as a diagnostic tool for industrial combustion. *Combustion and Flame*, *155*(3), 509-528.

[2] Smith, C. M., & Hoehler, M. S. (2018). Imaging through fire using narrow-spectrum illumination. *Fire Technology*, *54*(6), 1705-1723.

[3] Kim, K. S., Jung, S., & Kwon, S. (2022). Optical visualization of hypergolic burning spray structure using blue light spectrum. *Acta Astronautica*, *193*, 230-236.

[4] O'Brien, J. J., Loudermilk, E. L., Hornsby, B., Hudak, A. T., Bright, B. C., Dickinson, M. B., ... & Ottmar, R. D. (2015). High-resolution infrared thermography for capturing wildland fire behaviour: RxCADRE 2012. *International Journal of Wildland Fire*, *25*(1), 62-75.

[5] Wang, J., Roudini, S., Hyer, E. J., Xu, X., Zhou, M., Garcia, L. C., ... & Da Silva, A. M. (2020). Detecting nighttime fire combustion phase by hybrid application of visible and infrared radiation from Suomi NPP VIIRS. *Remote Sensing of Environment*, *237*, 111466.

[6] Paugam, R., Wooster, M. J., & Roberts, G. (2012). Use of handheld thermal imager data for airborne mapping of fire radiative power and energy and flame front rate of spread. *IEEE Transactions on Geoscience and Remote Sensing*, *51*(6), 3385-3399.

[7] Roy, D. P., Boschetti, L., & Trigg, S. N. (2006). Remote sensing of fire severity: assessing the performance of the normalized burn ratio. *IEEE Geoscience and Remote Sensing Letters*, *3*(1), 112-116.

[8] Johnston, J. M., Wooster, M. J., & Lynham, T. J. (2014). Experimental confirmation of the MWIR and LWIR grey body assumption for vegetation fire flame emissivity. *International Journal of Wildland Fire*, *23*(4), 463-479.

[9] Meléndez, J., & Guarnizo, G. (2021). Multispectral Mid-Infrared Camera System for Accurate Stand-Off Temperature and Column Density Measurements on Flames. *Sensors*, *21*(24), 8395.

[10] Àgueda, A., Pastor, E., Pérez, Y., & Planas, E. (2010). Experimental study of the emissivity of flames resulting from the combustion of forest fuels. *International Journal of Thermal Sciences*, *49*(3), 543-554.

[11] Socrates, G. (2004). *Infrared and Raman characteristic group frequencies: Tables and charts*. John Wiley & Sons.

[12] Cheng, Y., Tian, C., & Huang, Z. (2023). Three-dimensional reconstruction of flame temperature and H_2O concentration using water vapor integrated spectral band emission. *Journal of Quantitative Spectroscopy and Radiative Transfer*, *294*, 108404.

[13] Smith, E. C. W. (1940). The emission spectrum of hydrocarbon flames. *Proceedings of the Royal Society of London. Series A. Mathematical and Physical Sciences*, *174*(956), 110-125.

[14] Gaydon, A. (2012). *The spectroscopy of flames*. Springer science & business media.

[15] Veraverbeke, S., Dennison, P., Gitas, I., Hulley, G., Kalashnikova, O., Katagis, T., ... & Stavros, N. (2018). Hyperspectral remote sensing of fire: State-of-the-art and future perspectives. *Remote Sensing of Environment*, *216*, 105-121.

[16] Scafutto, R. D. P. M., & de Souza Filho, C. R. (2019). Detection of heavy hydrocarbon plumes (Ethane, propane and Butane) using airborne longwave (7.6–13.5 μm) infrared hyperspectral data. *Fuel*, *242*, 863-870.

[17] de Souza Filho, C. R., & Scafutto, R. D. (2024). A Comprehensive Compilation of Spectral Libraries for Petroleum Hydrocarbons (PHC) Encompassing VNIR-SWIR-TIR Ranges. *Scientific Data*, *11*(1), 1073.

[18] Qiu, X., Xi, T., Sun, D., Zhang, E., Li, C., Peng, Y., ... & Wang, G. (2018). Fire detection algorithm combined with image processing and flame emission spectroscopy. *Fire Technology*, *54*, 1249-1263.

[19] Piscini, A., & Amici, S. (2015, October). Fire detection from hyperspectral data using neural network approach. In *Remote Sensing for Agriculture, Ecosystems, and Hydrology XVII* (Vol. 9637, pp. 287-294). SPIE.

[20] Lai, Y., Liu, X., Davies, M., Fisk, C., Holliday, M., King, D., ... & Willmott, J. (2024). Characterisation of wood combustion and emission under varying moisture contents using multiple imaging techniques. *Fuel*, *373*, 132397.

[21] Xie, J., Paldus, B. A., Wahl, E. H., Martin, J., Owano, T. G., Kruger, C. H., ... & Zare, R. N. (1998). Near-infrared cavity ringdown spectroscopy of water vapor in an atmospheric flame. *Chemical Physics Letters*, *284*(5-6), 387-395.

[22] Ren, T., Li, H., Modest, M. F., & Zhao, C. (2021). Efficient two-dimensional scalar fields reconstruction of laminar flames from infrared hyperspectral measurements with a machine learning approach. *Journal of Quantitative Spectroscopy and Radiative Transfer*, *271*, 107724.

[23] Rawlins, W. T., Lawrence, W. G., Marinelli, W. J., Allen, M. G., & Piltch, N. (2001, January). Hyperspectral infrared imaging of flames using a spectrally scanning fabry-perot filter. In *2nd Joint Meeting of the US Sections of the Combustion Institute* (No. SR-1063).

[24] Hsu, P. S., Lauriola, D., Jiang, N., Miller, J. D., Gord, J. R., & Roy, S. (2017). Fiber-coupled, UV–SWIR hyperspectral imaging sensor for combustion diagnostics. *Applied Optics*, *56*(21), 6029-6034.

[25] Atherton, P. D., Reay, N. K., Ring, J., & Hicks, T. R. (1981). Tunable fabry-perot filters. *Optical Engineering*, *20*(6), 806-814.

[26] https://hinalea.ai, accessed 27/11/2024.

[27] Kuhn, J., Bobrowski, N., Lübcke, P., Vogel, L., & Platt, U. (2014). A Fabry–Perot interferometer-based camera for two-dimensional mapping of SO 2 distributions. *Atmospheric Measurement Techniques*, *7*(11), 3705-3715.

[28] Jørgensen, A. L., Larsen, M. N., Petrunin, V., Kjelstrup-Hansen, J., & Jørgensen, B. (2022). Surface temperature determination using long range thermal emission spectroscopy based on a first order scanning Fabry-Pérot interferometer. *Optics Express*, *30*(2), 2186-2196.

[29] Larsen, M. N., Jørgensen, A. L., Petrunin, V., Kjelstrup-Hansen, J., Jørgensen, B., & Hinge, M. (2024). Classification of black plastic types by hyperspectral imaging based on long-wave infrared emission spectroscopy. *Polymer Testing*, *141*, 108629.

[30] Centurioni, E. (2005). Generalized matrix method for calculation of internal light energy flux in mixed coherent and incoherent multilayers. *Applied optics*, *44*(35), 7532-7539 [https://doi.org/10.1364/AO.44.007532]

[31] Gordon, I. E., Rothman, L. S., Hargreaves, E. R., Hashemi, R., Karlovets, E. V., Skinner, F. M., ... & Yurchenko, S. N. (2022). The HITRAN2020 molecular spectroscopic database. *Journal of Quantitative Spectroscopy and Radiative Transfer*, *277*, 107949. [doi:10.1016/j.jqsrt.2021.107949]

[32] Coblentz Society, Inc., "Evaluated Infrared Reference Spectra" in *NIST Chemistry WebBook*, NIST Standard Reference Database Number 69, Eds. P.J. Linstrom and W.G. Mallard, National Institute of Standards and Technology, Gaithersburg MD, 20899 [https://doi.org/10.18434/T4D303]

[33] Xie, J., Paldus, B. A., Wahl, E. H., Martin, J., Owano, T. G., Kruger, C. H., ... & Zare, R. N. (1998). Near-infrared cavity ringdown spectroscopy of water vapor in an atmospheric flame. *Chemical Physics Letters*, *284*(5-6), 387-395.

[34] Schefer, R. W., Kulatilaka, W. D., Patterson, B. D., & Settersten, T. B. (2009). Visible emission of hydrogen flames. *Combustion and Flame*, *156*(6), 1234-1241.

[35] Scafutto, R. D. P. M., & de Souza Filho, C. R. (2019). Detection of heavy hydrocarbon plumes (Ethane, propane and Butane) using airborne longwave (7.6–13.5 μm) infrared hyperspectral data. *Fuel*, *242*, 863-870.

[36] Tolchenov, R. N., Tennyson, J., Brault, J. W., Canas, A. A. D., & Schermaul, R. (2002). Weak line water vapor spectrum in the 11 787–13 554 cm− 1 region. *Journal of Molecular Spectroscopy*, *215*(2), 269-274.

[37] Bernath, P. F. (2002). The spectroscopy of water vapour: Experiment, theory and applications. *Physical Chemistry Chemical Physics*, *4*(9), 1501-1509.

[38] Carleer, M., Jenouvrier, A., Vandaele, A. C., Bernath, P. F., Merienne, M. F., Colin, R., ... & Savin, V. A. (1999). The near infrared, visible, and near ultraviolet overtone spectrum of water. *The Journal of Chemical Physics*, *111*(6), 2444-2450.

[39] Ballester, J., & García-Armingol, T. (2010). Diagnostic techniques for the monitoring and control of practical flames. *Progress in Energy and Combustion Science*, *36*(4), 375-411.

[40] Hernandez, R., & Ballester, J. (2008). Flame imaging as a diagnostic tool for industrial combustion. *Combustion and Flame*, *155*(3), 509-528.

[41] Plyler, E. K., & Plyler, B. E. K. (1948). Infrared radiation from a bunsen flame. *J. Res. Nat. Bur. Stand*, *40*, 113.

[42] Plyler, E. K. (1948). The Infrared Emission Spectra of CO_2 and H_2O Molecules. *Science*, *107*(2767), 48-48.

[43] DiStasio Jr, R. J., & Resmini, R. G. (2010, May). Atmospheric compensation of thermal infrared hyperspectral imagery with the emissive empirical line method and the in-scene atmospheric compensation algorithms: a comparison. In *Algorithms and Technologies for Multispectral, Hyperspectral, and Ultraspectral Imagery XVI* (Vol. 7695, pp. 805-816). SPIE [https://doi-org.proxy1-bib.sdu.dk/10.1117/12.849898]

[44] Ottesen, D. K., & Stephenson, D. A. (1982). Fourier transform infrared (FT-IR) measurements in sooting flames. *Combustion and Flame*, *46*, 95-104.

[45] Zheng, S., Zhang, M., Yang, Y., Na, M., & Lu, Q. (2024). Simultaneous reconstruction of temperature and concentration of H2O and soot based on infrared emission spectrum by inverse analysis. *International Journal of Thermal Sciences*, *195*, 108641.

[46] Bernath, P. F. (2000). 6 Infrared emission spectroscopy. *Annual Reports Section" C"(Physical Chemistry)*, *96*, 177-224.

[47] Drysdale, D. (2011). *An Introduction to Fire Dynamics*. John Wiley & Sons.

[48] Lindstedt, R. P., & Skevis, G. (1997). Chemistry of acetylene flames. *Combustion Science and Technology*, *125*(1-6), 73-137 [https://doi.org/10.1080/00102209708935656].

[49] Kochanov, R. V., Gordon, I. E., Rothman, L. S., Wcisło, P., Hill, C., & Wilzewski, J. S. (2016). HITRAN Application Programming Interface (HAPI): A comprehensive approach to working with spectroscopic data. *Journal of Quantitative Spectroscopy and Radiative Transfer*, *177*, 15-30.

[50] Strässle, R.M., Faldella, F. & Doll, U. (2024) Deep learning-based image segmentation for instantaneous flame front extraction. *Exp Fluids* **65**, 94. https://doi.org/10.1007/s00348-024-03814-z

[51] Emmy Prema, C., Vinsley, S.S. & Suresh, S. (2018) Efficient Flame Detection Based on Static and Dynamic Texture Analysis in Forest Fire Detection. *Fire Technol* **54**, 255–288. https://doi.org/10.1007/s10694-017-0683-x

Supporting Information (SI): Signatures of Flames by Long-Wave Infrared Hyperspectral Imaging

Mads Nibe Larsen[†,‡], Iben Hansen-Bruhn[£], Anders Løchte Jørgensen[‡], Bjarke Jørgensen[‡], Jakob Kjelstrup-Hansen[†,*]

[†]NanoSYD, Mads Clausen Institute, University of Southern Denmark, 6400 Sønderborg, Denmark
[‡]Newtec Engineering A/S, 5230 Odense, Denmark.
[£]DBI - The Danish Institute of Fire and Security Technology, 2650 Hvidovre, Denmark.
*Corresponding author

CONTENT

S1. SPECTRAL FILTER TRANSMISSION 2
S2. EFFECT OF OFFSET CORRECTION 3
S3. EFFECT OF SPECTRAL SHIFT CORRECTION 4
S4. EFFECT OF SPECTRAL CALIBRATION 5
S5. SYSTEM RESPONSE MATRIX 6
S6. K-means on hyperspectral images of flames 7
S7. EXTRACTED FLAME INTERFEROGRAMS 8
S8. PRINCIPAL COMPONENT ANALYSIS 20
S9. EXTRACTED FEATURES FOR EACH FLAME SPECTRUM 16
S10. SPECTRAL FEATURES OF FUEL GAS IN THE LWIR REGION 19
S11. ACETYLENE AND BLACK BODY INTERFEROGRAMS 23
S12. CARBON DIOXIDE ABSORBANCE SPECTRUM 24
S13. HIGH TEMPERATURE WATER ABSORPTION SPECTRUM 25
S14. REFERENCES 26

S1. SPECTRAL FILTER TRANSMISSION

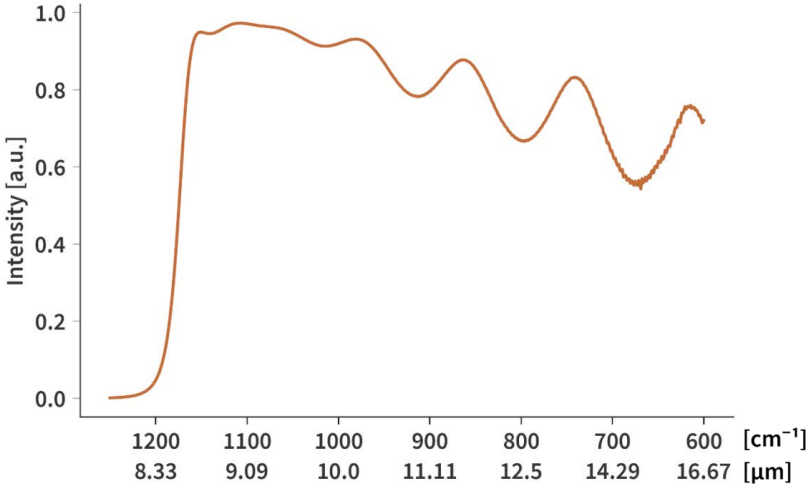

Figure S1.1: Transmission spectrum of long-wave pass filter measured on a Perkin Elmer Spectrum 65 FTIR spectrometer.

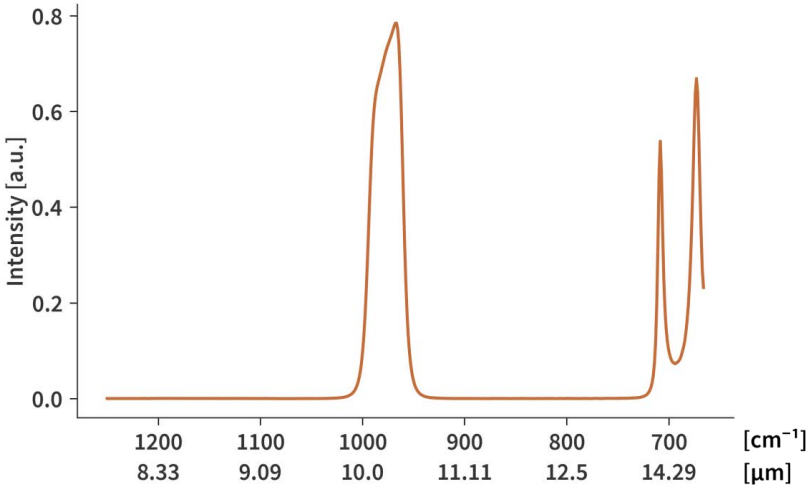

Figure S1.2: Transmission spectrum of 10.26 µm band pass filter measured on a Perkin Elmer Spectrum 65 FTIR spectrometer.

S2. EFFECT OF OFFSET CORRECTION

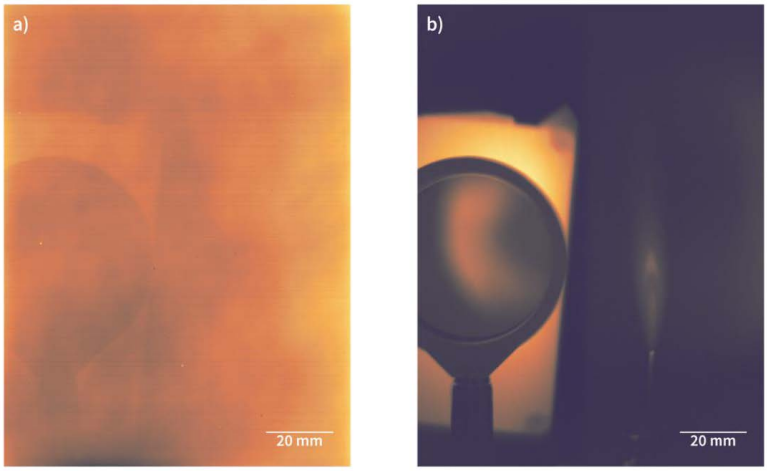

Figure S2.1: a) Image of propane at 5.6 µm cavity length before offset correction. b) Same image as in a) but after offset correction.

S3. EFFECT OF SPECTRAL SHIFT CORRECTION

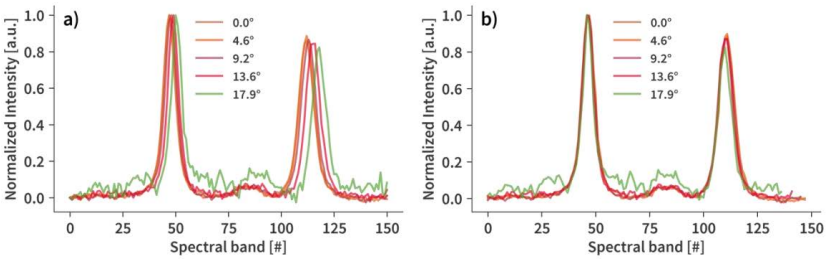

Figure S3.1: Normalized 5×5-pixel averages at different positions across the detector. The data cube shows a 60 ºC hotplate imaged through a 10.26 µm bandpass filter (a) before and (b) after correction of the spectral axis due to spectral shift caused by change in incidence angle.

S4. EFFECT OF SPECTRAL CALIBRATION

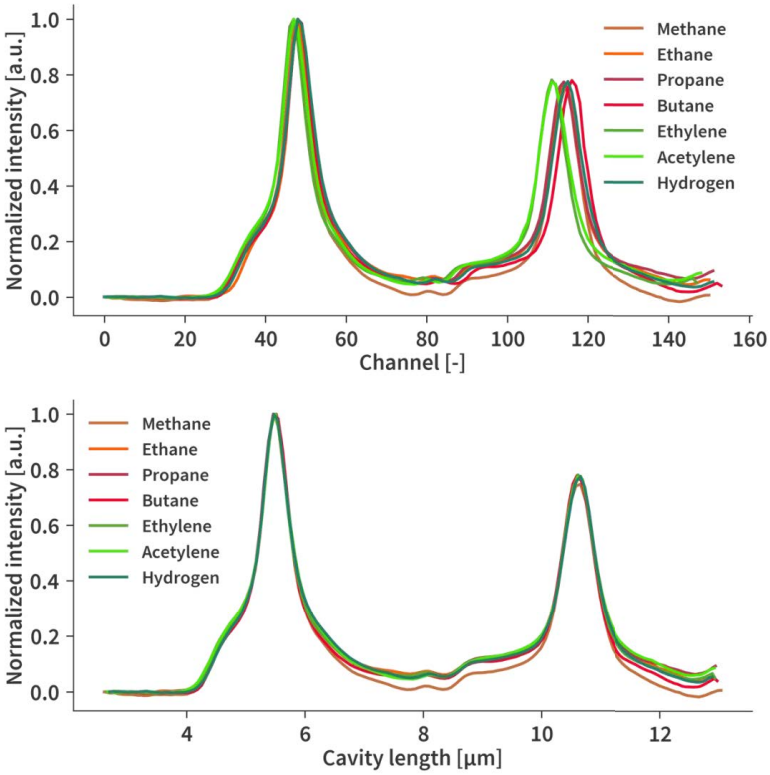

Figure S4.1: Normalized interferograms of the bandpass filter (ROI IV) used for spectral alignment in each of the data cubes.

S5. SYSTEM RESPONSE MATRIX

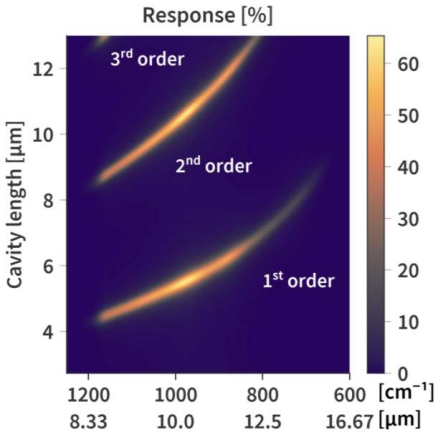

Figure S5.1: System matrix describing the relationship between the wavelength (first axis), the cavity length (second axis) and the system response (transmission through SFPI as well as the detector and long-wave pass filter response).

S6. K-means on hyperspectral images of flames

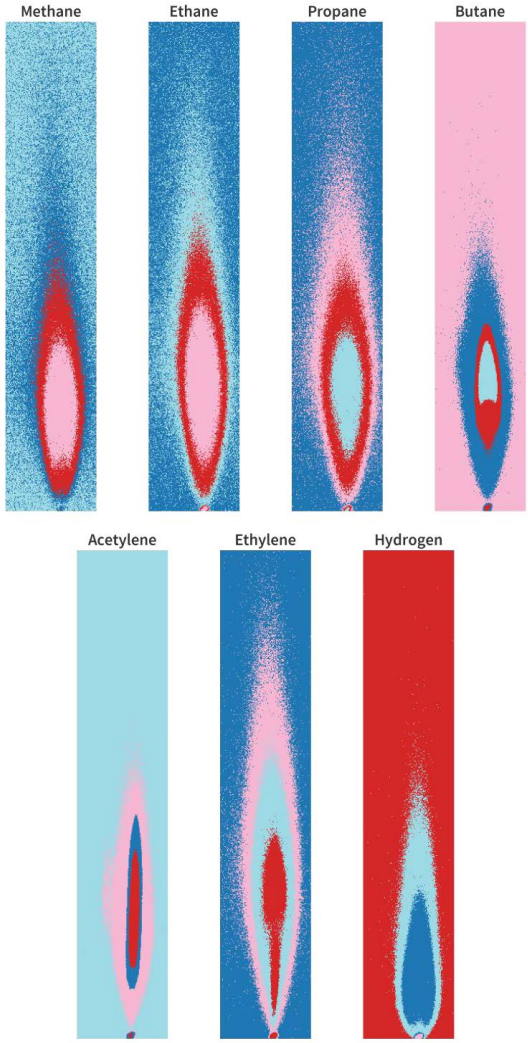

Figure S6.1: K-means using k=4 clusters to divide flames into regions based on the interferogram in each pixel of the hyperspectral images.

S7. EXTRACTED FLAME INTERFEROGRAMS

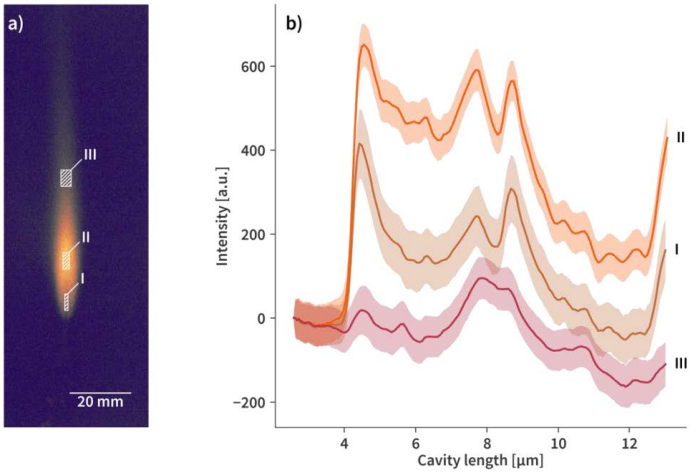

Figure S7.1: a) Methane at 8.0 µm cavity length. b) Mean interferograms (ROI I to III) as a function of cavity length for the entire data cube. Lighter shades mark 1 standard deviation.

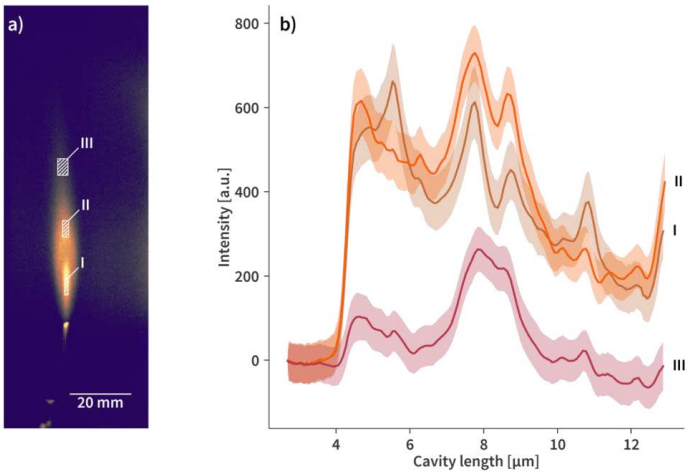

Figure S7.2: a) Ethane at 5.6 µm cavity length. b) Mean interferograms (ROI I to III) as a function of cavity length for the entire data cube. Lighter shades mark 1 standard deviation.

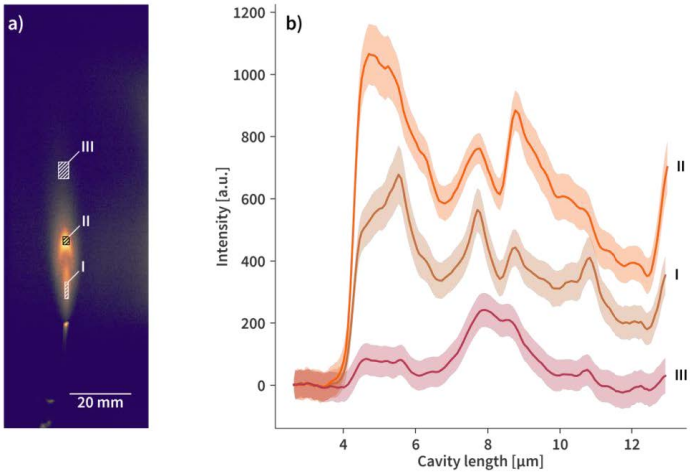

Figure S7.3: a) Propane at 5.6 µm cavity length. b) Mean interferograms (ROI I to III) as a function of cavity length for the entire data cube. Lighter shades mark 1 standard deviation.

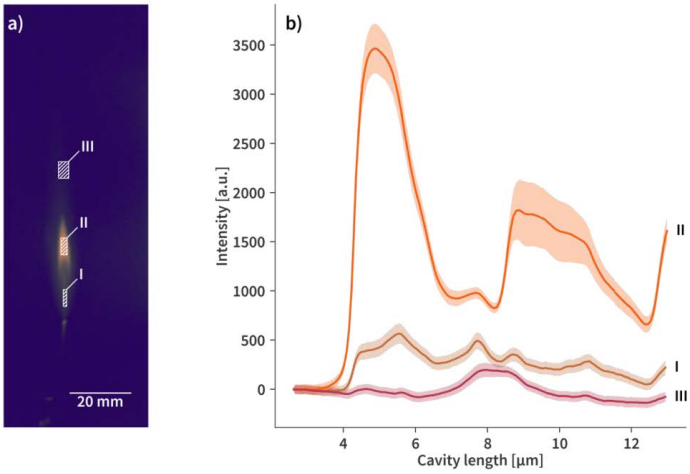

Figure S7.4: a) Butane at 6.0 µm cavity length. b) Mean interferograms (ROI I to III) as a function of cavity length for the entire data cube. Lighter shades mark 1 standard deviation.

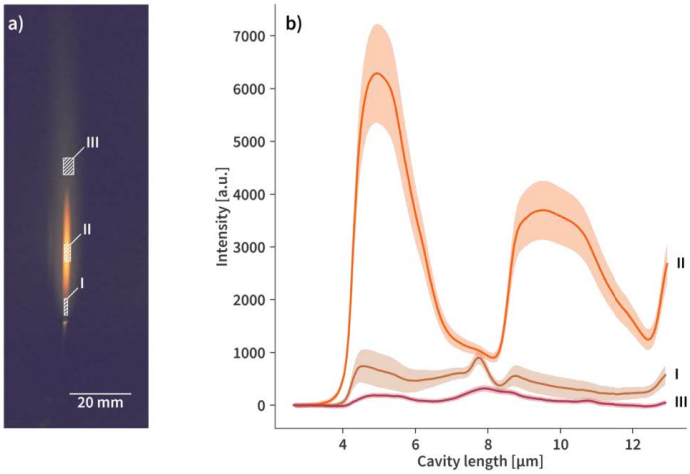

Figure S7.5: a) Acetylene at 8.5 µm cavity length. b) Mean interferograms (ROI I to III) as a function of cavity length for the entire data cube. Lighter shades mark 1 standard deviation.

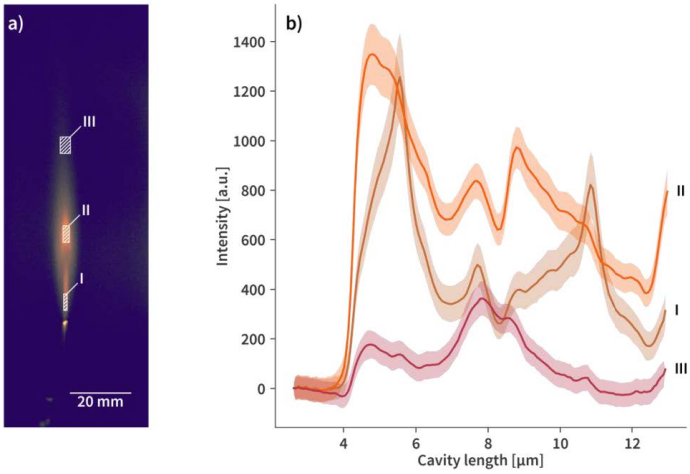

Figure S7.6: a) Ethylene at 6.1 µm cavity length. b) Mean interferograms (ROI I to III) as a function of cavity length for the entire data cube. Lighter shades mark 1 standard deviation.

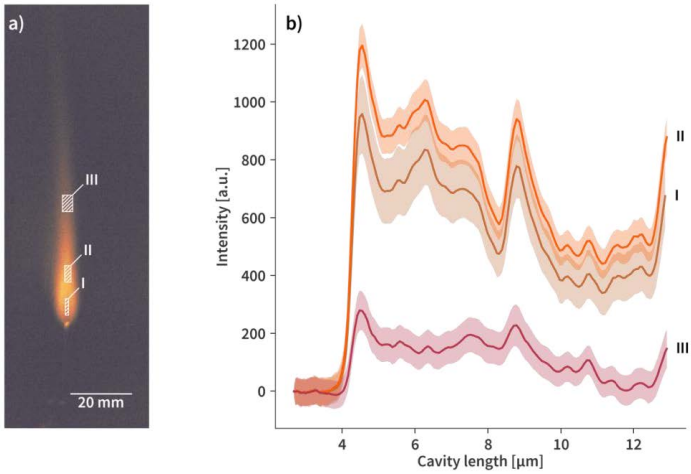

Figure S7.7: a) Hydrogen at 8.3 µm cavity length. b) Mean interferograms (ROI I to III) as a function of cavity length for the entire data cube. Lighter shades mark 1 standard deviation.

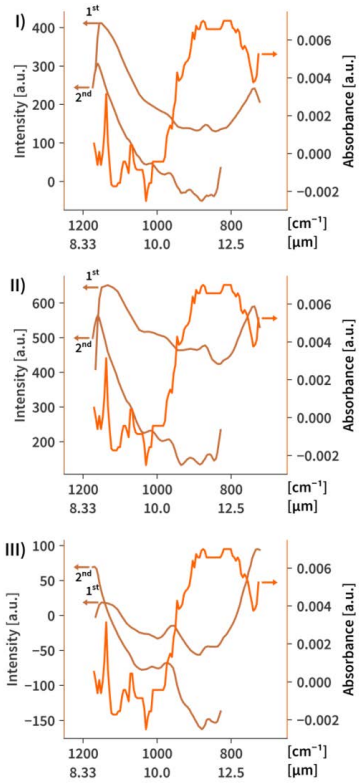

Figure S7.8: Translated methane interferograms onto wavenumber/wavelength axis for regions I, II, and III in a), b), and c), respectively. The orange curve shows the FTIR absorbance spectrum of methane [SI-R1]

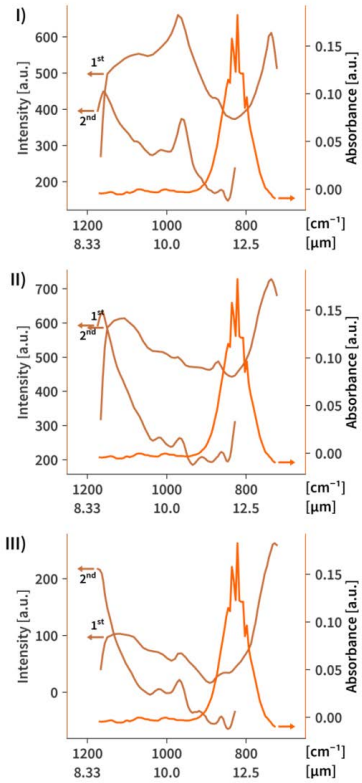

Figure S7.9: Translated ethane interferograms onto wavenumber/wavelength axis for regions I, II, and III in a), b), and c), respectively. The orange curve illustrates the FTIR absorbance spectrum of ethane [SI-R1].

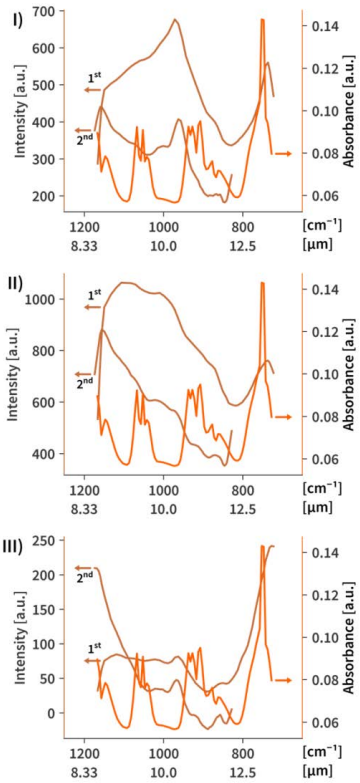

Figure S7.10: Translated propane interferograms onto wavenumber/wavelength axis for regions I, II, and III in a), b), and c), respectively. The orange curve illustrates the FTIR absorbance spectrum of propane [SI-R1].

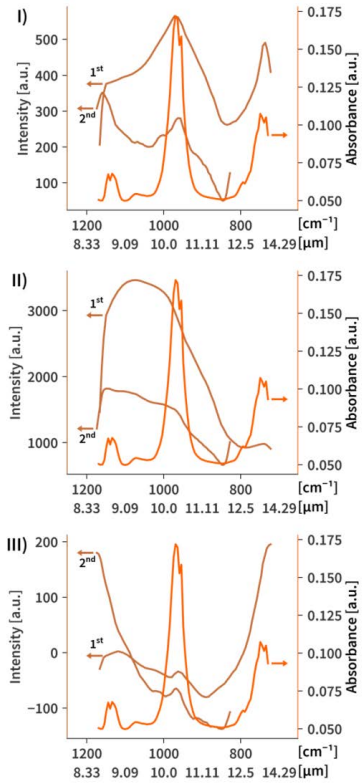

Figure S7.11: Translated butane interferograms onto wavenumber/wavelength axis for regions I, II, and III in a), b), and c), respectively. The orange curve illustrates the FTIR absorbance spectrum of butane [SI-R1].

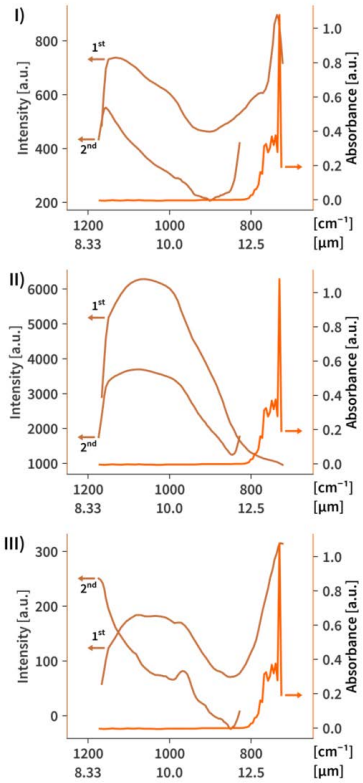

Figure S7.12: Translated acetylene interferograms onto wavenumber/wavelength axis for regions I, II, and III in a), b), and c), respectively. The orange curve illustrates the corresponding FTIR absorbance spectrum [SI-R1].

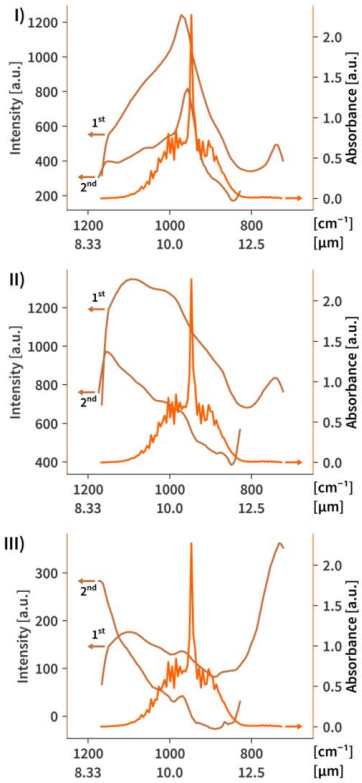

Figure S7.13: Translated ethylene interferograms onto wavenumber/wavelength axis for regions I, II, and III in a), b), and c), respectively. The orange curve illustrates the corresponding FTIR absorbance spectrum [SI-R1].

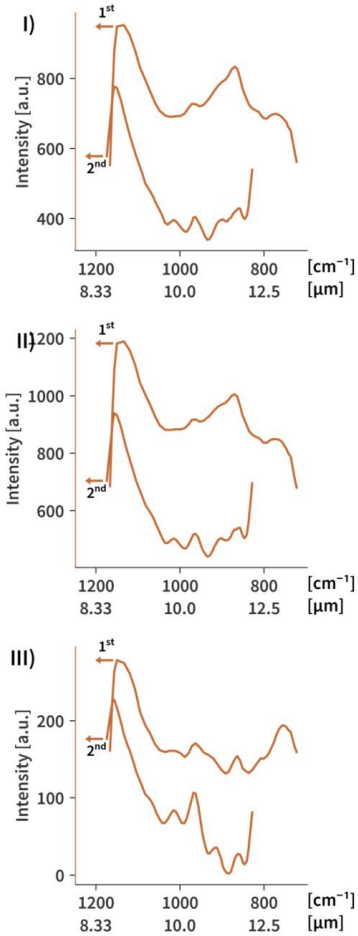

Figure S7.14: Translated hydrogen interferograms into wavenumber/wavelength axis for regions I, II, and III in a), b), and c), respectively. The orange curve illustrates the corresponding FTIR absorbance spectrum [SI-R1].

S8. EXTRACTED FEATURES FOR EACH FLAME SPECTRUM

Methane		Peaks								Shoulders				
Region I	Cavity length [μm]	4.5	6.4	7.8	8.7	10.2	10.8	11.5		5.5	5.9			
	Wavenumber [1/cm]	1148 ±29	863 ±23	737 ±16	1160 ±14	1016 ±19	964 ±18	909 ±16		979 ±30	919 ±32			
Region II	Cavity length [μm]	4.6	6.3	7.8	8.7	10.2	10.8	11.5	12.2	5.3	5.9	9.5		
	Wavenumber [1/cm]	1132 ±32	870 ±23	737 ±16	1160 ±14	1016 ±19	964 ±18	909 ±16	858 ±13	997 ±33	919 ±32	1076 ±18		
Region III	Cavity length [μm]	4.5	5.7	7.9	10.2	10.7	12.2			5.0	6.4	8.6	9.5	11.5
	Wavenumber [1/cm]	1148 ±29	952 ±31	727 ±15	1010 ±19	969 ±18	858 ±13			1058 ±33	857 ±22	1169 ±11	1083 ±18	904 ±16
Ethane														
Region I	Cavity length [μm]	5.6	7.8	8.8	10.9	12.2				4.3	5.8	9.3	10.3	11.5
	Wavenumber [1/cm]	970 ±30	737 ±16	1156 ±16	959 ±18	863 ±13				1166 ±16	942 ±32	1097 ±18	1003 ±19	904 ±16
Region II	Cavity length [μm]	4.7	6.3	7.8	8.7	10.2	10.8	11.5	12.2	5.0	5.7	9.6		
	Wavenumber [1/cm]	1106 ±32	870 ±23	737 ±16	1160 ±14	1016 ±19	964 ±18	909 ±16	863 ±13	1058 ±33	952 ±31	1069 ±18		
Region III	Cavity length [μm]	4.7	5.6	7.9	10.2	10.8	11.4	12.2		5.1	6.4	8.5		
	Wavenumber [1/cm]	1118 ±33	963 ±30	727 ±15	1016 ±19	964 ±18	914 ±17	858 ±13		1034 ±35	863 ±23	1174 ±13		
Propane														
Region I	Cavity length [μm]	5.6	7.8	8.8	10.9					4.3	6.2	9.5	10.4	11.5
	Wavenumber [1/cm]	970 ±30	737 ±31	1156 ±16	959 ±18					1166 ±16	876 ±24	1076 ±18	991 ±18	909 ±16
Region II	Cavity length [μm]	4.8	7.8	8.8	10.2	12.1				5.3	6.2	9.5	10.6	
	Wavenumber [1/cm]	1094 ±32	737 ±16	1156 ±16	1016 ±19	867 ±13				1008 ±35	876 ±24	1083 ±18	974 ±18	
Region III	Cavity length [μm]	4.7	5.6	6.5	7.9	8.6	10.2	10.8	12.3	11.3				
	Wavenumber [1/cm]	1118 ±33	963 ±30	851 ±23	727 ±15	1169 ±12	1010 ±19	964 ±18	854 ±13	919 ±17				

Butane		Peaks					Shoulders			
Region I	Cavity length [µm]	5.6	7.8	8.8	10.9		4.6	10.3	11.5	
	Wavenumber [1/cm]	970 ±30	737 ±16	1156 ±16	959 ±18		1132 ±32	1003 ±19	904 ±16	
Region II	Cavity length [µm]	4.9	7.8	8.9			9.5	10.6		
	Wavenumber [1/cm]	1069 ±33	737 ±16	1142 ±18			1083 ±18	980 ±18		
Region III	Cavity length [µm]	4.7	5.6	8.0	8.6	10.8	5.1	9.3	10.2	11.5
	Wavenumber [1/cm]	1118 ±33	963 ±30	722 ±14	1169 ±12	964 ±18	1034 ±35	1104 ±18	1010 ±19	909 ±16
Acetylene										
Region I	Cavity length [µm]	4.6	7.8	8.8			5.2	7.3		
	Wavenumber [1/cm]	1132 ±32	737 ±16	1156 ±16			1021 ±35	776 ±18		
Region II	Cavity length [µm]	5.0	9.6				11.6			
	Wavenumber [1/cm]	1058 ±33	1069 ±18				898 ±15			
Region III	Cavity length [µm]	4.9	5.6	8.0	10.8		8.5	9.5	11.3	
	Wavenumber [1/cm]	1069 ±33	970 ±30	722 ±14	964 ±18		1174 ±13	1083 ±18	919 ±17	
Ethylene										
Region I	Cavity length [µm]	5.6	7.8	8.9	10.9		5.0	6.2	9.7	11.7
	Wavenumber [1/cm]	970 ±30	737 ±16	1150 ±18	959 ±18		1058 ±33	876 ±24	1063 ±18	889 ±15
Region II	Cavity length [µm]	4.8	7.7	8.9	12.0		5.2	6.2	9.0	10.8
	Wavenumber [1/cm]	1094 ±32	742 ±16	1150 ±18	872 ±14		1021 ±35	876 ±24	1134 ±19	964 ±18
Region III	Cavity length [µm]	4.8	5.6	7.9	8.6	10.8	6.4	9.3	10.2	
	Wavenumber [1/cm]	1094 ±32	963 ±30	727 ±15	1169 ±12	964 ±18	863 ±23	1104 ±18	1016 ±19	

Hydrogen		Peaks									Shoulders		
Region I	Cavity length [µm]	4.6	5.6	6.3	7.3	8.9	10.2	10.8	11.5	12.2	6.9	9.7	
	Wavenumber [1/cm]	1132 ±32	963 ±30	870 ±23	770 ±17	1150 ±18	1016 ±19	964 ±18	904 ±16	858 ±13	812 ±21	1063 ±18	
Region II	Cavity length [µm]	4.6	5.6	6.3	7.3	8.9	10.2	10.8	11.5	12.2	6.9	9.6	
	Wavenumber [1/cm]	1132 ±32	963 ±30	870 ±23	770 ±17	1150 ±18	1016 ±19	964 ±18	904 ±16	858 ±13	812 ±21	1069 ±18	
Region III	Cavity length [µm]	4.5	5.6	6.4	7.5	8.8	10.2	10.8	11.4	12.2	7.0	8.1	9.6
	Wavenumber [1/cm]	1148 ±29	963 ±30	863 ±23	753 ±17	1156 ±16	1010 ±19	964 ±18	914 ±17	858 ±13	801 ±19	714 ±14	1069 ±18

Table S8.1: Extracted spectral peaks and shoulders from remapped interferograms for each of the three flame ROIs. The uncertainties indicated by ± show the spectral resolution of the SFPI at the given cavity length as defined by half the FWHM of the system.

S9. SPECTRAL FEATURES OF FUEL GAS IN THE LWIR REGION

A summary of fuel hydrocarbon spectral features (i.e. fuel gas, not flames) according to FTIR literature is presented in Table S9.1. In general, table S9.1 shows that straight chain alkanes exhibit doublets at 1175-1120 cm^{-1}, -C-C- skeleton stretch vibrations at 1100-1040 cm^{-1} and rocking vibrations (i.e. CH, CH_2, CH_3) in the region around 900-800 cm^{-1}. Lastly, bending vibrations of C-H for all hydrocarbons are present from 880 to 700 cm^{-1} with one to three bands. These features can to some extent be traced in the flame interferograms (Fig. 5) but remains blended with transmission signal from combustion products, CO_2 and H_2O.

Table S9.1: Spectral features of hydrocarbons in the relevant spectral range [S1-R1].

Range [cm^{-1}]	Ethane, C_2H_6	Propane, C_2H_8	Butane, C_2H_{10}	Ethylene, C_2H_4	Acetylene, C_2H_2	Assign.
1200-1100	1175-1120	1130-1000	1120-1090	1180-1010		CC str ot
1100-1000	1100-1040	1060-900	1110-1080	1010-940	1020-905	CC def str
1000-800			1005-930	980-810	970-890	
900-800	880	925	910-855*	895-885		CH_3 rock
800-700		785-770	745-735	720-680	730-575**	CH_2 rock
700-600				690-610		CH wag

*Doublet, **broad. Str = stretch, ot = overtone, rock = rocking vibration, wag = wagging vibration.

S10. PRINCIPAL COMPONENT ANALYSIS

A principal component analysis (PCA) was conducted on the averaged interferograms from each ROI across all of the data cubes. Standard Normal Variate (SNV) was performed on each averaged interferogram before the PCA. SNV performed on the interferogram I is defined as

$$SNV(I) = \frac{I - \bar{I}}{STD(I)}$$

Where $\bar{I}$ is the mean value of the interferogram and $STD(I)$ is its standard deviation. Each interferogram has been projected onto the first and second principal component (PC) as presented in Fig. S10.1. The percentages in the parentheses indicate the explained variance of the given component. A scree plot is given in Fig. S10.2 showing the explained variance of the first 20 components. At the 21st PCs, the explained variance drops to $\approx 10^{-13}$. The colors in Fig. S10.1 correspond to which region of interest (ROI), the interferogram is taken from, and the fuel type is written next to each point.

A large overlap is observed between ROI I and ROI II, while ROI III (with the exception of hydrogen) is clustered to the lower right. This is expected since ROI III should primarily contain reaction products, which are CO_2 and H_2O for all hydrocarbons, and purely H_2O for hydrogen.

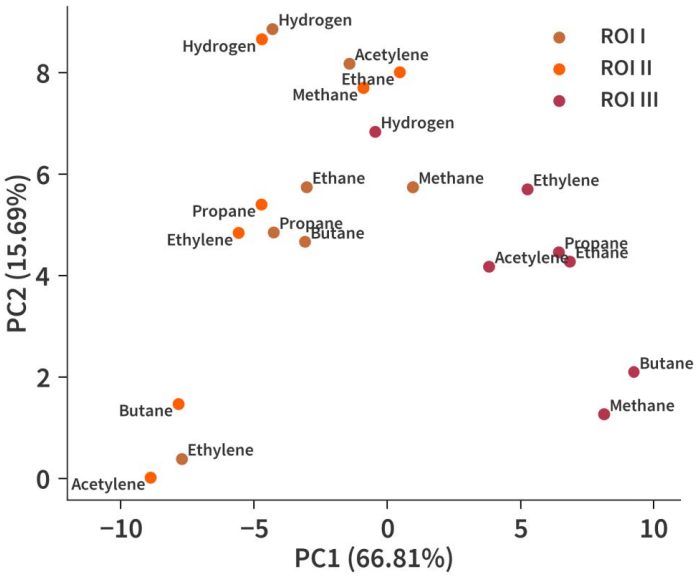

Figure S10.1: Score plot of averaged interferograms from each ROI and for each fuel type.

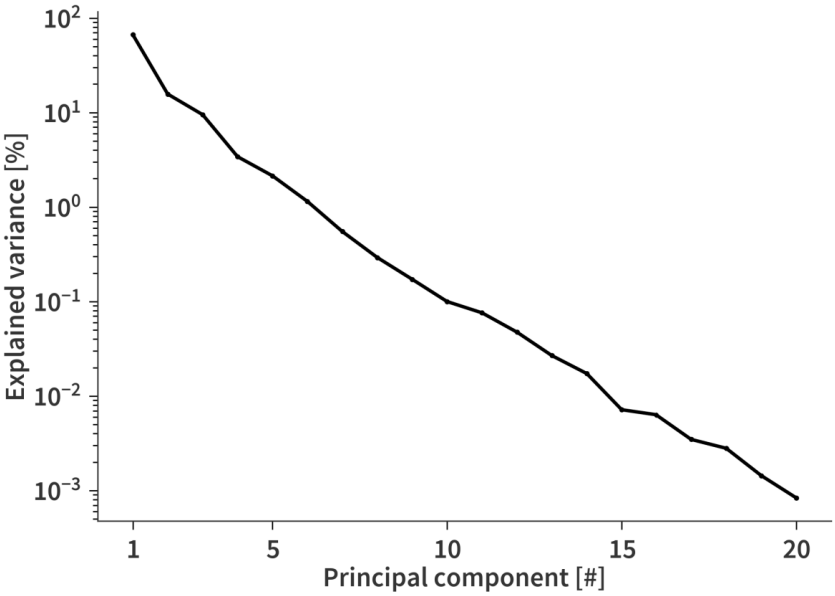

Figure S10.2: Scree plot showing the explained variance of each PC.

Fig. S10.3 show the loadings of the first six PCs. The 7th PC has an explained variance < 1%. The loading of PC1 strongly correlates with the interferograms of ROI III as it is also seen in Fig. S10.1. Additionally, the loadings of PC2 and PC3 are inversely correlated with the ethylene component, which is found in ROI I and II of most of the hydrocarbons.

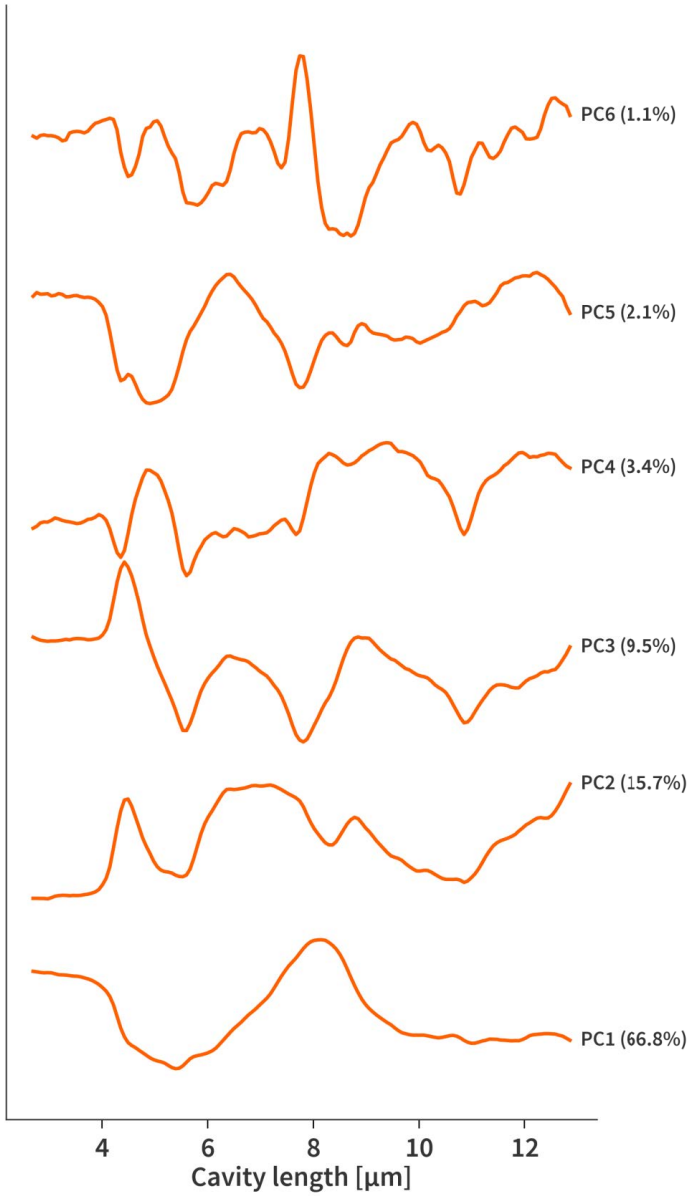

Figure S10.3: Loadings of the first six PCs. The percentages in the parentheses denote the explained variance of each respective PC. The plots have been offset for clarity.

S11. ACETYLENE AND BLACK BODY INTERFEROGRAMS

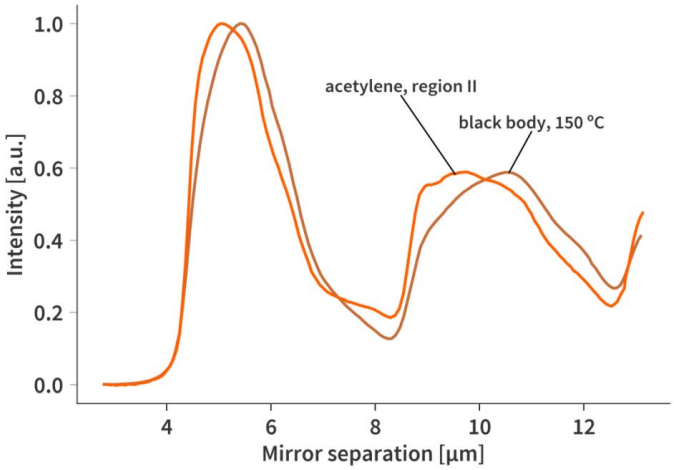

Figure S11.1: Normalized interferograms of acetylene sampled at region II and a 150 ºC black body radiator.

S12. CARBON DIOXIDE ABSORBANCE SPECTRUM

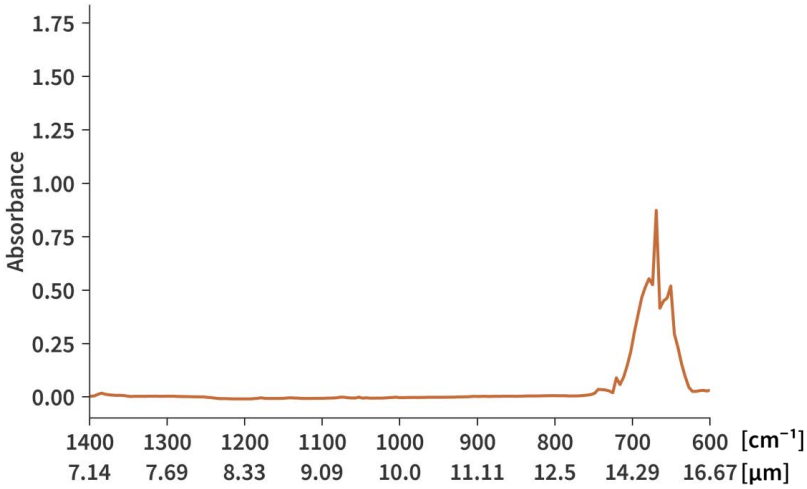

Figure S12.1: Carbon Dioxide absorbance spectrum [SI-R2].

S13. HIGH TEMPERATURE WATER ABSORPTION SPECTRUM

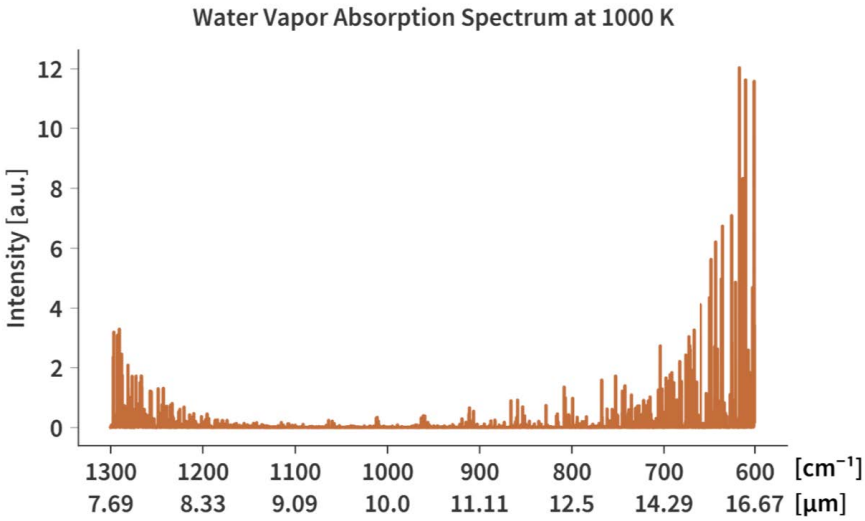

Figure S13.1: Absorption spectrum of water vapor at 1000 K compiled from the HITRAN library [SI-R3].

S14. REFERENCES

[SI-R1] Socrates, G. (2004). Infrared and Raman characteristic group frequencies: Tables and charts. John Wiley & Sons.

[SI-R2] Coblentz Society, Inc., "Evaluated Infrared Reference Spectra" in *NIST Chemistry WebBook*, NIST Standard Reference Database Number 69, Eds. P.J. Linstrom and W.G. Mallard, National Institute of Standards and Technology, Gaithersburg MD, 20899, https://doi.org/10.18434/T4D303

[SI-R3] R.V. Kochanov, I.E. Gordon, L.S. Rothman, P. Wcislo, C. Hill, J.S. Wilzewski, HITRAN Application Programming Interface (HAPI): A comprehensive approach to working with spectroscopic data, *J. Quant. Spectrosc. Radiat. Transfer* **177**, 15-30 (2016)

F. Digital PID Controller for SFPI

This section elaborates on the experimental details presented in Section 4.8. The primary challenge addressed is the control of the mirrors in the SFPI during transmittance measurements performed using an FTIR spectrometer. A GUI was developed to facilitate this process, which can be accessed at https://madsnibe.com/HSTI/other_files/mirror_stepper_pid_all_piezos3.py. While the code is not complex, designing a GUI requires many lines of code, and the full implementation is therefore not included here. The GUI allows users to apply a uniform voltage (controlled via 16-bit values corresponding to 0–75 V) across all piezo actuators simultaneously.

Figure F.1 illustrates the laser diode interferogram for a single laser/photodiode pair as increasing voltages are applied across all piezo actuators. As shown in Figure F.1a, the piezo actuators exhibit significant drift during the 'holding' segments when a constant voltage is applied. This is a problem when performing FTIR transmittance measurements, as the drift would lead to spectral broadening. The drift is mitigated using the Python-based GUI, which acts as a digital PID controller (proportional–integral–derivative), allowing for minor adjustments to the voltages to retain a constant mirror separation. This is demonstrated in Figure F.1b, showing significantly more stable signal output during the 'holding' segment.

While this software successfully maintains a constant distance when the mirrors are not intended to move, it does not ensure equal displacement of all three actuators. This could cause the mirrors to become misaligned during cavity expansion. However, in testing, all three actuators lie

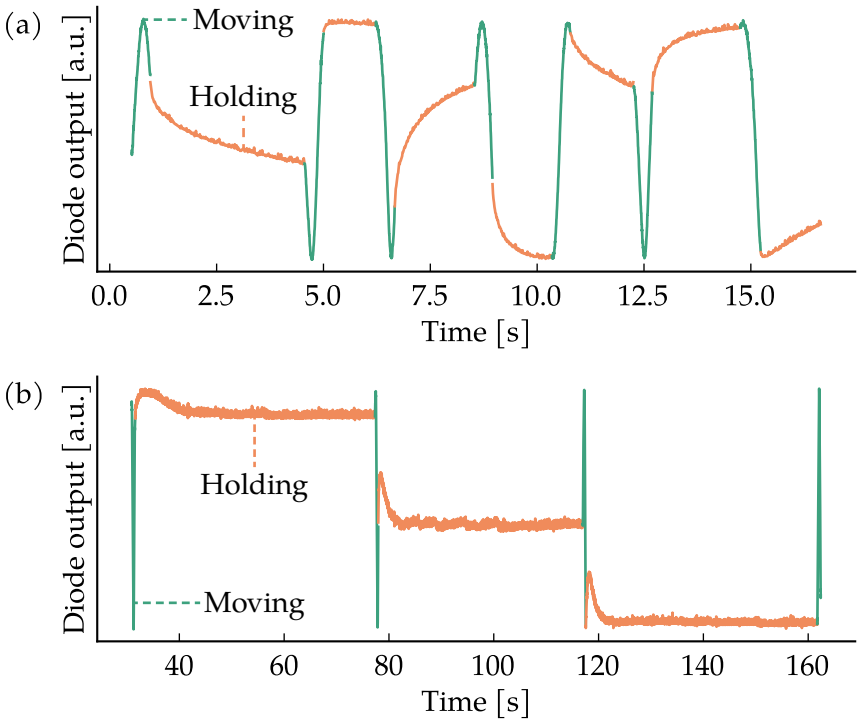

Figure F.1: Output of a single diode as a function of time. The output is divided into segments. The 'moving' segment describes the part of the sweep where the mirror is supposed to move following changes in the applied voltage. The 'holding' segment is the part of the sweep, where the mirrors are supposed to be stationary. A constant voltage is applied during the 'holding' segment in (a) leading to drift. A digital PID controller is implemented in (b), where the 'holding' segment shows a more constant value.

within a single fringe of each other across an expansion of 11.2 µm. That means that the difference in expansion across all three actuators is $< \lambda_{\text{eff}}/2$. Here, λ_{eff} os the 'effective wavelength' of the laser diodes, where the angle of incidence is taken into account. Additionally, since the FTIR spectrometer's spot size is limited to a few cm², this effect has less of an impact, allowing for stable FTIR measurements without significant mirror drift during the acquisition process.

The mirrors are now capable of maintaining a constant separation during measurements. It is possible to estimate their displacement by analyzing the laser diode outputs corresponding to the "moving" segments in which

the cavity expands. Figure F.2a illustrates successive 'moving' segments plotted adjacently, with vertical bars marking the boundaries between segments. The numbers above each segment indicate the fractional fringe contained within that segment. Determining the fraction of a fringe covered in a segment is inherently subjective. However, when the end of a segment coincides with a fringe peak or trough, these estimates can be cross-referenced with the cumulative fringe count.

This process is repeated for each of the three laser diodes, producing a set of displacement measurements for the piezoelectric actuators controlling the mirrors. The average displacement from the three diodes is taken as the representative value for the entire SFPI. It is assumed that the effective wavelength, defined as a combination of wavelength

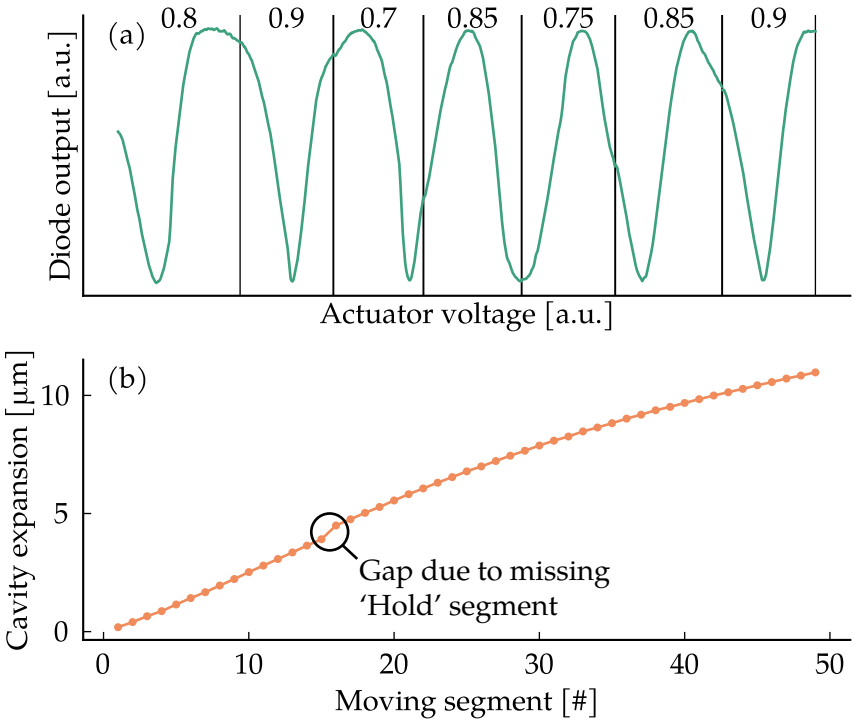

Figure F.2: Estimation of mirror displacement by sequentially plotting the "moving" segments, as shown in (a). Vertical bars indicate transitions between segments, while the numbers represent the fractional fringe content within each segment.

and reflection angle, is identical for all three diodes, with $\lambda_{\text{eff}} = 663$ nm. This effective wavelength is determined to provide the best fit between experimental measurements and GMM calculations (see Section 4.8). For each completed fringe, the mirrors displace by $\lambda_{\text{eff}}/2$.

It is important to note that the λ_{eff} associated with this SFPI differs from that of the imager used for the majority of this work, as this experiment employs a different SFPI prototype. By quantifying the fractional fringes for each 'moving' segment, the cumulative fringe count can be multiplied by $\lambda_{\text{eff}}/2$ to estimate the relative cavity expansion, as shown in Figure F.2b. This estimation, however, provides only the relative mirror displacement; the absolute cavity length requires an offset adjustment, as described in Section 4.8.

G. Generalized Matrix Method Python Function

The Python functions presented in Code Block G.1 constitute a critical component of the developed methodology, as they generate the system matrix that establishes the relationship between the transmittance of the SFPI, the cavity length, and the wavelength. This functionality is fundamental for simulating interferograms based on FTIR measurements and for transforming interferograms into spectra as a function of wavelength or wavenumber.

```
import numpy as np
def fpi_gmm(m_seps=np.array([10e-6]), lams =
    np.array([10e-6]), angle = 0, degrees = True,
    fraction_s_pol = 0.5, n_points = 7, mirror_height =
    150e-9):
     if degrees == True: #Convert angle to radians
          angle = np.radians(angle)
     # The first part is for taking the curvature of the
         mirrors into account, as they effectively
         broaden the spectra. Firstly the mirror surface
         (a circle) is broken up into n_point segments.
         The area of each segment is calculated and is
         converted to a fraction of the total area.
         Additionally, a mirror separation correction is
         calculated at n_points - 1 equally spaced
         locations along the mirror axis (radially
         outwards). The transmittance and reflectance is
         calculated for each point and is scaled
         according to the fractional area of the segment.
     diameter = 43e-3  # mirror diameter: Maximum height
         difference between mirror center and edges
```

```
    R = mirror_height / 2 + (diameter ** 2) / (8 * mirror_height)  # radius of mirror curvature
    n_points = int(n_points) #points must be an integer
    if n_points > 1:
        r_area = np.linspace(0, diameter / 2, n_points)  # radii used for area calculations
        r_eval = r_area + np.diff(r_area)[0] / 2  # radii at which the mirror separation difference is calculated
        r_area = np.delete(r_area, 0)  # Since the first radius is 0, the area is also 0 and is therefore omitted
        r_eval = np.delete(r_eval,-1)  # The evaluation points lie in the middle between r_area, but the final r_eval is outside the mirror and is therefore deleted
        area = []
        diff = []
        for i in range(n_points - 1):
            diff.append(mirror_dist_diff(r_eval[i], R))
            if i == 0:
                area.append(np.pi * r_area[i] ** 2)  # area of circle
            else:
                area.append(np.pi * (r_area[i] ** 2 - r_area[i - 1] ** 2))  # area of ring
        total_area = sum(area)
        mirror_fractions = np.array(area) / total_area
    else:
        mirror_fractions = [1]
        diff = [0]

    # The blocks refer to:
    # block1 - antireflective coating left half
    # block2_1: mirror coating left half
    # block2_2: mirror coating right half
    # block3: antireflective coating right half

    #list containing functions for calculating ior for each layer in the antireflective coating
    ar_functions = [n_air, n_ThF4, n_ZnSe, n_ThF4, n_ZnSe, n_ThF4, n_ZnSe] #Also contains the layers immediately to the left and right of the
```

```
anti-reflective coating
    n_block1 = [] #list of refractive indices
    d_block1 = np.array([np.inf, 4350, 250, 940, 500, 340, np.inf]) * 1e-9 #layer thicknesses
    Z_block1 = np.array([0, 0, 0, 0, 0, 0]) * 1e-9 #list of interface RMS heights
    for func in ar_functions:
        n_block1.append(func(lams))
    n_block1 = np.array(n_block1)
    n_block3 = n_block1[::-1] #the lists are mirrored to match the other half of the FPI
    d_block3 = d_block1[::-1]
    Z_block3 = Z_block1[::-1]

    # Now do the same, but for the mirror coatings (excluding the air gap)
    mirror_functions = [n_ZnSe, n_Ge, n_ZnS, n_ThF4, n_ZnS, n_Ge, n_air]
    n_block2_1 = []
    d_block2_1 = np.array([np.inf, 1255, 20, 1785, 20, 510, np.inf]) * 1e-9
    Z_block2_1 = np.array([0, 0, 0, 0, 0, 0]) * 1e-9
    for func in mirror_functions:
        n_block2_1.append(func(lams))
    n_block2_1 = np.array(n_block2_1)
    n_block2_2 = n_block2_1[::-1]
    d_block2_2 = d_block2_1[::-1]
    Z_block2_2 = Z_block2_1[::-1]

    #angle in each layer from Snell's law
    if angle != 0:
        angles_block1 = []
        angles_block1.append(np.ones_like(lams)*angle)
        for i in range(n_block1.shape[0]-1):
            angles_block1.append(np.arcsin(
                np.sin(angles_block1[-1]) *
                np.real(n_block1[i, :]) /
                np.real(n_block1[i+1, :])))
        angles_block2_1 = []
        angles_block2_1.append(angles_block1[-1])
        for i in range(len(n_block2_1)-1):
            angles_block2_1.append(np.arcsin(
                np.sin(angles_block2_1[-1]) *
```

```
                np.real(n_block2_1[i, :]) /
                np.real(n_block2_1[i+1, :])))
        angles_block2_2 = []
        angles_block2_2.append(angles_block2_1[-1])
        for i in range(len(n_block2_2)-1):
            angles_block2_2.append(np.arcsin(
                np.sin(angles_block2_2[-1]) *
                np.real(n_block2_2[i, :]) /
                np.real(n_block2_2[i+1, :])))
        angles_block3 = []
        angles_block3.append(angles_block2_2[-1])
        for i in range(len(n_block3)-1):
            angles_block3.append(np.arcsin(
                np.sin(angles_block3[-1]) *
                np.real(n_block3[i, :]) /
                np.real(n_block3[i+1, :])))
        angles_block1 = np.array(angles_block1)
        angles_block2_1 = np.array(angles_block2_1)
        angles_block2_2 = np.array(angles_block2_2)
        angles_block3 = np.array(angles_block3)
    else:
        angles_block1 = np.zeros_like(n_block1)
        angles_block2_1 = np.zeros_like(n_block2_1)
        angles_block2_2 = np.zeros_like(n_block2_2)
        angles_block3 = np.zeros_like(n_block3)


    #Calculate the index of refraction for ZnSe and air
        for all relevant wavelengths
    ns_ZnSe = n_ZnSe(lams)
    ns_air = n_air(lams)

    #Matrices for containing the transmittance and
        reflectance
    transmittance_matrix = np.zeros([len(m_seps),
        len(lams)])
    reflectance_matrix = np.zeros([len(m_seps),
        len(lams)])

    #For each wavelength calculate all the relevant
        transfer matrices. These are converted to their
        absolute counterparts
    #to accommodate for the incoherent ZnSe layer
```

```
    #Do to speed, the calculations are split up depending on whether the incidence is normal or not
    if angle == 0: #normal incidence
        for i, lam in enumerate(lams):
            T1 = transfer_matrix(n_block1[:,i], d_block1, Z_block1, lam)
            T1_abs = abs_transfer_matrix(T1)
            T2_1 = transfer_matrix(n_block2_1[:,i], d_block2_1, Z_block2_1, lam)
            T2_2 = transfer_matrix(n_block2_2[:,i], d_block2_2, Z_block2_2, lam)
            T3 = transfer_matrix(n_block3[:,i], d_block3, Z_block3, lam)
            T3_abs = abs_transfer_matrix(T3)
            P_ZnSe_abs = abs(p_matrix(ns_ZnSe[i], 5e-3, lam))**2
            T1_ZnSe_abs = T1_abs@P_ZnSe_abs
            T3_ZnSe_abs = P_ZnSe_abs@T3_abs

            #Now calculate the effective transfer matrix for all mirror separations. The results are converted to transmittance and reflectance.
            for j, m_sep in enumerate(m_seps):
                T = 0
                R = 0
                for d, frac in zip(diff, mirror_fractions):
                    P_air = p_matrix(ns_air[i], m_sep + d, lam)
                    T2 = T2_1 @ P_air @ T2_2
                    T2_abs = abs_transfer_matrix(T2)
                    T_combined = T1_ZnSe_abs @ T2_abs @ T3_ZnSe_abs
                    T += 1 / T_combined[0, 0] * frac
                    R += T_combined[1,0]/T_combined[0,0] * frac
                transmittance_matrix[j,i] = T
                reflectance_matrix[j,i] = R
    else:
        for i, lam in enumerate(lams):
```

```
            T1 = transfer_matrix_angular(n_block1[:,
                i], d_block1/np.cos(angles_block1[:,i]),
                angles_block1[:,i], fraction_s_pol,
                Z_block1, lam)
            T1_abs = abs_transfer_matrix(T1)
            T2_1 =
                transfer_matrix_angular(n_block2_1[:,
                i],
                d_block2_1/np.cos(angles_block2_1[:,i]),
                angles_block2_1[:,i], fraction_s_pol,
                Z_block2_1, lam)
            T2_2 =
                transfer_matrix_angular(n_block2_2[:,
                i],
                d_block2_2/np.cos(angles_block2_2[:,i]),
                angles_block2_2[:,i], fraction_s_pol,
                Z_block2_2, lam)
            T3 = transfer_matrix_angular(n_block3[:,
                i], d_block3/np.cos(angles_block3[:,i]),
                angles_block3[:,i], fraction_s_pol,
                Z_block3, lam)
            T3_abs = abs_transfer_matrix(T3)
            P_ZnSe_abs1 = abs(p_matrix(ns_ZnSe[i],
                5e-3/np.cos(angles_block1[-1,i]), lam))
                ** 2
            T1_ZnSe_abs = T1_abs @ P_ZnSe_abs1
            P_ZnSe_abs2 = abs(p_matrix(ns_ZnSe[i],
                5e-3/np.cos(angles_block2_2[-1,i]),
                lam)) ** 2
            T3_ZnSe_abs = P_ZnSe_abs2 @ T3_abs

            # Now calculate the effective transfer
                matrix for all mirror separations. The
                results are converted to transmittance
                and reflectance.
            for j, m_sep in enumerate(m_seps):
                T = 0
                R = 0
                for d, frac in zip(diff,
                    mirror_fractions):
                    P_air = p_matrix(ns_air[i], (m_sep
                        +
                        d)/np.cos(angles_block2_1[-1,i]),
```

```
                        lam)
                    T2 = T2_1 @ P_air @ T2_2
                    T2_abs = abs_transfer_matrix(T2)
                    T_combined = T1_ZnSe_abs @ T2_abs @ T3_ZnSe_abs
                    # T_combined = T2
                    n_ratio = np.real(ns_air[i] * np.cos(angles_block3[-1, i])) / np.real(ns_air[i] * np.cos(angles_block1[0, i]))
                    T += 1 / T_combined[0, 0] * n_ratio * frac
                    R += T_combined[1, 0] / T_combined[0, 0] * frac
                transmittance_matrix[j, i] = T
                reflectance_matrix[j, i] = R
    return transmittance_matrix, reflectance_matrix

# function for calculating the transfer matrix of an entire stack of layers
def transfer_matrix(n_stack, d_stack, Z_stack, lam):
    T_matrix = t_matrix(n_stack[0], n_stack[1], Z_stack[0], lam)
    for j in np.arange(1, len(n_stack) - 1):
        T_matrix = T_matrix @ p_matrix(n_stack[j], d_stack[j], lam) @ t_matrix(n_stack[j], n_stack[j+1], Z_stack[j], lam)
    return T_matrix

def transfer_matrix_angular(n_stack, d_stack, angle_stack, fraction, Z_stack,  lam):
    T_matrix = t_matrix_angular(n_stack[0], n_stack[1], angle_stack[0], angle_stack[1], fraction, Z_stack[0], lam)
    for j in np.arange(1, len(n_stack) - 1):
        T_matrix = T_matrix @ p_matrix(n_stack[j], d_stack[j]/np.cos(angle_stack[j]), lam) @ t_matrix_angular(n_stack[j], n_stack[j+1], angle_stack[j], angle_stack[j+1], fraction, Z_stack[j], lam)
    return T_matrix

```

```
# function for converting a transfer matrix to absolute values
def abs_transfer_matrix(transfermatrix):
    t = 1 / transfermatrix[0, 0]
    t_prime = (transfermatrix[0, 0] * transfermatrix[1, 1] - transfermatrix[0, 1] * transfermatrix[1, 0]) / transfermatrix[0, 0]
    r = transfermatrix[1, 0] / transfermatrix[0, 0]
    r_prime = - transfermatrix[0, 1] / transfermatrix[0, 0]
    return 1 / (abs(t) ** 2) * np.array([[1, -abs(r_prime) ** 2], [abs(r) ** 2, abs(t * t_prime) ** 2 - abs(r * r_prime) ** 2]])

# function for calculating the transmission matrix
def t_matrix(n1, n2, Z=0, lam = 1):
    if Z == 0: # measurable speed up, if the exponents do not have to be calculated in case of no roughness.
        a = 1
        b = 1
        c = 1
    else:
        s = 2*np.pi*Z
        a = np.exp(-2*(s*n1/lam)**2)
        b = np.exp(-2*(s*n2/lam)**2)
        c = np.exp(-0.5 * ((s*n2/lam)**2 * (n1 - n2)**2))
    r = a*reflectance(n1, n2)
    r_prime = b*reflectance(n2, n1)
    t = c*transmittance(n1, n2)
    t_prime = c*transmittance(n2, n1)
    matrix = np.array([[1, -r_prime], [r, t*t_prime-r*r_prime]])
    return (1/t) * matrix

def t_matrix_angular(n1, n2, theta1, theta2, fraction, Z=0, lam = 1):
    if Z == 0: # measurable speed up, if the exponents do not have to be calculated in case of no roughness.
        a = 1
        b = 1
```

```
        c = 1
    else:
        s = 2*np.pi*Z
        a = np.exp(-2*(s*n1/lam)**2)
        b = np.exp(-2*(s*n2/lam)**2)
        c = np.exp(-0.5 * ((s*n2/lam)**2 * (n1 - n2)**2))
    r = a*reflectance_angular(n1, n2, theta1, theta2, fraction)
    r_prime = b*reflectance_angular(n2, n1, theta2, theta1, fraction)
    t = c*transmittance_angular(n1, n2, theta1, theta2, fraction)
    t_prime = c*transmittance_angular(n2, n1, theta2, theta1, fraction)
    matrix = np.array([[1, -r_prime], [r, t*t_prime-r*r_prime]])
    return (1/t) * matrix

# calculate the phase matrix
def p_matrix(n, d, lam):
    P = np.zeros([2,2], dtype=np.complex_)
    P[0, 0] = np.exp(1j * n * 2 * np.pi * d / lam)
    P[1, 1] = np.exp(-1j * n * 2 * np.pi * d / lam)
    return P

# calculate the reflectance based on refractive indices
def reflectance(n1, n2):
    return (n1 - n2)/(n1 + n2)

# calculate the reflectance based on refractive indices and angles
def reflectance_angular(n1, n2, theta1, theta2, fraction):
    rs = (n1*np.cos(theta1) - n2*np.cos(theta2))/(n1*np.cos(theta1) + n2*np.cos(theta2))
    rp = -(n2*np.cos(theta1) - n1*np.cos(theta2))/(n2*np.cos(theta1) + n1*np.cos(theta2)) ##### NOTICE THE CHANGE OF SIGN FOR rp - SEE STEVEN BYRNES #####
    return fraction*rs + (1-fraction)*rp

```

```
# calculate the transmittance based on refractive indices
def transmittance(n1, n2):
    return 2*n1/(n1 + n2)

# calculate the transmittance based on refractive indices and angles
def transmittance_angular(n1, n2, theta1, theta2, fraction):
    ts = 2*n1*np.cos(theta1)/(n1*np.cos(theta1) + n2*np.cos(theta2))
    tp = 2*n1*np.cos(theta1)/(n2*np.cos(theta1) + n1*np.cos(theta2))
    return fraction*ts + (1-fraction)*tp

# calculate the phase gained from traveling in a medium
def phase(n, d, lam):
    return np.exp(1j * n * 2 * np.pi * d / lam)

# function for calculating the deviation from the perfectly flat mirror at radius r from the mirror center.
def mirror_dist_diff(r, R):
    return -2 * (0.5 * (2 * R - np.sqrt(4 * R ** 2 - (2 * r) ** 2)))

######## Functions for calculating the refractive indices of different materials ########

def n_air(lams):
    return np.ones_like(lams, dtype=np.complex_)

def n_ThF4(lams):
    # Handbook of Optical Constants of Solids II, 1998, page 1051
    lams = lams * 1e6
    k = 0.00189 - 0.00015 * lams + 0.00001 * lams ** 2
    n = 1.118 + 2.46 / lams - 2.98 / (lams ** 2)  # - ThF4_k_interp*1j
    return n - k * 1j

def n_ZnSe(lams):
```

```
    # Handbook of Optical Constants of Solids II, page 737
    lams = lams * 1e6
    n = np.sqrt(4 + 1.9 * lams ** 2 / (lams ** 2 - 0.113)) - 0j
    return n

def n_ZnS(lams):
    # Handbook of Optical Constants of Solids I, page 600
    w = (1 / lams) * 1e-2
    wL = 352  # cm^-1
    wT = 282  # cm^-1
    T = 6.77  # cm^-1
    eps_inf = 5.7
    n = np.sqrt(eps_inf * (1 + (wL ** 2 - wT ** 2) / (wT ** 2 - w ** 2 + T * w * 1j)))
    return np.real(n) + np.imag(n)*1j

def n_Ge(lams):
    temperature = 293.15
    # Handbook of Optical Constants of Solids I, page 465 - for bulk
    lams = lams * 1e6
    # https://doi.org/10.1016/j.mssp.2018.04.019 - for thin film
    A = 4.1463
    B = 0.57268
    C = 0.087329
    n = A + B / (lams ** 2) + C / (lams ** 4)
    alpha = 0.064314
    Eg = 0.77285
    Eu = 0.142
    k = alpha * np.exp((1.24 / lams - Eg) / Eu) # also from https://doi.org/10.1016/j.mssp.2018.04.019
    return n - k * 1j
```

Code Block G.1: Python functions used to calculate the transmittance matrix of SFPI using the GMM method. This function is able to handle broadening caused by concave mirrors as well as considering oblique light incidence.

H. Python GUI: Hyperspectral Viewer

A custom hyperspectral image viewer and analyzer has been developed using Python, employing the Tkinter library for the graphical user interface. This tool enables basic data processing and facilitates the extraction of mean spectra based on user-defined colored selections. An (almost) stable version can be downloaded from https://madsnibe.com/assets/other_files/HSTI_viewer_w_PCA.zip. Many of the most used Python functions throughout this project have also been compiled into a Python package, which can be downloaded from PyPi: https://pypi.org/project/HSTI/. This work has also been documented in [86], where a more thorough description can be found.

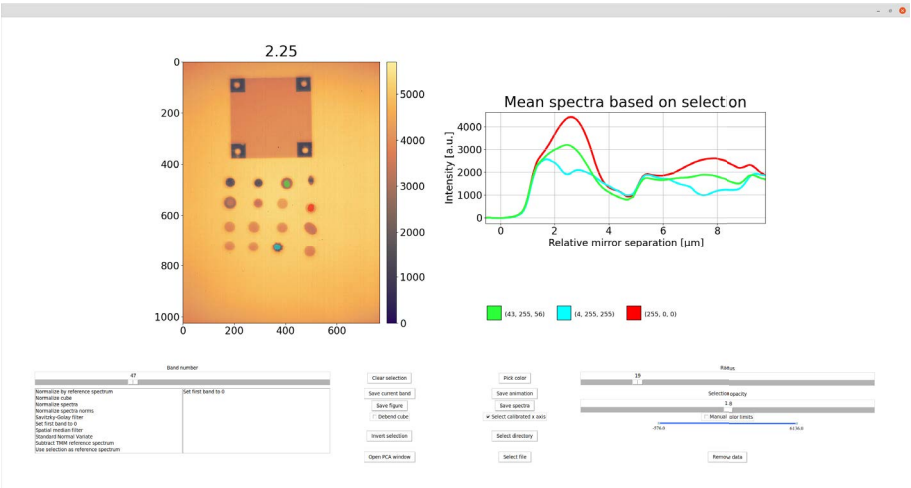

Figure H.1: Screenshot of the hyperspectral viewer displaying a hyperspectral thermal image of various gemstones. Red and green selections are shown, which have been used to extract mean interferograms. Reprint from [86]

An example of a hyperspectral thermal image displaying a collection of various gemstones (same as presented in subsection 8.4.2) is shown in Figure H.1.

Loading an Image

If the image is acquired from the LWIR HSC, it can be loaded using the `Select directory` button. The directory containing the "/images/capture/" folder (matching the standard data output format of the camera) must be specified. Alternatively, if the hyperspectral image is in ".pam" or ".npy" format, the `Select file` button should be used. The numpy array must have exactly three dimensions, where the third dimension (axis 2) contains the spectral information.

Scrolling Through the Bands

The leftmost slider, labeled `Band number`, allows users to navigate through the bands of the data cube. As the slider is adjusted, the displayed image in the viewer updates accordingly. By default, the color range dynamically adjusts for each band. However, the range can be fixed by enabling the `Manual color limits` checkbox in the bottom-right corner. The accompanying sliders can then be used to manually set the lower

and upper bounds of the color range.

Extracting Mean Spectrum or Interferograms

The viewer enables the extraction of mean spectra or interferograms through interactive selection directly on the displayed image. Users can draw a selection by left-clicking and dragging the mouse across the image. This action creates a colored mask, which is superimposed on the image. Upon releasing the mouse button, the mean spectrum corresponding to the selected region is computed and plotted in the associated color in the plot on the right.

Different colors can be assigned to selections using the `Pick color` button. Once a color has been applied, it appears as a swatch beneath the plot. Clicking a swatch activates the associated color, allowing additional modifications to the corresponding mask without needing to manually re-enter the RGB value.

The size of the selection brush, measured in pixels, can be adjusted using the `Radius` slider, while the transparency of the mask can be controlled using the `Selection opacity` slider. Right-clicking and holding acts as an eraser tool, removing previous selections wherever the mouse passes over. The `Clear selection` button clears all selections simultaneously. The `Invert selection` button converts all existing selections to a uniform color before inverting the mask.

Removing data

The mask can also be used to remove data. By pressing the `Remove data` button, all data with a marking (whatever the color) is replaced by NaNs. This facilitates further analysis without including the removed data. This is particularly useful in the case of PCA, which is sensitive to the clutter in the data.

Adding Preprocessing and Data Analysis

The viewer provides various preprocessing methods that can be applied to the entire data cube. All of the preprocessing steps outlined in section 2.5 are available. These are selected sequentially from a list, and the chosen steps are then presented on the right (Figure H.1). The extracted interferograms are updated accordingly.

Calibrated X-Axis

By default, the x-axis of the data cube is represented as a series of integers corresponding to the step number associated with each spectral channel. Users can enable calibration of the x-axis by selecting the `Select calibrated x-axis` checkbox.

It is possible to set the relative cavity expansion based on the interferograms generated by three laser diodes. Subsequently, the user is prompted to input an offset value. If the offset value is unknown, a default value of 0.0 µm is applied. It is also possible to provide custom x-axes by either using numpy polynomials, a numpy array, a .txt, or a

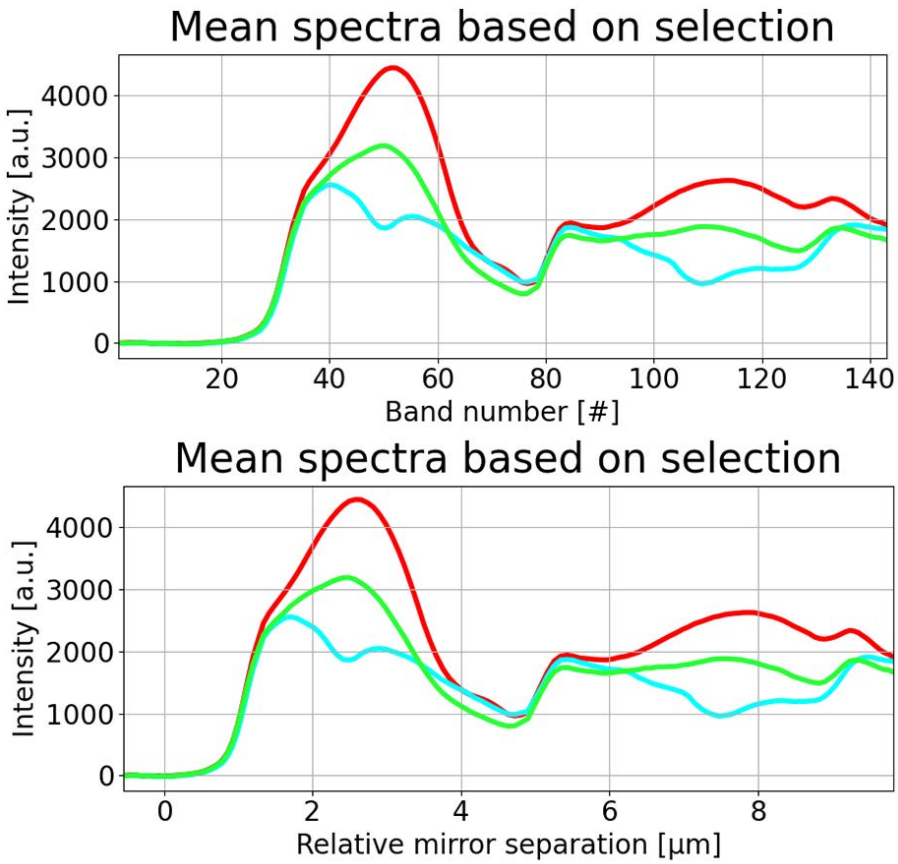

Figure H.2: Extracted interferograms before and after x-axis calibration. Reprint from [86]

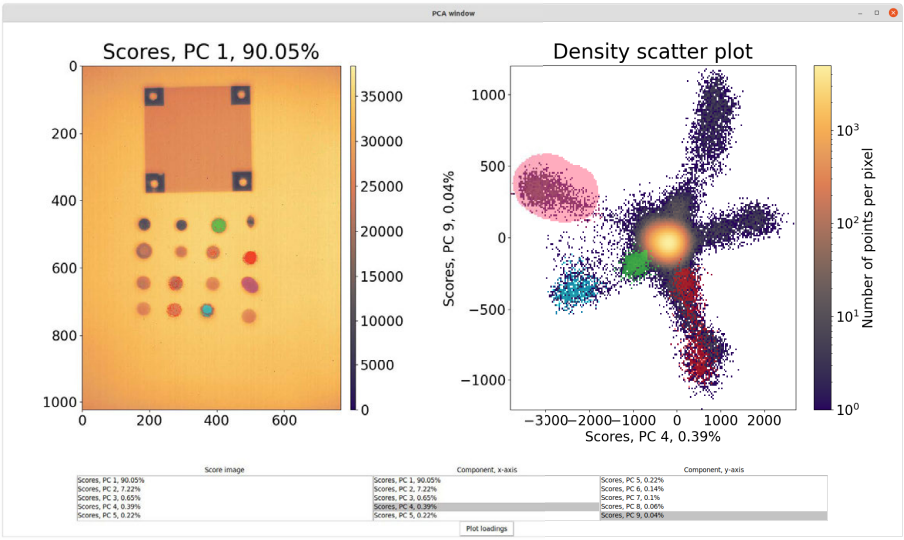

Figure H.3: Screenshot of the PCA window showing the score image and a density scatter plot of the PCA space. The pink selection is painted directly in the density scatter plot, while the blue, green and red are painted in the scores image (left), and then their position is found in the density scatter plot. Reprint from [86]

.csv file.

Principal Component Analysis

PCA can be performed on the data cube by selecting the `Open PCA window` button. This opens the PCA window where, on the left, a score image displays the contribution of individual pixels to a selected PC. Users can select different PCs from the list below the image. On the right, a density scatter plot illustrates a two-dimensional slice of the PCA space, where the PCs onto which the data is projected can be chosen using the `Component, x-axis` and `Component, y-axis` drop-down menus. The color bar indicates the pixel density within each bin of the scatter plot. The percentage associated with each PC denotes the proportion of the total variance explained by that component.

The interface supports interactive exploration of the PCA results. Users can paint specific regions in the score image to visualize how these correspond to clusters in the PCA space. The painting tool settings, including foreground color and brush radius, are synchronized with

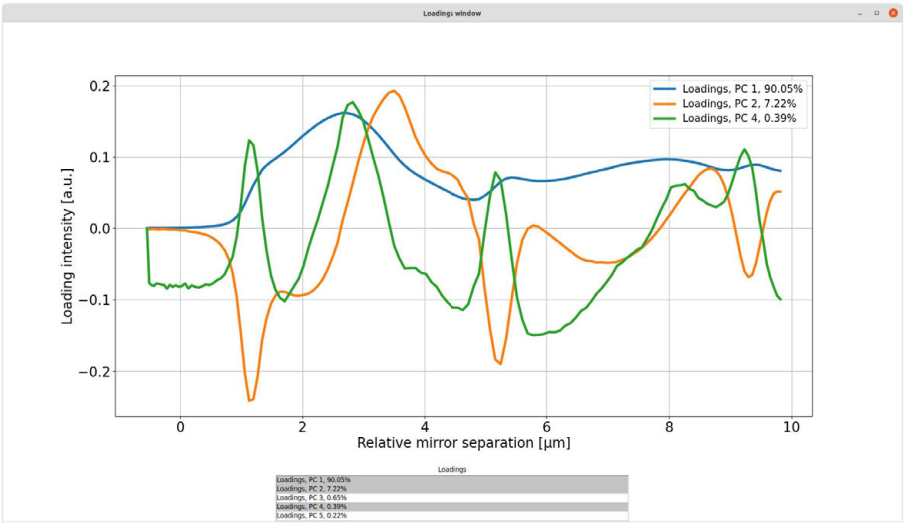

Figure H.4: Screenshot of the PCA loadings window showing individual loadings for selected PCs. Reprint from [86]

the main viewer. This functionality enables the identification of specific clusters and their spatial distribution. For example, in Figure H.3, a pink color has been used to select the upper-left branch of the density scatter plot. This selection corresponds to the gemstone located in the last column and second-to-last row of the data cube.

By selecting the `Plot loadings` button, users can access a new window that plots the loadings of each PC. Multiple PCs can be selected for simultaneous comparison.

I. Posters

This chapter is attributed to the posters which have been produced during the course of the project. They stand as a way of conveying how the hyperspectral imager works in a graphical form. Each section is dedicated to each of the three posters, giving a small introduction to each.

I.1 International Association for Spectral Imaging 2022

The initial poster covers the camera's construction, the theory behind converting FTIR spectra to interferograms, early spectral reconstructions, and a mineral analysis example.

NEWTEC

SDU

Capturing hyperspectral thermal images utilizing a first order scanning Fabry-Pérot interferometer

Mads Nibe Larsen[1&2], Anders Løchte Jørgensen[1], Victor Petrunin[1], Jakob Kjelstrup-Hansen[2], Bjarke Jørgensen[1]
[1] Newtec Engineering A/S, 5230 Odense M, Denmark
[2] NanoSYD, Mads Clausen Institute, University of Southern Denmark, 6400 Sønderborg, Denmark

1 Introduction

Hyperspectral imaging in the longwave infrared (LWIR) domain can be used to measure spectral features of materials corresponding to the vibrational frequencies of its atomic bonds. This information can be used to determine what material(s) are being imaged. The selection of commercially available hyperspectral thermal imagers is scarce, expensive and many require cryogenic cooling. We here present a relatively inexpensive, spectral scanning, hyperspectral thermal camera (HSTC), capable of being brought to the field.

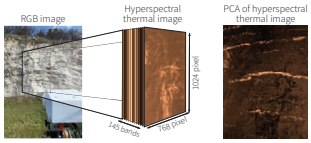

2 The camera

This hyperspectral thermal camera utilizes an uncooled microbolometer sensor capable of measuring thermal radiation with wavelengths ranging from **8 –15 µm**. This range is split up into smaller parts by placing a scanning Fabry-Pérot interferometer (SFPI) in front of the camera. The SFPI acts as a variable bandpass filter where the mirror separation determines the distribution of wavelengths reaching the sensor. A hyperspectral image cube is formed by sweeping the mirror separation distance from ≈ 3 – 12 µm and simultaneously acquiring ≈ 145 images with a spatial resolution is 768×1024 pixels. A detailed description of the hyperspectral imaging system is given in [1].

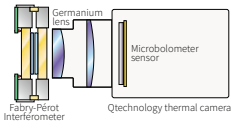

3 Use cases

Comparing hyperspectral thermal images and FTIR spectra

Many organic gases have spectral features in the LWIR region, and which can be recognized by the HSTC. Here we show how spectra of gaseous methanol recorded with HSTC can be compared to FTIR spectra.

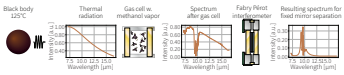

The spectra recorded by the HSTC are given in terms of mirror separation and *not* wavelength. Linear algebra is used to describe the relationship between the wavelength dependent spectrum passing through the SFPI and the spectrum recorded by the HSTC. Firstly, the transmission through the SFPI is found using a transfer matrix method (TMM) at several mirror separations. This is combined with the spectral sensitivity of the camera and forms a matrix, $\mathbf{\Lambda}$. The transmission spectrum of the gas is represented by the vector, $\mathbf{s}_\lambda$. Finally, the SFPI spectrum, $\mathbf{s}_{SFPI}$, can be readily found by:

$$\mathbf{\Lambda}\,\mathbf{s}_\lambda = \mathbf{s}_{SFPI},$$

which can be represented graphically as:

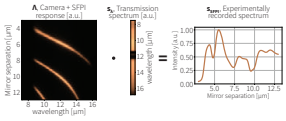

Since the experimentally recorded spectra are in terms of mirror separation, it must be converted to the wavelength domain for comparison with FTIR. This is done by multiplying by inv($\mathbf{\Lambda}$) from the left. However, the matrix must be regularized by adding a matrix, $\mathbf{M}$, representing the second derivative operator (finite difference). $\mathbf{M}$ has 2s along its diagonal, negative 1s above and below the diagonal, and 0s everywhere else. $\mathbf{M}$ is scaled by a factor, α, before adding it to $\mathbf{\Lambda}$. This form of regularization reduces oscillations in the resulting spectrum. Finally, the wavelength dependent transmission spectrum is calculated as

$$\mathbf{s}_\lambda = \mathrm{inv}(\mathbf{\Lambda}^T\mathbf{\Lambda} + \alpha\mathbf{M})\,\mathbf{\Lambda}^T\,\mathbf{s}_{SFPI}$$

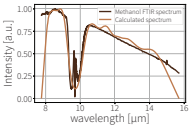

Detecting minerals

Another use case for the hyperspectral thermal camera is for distinguishing different types of minerals based on measured reflectance spectra. Here it is demonstrated how flint layers in a limestone cliff face is brought out using principal component analysis. The hyperspectral thermal image is captured at Boesdal limestone quarry.

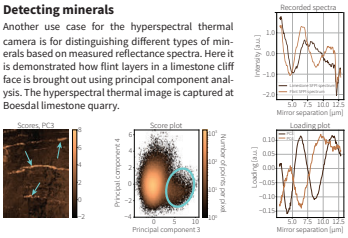

4 Conclusions

A thermal camera combined with a scanning Fabry-Pérot interferometer is capable of capturing hyperspectral images. The spectra are recorded in terms of mirror separation distance and must be converted to wavelengths for comparison with literature. Several improvements are envisioned for the system, such as improved mirror control, and inclusion of RGB data (visual range).

mani@newtec.dk
nibe@mci.sdu.dk

Read more

[1] Anders Løchte Jørgensen, Mads Nibe Larsen, Victor Petrunin, Jakob Kjelstrup-Hansen, and Bjarke Jørgensen, "Surface temperature determination using long-range thermal emission spectroscopy based on a first order scanning Fabry-Pérot interferometer," Opt. Express 30, 2186-2196 (2022)

IASIM 2022

I.2 SPIE Defence and Commercial Sensing 2024

This poster focuses on how incident light transmitted through a gas cell is converted into interferograms. (Almost) the same poster won a poster prize at the Annual meeting of the Danish Physical Society in 2022.

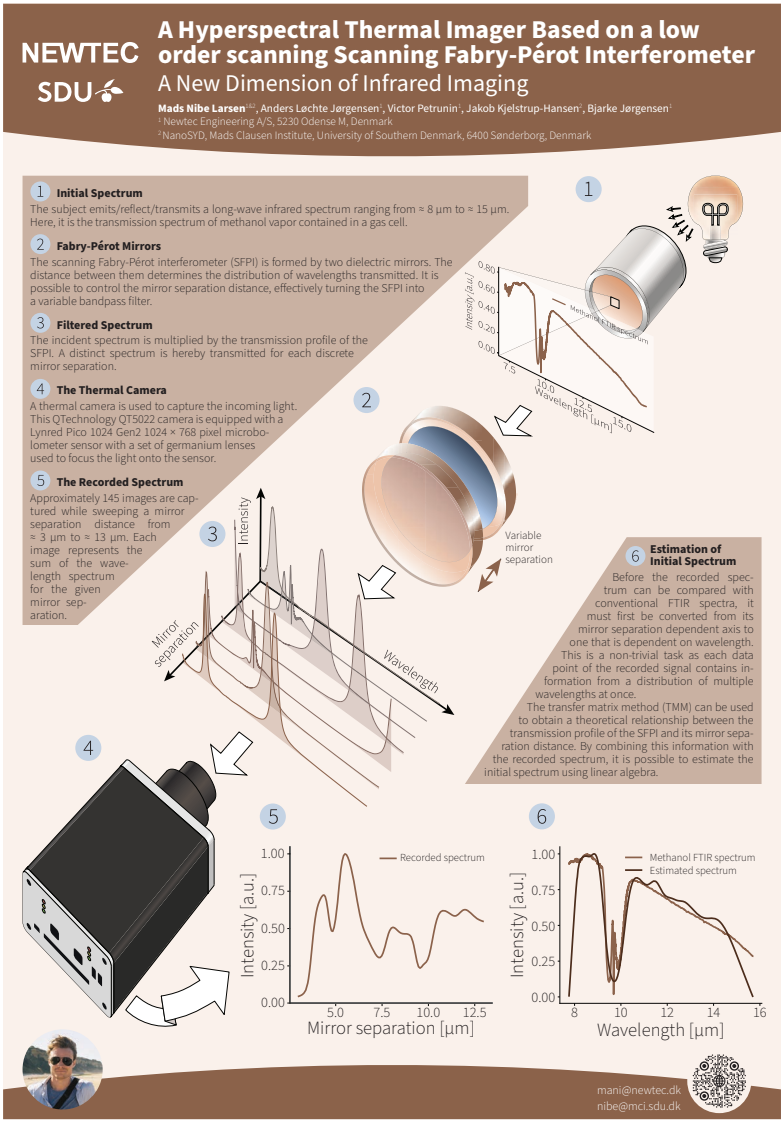

I.3 International Association for Spectral Imaging 2024

A more technical description of how the camera works - especially of how the mirrors are controlled. Furthermore, it gives a short explanation of how the incident light is converted into interferograms.

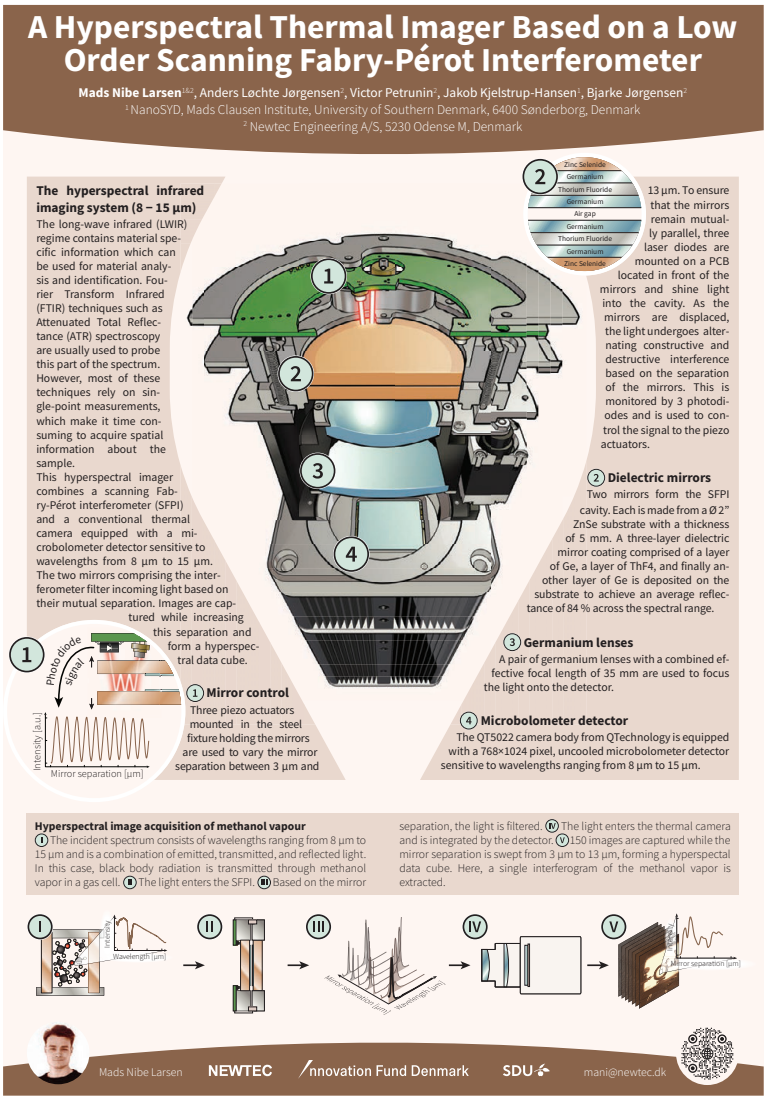

Bibliography

[1] Anders Christian Løchte Jørgensen. "Methodologies for Hyperspectral Thermal Imaging". DOI: https://doi.org/10.21996/4vpg-yk48. PhD thesis. Odense, Denmark: Syddansk Universitet, 2022. URL: https://portal.findresearcher.sdu.dk/en/publications/methodologies-for-hyperspectral-thermal-imaging.

[2] Exosens. *Telops Hypercam*. en. URL: https://www.exosens.com/products/hyperspectral-cameras (visited on 01/28/2025).

[3] Mads Nibe Larsen et al. "Classification of commercial plastics using hyperspectral long wave infrared emission imaging". In: *Spectrochimica Acta Part A: Molecular and Biomolecular Spectroscopy* 329 (2025), page 125501. ISSN: 1386-1425. DOI: 10.1016/j.saa.2024.125501. URL: https://www.sciencedirect.com/science/article/pii/S1386142524016676.

[4] Mads Nibe Larsen et al. "Classification of black plastic types by hyperspectral imaging based on long-wave infrared emission spectroscopy". In: *Polymer Testing* 141 (Dec. 2024), page 108629. ISSN: 0142-9418. DOI: 10.1016/j.polymertesting.2024.108629.

[5] G. Leslie Squires. *quantum mechanics*. 2024. URL: https://www.britannica.com/science/quantum-mechanics-physics (visited on 10/14/2024).

[6] Frank L. Pedrotti, Leno M. Pedrotti, and Leno S. Pedrotti. "1 Nature of Light". In: *Introduction to Optics*. Third. Cambridge University Press. ISBN: 978-1-108-42826-2.

[7] Michael Vollmer and Klaus-Peter Möllmann. *Infrared Thermal Imaging - Fundamentals Research and Applications*. 2nd reprint. Wiley-VCH Verlag GmbH & Co. KGaA, 2010. ISBN: 978-3-527-40717-0.

[8] H Leuenberger and R A Person. "Compilation of Radiation Shape Factors for Cylindrical Assemblies". en. In: *American Society of Mechanical Engineers* 56-A-144 (Nov. 1956).

[9] Y. Cengel. *Heat Transfer: A Practical Approach*. McGraw-Hill Education, 2004. ISBN: 9780071236447. URL: https://books.google.dk/books?id=xYASMQAACAAJ.

[10] Frank L. Pedrotti, Leno M. Pedrotti, and Leno S. Pedrotti. *Introduction to Optics*. Third. Cambridge University Press. ISBN: 978-1-108-42826-2.

[11] Duncan Lawson. "The Blackbody Fraction, Infinite Series and Spreadsheets*". In: URL: https://api.semanticscholar.org/CorpusID:207981402.

[12] J. Steketee. "The influence of cosmetics and ointments on the spectral emissivity of skin." eng. In: *Physics in medicine and biology* 21.6 (Nov. 1976). Place: England, pages 920–930. ISSN: 0031-9155. DOI: 10.1088/0031-9155/21/6/002.

[13] Xianglei Huang et al. "An Observationally Based Global Band-by-Band Surface Emissivity Dataset for Climate and Weather Simulations". English. In: *Journal of the Atmospheric Sciences* 73.9 (Sept. 2016). Place: Boston MA, USA Publisher: American Meteorological Society, pages 3541–3555. DOI: 10.1175/JAS-D-15-0355.1. URL: https://journals.ametsoc.org/view/journals/atsc/73/9/jas-d-15-0355.1.xml.

[14] Miko. *Hyperspectral vs multispectral cameras: understanding advantages and limitations in spectral imaging*. en-US. URL: https://www.specim.com/technology/hyperspectral-vs-multispectral-cameras/ (visited on 10/21/2024).

[15] Mads. Peters and Syddansk Universitet. Det Tekniske Fakultet. "Development of Scanning and Snapshot Hyperspectral Imaging Systems for Industrial Sorting Machines." eng. PhD thesis. Odense, 2024.

[16] I. T. Jolliffe. *Principal Component Analysis*. Springer Series in Statistics. New York, NY: Springer New York, NY, Oct. 2002. ISBN: 978-0-387-95442-4. DOI: 10.1007/b98835.

[17] Rasmus Bro and Age K. Smilde. "Principal component analysis". In: *Analytical Methods* 6.9 (2014). Publisher: The Royal Society of Chemistry, pages 2812–2831. ISSN: 1759-9660. DOI: 10.1039/C3AY41907J. URL: http://dx.doi.org/10.1039/C3AY41907J.

[18] Steven L. Brunton and J. Nathan Kutz. *Data-Driven Science and Engineering: Machine Learning, Dynamical Systems, and Control*. Cambridge: Cambridge University Press, 2019. DOI: 10.1017/9781108380690.

[19] Abraham. Savitzky and M. J. E. Golay. "Smoothing and Differentiation of Data by Simplified Least Squares Procedures." In: *Analytical Chemistry* 36.8 (July 1964). Publisher: American Chemical Society,

pages 1627–1639. ISSN: 0003-2700. DOI: 10.1021/ac60214a047. URL: https://doi.org/10.1021/ac60214a047.

[20] *savgol_filter — SciPy v1.14.1 Manual*. URL: https://docs.scipy.org/doc/scipy/reference/generated/scipy.signal.savgol_filter.html (visited on 11/19/2024).

[21] Kevin P. Murphy. *Probabilistic Machine Learning: An introduction*. MIT Press, 2022.

[22] Gilbert Strang. *Linear algebra and learning from data*. English. Wellesley, MA: Wellesley-Cambridge Press, 2019. ISBN: 9780692196380;0692196382;

[23] Lynred. *PICO1024Gen2*. URL: https://www.lynred.com/products/pico1024gen2 (visited on 11/06/2024).

[24] A. J. Syllaios et al. "Amorphous Silicon Microbolometer Technology". In: *MRS Online Proceedings Library* 609.1 (July 2000), page 144. ISSN: 1946-4274. DOI: 10.1557/PROC-609-A14.4. URL: https://doi.org/10.1557/PROC-609-A14.4.

[25] "19 - Electrical properties". In: *Smithells Metals Reference Book (Eighth Edition)*. Edited by W.F. Gale and T.C. Totemeier. Num Pages: 19-10. Oxford: Butterworth-Heinemann, Jan. 2004, pages 19–1. ISBN: 978-0-7506-7509-3. DOI: 10.1016/B978-075067509-3/50022-1. URL: https://www.sciencedirect.com/science/article/pii/B9780750675093500221.

[26] Ramon Pallàs-Areny and John G. Webster. *Sensors and Signal Conditioning*. en. 2nd ed. New York, NY: Wiley, 2001. ISBN: 978-0-471-33232-9.

[27] Grzegorz Bieszczad and Mariusz Kastek. "Measurement of Thermal Behavior of Detector Array Surface with the Use of Microscopic Thermal Camera". en. In: *Metrology and Measurement Systems* 18.4 (Jan. 2011), pages 679–690. ISSN: 0860-8229. DOI: 10.2478/v10178-011-0064-6. URL: http://journals.pan.pl/dlibra/publication/103836/edition/89843/content (visited on 06/26/2023).

[28] Arnold Daniels. *Field guide to infrared systems, detectors, and FPAs*. en. 2nd ed. SPIE field guides FG15. Bellingham , Wash: SPIE press, 2010. ISBN: 978-0-8194-8080-4.

[29] Exosens. *High-Performance FAST Cameras*. en. URL: https://www.exosens.com/products/high-performance-fast-cameras (visited on 11/01/2024).

[30] Jinqiang Gan and Xianmin Zhang. "A review of nonlinear hysteresis modeling and control of piezoelectric actuators". In: *AIP Advances* 9.4 (Apr. 2019), page 040702. ISSN: 2158-3226. DOI: 10.1063/1.5093000. URL: https://doi.org/10.1063/1.5093000 (visited on 11/26/2024).

[31] William J. Marinelli et al. "Tunable Fabry–Perot etalon-based long-wavelength infrared imaging spectroradiometer". en. In: *Applied Optics* 38.12 (Apr. 1999), page 2594. ISSN: 0003-6935, 1539-4522. DOI: 10.1364/AO.38.002594. URL: https://opg.optica.org/abstract.cfm?URI=ao-38-12-2594 (visited on 07/03/2024).

[32] Shefford P. Baker and William D. Nix. "Mechanical properties of thin films on substrates". In: volume 1323. Dec. 1990, pages 263–276. DOI: 10.1117/12.22398. URL: https://doi.org/10.1117/12.22398.

[33] Anders Løchte Jørgensen et al. "Surface temperature determination using long range thermal emission spectroscopy based on a first order scanning Fabry-Pérot interferometer". en. In: *Optics Express* 30.2 (Jan. 2022), page 2186. ISSN: 1094-4087. DOI: 10.1364/OE.441798. URL: https://opg.optica.org/abstract.cfm?URI=oe-30-2-2186 (visited on 04/21/2023).

[34] Steven J. Byrnes. *Multilayer optical calculations*. en. arXiv:1603.02720 [physics]. Dec. 2020. DOI: https://doi.org/10.48550/arXiv.1603.02720. URL: http://arxiv.org/abs/1603.02720 (visited on 01/24/2023).

[35] Edward D. Palik. *Handbook of Optical Constants of Solids : Volume 2*. Chantilly, UNITED STATES: Elsevier Science & Technology, 1991. ISBN: 978-0-08-055630-7. URL: http://ebookcentral.proquest.com/lib/sdub/detail.action?docID=328564.

[36] Huasong Liu et al. "Study on characterization method of optical constants of germanium thin films from absorption to transparent region". en. In: *Materials Science in Semiconductor Processing* 83 (Aug. 2018), pages 58–62. ISSN: 13698001. DOI: 10.1016/j.mssp.2018.04.019. URL: https://linkinghub.elsevier.com/retrieve/pii/S1369800117328202 (visited on 11/21/2023).

[37] Edward D. Palik. *Handbook of Optical Constants of Solids, Five-Volume Set : Handbook of Thermo-Optic Coefficients of Optical Materials with Applications*. Chantilly, UNITED STATES: Elsevier Science & Tech-

nology, 1997. ISBN: 978-0-08-052375-0. URL: http://ebookcentral.proquest.com/lib/sdub/detail.action?docID=635397.

[38] Charalambos C. Katsidis and Dimitrios I. Siapkas. "General transfer-matrix method for optical multilayer systems with coherent, partially coherent, and incoherent interference". en. In: *Applied Optics* 41.19 (July 2002), page 3978. ISSN: 0003-6935, 1539-4522. DOI: 10.1364/AO.41.003978. URL: https://opg.optica.org/abstract.cfm?URI=ao-41-19-3978 (visited on 12/18/2023).

[39] Kaare Brandt Petersen and Michael Syskind Pedersen. "The Matrix Cookbook". en. In: ().

[40] Taináh M. R. Santos et al. "Improving a Tikhonov regularization method with a fractional-order differential operator for the inverse black body radiation problem". In: *Inverse Problems in Science and Engineering* 28.11 (Nov. 2020). Publisher: Taylor & Francis _eprint: https://doi.org/10.1080/17415977.2020.1732957, pages 1513–1527. ISSN: 1741-5977. DOI: 10.1080/17415977.2020.1732957. URL: https://doi.org/10.1080/17415977.2020.1732957 (visited on 01/27/2023).

[41] Lothar Reichel and Qiang Ye. "Simple square smoothing regularization operators." eng. In: *ETNA. Electronic Transactions on Numerical Analysis* [*electronic only*] 33 (2008), pages 63–83. URL: http://eudml.org/doc/130624.

[42] R. Penrose. "A generalized inverse for matrices". In: *Mathematical Proceedings of the Cambridge Philosophical Society* 51.3 (1955), pages 406–413. DOI: 10.1017/S0305004100030401.

[43] Boris T. Polyak. *Introduction to Optimization*. Optimization Software, 1987. ISBN: 0-911575-14-6.

[44] B.T. Polyak. "Some methods of speeding up the convergence of iteration methods". In: *USSR Computational Mathematics and Mathematical Physics* 4.5 (Jan. 1964), pages 1–17. ISSN: 0041-5553. DOI: 10.1016/0041-5553(64)90137-5. URL: https://www.sciencedirect.com/science/article/pii/0041555364901375.

[45] Andersen Man Shun Ang. "Nonnegative Matrix and Tensor Factorizations: Models, Algorithms and Applications". en. PhD thesis. Université de Mons, Oct. 2020.

[46] Weijie Su, Stephen Boyd, and Emmanuel J. Candes. *A Differential Equation for Modeling Nesterov's Accelerated Gradient Method: Theory and Insights*. en. arXiv:1503.01243 [stat]. Oct. 2015. DOI: 10.48550/

arXiv.1503.01243. URL: http://arxiv.org/abs/1503.01243 (visited on 01/09/2025).

[47] Ophir Optronics Solutions Ltd. *Optical Coatings*. URL: https://www.ophiropt.com/en/s/ir-coatings (visited on 01/11/2025).

[48] Janine Connes and Pierre Connes. "Near-Infrared Planetary Spectra by Fourier Spectroscopy. I. Instruments and Results". In: *Journal of the Optical Society of America* 56.7 (July 1966). Publisher: Optica Publishing Group, pages 896–910. DOI: 10.1364/JOSA.56.000896. URL: https://opg.optica.org/abstract.cfm?URI=josa-56-7-896.

[49] Shang Zhang et al. "A Spectral Reconstruction Algorithm of Miniature Spectrometer Based on Sparse Optimization and Dictionary Learning". en. In: *Sensors* 18.2 (Feb. 2018), page 644. ISSN: 1424-8220. DOI: 10.3390/s18020644. URL: http://www.mdpi.com/1424-8220/18/2/644 (visited on 01/29/2024).

[50] Cheng-Chun Chang et al. "Spectrum reconstruction for filter-array spectrum sensor from sparse template selection". In: *Optical Engineering* 50.11 (2011), page 114402. DOI: 10.1117/1.3645086. URL: https://doi.org/10.1117/1.3645086.

[51] Plastics Europe. "Plastics—The Fast Facts 2023". In: (2023).

[52] OECD. *Global Plastics Outlook: Economic Drivers, Environmental Impacts and Policy Options*. Paris: OECD Publishing, 2022. DOI: 10.1787/de747aef-en. URL: https://doi.org/10.1787/de747aef-en.

[53] Peter G. Ryan et al. "Monitoring the abundance of plastic debris in the marine environment". In: *Philosophical Transactions of the Royal Society B: Biological Sciences* 364 (2009), pages 1999–2012. DOI: 10.1098/rstb.2008.0207. URL: http://doi.org/10.1098/rstb.2008.0207.

[54] Maria Tsakona and Ieva Rucevska. "Baseline report on plastic waste". In: *UNEP report, UNEP/CHW/PWPWG. 1/INF/4* (2020).

[55] A European Commission et al. *A European strategy for plastics in a circular economy*. 2018.

[56] Martin L. Henriksen et al. "Plastic classification via in-line hyperspectral camera analysis and unsupervised machine learning". In: *Vibrational Spectroscopy* 118 (2022), page 103329. ISSN: 0924-2031. DOI: https://doi.org/10.1016/j.vibspec.2021.103329. URL: https://www.sciencedirect.com/science/article/pii/S0924203121001247.

[57] S.M. Safavi et al. "Sorting of polypropylene resins by color in MSW using visible reflectance spectroscopy". In: *Waste Management* 30.11 (2010). Special Thematic Section: Sanitary Landfilling, pages 2216–2222. ISSN: 0956-053X. DOI: https://doi.org/10.1016/j.wasman.2010.06.023. URL: https://www.sciencedirect.com/science/article/pii/S0956053X10003405.

[58] Silvia Serranti and Giuseppe Bonifazi. "2 - Techniques for separation of plastic wastes". In: *Use of Recycled Plastics in Eco-efficient Concrete*. Edited by Fernando Pacheco-Torgal et al. Woodhead Publishing Series in Civil and Structural Engineering. Woodhead Publishing, 2019, pages 9–37. ISBN: 978-0-08-102676-2. DOI: https://doi.org/10.1016/B978-0-08-102676-2.00002-5. URL: https://www.sciencedirect.com/science/article/pii/B9780081026762000025.

[59] Offer Rozenstein, Eldon Puckrin, and Jan Adamowski. "Development of a new approach based on midwave infrared spectroscopy for post-consumer black plastic waste sorting in the recycling industry". In: *Waste Management* 68 (2017), pages 38–44. ISSN: 0956-053X. DOI: https://doi.org/10.1016/j.wasman.2017.07.023. URL: https://www.sciencedirect.com/science/article/pii/S0956053X17305160.

[60] Charles Signoret et al. "Alterations of plastics spectra in MIR and the potential impacts on identification towards recycling". In: *Resources, Conservation and Recycling* 161 (2020), page 104980. ISSN: 0921-3449. DOI: https://doi.org/10.1016/j.resconrec.2020.104980. URL: https://www.sciencedirect.com/science/article/pii/S0921344920302974.

[61] Acktar Ltd. *Ultra Black Coating for MWIR and LWIR | Acktar Optical Black Coating*. en-US. URL: https://acktar.com/product/ultra-black/ (visited on 01/22/2025).

[62] Peter Meinlschmidt and Volker Maergner. "Thermographic techniques and adapted algorithms for automatic detection of foreign bodies in food". In: *Thermosense XXV*. Edited by K. Elliott Cramer and Xavier P. Maldague. Volume 5073. International Society for Optics and Photonics. SPIE, 2003, pages 168–177. DOI: 10.1117/12.488701. URL: https://doi.org/10.1117/12.488701.

[63] James Colwill et al. "Energy-efficient Systems for the Sensing and Separation of Mixed Polymers". In: *Procedia CIRP* 62 (2017). 10th CIRP Conference on Intelligent Computation in Manufac-

turing Engineering - CIRP ICME '16. [Edited by: Roberto Teti, Manager Editor: Doriana M. D'Addona], pages 512–517. ISSN: 2212-8271. DOI: https://doi.org/10.1016/j.procir.2016.06.116. URL: https://www.sciencedirect.com/science/article/pii/S2212827117300768.

[64] Kyu-Seop Kim, Sangwoo Jung, and Sejin Kwon. "Optical visualization of hypergolic burning spray structure using blue light spectrum". In: *Acta Astronautica* 193 (2022), pages 230–236. ISSN: 0094-5765. DOI: https://doi.org/10.1016/j.actaastro.2022.01.007. URL: https://www.sciencedirect.com/science/article/pii/S0094576522000078.

[65] R. Hernández and J. Ballester. "Flame imaging as a diagnostic tool for industrial combustion". In: *Combustion and Flame* 155.3 (2008), pages 509–528. ISSN: 0010-2180. DOI: https://doi.org/10.1016/j.combustflame.2008.06.010. URL: https://www.sciencedirect.com/science/article/pii/S0010218008001983.

[66] Joseph J. O'Brien et al. "High-resolution infrared thermography for capturing wildland fire behaviour: RxCADRE 2012". In: *International Journal of Wildland Fire* 25.1 (2016), pages 62–75. URL: https://doi.org/10.1071/WF14165.

[67] Ronan Paugam, Martin J. Wooster, and Gareth Roberts. "Use of Handheld Thermal Imager Data for Airborne Mapping of Fire Radiative Power and Energy and Flame Front Rate of Spread". In: *IEEE Transactions on Geoscience and Remote Sensing* 51.6 (2013), pages 3385–3399. DOI: 10.1109/TGRS.2012.2220368.

[68] Juan Meléndez and Guillermo Guarnizo. "Multispectral Mid-Infrared Camera System for Accurate Stand-Off Temperature and Column Density Measurements on Flames". In: *Sensors* 21.24 (2021). ISSN: 1424-8220. DOI: 10.3390/s21248395. URL: https://www.mdpi.com/1424-8220/21/24/8395.

[69] George Socrates. *Infrared and Raman characteristic group frequencies: tables and charts*. en. 3. ed. Chichester Weinheim: Wiley, 2001. ISBN: 978-0-471-85298-8 978-0-470-09307-8.

[70] E. C. W. Smith. "The emission spectrum of hydrocarbon flames". In: *Proceedings of the Royal Society of London. Series A* 174 (1940), pages 110–125. DOI: 10.1098/rspa.1940.0009. URL: http://doi.org/10.1098/rspa.1940.0009.

[71] A. G. Gaydon. *The Spectroscopy of Flames*. 1st edition. Published: 13 November 2013 (Softcover), 06 December 2012 (eBook). Springer Dordrecht, 1974, pages XII, 412. ISBN: 978-94-009-5722-0. DOI: 10.1007/978-94-009-5720-6. URL: https://doi.org/10.1007/978-94-009-5720-6.

[72] Sander Veraverbeke et al. "Hyperspectral remote sensing of fire: State-of-the-art and future perspectives". In: *Remote Sensing of Environment* 216 (2018), pages 105–121. ISSN: 0034-4257. DOI: https://doi.org/10.1016/j.rse.2018.06.020. URL: https://www.sciencedirect.com/science/article/pii/S0034425718302980.

[73] W. T. Rawlins et al. "Hyperspectral infrared imaging of flames using a spectrally scanning Fabry-Perot filter". In: (Jan. 2001). No. SR-1063.

[74] Yufeng Lai et al. "Characterisation of wood combustion and emission under varying moisture contents using multiple imaging techniques". In: *Fuel* 373 (2024), page 132397. ISSN: 0016-2361. DOI: https://doi.org/10.1016/j.fuel.2024.132397. URL: https://www.sciencedirect.com/science/article/pii/S001623612401545X.

[75] R. V. Kochanov et al. "HITRAN Application Programming Interface (HAPI): A comprehensive approach to working with spectroscopic data". In: *Journal of Quantitative Spectroscopy and Radiative Transfer* 177 (2016), pages 15–30. DOI: 10.1016/j.jqsrt.2016.03.005.

[76] Inc. Coblentz Society. *Evaluated Infrared Reference Spectra*. Edited by P. J. Linstrom and W. G. Mallard. NIST Chemistry WebBook, NIST Standard Reference Database Number 69. Gaithersburg, MD, 20899: National Institute of Standards and Technology, 2023. DOI: 10.18434/T4D303. URL: https://doi.org/10.18434/T4D303.

[77] D.K. Ottesen and D.A. Stephenson. "Fourier transform infrared (FT-IR) measurements in sooting flames". In: *Combustion and Flame* 46 (1982), pages 95–104. ISSN: 0010-2180. DOI: https://doi.org/10.1016/0010-2180(82)90008-6. URL: https://www.sciencedirect.com/science/article/pii/0010218082900086.

[78] P. F. Bernath. "6 Infrared emission spectroscopy". In: *Annu. Rep. Prog. Chem., Sect. C: Phys. Chem.* 96 (0 2000), pages 177–224. DOI: 10.1039/B001200I. URL: http://dx.doi.org/10.1039/B001200I.

[79] D.A. Skoog, F.J. Holler, and S.R. Crouch. *Principles of Instrumental Analysis*. Cengage Learning, 2017. ISBN: 9781337468039. URL: https://books.google.dk/books?id=D13EDQAAQBAJ.

[80] B. Rousseau et al. "Direct simulation of the high temperature optical behaviour of a porous medium based on a CT image". In: *Colloids and Surfaces A: Physicochemical and Engineering Aspects* 300.1 (2007). Proceedings of the Fourth International TRI/Princeton Workshop "Characterization of Porous Materials: from Angstroms to Millimeters", pages 162–168. ISSN: 0927-7757. DOI: https://doi.org/10.1016/j.colsurfa.2006.12.038. URL: https://www.sciencedirect.com/science/article/pii/S0927775706009757.

[81] E. A. Vinogradov and V. A. Yakovlev. "Study of Thin Film Coatings by IR Phonon-Polariton Spectroscopy Methods". In: *Journal of Surface Investigation: X-ray, Synchrotron and Neutron Techniques* 12.1 (Jan. 2018), pages 139–144. ISSN: 1819-7094. DOI: 10.1134/S1027451018010330. URL: https://doi.org/10.1134/S1027451018010330.

[82] Surray NanoSystems. *About Vantablack | Surrey NanoSystems*. URL: https://www.surreynanosystems.com/about/vantablack (visited on 01/27/2025).

[83] Bruker. *Diamonds – Characterized by FTIR Spectroscopy*. Accessed: 2025-01-24. n.d. URL: https://www.optikinstruments.hr/runtime/cache/an-m81-diamonds-en-daa1b24eb7b29aa45a60e6d8355a40d7.pdf.

[84] S Vahur, A Kriiska, and I Leito. "INVESTIGATION OF THE ADHESIVE RESIDUE ON THE FLINT INSERT AND THE ADHESIVE LUMP FOUND FROM THE PULLI EARLY MESOLITHIC SETTLEMENT SITE (ESTONIA) BY MICRO-ATR-FT-IR SPECTROSCOPY". en. In: *Estonian Journal of Archaeology* 15.1 (2011), page 3. ISSN: 1406-2933. DOI: 10.3176/arch.2011.1.01. URL: http://www.kirj.ee/?id=19159&tpl=1061&c_tpl=1064 (visited on 01/27/2025).

[85] Mads Nibe Larsen et al. "A hyperspectral thermal imager based on a low order scanning Fabry-Pérot interferometer". In: *Image Sensing Technologies: Materials, Devices, Systems, and Applications XI*. Edited by Nibir K. Dhar, Achyut K. Dutta, and Sachidananda R. Babu. Volume 13030. International Society for Optics and Photon-

ics. SPIE, 2024, 130300E. DOI: 10.1117/12.3013384. URL: https://doi.org/10.1117/12.3013384.

[86] Mads Nibe Larsen. *Hyperspectral image viewer*. en. URL: https://madsnibe.com/HSTI_viewer/ (visited on 01/28/2025).

Index

Absorptance, 19
Airy function, 71
Angular spectral shift, 83

Background, 7
Baseline correction, 117, 155
Blackbody radiation, 21
Blackbody radiation function, 24, 26

Confusion matrix, 162, 164

Data cube, 31
Detector response, 126
Dictionary, 137, 138
Dispersion, 78

Electromagnetic spectrum, 9
Emissivity, 27
Exitance, 12, 15
Explained variance, 40

Fourier Transform, 129
Free spectral range, 75
Frobenius norm, 37
FWHM, 76

Gradient descent, 122

Heavy ball method, 124
Hyperspectral imaging, 31
Hyperspectral techniques, 32

Interference, 68
Interferogram, 114
Inverse square law, 14
Irradiance, 13

Kirchhoff's law, 29, 163

Lambertian radiator, 16, 17
    Exitance, 17
    Radiance, 16
    Radiant intensity, 16
Laser diode, 60
Least squares, 119
Lipschitz, 123
Long-Wave Infrared (LWIR), 10

MCT detector, 53
Microbolometer, 48
MSE, 120
Multispectral imaging (MSI), 31

NMF, 134
Non-uniformity correction, 52

Optical path difference, 69

Phase change upon reflection, 87, 104
Photon, 8
Planck's law, 22
Principal Component Analysis, 39, 158, 180, 198, 201, 205
Principal components, 40
Push broom, 32

QT5022, 46
QT5222, 46

Radiance, 14
Radiant energy, 12
Radiant exposure, 12
Radiant flux, 12, 15

Radiant intensity, 13, 16
Radiant power, 12, 15, 17, 18
Radiometry, 11
Reconstruction, 133, 141
    Linear Algebra, 111
Reflectance, 19
Refractive index, 8, 93
Regularization, 121, 133, 137
Remapping, 130
Responsivity, 51
RGB, 31
RMSE, 133

Savitzky-Golay filter, 155
Scanning Fabry-Pérot Interferometer
    SFPI, 67
SFPI, 56
Snapshot, 33
Solid angle, 11
Spectral bending, 83
Spectral exitance, 16
Spectral processing
    Baseline correction, 35
    Mean centering, 35
    Normalization, 36
    Savitzky-Golay filter, 37
    Standard Normal Variate, 37
Spectral resolution, 79
Spectral scanning, 33
Standard Normal Variate, 155, 198
Stefan-Boltzmann law, 21
Step size, 123
Steradian, 12
System matrix, 128, 131, 133, 139

The fundamental law of radiometry, 18
Thermal time constant, 50

Trace, 119
Transmittance, 19

View factor, 18

Wavelength, 9, 10
Wavenumber, 9
Wavenumbers, 10
Whisk broom, 32
Wien's displacement law, 23